Model-Based Sensor Placement for Component Condition Monitoring and Fault Diagnosis in Fossil Energy Systems

Final Scientific/Technical Report

DOE-TTU-FE00057

Reporting Period Start Date: 1/1/2011

Reporting Period End Date: 12/31/2015

Parham Mobed[1], Pratik Pednekar[2], Debangsu Bhattacharyya[2], Richard Turton[2], Raghunathan Rengaswamy[1]

[1]Texas Tech University, Lubbock Texas, USA

[2]West Virginia University, Morgantown, WV, USA

Date Report Issued: 29 January 2016

DE-FE-0005749

Disclaimer

Abstract:

Design and operation of energy producing, near "zero-emission" coal plants has become a national imperative. This report on model-based sensor placement describes a transformative two-tier approach to identify the optimum placement, number, and type of sensors for condition monitoring and fault diagnosis in fossil energy system operations. The algorithms are tested on a high fidelity model of the integrated gasification combined cycle (IGCC) plant. For a condition monitoring network, whether equipment should be considered at a unit level or a systems level depends upon the criticality of the process equipment, its likeliness to fail, and the level of resolution desired for any specific failure. Because of the presence of a high fidelity model at the unit level, a sensor network can be designed to monitor the spatial profile of the states and estimate fault severity levels. In an IGCC plant, besides the gasifier, the sour water gas shift (WGS) reactor plays an important role. In view of this, condition monitoring of the sour WGS reactor is considered at the unit level, while a detailed plant-wide model of gasification island, including sour WGS reactor and the Selexol process, is considered for fault diagnosis at the system-level. Finally, the developed algorithms unify the two levels and identifies an optimal sensor network that maximizes the effectiveness of the overall system-level fault diagnosis and component-level condition monitoring. This work could have a major impact on the design and operation of future fossil energy plants, particularly at the grassroots level where the sensor network is yet to be identified. In addition, the same algorithms developed in this report can be further enhanced to be used in retrofits, where the objectives could be upgrade (addition of more sensors) and relocation of existing sensors.

Table of Contents

Disclaimer 2
1 Introduction 13
1.1 Purpose 13
1.2 Relevance and Impacts 13
1.3 Task Completion 13
1.4 Approach 14
1.4.1 Scientific and Technical Review 14
1.4.2 2-Tier Sensor Placement 15
1.4.3 Problem Tractability 18
1.5 Computation Tools 19
1.6 Report Organization 19
2 Process Modeling 20
2.1 Sour Water Gas Shift Reactor 20
2.1.1 Process Description 22
2.1.2 Model Development 23
2.1.3 Solution Approach 27
2.1.4 Data Reconciliation 27
2.1.5 Results and Discussions 31
2.1.6 Conclusions 41
2.2 Gasification Process 42
2.2.1 Modeling 42
2.2.2 Computational Approach 59
2.2.3 Results and Discussions 62
2.2.4 Fault Simulation 76
2.3 Gasification Island 81
2.3.1 Model Development 81
2.3.2 Study of Fault Effects 84
3 Model Simplification and Order Reduction 88
3.1 Scaling Analysis 88

3.1.1 Scaling of WGS reactor model equations: 89
3.1.2 Calculation of scales and reference factors 91
3.1.3 Calculation of reaction rate scale 91
3.1.4 Calculation of scales based on inlet reaction rate 92
3.1.5 Reduced order model of WGS reactor 95
3.1.6 Reduced order model after scaling 99
3.1.7 Comparison of simulation results from reduced order model with that of detailed model 99
3.1.8 Comparison of scales with actual simulation 101
3.1.9 Scaling of unsteady WGS model 104
3.2 Method of Characteristics 106
3.3 In-Situ Adaptive Tabulation 109
3.3.1 Algorithm 109
3.3.2 Binary tree structure 112
3.3.3 ISAT for WGSR model 114
3.4 Conclusion 114
4 System-Level Sensor Placement 115
4.1 Introduction 115
4.2 Sensor Placement Approach 116
4.3 SDG and FES Algorithms in the Presence of Numerical Simulations 117
4.4 Sensor Placement Using Magnitude Ratio 119
4.5 Constraint matrix for FES and MR 122
4.6 Formulation Summary 123
4.6.1 Optimization Problem 123
4.6.2 Solution Approach 123
4.7 Network Decomposition 123
4.7.1 Method 125
4.7.2 Fault detection for decomposed system 127
5 Distributed Sensor Placement 128
5.1 State Estimation Development 128
5.1.1 Introduction 128
5.1.2 State estimation of DAE systems 129
5.1.3 Equality constrained state estimation of uncertain nonlinear DAEs 131

5.2 Distributed Sensor Placement Problem Formulation 136
5.2.1 Introduction 136
5.2.2 Summary of WGS Model simplification 138
5.2.3 EKF for simplified model 138
5.2.4 Genetic algorithm 140
6 Interpretation of Results 140
6.1 System-Level Sensor Placement 140
6.1.1 CSTR Case Study 141
6.1.2 Five-Tank Case Study 145
6.1.3 Tennessee Eastman Case Study 148
6.1.4 SELEXOL Process Case Study 151
6.1.5 Combined Cycle Case Study 154
6.1.6 System Decomposition 164
6.1.7 Conclusion 167
6.2 Distributed Sensor Placement 168
6.2.1 State Estimation Validation 168
6.2.2 Optimal Distributed Sensor Placement 177
6.2.3 Conclusion 183
6.3 2-tier Sensor Placement for Gasification Island 185
6.3.1 Fault Simulation 185
6.3.2 Results 190
7 Summary 203
8 Recommendations and research output 203
9 References 208

List of Figures

Figure 1. Schematic of the 2-tier sensor placement approach 15
Figure 2. Genetic algorithm approach..... 16
Figure 3. Diagnostic approach for fault diagnosis and condition monitoring..... 17
Figure 4. Diagram of the data reconciliation procedure 29
Figure 5. Arrhenius plot for the water gas shift reaction 31
Figure 6. CO mole fraction profile along the reactor when length is increased to 40 m 32
Figure 7. (a)COS mole fraction (b) Gas temperature profile along the reactor when length is increased to 40 m 33
Figure 8. CO mole fraction profile for different reactor diameters..... 34
Figure 9. Pressure profile for different reactor diameters 34
Figure 10 shows the relation between the *L/D* ratio and pressure drop at constant reactor volume. This result indicates that as *L/D* increases, the pressure drop keeps increasing. It should be noted that a lower pressure drop is desired in the WGS reactor system so that higher partial pressure of CO_2 can be achieved in the AGR unit. This is particularly important for achieving higher efficiency of the physical solvent-based CO_2 capture process in the IGCC plant.[31]Figure 10. Pressure drop vs. L/D ratio of the reactor 34
Figure 11. CO conversion profiles for different inlet gas temperatures..... 36
Figure 12. COS conversion profiles for different inlet gas temperatures 36
Figure 13. CO conversion transient for a step change in inlet temperature from 620 to 640 K 37
Figure 14. Temperature transient at the outlet of the reactor for a step change in inlet temperature from 620 to 640 K..... 38
Figure 15. CO conversion profile for different steam/CO molar ratio..... 39
Figure 16. Required (a) Diameter (b) Flow at different steam/CO molar ratios..... 39
Figure 17. Effect of catalyst deactivation over time on CO conversion 40
Figure 18. COS conversion along the reactor after the catalyst lifetime of 5 years..... 41
Figure 19. Slag formation and detachment. 43
Figure 20. Hybrid shrinking core shrinking particle (HSCSP) model. 45
Figure 21. Schematic of the formation mechanism of slag droplets and their deposition on the wall along with char particles and the subsequent formation of a slag layer on the gasifier wall. 46
Figure 22. Continuum phase domain for solid and gas integrated with the particle phase domain. 47
Figure 23. Schematic representation of the notations for denoting solids fractions in the continuum model. 48
Figure 24. Schematic of the recirculation model. 49
Figure 25. Transfer of information between the particle model and continuum model..... 52
Figure 26. Schematic showing the slag droplet deposition on the gasifier wall. 55
Figure 27. General plot showing the relation between the Vdep + and τ+ redrawn from Guha[114]. 56
Figure 28. Schematic of the mass, momentum and energy interactions in the slag layer. 58
Figure 29. Control structure implemented to simulate dynamic runs for the slagging gasifier. 62
Figure 30. Comparisons of the mole fractions of CO2, CO, H2 and ¬¬H2O (on dry basis) at the exit of the RSC with TECO data. 63
Figure 31. Comparison of the reaction rates between the shrinking particle model and hybrid shrinking core-shrinking particle model. 64
Figure 32. Comparison of carbon conversion of carbon between the gasifier model and the complete coalescence model. 64
Figure 33. Comparison of solids temperature profiles between the shrinking core and HSCSP model. 65

Figure 34. Variation of diameter of char particles, attached slag droplets, and average density of the char-slag system along the gasifier. 66
Figure 35. Deposition flux and slag layer thickness profile for base case PSD. 68
Figure 36. Slag droplet deposition flux and slag layer thickness for cases SD-5-50 and SD 60-10. 69
Figure 37. Comparison of the slag layer thickness for Case CC and base case. 69
Figure 38. Effect of change in O2/coal ratio on slag layer thickness at gasifier exit. 70
Figure 39. Variation of the maximum and minimum slag layer temperature due to change in O_2/Coal feed ratio. 71
Figure 40. Effect of silica ratio on exit viscosity and slag layer thickness. 72
Figure 41. Effect of ramp change in coal slurry flow rate on slag layer thickness at final CV. 73
Figure 42. Effect of ramp change in coal slurry flow rate on slag layer temperature at final CV. 73
Figure 43. Change in outlet gas composition and carbon conversion during coal switch from Illinois #6 to Pittsburgh #8 coal. 74
Figure 44. Deposition flux before and after change of coal from Illinois #6 to Pittsburgh #8. 74
Figure 45. Slag layer temperature and viscosity profile before and after the coal switch. 75
Figure 46. Transient response of slag layer and wall temperature and slag thickness at gasifier exit. 75
Figure 47. Slag penetration into the high chrome refractory at different time instances. 77
Figure 48. Steady state temperature profile along the refractory across the four layers. 78
Figure 49. Coal slurry set point variation in the gasifier model. 79
Figure 50. Wall temperature at the grid point selected for simulating degradation. 80
Figure 51. Time for first spall for the four cases. 80
Figure 52. Schematic representation of the Sour Water Gas Shift Reactor system developed in MATLAB. 82
Figure 53. Exchange of information between the SWGSR in MATLAB and the Selexol model in APD. 83
Figure 54. Temperature profile along reactor R2. 83
Figure 55. Profile of CO mole fraction along the length of reactor R2. 84
Figure 56. Plot of COS mole fraction along R2. 84
Figure 57. CO at the end of R1 as a result of a ramp change in the porosity. 85
Figure 58. COS at the end of R1 as a result of a ramp change in porosity. 85
Figure 59. Temperature at end of R1 as a result of a ramp change in porosity. 86
Figure 60. CO mole fraction at end of R2 as a result of ramp change in porosity. 86
Figure 61. COS mole fraction at end of R2 as a result of ramp change in porosity. 87
Figure 62. Temperature response at the exit of R2 as a result of ramp change in porosity. 87
Figure 63. CO response at the exit of the Selexol unit as a result of ramp change in porosity. 88
Figure 64. Typical variation of exothermic reaction rate along the length of the reactor. 92
Figure 65. Concentration profile of COS from detailed and reduced model for WGS reactor. 101
Figure 66. Temperature profile from detailed and reduced model for WGS reactor. 101
Figure 67. Dynamic response of outlet gas temperature for a step up of 20 degrees in the inlet gas temperature from detailed and reduced order model. 106
Figure 68. Schematic figure showing the characteristic lines in (z-t) plane. 107
Figure 69. Schematic figure showing the approximation involved in the solution of dependent variable along characteristic lines. 108
Figure 70. Dynamic response of outlet gas temperature for a step up of 20 degrees in the inlet gas temperature from detailed and reduced order model. 108
Figure 71. Concept of direct integration and ISAT when the model is solved several times. 109
Figure 72. Addition of record in a solution space. 111
Figure 73. Growth of EOA where grow EOA encompasses the initial EOA and the query point. 112

Figure 74. Binary tree showing nodes and leaves. 113
Figure 75. Binary tree shown in search space where represent a new query point . Corresponding binary tree structure is shown on the right hand side. 114
Figure 76. Dynamic simulation of WGSR model using ISAT with retrieval and direct integration (DI). 114
Figure 77. Flowchart of FES algorithm in presence of numerical solution 119
Figure 78. Magnitude ratio for example in Table 18 120
Figure 79. Flowchart of MR algorithm 122
Figure 80. Representation of adjacency matrix 125
Figure 81. Pseudo-fault representation for two sub-systems. 127
Figure 82. Schematic of the CSTR system[182] 141
Figure 83. Schematic of the five-tank case-study[181] 145
Figure 84. TE process flowsheet[196] 149
Figure 85. Schematic of the SELEXOL process[198] 152
Figure 86. Schematic of the combined cycle power plant. 155
Figure 87. Schematic of the high pressure steam generation vessel. 156
Figure 88. Schematic of the heat exchanger between the syngas stream and the high pressure steam. 156
Figure 89. Schematic of the condenser where steam/condensate is cooled by cooling water. 157
Figure 90. Schematic of the heat exchanger (part of HRSG) where the combusted syngas is used to superheat the steam. 157
Figure 91. Schematic of the gas turbine combustor. 157
Figure 92. Heat exchanger cooling combusted syngas with intermediate pressure steam. 158
Figure 93. Volumetric flow rate of the leaking steam stream into the syngas stream due to Fault 2. 159
Figure 94. Temperature change of the Syngas stream at the outlet of the Heat exchanger due to Fault 2. 159
Figure 95. Flow rate change of the syngas stream exiting the heat exchanger due to Fault 2. 160
Figure 96. Temperature change of the flue gas at the outlet of the superheater due to Fault 4. 160
Figure 97. Change in Flow rate of Combusted Syngas stream due to Fault 4. 161
Figure 98. Change in Temperature of the outlet Syngas stream due to Fault 7. 161
Figure 99. Number of irresolvable faults (left) and the corresponding sensor network cost (right) at different MR threshold values 163
Figure 100. Actual, measured and estimated values of differential variable x_1. 170
Figure 101. Actual, measured and estimated values of differential variable x_2. 171
Figure 102. Actual, measured and estimated values of algebraic variable z 171
Figure 103. Schematic of the WGSR system 172
Figure 104. Actual (-), measured (*) and estimated (--) value at 9th grid-point on the reactor for (a) y_{CO} ($RMSE_{data} = 5.005 \times 10^{-3}$, $RMSE_{est} = 3.852 \times 10^{-3}$) (b) y_{H2O} ($RMSE_{data} = 5.003 \times 10^{-3}$, $RMSE_{est} = 3.827 \times 10^{-3}$) (c) T_g ($RMSE_{data} = 7.978 \times 10^{-3}$, $RMSE_{est} = 4.945 \times 10^{-3}$) 175
Figure 105. Actual (-), measured (*) and estimated (--) value at 9th grid-point on the reactor for (a) P ($RMSE_{data} = 1.998 \times 10^{-3}$, $RMSE_{est} = 0.894 \times 10^{-3}$ using Filter II) (b) P ($RMSE_{est} = 5.312 \times 10^{-3}$ using Filter I). 175
Figure 106. Normalized fitness evolution for each model 180
Figure 107. Change in CO mole fraction at the exit of the SWGSR due to faults. 186
Figure 108. Change in COS mole fraction at the exit of the SWGSR due to faults. 186
Figure 109. Change in outlet temperature of the SWGSR due to faults. 187
Figure 110. HE configuration 1: leak simulated as mixing of inlet high pressure stream into outlet low pressure stream. 189

Figure 111. HE configuration 2: leak simulated as mixing of outlet high pressure stream into inlet low pressure stream..... 189
Figure 112. GA progress for different faults..... 192
Figure 113. Fault severity estimation using optimal solution for fault (a) F_{25} (b) F_{26} (c) F_{27} (d) F_{31} (e) F_{32} 194
Figure 114. Fault severity estimation using final sensor network for fault (a) F_{25} (b) F_{26} (c) F_{27} (d) F_{31} (e) F_{32}..... 196
Figure 115. Actual (-), measured (*) and estimated (--) value of different states at the outlet of the reactor for fault F_{25}..... 198
Figure 116. Actual (-), measured (*) and estimated (--) value of different states at the outlet of the reactor for fault F_{26}..... 199
Figure 117. Actual (-), measured (*) and estimated (--) value of different states at the outlet of the reactor for fault F_{27}..... 200
Figure 118. Actual (-), measured (*) and estimated (--) value of different states at the outlet of the reactor for fault F_{31}..... 201
Figure 119. Actual (-), measured (*) and estimated (--) value of different states at the outlet of the reactor for fault F_{32}..... 202

List of Tables

Table 1. Properties of Catalyst Q[61] 28
Table 2. Standard deviation of different variables[81,82] 29
Table 3. Comparison of the reconciled and original mole fractions[61] 30
Table 4. Simulation condition[83] 31
Table 5. Model parameters and input conditions 60
Table 6. Proximate and Ultimate analysis of Illinois #6 and Pittsburgh #8 coal [As-Received (wt %)] 61
Table 7. Validation data from TECO power plant[140] 62
Table 8. Comparison between outlet mole fractions of SCM and HSCSP models 65
Table 9. Comparison of the results from this work with the existing literature[91,142] 67
Table 10. Simulated particle size distributions 68
Table 11. Silica ratios calculated for Illinois #6 coal taken from literature 71
Table 12. Parameters and inlet conditions for WGS reactor 95
Table 13. Values of dimensionless group for the WGS reactor model 97
Table 14. Metric for comparing reduced and detailed model simulation 100
Table 15. Exact values and approximate values of the scales 102
Table 16. WGS reactor dimensionless equations are shown as algebraic equations with their corresponding values from simulation and scaling analysis 103
Table 17. Summary of detailed and reduced order model 105
Table 18. SDG example 120
Table 19. Type and cost of each sensor used in all case studies[190] 141
Table 20. List of measured variables in CSTR system 141
Table 21. List of simulated faults and the corresponding affected sensors in CSTR system 142
Table 22. Results of applying different algorithms to CSTR system 142
Table 23. Fault resolution by SDG, FES and MR in CSTR system 143
Table 24. List of measured variables in five-tank case-study 145
Table 25. List of simulated faults and the corresponding affected sensors in five-tank case-study 145
Table 26. Results of applying different algorithms to five-tank case-study 146
Table 27. Fault resolution by SDG, FES and MR in five-tank case-study 147
Table 28. List of measured variables in TE process[197] 149
Table 29. List of simulated faults in TE process[197] 150
Table 30. Results of applying different algorithms to TE process 150
Table 31. Fault resolution by SDG, FES and MR in TE process 151
Table 32. List of measured variables in SELEXOL process 152
Table 33. List of simulated faults in SELEXOL process 153
Table 34. Results of applying different algorithms to SELEXOL process 154
Table 35. Faults at different severity level simulated in the combined cycle model 162
Table 36. Weight and threshold of each variable in the sensor placement algorithms 162
Table 37. SDG and FES algorithms results 162
Table 38. MR algorithm results 163
Table 39. Sensitivity analysis of number of sub-systems 165
Table 40. Sensitivity analysis of number of nodes and fault nodes 166
Table 41. Sensitivity analysis of number of cross-connections 167
Table 42. Comparison of RMSE and SSE values for measured and estimated values 172
Table 43. Summary of equations for Water gas shift reactor 172
Table 44. Summary of the parameters of the WGSR model used in this work 173

Table 45. Sum of squared errors value when fixed points measure the same type of states 176
Table 46. Sum of squared errors with one missing measurement 177
Table 47. SSE values with measurement combination 177
Table 48. Water gas shift reactor model parameters 178
Table 49. Process noise variance values for different models 179
Table 50. Sensor placement results and computation time for each model 181
Table 51. Sensor placement results comparison of Model I and Model V for different number of sensors 182
Table 52. Effect of process noise covariance on the sensor placement results 182
Table 53. Effect of initial error covariance on the sensor placement results 183
Table 54. Faults simulated on the SELEXOL side of the integrated model 188
Table 55. Faults simulated on the SWGSR side of the integrated model 190
Table 56. System-level sensor placement results of gasification island 190
Table 57. List of sensors and unresolved fault sets for FES & MR algorithm with low MR threshold level 191
Table 58. Reactor and state estimation parameters 192
Table 59. Optimal location and type of sensors for different faults 193
Table 60. Comparison of normalized fitness values for GA solution and final sensor network 197

1 Introduction

1.1 Purpose

The goal of this project is to establish a comprehensive methodology to determine the type, location, and number of sensors required for component condition monitoring and fault diagnosis in fossil energy systems. Through a transformative two-tier framework, the project seeks to develop a model-based sensor placement methodology that addresses: (i) Sensor placement for fault diagnosis based on tractable models that are developed from the system level dynamic model, (ii) Identification of precise locations for component condition monitoring based on distributed component level models.

The theoretical and computational efforts undertaken as a part of this project are delivered as a framework that can be used in combination with simulations of fossil energy systems. The framework developed in this project can be enhanced to include any other simulation system through appropriate use of first-principles modeling and state estimation techniques.

1.2 Relevance and Impacts

It is well known that considerable coal resources exist in the United States. However, coal utilization is accompanied by the associated pollution related concerns. In response to this, design and operation of energy producing, near "zero-emission" coal plants has become a national imperative. This report on model-based sensor placement will provide a formal approach to identify the optimum placement, number, and type of sensors that will be sufficient for condition monitoring and fault diagnosis in fossil energy system operations. This work could have a major impact on the design and operation of future fossil energy plants, particularly at the grassroots level where the sensor network is yet to be identified. In addition, the same algorithms developed in this report can be further enhanced to be used in retrofits, where the objectives could be upgrade (addition of more sensors) and relocation of existing sensors.

1.3 Task Completion

Table I shows the list of tasks proposed in this project and the corresponding section in this report where the results for the identified tasks are reported.

Table I. Completed tasks and the corresponding sections for the completion of the project

Task		Description	Section
2	2.1	Development of the distributed sensor placement algorithm using UIF and genetic search	2.1.1 3 5 6.2
	2.2	Development of the algorithm for sensor placement for system-level fault diagnosis with enhancements to the qualitative math model. Tested on SELEXOL plant	4.1-4.3 6.1.1-6.1.4
	2.3	Identification of the faults in the gasification island and in the gasifier, further development of the water gas shift reactor model, and model enhancement to incorporate simulation models for faults and disturbances in the WGSR	2.1.2 2.2 6.2.2 6.3.1
3	3.1	Implementation of the condition monitoring sensor placement algorithm on the WGS model. System-level faults will not be considered here but will be considered once the two-tier sensor placement is complete	6.2.1
	3.2	Further development of plant-wide sensor placement	4.4

		algorithms to include the reliability approach and development of Integer Linear Programming	
	3.3	Identification of faults and model enhancement to incorporate faults in the combined cycle island	6.1.5
4	4.1	Identification of sensor placement for plant-wide fault diagnosis using the plant-wide dynamic simulation model	6.3.2.1
	4.2	Validation of the identified sensor placement for condition monitoring in WGSR and make necessary enhancements	6.2.1
	4.3	Thorough testing of the already identified distributed sensor placement for condition monitoring using the nonlinear WGSR model. Only the faults in the WGSR will be considered. The impact of the system-level faults will be evaluated after the integrated two-tier sensor placement is completed.	6.3.2.1
5	5.1	Synthesis of the optimal sensor network by considering the two-tier design algorithm for plant-level fault diagnosis and unit-level condition monitoring and validation of the algorithm	6.3
	5.2	Summary of the project	7

1.4 Approach

1.4.1 Scientific and Technical Review

This report includes the development of algorithms that can determine the optimized sensor locations and types for robust condition monitoring and fault diagnosis in a fossil energy-derived power generation system. With these objectives in mind, in this report, we will develop algorithms for maximizing the effectiveness of the sensor network for system-level fault diagnosis and component-level condition monitoring. The root cause for productivity losses and shut-downs are called “faults” in this report. The algorithms are developed for and tested on a high fidelity model of the integrated gasification combined cycle (IGCC) plant. For a condition monitoring network, whether equipment should be considered at a unit level or a systems level depends upon the criticality of the process equipment, its likeliness to fail, and the level of resolution desired for any specific failure. Because of the presence of a higher fidelity model at the unit level, a sensor network can be designed to monitor the spatial profile of the states and estimate fault severity levels. In an IGCC plant, besides the gasifier, the sour water gas shift (WGS) reactor plays an important role. Yet, it is one of the equipment with the high likelihood to failure because of the harsh conditions that it is subjected to. In view of this, we have considered condition monitoring of the sour WGS reactor at the unit level, while a detailed plant-wide model of gasification island (including sour WGS reactor and the Selexol process) is considered for fault diagnosis at the system-level. Finally, the developed algorithms unify the two levels and identify an optimal sensor network that maximizes the effectiveness of the overall system-level fault diagnosis and component-level condition monitoring. Measurement and model uncertainties are naturally handled in the solution approach while sensor failure probabilities and failure occurrence probabilities can be easily included, if required.

While there is considerable amount of literature on sensor placement, computationally efficient sensor placement algorithms that provide a comprehensive solution as envisaged in this report are minimal.

Through a transformative two-tier sensor placement framework that incorporates already developed technology, when available, in combination with novel ideas reported here, we seek to solve this comprehensive sensor network problem. The sensor placement problem in its broadest sense has to use information regarding - available sensors and their failure rates, available failure information and their occurrence rates, component and system models, criticality of the individual components to the process, nature of the component models available (lumped, distributed) - to provide recommendations regarding the location, type, and number of sensors for an efficient component monitoring and fault diagnosis network. This is a challenging problem because while component-level approaches will fail to utilize the synergistic system-level interactions, a system-level view will result in computational intractability. This has been a major challenge in developing efficient solutions to this problem. The reported solution approach follows a "divide-and-conquer" philosophy. The key to the success of this philosophy is in using appropriate models and information at the correct level of the problem. This is depicted in **Error! Not a valid bookmark self-reference.**.

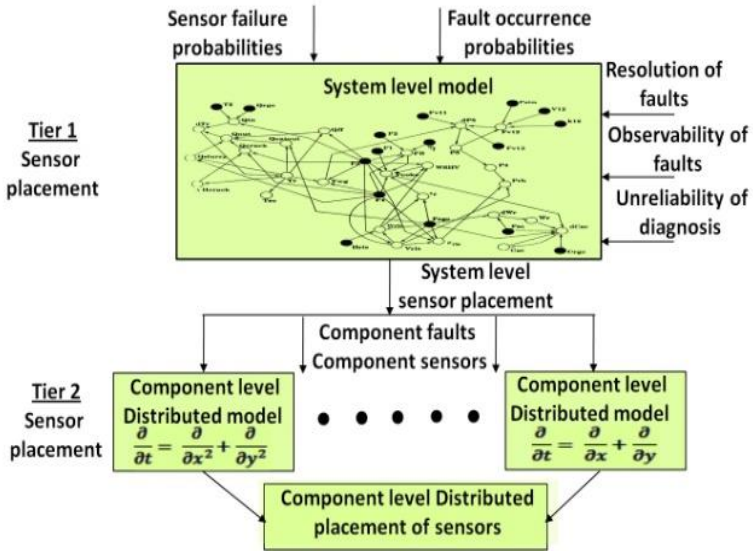

Figure 1. Schematic of the 2-tier sensor placement approach

1.4.2 2-Tier Sensor Placement

The sensor placement problem is decoupled into two tiers. Tier I deals with system-level sensor placement. A model that is appropriate at this level, that is, a qualitative math model is used. It should be noted that a plant-scale coupled Partial Differential Equations (PDEs) can run into thousands of equations and solving them within an optimization loop for sensor placement will likely be computationally intractable. The previous works have demonstrated the use of graph models such as the Signed Directed Graph (SDG) model for plant-level diagnosis.[1,2,3,4,5,6,7] The objective function for sensor placement is a critical component in the resulting sensor placement algorithms. Resolving all the hypothesized faults could be one objective.[8] An alternate objective is to maximize reliability of the fault diagnosis network with maximum possible resolution of failure origins as constraints imposed on the solution. The original cost minimization formulation with maximum resolution satisfies the objective efficiently and will be used in tier I sensor placement. The maximum resolution that is possible is a complex function of both the system characteristics and the model that is used in the sensor placement approach. Our reported approach ensures that all the faults that are resolvable are indeed resolved by the sensor placement algorithm and at the same time the fault diagnosis network is highly cost effective. Bhushan and Rengaswamy[5] showed

how this sensor placement problem could be converted to an Integer Linear Programming (ILP) problem using some transformations. This is the solution approach that will be used in this report. Tier I solution will identify the optimal cost sensor placements that achieve the maximum resolution possible given the system description and the qualitative cause-effect mathematical model of the system in presence of the numerical solution (obviously this system model will also include the faults and sensors of the individual components that are considered in tier II). Moreover, our contention is that it is more natural to handle this problem at a component level with high fidelity math models. This integrates system-level fault diagnosis with component level condition monitoring. As a result, tier II sensor placement goal is estimation of failure severity at the component-level. The sensors identified at this level help not only in estimation of failure severity at the component-level but also in failure resolution when needed. This goal is achieved by coupling appropriate state and parameter estimation techniques (can be thought of as an unknown input filter (UIF)) with a Genetic Algorithm (GA) optimization approach as shown in Figure 2. A filter needs to be used because of the need to estimate severity levels. By augmenting fault magnitudes as parameters in the filter, failure severity can be estimated. The main objective of tier II sensor placement is the identification of the sensor locations. For this, the distributed model is converted to an Ordinary Differential Equation (ODE) model that the state and parameter approaches work with. This is achieved by discretizing the distributed model using method of lines. This is a well-known approach for

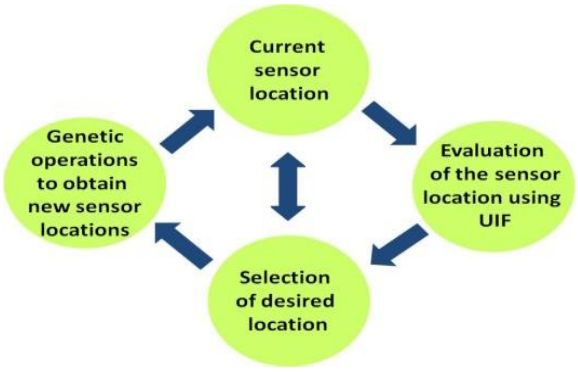

Figure 2. Genetic algorithm approach

converting PDE to ODE.

Optimized sensor locations are identified using a genetic algorithm (GA) approach as shown in Figure 2. The decision variables are discrete (1 if a sensor is placed at a particular distributed location and 0 if not). The objective function is usually a squared error between the actual and estimated failure severities.

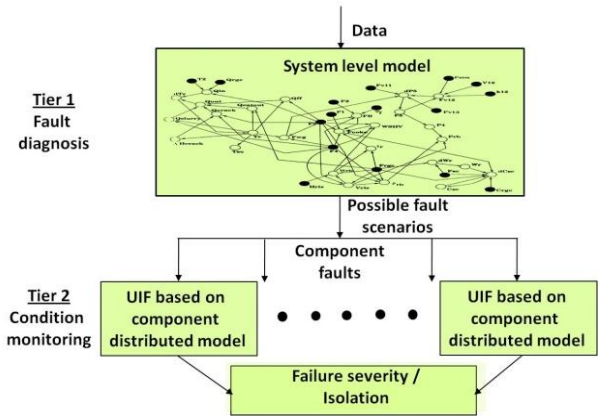

Figure 3. Diagnostic approach for fault diagnosis and condition monitoring

Further, the objective function - which reflects how well the actual location and the severity of the fault is captured for a particular sensor network - is nonlinear and does not have a closed form analytical expression. This makes it difficult to optimize the sensor locations using standard math programming based approaches. Evolutionary algorithm approaches have been demonstrated to successfully solve such problems in several application areas.[8,9,10,11,12] Once these sensor locations are identified, the actual fault diagnosis and condition monitoring in real-time can also be achieved using the models and methods used in the sensor placement algorithm as shown in Figure 3. Given a list of possible failures, plant-level data with the qualitative model is used to obtain the optimal sensor network. Based on the faults, the corresponding state and parameter estimator is run to estimate failure severity. Hence the sensor placement algorithms seamlessly develop a fault diagnosis and condition monitoring approach for eventual verification of the suggested sensor locations.

As mentioned before, the IGCC plant will be considered for the sensor placement in this report. Although, several configurations of IGCC plants are possible, the focus of the current work will be on a plant based on case #2 from the baseline DOE study[13] that incorporates a GEE-type gasifier with CO_2 capture and removal. Gasification island and the combination cycle island are considered in this model. The plant model includes an entrained, downflow, GEE-type gasifier with a radiant syngas cooler (RSC), a two-stage sour water gas shift (WGS) conversion process with inter-stage cooling, a physical absorption process, and two advanced "F" class combustion turbines partially integrated with an elevated-pressure air separation unit (ASU). Typical faults in this plant include the blocking of the radiant syngas cooler (RSC), leakage in pipes in the black water service, leakage in the sour syngas pipe before and after sour WGS reactors, failure of the ASU MAC (Main Air Compressor), leakage in the Claus Catalytic Reactor, mechanical failure of the main BFW (Boiler Feed Water) pump, poisoning of the sour WGS reactor catalyst, poisoning of the Claus plant catalyst, fouling of the heat exchangers particularly those in the black-water, and sour-water service and the exchangers in the Claus plant, etc. It is guaranteed that all the possible faults are identified and considered, but the faults critical for improving the availability of the IGCC plant are considered although some remain unresolved. The various types of sensors that will be considered in this report include temperature, pressure, flow, level, and composition sensors. Base case sensor placements will be generated using such sensors. The reports from the TECO IGCC plant at Polk county, Florida provide immense insight into many of the typical problems. Let's consider examples from one such report and how that will be modeled in Aspen Plus Dynamics. In an assessment of the plant availability during October, 2000-September, 2001 run of the TECO plant, the following faults were mentioned that led to shutdown during this fifth year of operation: 5 forced outages due to syngas and blackwater line leaks, plugged RSC outlet line, syngas scrubber outage, icing in the main exchanger in the

ASU due to missed steps in the regeneration cycle of the air dryer, deposit of the heat stable salt in the MDEA absorber, etc.[14] It was mentioned that, "We could have eliminated or mitigated the losses in most cases.[14] These faults can be simulated in the Aspen Plus Dynamics and the transient results can be used in the fault diagnosis algorithm. For example, the leak in the syngas line can be simulated by adding a pipe with a valve to the syngas line and opening the valve slowly through a "Flowsheet Task" in Aspen Plus Dynamics. The deposit of a solid in the tray of a distillation column can be simulated by slowly blocking the open area of the tray implemented through script in Aspen Plus Dynamics. These changes can be done manually or by some predefined function written in script of Aspen Plus Dynamics. The commissioning, operational, and project execution experiences of the TECO IGCC power plant at Polk Country, Florida are extensively used in this project for identification of the faults at the plant level as well as at the unit level. A number of reports detailing the various phases of this plant are available in the public domain.[14,15,16,17,18,19] The reports of the pilot plant studies and the issues faced in the commercialization of the Texaco process are also available.[20,21,22,23] Cool Water IGCC plant also had Texaco gasifier, report of which is also available.[24,25] Project and operational reports of plants using non-GEE-type gasifiers are also available.[26,27] Operational experiences of these projects will also be utilized whenever applicable. Issues and concerns of various commercial gasifiers have been mentioned in a DOE report.[28] A thorough review of the existing literature has led us to come up with a list of frequent and important faults encountered in an IGCC plant especially in sour WGS reactor.

The main problem in the sour WGS reactor is the catalyst poisoning that includes catalyst activity, porosity and surface area reduction. These faults can be simulated by changing the activity, porosity or surface area of the catalyst in the sour WGS reactor model, respectively. In this project, a 1-d first principles sour WGS reactor model is developed and used. This model considers mass, momentum, and energy balances as well as detailed kinetic models of the water gas shift and carbonyl sulfide hydrolysis reactions.

1.4.3 Problem Tractability

1.4.3.1 Model Simplification and Order Reduction

Even if the first-principles model is tractable, embedding a first-principles model in an optimization loop may be intractable. The component level sensor placement algorithm consists of three primary computational modules that form an optimization loop: (i) solution to the first principles model, (ii) solution to the filter problem, and (iii) GA-related computations. States in the process model are estimated by solving the filter equations. If the process model is nonlinear, the model must be integrated and linearized at every time step of the state estimation, which adds to the complexity of the problem. The GA optimizes a defined objective function and searches in the vast solution space for the optimal solutions, where each attempt of the GA requires performing a state estimation of the process model, thus, making the component-level sensor placement significantly computationally intensive and time consuming. In order to reduce the computational complexity, an efficient approach is to reduce the complexity of the process model, thus, the computations will be reduced for the entire optimization loop. A simple way to reduce the complexity of a process model is to linearize the model around the operating point. However, in presence of faults, this approach may lead to unacceptable inaccuracies. The approach taken in this project for model simplification and order reduction is a combination of scaling analysis, method of characteristic and in-situ adaptive tabulation (ISAT). The model simplification is attempted and implemented in component-level sensor placement. The method of characteristics and ISAT are attempted to show how they can be implemented in the distributed sensor placement approach. The implementation of scaling analysis at the component-level sensor placement is found to be sufficient for the work envisaged in this project and the implementation of the reduced order models are recommended for future efforts in component-level sensor placement.

1.4.3.2 Network Decomposition

The use of graph models for plant-level sensor placement promises significant reduction in computations compared to the use of plant-scale coupled PDEs. Although the plant-level sensor placement is performed by solving an ILP working on signed directed graphs, there are limitations on how large the graph networks can be when considering fault resolution. Moreover, as more information is added to the plant-level sensor placement algorithm, the plant-wide sensor placement will likely be computationally complex. A general approach in graph theory for reducing the computational complexity is the use of graph partitioning techniques. In graph partitioning techniques, the graph is divided into smaller components with components holding specific properties. Due to the nature of graph partitioning problem, these problems are generally solved by developing heuristic and approximation algorithms. Typically, the graph partitioning problem attempts to group most interacting components together and minimize the interaction between the groups. In this project, we have attempted to study the effect of different parameters including computation time, fault resolution and sensor network cost on graph partitioning algorithms with fault detection and diagnosis as the objective. The result of this study opens the door for further progress and can help researchers when developing partitioning algorithms for fault detection and diagnosis.

1.5 Computation Tools

MATLAB®, a computing environment developed by MathWorks®, is one of the main engineering software used in this project for modeling and optimization. Except for the gasifier model developed in Aspen Plus®, all of the system- and component-level sensor placement algorithms and the corresponding simulations are performed in MATLAB environment. Aspen Plus is chemical process simulation software developed by AspenTech that is used in this report for modeling and simulation of gasifier. The Simulink interface developed by MathWorks links the Aspen Plus to MATLAB for simulation of integrated systems including gasification island and combined cycle. IBM ILOG CPLEX® optimization toolbox for MATLAB is used within MATLAB environment for solving integer linear programming problems in system-level sensor placement while other optimization problems are solved using MATLAB's default optimization toolbox. The final optimization of component-level sensor placement which involves genetic search can be efficiently performed in parallel. The parallel computation is provided by Texas Tech University's High Performance Computing Center (HPCC). HPCC's computing resource, Hrothgar, has 86 teraflops in 7680 2.8 GHz cores and 12.3 teraflops in 1024 3.0 GHz cores. However, the regular MATLAB parallel computation license on HPCC is limited to use of 12 cores (increased to 20 cores in 2015) per each computing job.

1.6 Report Organization

Section 1.0 – Introduction: Discusses the purpose, relevance and impacts of the study. The fundamental information and overall approach of the study is briefly described.

Section 2.0 – Process Modeling: Describes the development of process models for sour water gas shift reactor and gasifier in complete detail. Simulation studies for model validation and sensitivity studies are also provided.

Section 3.0 – Model Simplification and Order Reduction: Provides a mathematical approach for simplifying the sour gas shift process model, as well as well-known techniques for order reduction, including the method of characteristics and in-situ adaptive tabulation.

Section 4.0 – System-Level Sensor Placement: Describes qualitative-analysis of causal models for fault detection and introduces an enhancement to previously developed algorithms. Implementation of algorithms in presence of numerical simulations is discussed as well. The necessity of graph partitioning for fault detection, as well as a method for sensitivity analysis of network systems is described.

Section 5.0 – Distributed Sensor Placement: Explains the constrained state estimation and the genetic algorithm involved in distributed sensor placement. For state estimation, the development and formulation of constrained extended Kalman filter for differential and algebraic systems are described, as well as the implementation on the sour water gas shift model and its simplified model. The optimization problem for sensor placement and the genetic algorithm properties used for finding its solution are also discussed.

Section 6.0 – Interpretation of Results: This section provides case studies for the algorithms developed in the previous sections. After validating the results, the algorithms are implemented on the gasification island to identify a 2-tier sensor placement approach for fault detection and fault severity estimation. The faults that are considered in the gasification island are also explained in this section.

Section 7 – Summary: Discusses the overall study results and conclusions.

Section 8 – Recommendations: Discusses the direction for future research and provides explanation of the use of 2-tier sensor placement framework for other systems. The publication output from the project is also described.

Section 9 – References

2 Process Modeling

2.1 Sour Water Gas Shift Reactor

Fossil fuels are the main sources of non-renewable energy used by humans. Among these fuels, coal is found in abundance in U.S., while costing less (on a specific energy basis) than other fossil fuels. The major drawback to using coal is the growing concern of the impact of global greenhouse gas emissions and the effect of tighter emission regulations on the coal-based power plants. In addition to carbon and hydrogen, coal contains significant amounts of impurities, such as sulfur compounds and mercury, as a result burnt coal not only produces carbon dioxide (CO_2), a major component of greenhouse gas, but also other pollutants that are hazardous to the environment. To overcome these problems, coal power plants should capture and sequestrate CO_2. However, efficiency of traditional coal power plants, such as subcritical and supercritical power plants, are largely affected by addition of CO_2 capture.[29] Therefore, advanced technologies such as integrated gasification combined cycle (IGCC) have been developed over the years that yield higher efficiencies in comparison to the traditional power plants and offer near-zero emission power generation by allowing capture and sequestration of CO_2.[30,31] In an IGCC plant, the coal is converted via a gasification process into syngas that is rich in hydrogen (H_2) and carbon monoxide (CO). The syngas, treated in a sour water gas shift (WGS) process, produces valuable H_2, removable CO_2 by hydrolysis of unwanted CO, and removable hydrogen sulfide (H_2S) by hydrolysis of the harmful sulfur compounds such as carbonyl sulfide (COS). The syngas is then passed through an acid gas removal (AGR) process to remove H_2S and CO_2 and purified hydrogen is eventually burned in a combustion turbine as part of the combined cycle to produce power. The combined cycle constitutes a combustion turbine that produces energy by combusting the hydrogen and a steam cycle that first generates steam by recovering the heat of combustion from the gas turbine effluent stream and then produces energy by expanding the resulting steam in steam turbines. This combined cycle operation is more efficient than its rival, traditional pulverized coal plants, which benefit only from power generation from steam turbines.

However, the cost, availability, and complexity are disadvantages of IGCC technology that must be addressed before IGCC can be the prime technology for coal-based power generation. These disadvantages can be addresses by utilizing a combination of developments including design and optimization of each component of the IGCC plant.

To satisfy the overall CO_2 capture target in an IGCC plant with CO_2 capture, a certain extent of CO to CO_2 conversion must be achieved in the WGS reactors.[31] The water gas shift process can be sweet or sour.[32] The activity of conventional sweet shift catalysts such as iron- or copper-based catalysts reduce in presence of sulfur due to sulfur poisoning.[33,34] Therefore, in a sweet shift process, the COS present in the syngas is first hydrolyzed to H_2S and then H_2S is captured in an AGR unit before sending the syngas to the WGS reactors. Therefore, the plants with sweet shift processes require two reactor systems- a COS hydrolysis reactor system and a WGS reactor system. These are called reactor systems as one or more reactors with inter-stage coolers may be needed depending on the desired extent of conversion and process operating conditions. As the water contained in the syngas is cooled and condensed before sending it to the AGR unit, the syngas must be reheated and before sending it to the sweet shift reactors, substantial amount of steam must be injected to the syngas in order to drive the reaction equilibrium towards the products. In an IGCC process, the syngas from the gasifier passes through a water scrubber.[31] The syngas at the outlet of the scrubber is saturated with water and can be made available at a temperature that is suitable for the WGS reactor inlet. Therefore, if the sour syngas from the outlet of the scrubber is shifted, a higher overall efficiency can be achieved in comparison to the sweet shift process because of the higher temperature of the syngas and lower requirement of additional steam.[35,36,37,38] However, a sulfur-tolerant catalyst is required because of the presence of COS and H_2S in the syngas. The sulfide-treated Cobalt/Molybdenum (Co/Mo) and Nickel/Molybdenum (Ni/Mo) impregnated alumina catalysts are sulfur-tolerant and can catalyze the shift reaction.[39,40,41] In addition, typical sour shift catalysts can convert COS and other organic sulfur compounds into H_2S, which also helps in capturing H_2S since it is removed easier than COS from the syngas in the AGR unit.[42] Actually, sulfur-tolerant catalysts require sulfur in the syngas to remain active and can operate in a wide temperature range.[43] Moreover, the startup procedure for the sour water gas shift catalysts is less complex.[44] In addition, the sour shift catalysts are less sensitive to operational conditions.[44] Because of these advantages, a sour shift process is preferred in an IGCC plant with CO_2 capture and a separate COS hydrolysis reactor is not needed.

The water gas shift reaction is a well-studied equilibrium reaction where several models of the sweet shift reactor have been developed.[43,45,46,47,48,49] Giunta et al.[49] have performed an extensive study on a 2-D heterogeneous dynamic model, validated with experimental data. In their work, consideration of the intraparticle mass transfer limitations by the definition of effectiveness factor, although negligible at catalyst diameters below 0.8 mm, returns good results for industrial-sized reactors, which have larger catalysts.[47] Adams and Barton[47] have developed a 1-D heterogeneous dynamic model and validated with the work of Choi and Stenger[50]. Steady-state models of WGS reactor and their validation with the experimental data have been reported in the work of Ding and Chan[46] and Chen et al.[51]. Francesconi et al.[48] have discussed optimization of the reactor at steady-state condition.

Most of the efforts in modeling the WGS reactors have focused on the sweet shift process where several catalysts at different conditions have been studied.[52,53,54,55,56] In comparison to the vast amount of work on the sweet shift catalysts, the amount of work on the sour shift catalysts is very little. A few experimental works can be found that have investigated the performance of the sour shift catalysts and have performed kinetic studies in the presence of a sulfiding agent such as COS or H_2S, which are typically present at reasonable concentrations in the syngas obtained from a coal-fired gasifier.[33,40,57,58,59,60] Additionally, computational models developed for sour shift reactors are rare. Bell and Edgar[43,45] have developed 1-D pseudo-homogeneous model of a reactor that is filled with the Co/Mo based catalyst, which is similar to the catalyst used in this work with the exception that the catalyst used in this work is promoted with cesium.[61] Although they verified their steady-state and dynamic model with experimental results, their lab-scale reactor model cannot be scaled up to an industrial reactor due to their assumptions that are

exclusive to lab-scale models and under-predict the results for industrial-scale reactors. In their work, they have ignored the momentum balance while modeling their reactor; therefore, information on the pressure drop across the reactor is not included. Pseudo-homogeneous models are sufficient only when intra-particle heat and mass transfer limitations are negligible, which is not the case for an industrial-scale reactor.[62] Since a typical industrial-scale sour shift reactor is filled with larger catalyst particles and operates at higher pressures compared to catalyst particle size and operating pressure in experimental studies, their model cannot be used for studying the performance of the reactor under industrial conditions. Here, all these issues are addressed and a model that is applicable to both lab- and industrial-scale reactors is developed.

In almost all the papers, both experimental and computational, COS hydrolysis reaction concurrent with the WGS reaction have not been studied. It must be noted that a significant conversion of COS in the shift reactor(s) is desired so that the resulting H_2S can be captured in the acid gas removal unit for satisfying the overall specifications on sulfur emission.[31] COS hydrolysis reaction would be expected to occur on the sour shift catalysts since the typical sour shift catalysts use Co/Mo supported on alumina and alumina has been reported to catalyze the COS hydrolysis reaction.[63,64,65] With this motivation, we have developed a dynamic model of a sour shift reactor by considering both WGS and COS hydrolysis reactions and have used this model for the typical feed conditions of an IGCC plant. For validating the model, experimental data are required for reactors where the feed contains COS in addition to the typical species present in the syngas. Unfortunately, the only experimental data that we could find in the existing literature for such feed conditions contain high measurement errors that necessitate reconciliation of the reported data.[61,66] Therefore, an algorithm is developed for data reconciliation and estimation of the kinetic parameters. The developed model is then used to study the effect of the length and diameter of the reactor, the steam-to-CO ratio, and the inlet temperature of the syngas on the key operating variables. In addition, dynamic responses are studied by simulating the change in the inlet temperature and catalyst activity that might occur due to poisoning of the catalyst or due to change in the catalyst microstructure during the course of reactor operation.

2.1.1 Process Description

The two key reactions that take place in the catalytic sour WGS reactor are the water gas shift reaction,

$$CO + H_2O \leftrightarrow H_2 + CO_2 \quad (1)$$

and COS hydrolysis reaction,

$$COS + H_2O \leftrightarrow H_2S + CO_2 \quad (2)$$

Both reactions are exothermic and feasible over wide range of temperatures. The standard heat of reactions are 41.1 kJ/mol and 30.2 kJ/mol for WGS reaction and COS hydrolysis, respectively.[67] For both reactions, low temperatures are preferred thermodynamically as the equilibrium will be pushed toward the products whereas high temperatures are preferred due to the reaction kinetics. Thus, there is a trade-off between thermodynamics and reaction kinetics for these reactions. Hence conventionally, this process is carried out in 2-stages and involves high- and low-temperature reactors with inter-stage cooling.

The catalyst modeled is a Cs promoted Co/Mo impregnated alumina that is commercially available as "Aldridge".[68] Overstreet[66] and Berispek[61] have studied this catalyst extensively for different weight percents of cobalt and molybdenum oxides and tabulated the results for each catalyst. In this report, published experimental data for catalyst "Q" in the work of Berispek[61] are reconciled by solving an optimization problem and the intrinsic kinetic parameters of the WGS reaction are estimated by performing regression analysis using the reconciled data.

In the next section, modeling of the 1-D heterogeneous sour WGS reactor is explained in detail. The modeling is followed by a section that describes the data reconciliation procedure proposed for extracting

the kinetic parameters essential to the model. In the last section, a commercial size reactor that operates within typical sour WGS process conditions is simulated and the effects of different parameters on the performance of the reactor are presented.

2.1.2 Model Development

The mathematical model of the plug-flow reactor is developed by deriving the conservation laws for mass, energy and momentum. For this, radial variations of transport variables are neglected and the gradients are only considered in axial direction. In this section H_2, CO, CO_2, H_2S, H_2O and COS are considered to be present in the system. Although in industries other gasses such as N_2, Ar and O_2 may be present, the model equations can be extended easily to include these components, as they are present in very small quantities and do not react. In general, the model can be applied to any sour gas shift reactor with any catalyst, but, since kinetic parameters for sour gas shift reactor catalyst are rarely available, the model is used to extract the kinetic parameters from available experimental data for the "Aldridge" catalyst through a data reconciliation procedure.[68] A previous study of COS hydrolysis over alumina-based catalysts showed that the reaction follows an Eley-Rideal mechanism.[69] Hence, kinetic parameters for the COS hydrolysis are obtained from the work of Svoronos et al.[69], whereas the rate parameters for the WGS reaction are obtained through data reconciliation considering a pseudo-first order reaction.[61]

2.1.2.1 Physical Properties

The syngas heat capacity is calculated assuming ideal mixture, as shown in Eqn. (3).[67]

$$C_p = \sum_{i=1}^{N} y_i C_{p,i} \tag{3}$$

The viscosity of the syngas, μ, is estimated from Eqn. (4) as:[47]

$$\mu = \sum_{i=1}^{N} \frac{y_i \mu_i}{\sum_{j=1}^{N} \sqrt{M_j / M_i}} \tag{4}$$

where M is molecular weight of species denoted by indices i and j.

Assuming interactions between all pairs in the syngas, thermal conductivity of the mixture can be approximated by using the molar average thermal conductivity, Eqn. (5).

$$\lambda = \sum_{i=1}^{N} y_i \lambda_i \tag{5}$$

The effective diffusivity, D_e, is related to binary diffusivity, D_{ij}, through Eqn. (6):[47]

$$D_{eff,ij} = D_{ij} \left(\frac{\varepsilon}{\tau} \right) \tag{6}$$

It is difficult to find accurate tortuosity values for the catalyst; however, since the tortuosity of water gas shift catalysts are in the range of 2-9, a tortuosity value of 5 is chosen.[47] The porosity of the catalyst, ε, is assumed to be 0.38.[48] The binary diffusivity,D_{ij}, is the binary diffusivity of species *i* into species *j*. An approximate equation for diffusion of species *i* into a mixture is given as:[47]

$$D_{i,m} = \frac{1 - y_i}{\sum_{j \neq i}(\frac{y_j}{D_{eff,ij}})}$$

An analysis of the diffusivity of reactants, CO and H_2O, into the mixture in an industrial scale reactor showed that the diffusivity of H_2O into the mixture is the lowest and thus considered as the rate limiting for the WGS reaction. The binary diffusivities are calculated using Eqn. (7a)-(7b).[47,73]

$$D_{ij} = (AT^B/P)[\ln(C/T)]^{-2D}\exp(-E/T - F/T^2) \quad (7a)$$

$$D_{ij} = B/P \quad (7b)$$

Note that useful information for calculating the heat capacity, viscosity, thermal conductivity and binary diffusivity can be found in the work of Adams and Barton[67].

2.1.2.2 Model Equations for Catalyst Pellets

The 1-D heterogeneous model has been developed using the effectiveness factor to account for intraparticle mass transfer limitations. For a first-order reaction, the overall effectiveness factor relates the actual reaction rate, r, to the reaction rate evaluated at the bulk concentration using various system parameters, such as reaction rate constant, k, and mass transfer coefficient, k_c.[60]

$$-r_A = \Omega k C_{A,bulk} \quad (8)$$

where the overall effectiveness factor is defined as:

$$\Omega = \frac{\eta}{1 + \eta k/k_c a_c} \quad (9)$$

The effectiveness factor is a function of Thiele modulus, ϕ, and for a spherical catalyst it is calculated as:

$$\eta = \frac{3}{\phi^2}(\phi \coth \phi - 1) \quad (10)$$

and Thiele modulus is given as:

$$\phi = \frac{d_{cat}}{2}\sqrt{\frac{k}{D_e}} \quad (11)$$

The mass transfer coefficient can be calculated from Thoenes-Kramers correlation:[71]

$$k_c = \frac{1 - \varepsilon}{\varepsilon}\frac{D_{i,m}}{d_{cat}} Re^{1/2} Sc^{1/3} \quad (12)$$

where the diffusion of H_2O into the mixture is considered for $D_{i,m}$ since it is rate limiting. Schmidt number, Sc, and Reynolds number, Re, are calculated from:

$$Sc = \frac{\mu}{\rho D_e} \quad (13)$$

$$Re = \frac{\rho u d_{cat}}{\mu(1 - \varepsilon)} \quad (14)$$

The surface area per unit volume of the pellet, a_c, is estimated by Eqn. (15) and assuming ideal gas behavior, the linear gas velocity, u, is given by Eqn. (16):[19-20]

$$a_c = 6(1 - \varepsilon)/d_{cat} \quad (15)$$

$$u = \frac{GRT}{P} \quad (16)$$

2.1.2.3 Species Balance

Conservation equations are derived for all gas phase species:

$$\frac{\partial C_i}{\partial t} = -\frac{1}{A_c \varepsilon}\frac{\partial F_i}{\partial z} + \left(\sum r_i\right)\frac{1-\varepsilon}{\varepsilon} \tag{17}$$

The above equation is rewritten assuming ideal gas behavior for the syngas mixture:[19]

$$\frac{\partial C_i}{\partial t} = -GR\frac{T_{gas}}{P}\frac{\partial C_i}{\partial z} - C_i GR\left[\frac{1}{P}\frac{\partial T_{gas}}{\partial z} - \frac{T_{gas}}{P^2}\frac{\partial P}{\partial z}\right] + (r_{WGS,i} + r_{Hyd,i})\frac{1-\varepsilon}{\varepsilon} \tag{18}$$

where C_i is the molar concentration of species i, z is the axial position, T is the gas phase temperature, P is pressure, R is the universal gas constant, and G is the molar flux, calculated using Eqn. (19) and the total inlet molar flow rate, F_0, entering the reactor with diameter d_{rct} as below:[19]

$$G = \frac{4F_0}{\pi d_{rct}^2 \varepsilon} \tag{19}$$

The boundary condition at the inlet to the reactor ($at\ z = 0$) can be expressed as $C_i = C_{i,in}$, $T_{gas} = T_{in}$, and $P = P_{in}$, where $C_{i,in}$, T_{in} and P_{in} are the concentration, temperature and pressure of the gas at the inlet to the reactor.

2.1.2.4 Momentum Balance

A simplified momentum conservation equation is considered assuming pseudo-steady state. This approach only requires a model for calculating the pressure drop along the reactor. The Ergun equation is used for calculating the axial pressure profile in a packed bed, rewritten as:[72]

$$\frac{dP}{dz} = \frac{\rho u^2}{d_{cat}}\left(\frac{1-\varepsilon}{\varepsilon^3}\right)\left(1.75 + \frac{150}{Re}\right) \tag{20}$$

where ρ is the density of the fluid.

2.1.2.5 Gas phase energy balance

The temperature variation across the reactor can be obtained by deriving the gas phase energy balance:

$$\frac{\partial T_{gas}}{\partial t} = \frac{1}{\rho_{gas} C_p}\left[-C_p G\frac{\partial T_g}{\partial z} + \frac{h_f a_c}{\varepsilon}\left(T_{cat} - T_{gas}\right)\right] \tag{21}$$

where the heat transfer coefficient, h_f, can be estimated using:[45]

$$h_f = 1.37\left(\frac{0.357}{\varepsilon}\right)(C_p G M)\left(\frac{\mu}{d_{cat} G M}\right)^{0.359}\left(\frac{\lambda M}{C_p \mu}\right)^{2/3} \tag{22}$$

The boundary condition can be expressed as $T_{gas}\ (at\ z = 0) = T_{in}$, where T_{in} is the temperature of the gas at the inlet to the reactor.

2.1.2.6 Catalyst phase energy balance

Assuming that the temperature only varies in the *z* direction and neglecting radial temperature profile, the adiabatic energy balance for the catalyst phase is:

$$\frac{\partial T_{cat}}{\partial t} = \frac{1}{\rho_{cat} C_{p,cat}}\left[K_{cat}\frac{\partial^2 T_{cat}}{\partial z^2} - \frac{h_f a_c}{1-\varepsilon}\left(T_{cat} - T_{gas}\right) + r_{WGS}\Delta H_{R,WGS} + r_{Hyd}\Delta H_{R,hyd}\right] \tag{23}$$

For the catalyst phase temperature, following boundary conditions are considered: $\partial T_{cat}/\partial z\ (z = L) = 0$ and $T_{cat}(z = 0) = T_{gas}$. Thermal conductivity of the catalyst is assumed to be the same as pure alumina, 35 W/m-K. Additionally, this equation requires the calculation of the heats of reaction using the enthalpy defined as:

$$H_i = \Delta H^f_{298} + \int_{298}^{T} C_{p,i}(T)dT \tag{24}$$

2.1.2.7 The standard heat of formation of CO, CO_2, COS, H_2O and H_2S are -110.5, -393.5, -142, -241.9, and -20.63 kJ/mol, respectively.[67]Reaction kinetics

Although the WGS reaction has been studied over sulfur-tolerant catalysts, such as Co/Mo catalyst, kinetics of the COS hydrolysis on the sour Shift catalyst are rarely reported. Thus, the parameters of COS hydrolysis are derived from the open literature for alumina-based catalyst.[69] However, the parameters for the WGS reaction are obtained by analyzing the available experimental data. However, since the presence of measurement error is common in the data collected in experimental studies, a data reconciliation procedure is developed to obtain consistent data.

The rate equation for COS hydrolysis considering Eley-Rideal mechanism is expressed as:[41]

$$-r_{hyd} = k_{Hyd}\ \frac{P_{COS}}{1 + K_{eq,hyd}P_{H_2O}} \tag{25}$$

where the partial pressures are in kPa and the rate and equilibrium constants are given as:[69]

$$k_{hyd} = 4223.32exp\left(\frac{-25270\ [\frac{J}{mol}]}{RT_{cat}}\right) \tag{26}$$

$$K_{eq,hyd} = exp\left(\frac{10010[K]}{T_{cat}} - 15.89\right) \tag{27}$$

Considering a pseudo-first order equilibrium reaction, the rate equation for the WGS reaction can be expressed as:

$$-r_{WGS} = \Omega k_{WGS}P\left(x_{CO} - \frac{x_{CO_2}\,x_{H_2}}{K_{eq,WGS}\,x_{H_2O}}\right) \tag{28}$$

where P is the pressure in atm and the rate constant, k_{WGS}, follows the Arrhenius equation and the equilibrium constant, $K_{eq,WGS}$, is given by Moe[74]:

$$k_{WGS} = k_0 exp\left(\frac{-E_a}{RT}\right) \tag{29}$$

$$K_{eq,WGS} = exp\left(\frac{4577.8[K]}{T_{cat}} - 4.33\right) \tag{30}$$

2.1.2.8 Pressure scale-up

The reaction kinetics derived from experimental data obtained at lower pressure are not applicable to industrial-sized reactors since they result in over-prediction of the reaction rates by orders of magnitude. Therefore, a pressure scale-up factor is used to address such over-predictions at high pressures. The reaction rate at higher pressures is related to the rate at atmospheric pressure as:[47]

$$r'_{WGS} = P_{scale}\ r_{WGS} \tag{31}$$

where P_{scale} is the pressure scale factor which is expressed as:[19]

$$P_{scale} = P^{\left(0.5-\frac{P}{500}\right)} \quad (32)$$

where P is the pressure in atm. Basically, Eqn. (32) implies that the reaction rate above atmospheric pressure is in the range of 1-5 times the reaction at atmospheric pressure and the equation is reported to be valid up to 55 atm.[47] So, the rate equation for the WGS reaction in Eqn. (28) is rewritten for high pressures as:

$$-r'_{WGS} = \Omega k_{WGS} P_{Scale} \left(x_{CO} - \frac{x_{CO_2}\, x_{H_2}}{K_{eq,WGS}\, x_{H_2O}} \right) \quad (33)$$

2.1.2.9 Catalyst deactivation

The catalyst loses its activity over time mainly due to poisoning, fouling, and thermal and mechanical degradation. However, here, the catalyst is assumed to deactivate only due to thermal degradation (sintering). The catalyst activity is defined in terms of reaction rates for both WGS reaction and COS hydrolysis as:[21]

$$a_{(t)} = \frac{r_{(t)}}{r_{(0)}} \quad (34)$$

The catalyst deactivation equation is given by:[21]

$$\frac{da}{dt} = k_d (a - a_\infty)^m \quad (35)$$

where m, the order of sintering, is reported to be either 1 or 2; a_∞ is limiting activity at infinite time; and k_d is the sintering rate constant. In the work of Giunta et al.[49], the catalyst activity is given at some point in time which gives a good estimate for the a_∞ in this work.[49,76] Also here, m is assumed to be 2 and k_d is found by integrating Eqn. (35) for expected life time of Co/Mo catalyst, 5 years, until the catalyst reaches 99% of its limiting activity.[49,76,77]

2.1.3 Solution Approach

The system consists of a set of partial differential equations (PDEs) representing the state of the system. The PDEs in the modeling equations are converted to ODEs using the method of lines, where the spatial derivatives are discretized using a backwards difference method. However for solving the equations, the rate parameters for the water gas shift reaction need to be obtained from the available experimental data.[61] The experimental data were generated from an isothermal reactor under steady-state conditions.[61] Therefore, the energy balance equations are eliminated to achieve an isothermal reactor and the time derivatives are set to zero. The resulting set of nonlinear equations is solved using a trust-region-dogleg algorithm by 'fsolve' function in MATLAB. Later, a dynamic adiabatic reactor is simulated by scaling up the reactor and using the obtained parameters. In the data reconciliation simulations, 100 grid points are assumed for discretization of a 10 centimeter reactor. Increasing the number of grid points to 200, resulted in less than 0.01% deviation in estimating the rate constant but increased the simulation time. Since the reactor model is used multiple times in data reconciliation and gross error detection, to reduce the simulation burden, 100 grid points are considered for the simulations. Equations are solved for the 26 meter long industrial reactor considering 300 grid points since increasing the grid points to 900 resulted only in less than 0.1% improvement in error and substantially longer processor time to solve the equations.

2.1.4 Data Reconciliation

The experimental data from Berispek[61] are used to obtain the kinetic parameters of the WGS reaction. The experimental work has a dry-feed with a given composition passing through a water saturator, which is maintained at 60˚C. Before entering the reactor, flowrate of the wet-feed is measured. The effluent of the catalytic reactor passes through a gas sampling valve where the gas sample is collected and is analyzed by

a gas chromatograph. The outlet compositions from the sour shift reactor are reported for various reactor temperatures and wet-feed flowrates. The reactor operates at close to atmospheric pressure (715 mm Hg at the inlet) and the temperature is varied from 200 to 400°C in increments of 25°C. In this laboratory reactor (with a length of 10 cm and a diameter of 3/16 inches), the temperature is maintained constant along the reactor resulting in an isothermal condition and the reactor is filled with the "Aldridge"[68] catalyst. Even though several catalysts are investigated in the work of Berispek[61], Catalyst Q has been considered here. Various properties of Catalyst Q, shown in Table 1, are used for obtaining the kinetic parameters.

Table 1. Properties of Catalyst Q[61]

Property	Value
Mesh range	20/60
Surface area	279 m^2/g
Density	0.65 g/cm^3
Porosity	0.38
Tortuosity†	5
Weight of the catalyst	5.24 g
Weight of the inert solids	1.2 g

†Tortuosity is assumed for the catalyst

In general, experimental data obtained from instruments such as temperature sensors, flow meters, and gas chromatographs are prone to measurement errors; however, mathematical techniques can be helpful in correcting the errors in order to get estimates close to the actual values. In the Berispek's[61] experimental work, COS and H_2S are found in very small quantities, less than two percent, and high measurement errors can be observed in the reported compositions. For instance, even though the feed to the reactor contains COS, the results of gas chromatography show no sulfur compounds at the outlet of the reactor for a particular catalyst while the results are considerably different for another catalyst.[61] The discrepancy in the outlet mole fractions of COS and H_2S reported for different catalysts justifies our expectation that these measurements are associated with high errors and require careful consideration as the sulfur balances are violated. Therefore in our work, a data reconciliation technique is used to minimize the measurement errors.

In the experimental data, the dry feed composition before the saturator, wet stream flowrate at the inlet of reactor, and the gas composition at the outlet of the reactor have been reported.[61] These data are inadequate for calculating the mole fraction of the gas at the inlet of the reactor as the extent of saturation in the saturator before entering the reactor is unknown. It should be noted that as the flowrate of the dry gas feed is changed, it is expected that the extent of saturation can also vary. In addition, discrepancy in the experimental data has been observed as reported before. Hence, the data on outlet mole fractions are reconciled by a sequential process as described below. To perform the data reconciliation, the water saturator used in the experiments is assumed as a stream of steam with unknown flowrate, which is well mixed with the dry feed of known composition and unknown flowrate before entering the reactor.

Figure 4 shows the method used to obtain the reconciled data and the corresponding parameters. In this approach, data corresponding to different operating conditions are individually reconciled, resulting in reconciled data and consolidated reaction rate constants at specific flow rates and temperatures. Then, the estimated reaction rate constants are used to calculate the activation energy and frequency factor of the WGS reaction. An alternative approach is to include all the data in a single formulation and directly

estimate the activation energy and frequency factor. However, due to the presence of gross errors, this approach results in undesired estimation errors.[78,79,80] A gross error detection approach based on the work of Narasimhan et al.[79,80] is performed and gross errors are detected in the reported mole fractions of COS and H_2S. To do this, a null hypothesis is assumed and the objective functions for all individual experiments are calculated based on the sequential data reconciliation shown in Figure 4 and the objective functions are summed up. Then, separate data reconciliations are performed assuming a single gross error hypothesized. The test statistic is obtained as the maximum difference in objective function values between the null hypothesis and the gross error model of each variable. This approach is done in series until the test statistic is less than the test criteria, which is equal to chi-square value with the correct degrees of freedom at 5% level of significance.[79,80] This approach resulted in the identification of COS and H_2S sensors as having gross errors.

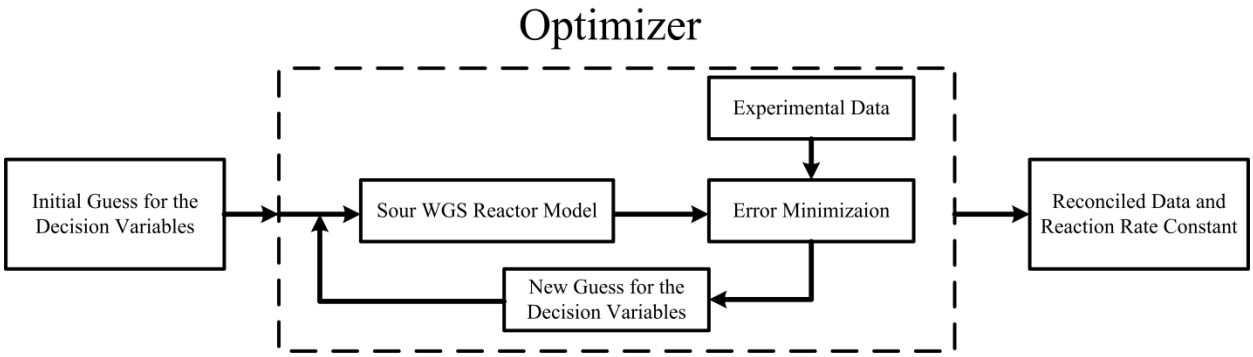

Figure 4. Diagram of the data reconciliation procedure

The decision variables for the objective function for this problem are: dry gas flow rate; F_{dry}; steam flow rate; F_{stm}; and the rate constant for the water gas shift reaction, k_{WGS}. The WGS reactor model is simulated to generate the outlet mole fractions by using the guesses for the decision variables. The optimizer minimizes the sum of the squared error between the model output and the experimental data as shown in Eqn. (36) until it finds the optimal values of the decision variables. The objective function involves two terms: the first term reduces the error between the outlet mole fractions from the model (y_{model}) (reconciled values) and the experiments(y_{exp}), while the second term reduces the error in the overall inlet flow rate. Since no information on the standard deviations for the gas chromatography measuerments is provided in the work of Berispek[61], standard deviation values used in the objective function are taken from the literature and are listed in Table 2. Note that COS and H_2S are omitted from the objective function due to the gross errors that exist in these measured values. The outlet mole fractions and a consolidated rate constant are estimated by using the proposed optimization formulation. It is worth mentioning that, as can be seen in Figure 4, the data reconciliation is performed using a sequential approach. As a result, the model equations are embedded in the objective function and do not participate as constraints in the formulation. Therefore, an unconstrained optimization problem is solved individually for all flows at each temperature, which results in separate rate constants at each temperature. However, since the problem is non-convex, multiple simulations with different initial conditions are performed and the best solutions are retained. The optimization problem is solved in MATLAB using the 'fmin' function.

Table 2. Standard deviation of different variables[81,82]

Species	Standard deviation
H_2	1%

CO	1%
CO_2	1.4%
H_2S	0.07%
H_2O†	1%
COS†	0.07%
Flowrate	3%

†Standard deviation for H_2O and COS are assumed

$$\min_{F_d, F_s, k_{WGS,}} \sum_{\substack{j = H_2, CO, \\ CO_2, H_2O}} \left[\frac{y_{model,j} - y_{exp,j}}{\sigma_j}\right]^2 + \left[\frac{F_{dry} + F_{stm} - F_{exp}}{\sigma_F F_{exp}}\right]^2 \quad (36)$$

Table 3 shows the inlet and outlet mole fractions and the feed flow to the reactor ($F_{dry} + F_{stm}$) for both the experimental and reconciled outputs at a particular temperature and flowrate. Reconciled mole fractions of H_2, CO_2, CO and H_2O are in reasonable agreement with the experimental data.

Table 3. Comparison of the reconciled and original mole fractions[61]

Species	Original Data	Reconciled Data
H_2	0.5467	0.5406
CO	0.2286	0.2289
CO_2	0.1314	0.1371
H_2S	0.0062	0.0113
H_2O	0.0852	0.0818
COS	0.0019	0.0003
Flowrate[cm^3/min]	92.6	92.5

Figure 5 is an Arrhenius plot for the obtained WGS reaction rate constant. Following values are obtained for the parameters, E_a is 56,332 J/mol and k_0 is 810,125 mol/m^3-atm-s. These rate parameters are used in Eqn. (29) for simulating the industrial scale reactor as described in the next section.

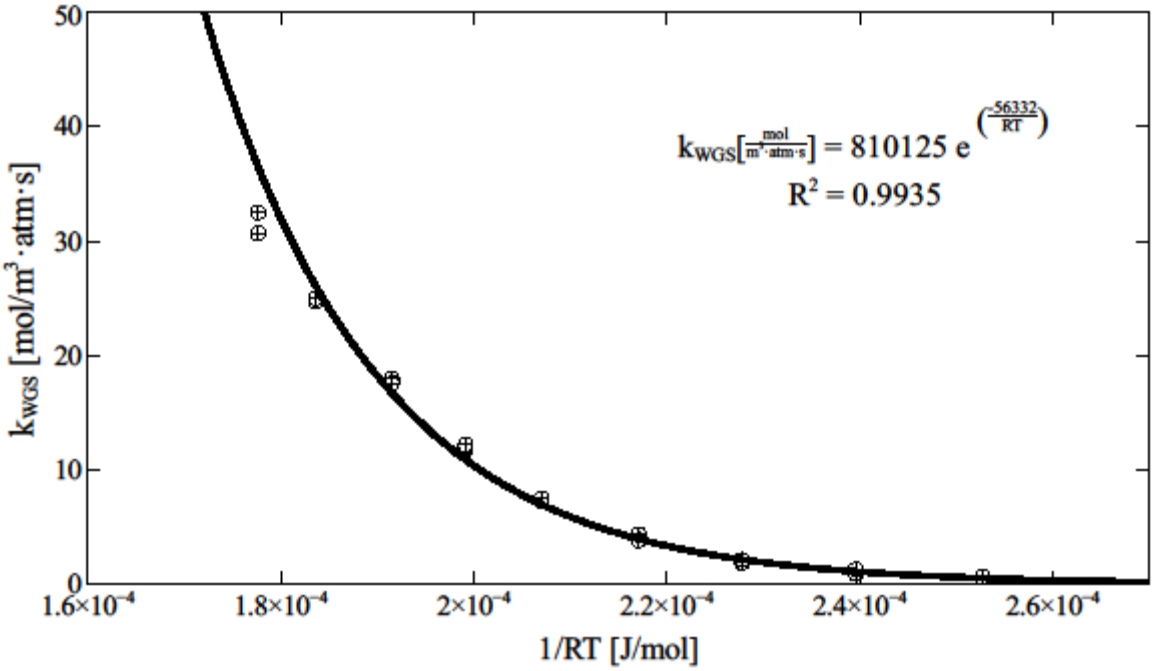

Figure 5. Arrhenius plot for the water gas shift reaction

2.1.5 Results and Discussions

A typical industrial sour gas shift process operates adiabatically and typically under high pressure. Considering an overall target of 90% carbon capture in an IGCC plant, a 2-stage WGS reactor system with high- and low-temperature reactors arranged in series with interstage coolers is required.[31] However, only the first stage is simulated here where the reactor is used to study the effect of different parameters on the reactor operation and the carbon capture goals are not considered explicitly as a 2-stage would then be required. The syngas in this simulation is composed of H_2, CO, CO_2, H_2S, H_2O and COS with mole fractions of 0.21929, 0.23021, 0.08880, 0.00465, 0.45696 and 9×10^{-5}, respectively.[83] The reactor is filled with "Aldridge"[68] catalyst, catalyst Q, 2.2 mm in diameter and with porosity of 0.38; and the reactor is assumed to have no heat loss to the surrounding to satisfy the adiabatic condition.[61] With given composition and pressure for an IGCC case study, the reactor volume and the inlet temperature are adjusted to size a reactor with 10% overdesign and assuming length to diameter (*L/D*) of about 5.5.[83] Table 4 shows the sizing and operating conditions of the reactor.

Table 4. Simulation condition[83]

Condition	Value
Length	29 m
Diameter	5.2 m
Flow	4.9 kmol/s
Inlet Temperature	620 K

Inlet Pressure	54.437 atm

Figure 6 shows the CO mole fraction profile along the reactor with length increased to 40 meters. As the water gas shift reaction is equilibrium-limited, conversion will not change after reaching the equilibrium. This implies that for all operating conditions, a minimum length of the reactor is required to reach equilibrium. As in Figure 6, equilibrium is reached within almost the first 29 m of the reactor. Figures 7a and 7b show the COS mole fraction and gas temperature, respectively, as a function of the length of the reactor. In Figure 7a, it appears that only 9 m of the reactor is required for COS hydrolysis to reach completion. Since COS hydrolysis is faster compared to WGS reaction, as in the sweet WGS reactor, the design would only require the first 29 meters of the reactor because no conversion is achieved after this point. When considering the design parameters for the sour WGS reactor, the required dimensions should be decided by considering the desired extent of WGS reaction. Although a longer reactor will have higher overall conversion, several other factors such as equipment cost and allowable pressure drop should be considered for deciding the final dimensions of the reactors. Note that in the subsequent studies the reactor length is fixed at 29 m.

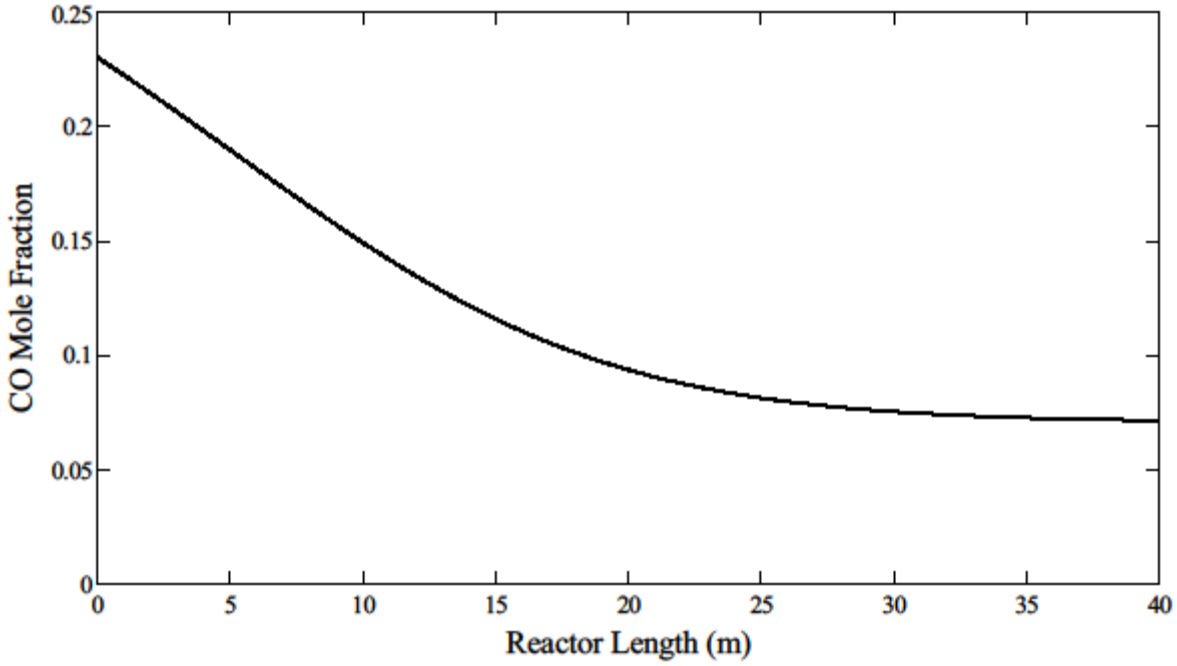

Figure 6. CO mole fraction profile along the reactor when length is increased to 40 m

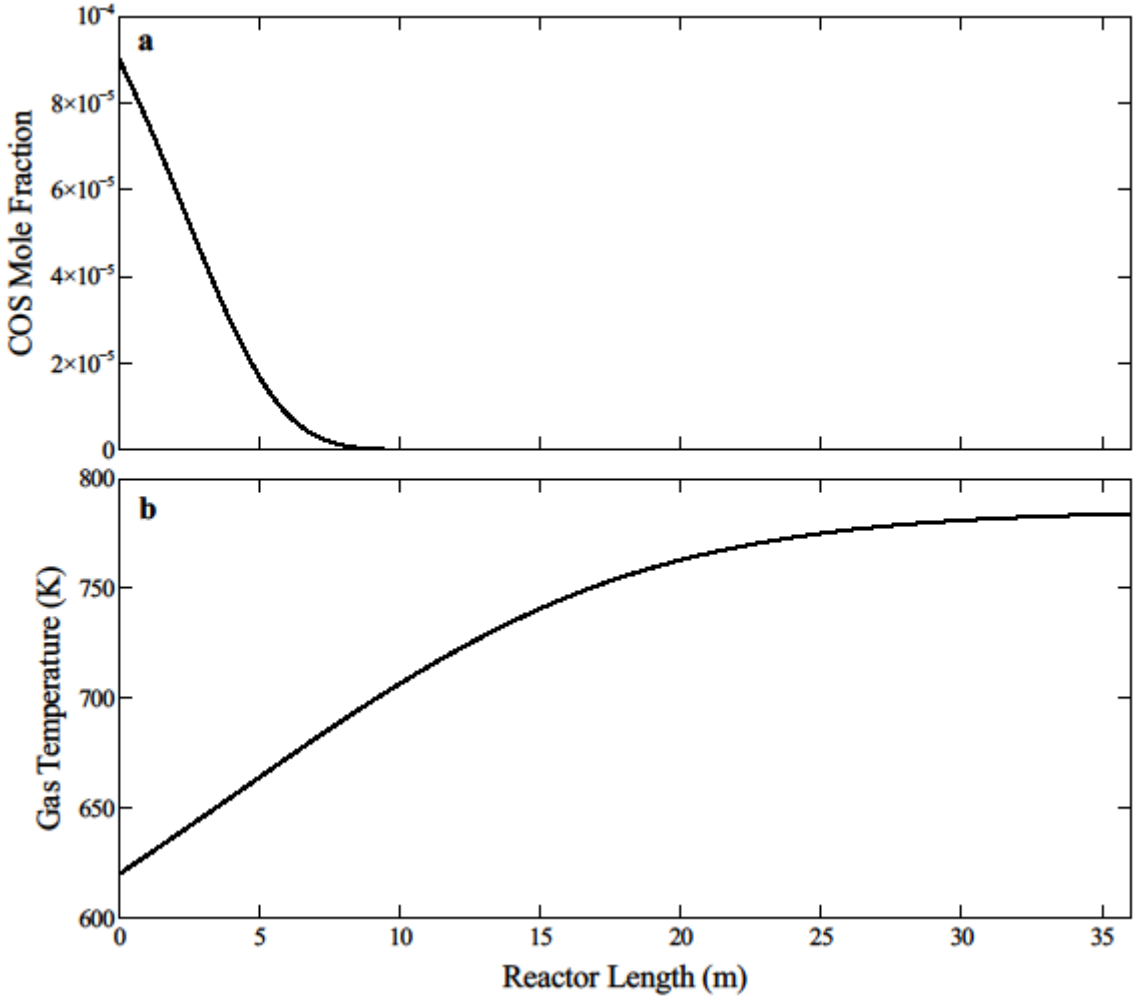

Figure 7. (a)COS mole fraction (b) Gas temperature profile along the reactor when length is increased to 40 m

Figure 8 shows the axial profile of CO mole fraction as the reactor diameter is changed. For a given length, an increase in the diameter of the reactor increases the conversion of CO if equilibrium is not reached. It should be noted that an almost complete COS conversion is achieved for all diameters shown in Figure 8. Figure 9 shows the corresponding pressure profile. It is observed that as the diameter is decreased beyond certain value, the pressure drop increases substantially.

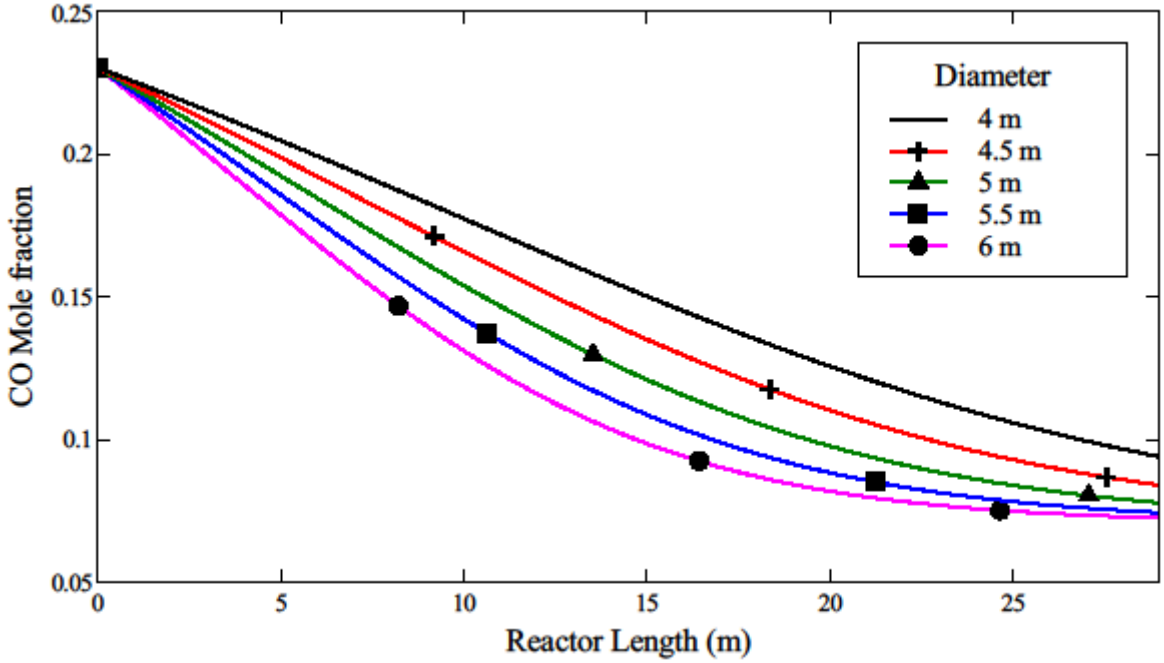

Figure 8. CO mole fraction profile for different reactor diameters

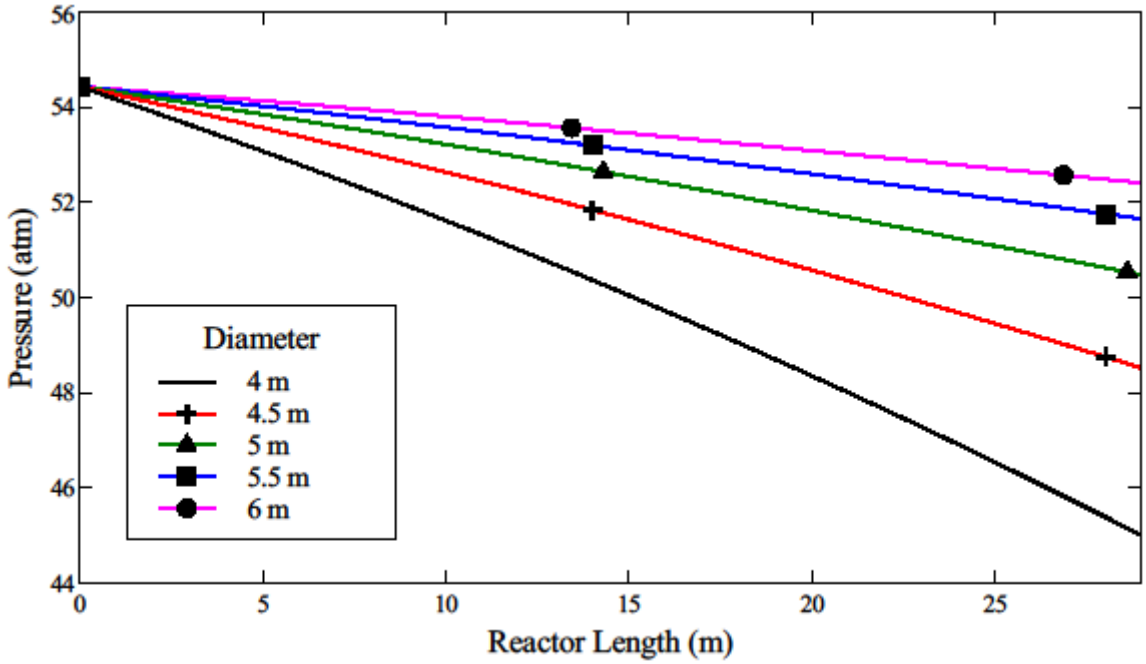

Figure 9. Pressure profile for different reactor diameters

Figure 10 shows the relation between the *L/D* ratio and pressure drop at constant reactor volume. This result indicates that as *L/D* increases, the pressure drop keeps increasing. It should be noted that a lower pressure drop is desired in the WGS reactor system so that higher partial pressure of CO_2 can be achieved in the AGR unit. This is particularly important for achieving higher efficiency of the physical solvent-based CO_2 capture process in the IGCC plant.[31]

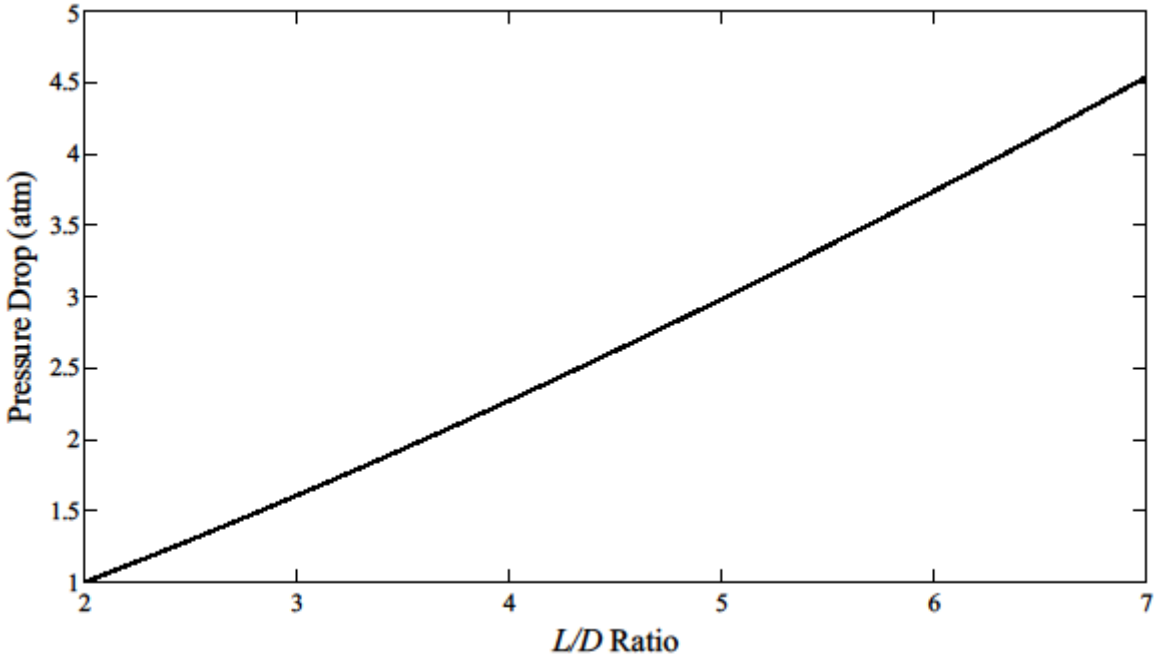

Figure 10. Pressure drop vs. L/D ratio of the reactor

Figures 11-12 show the conversion of CO and COS along the reactor for different inlet gas temperatures. As seen in Figure 11, the conversion at the outlet remains fairly constant, however, the conversion along the reactor reduces as the inlet temperature decreases. Even though the conversion of CO is slightly affected by the change in the inlet temperature, the COS conversion is not affected at higher inlet temperatures as seen in Figure 12. Figure 11 shows that the CO conversion decreases as the inlet temperature changes from 620 K. This happens due to the interplay between the thermodynamics and reaction kinetics as mentioned before. However, one can argue that reducing the temperature will not significantly reduce the conversion; and recovered heat from reducing the inlet temperature would increase the efficiency of the steam cycle. This is later studied when considering the effect of catalyst deactivation on the performance of the reactor.

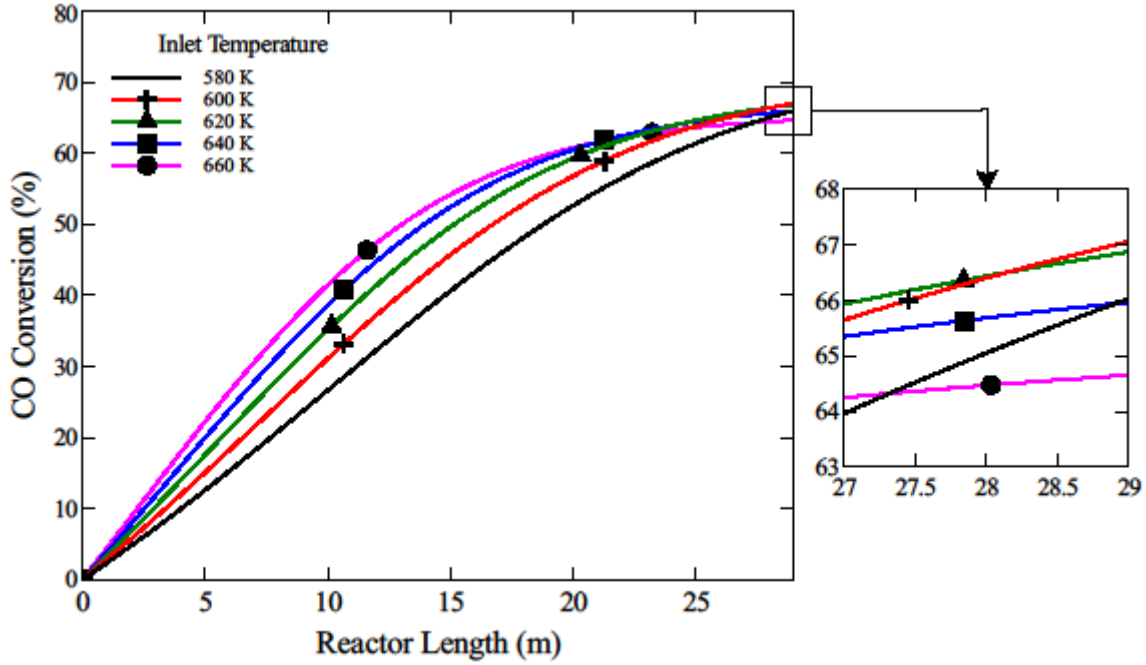

Figure 11. CO conversion profiles for different inlet gas temperatures

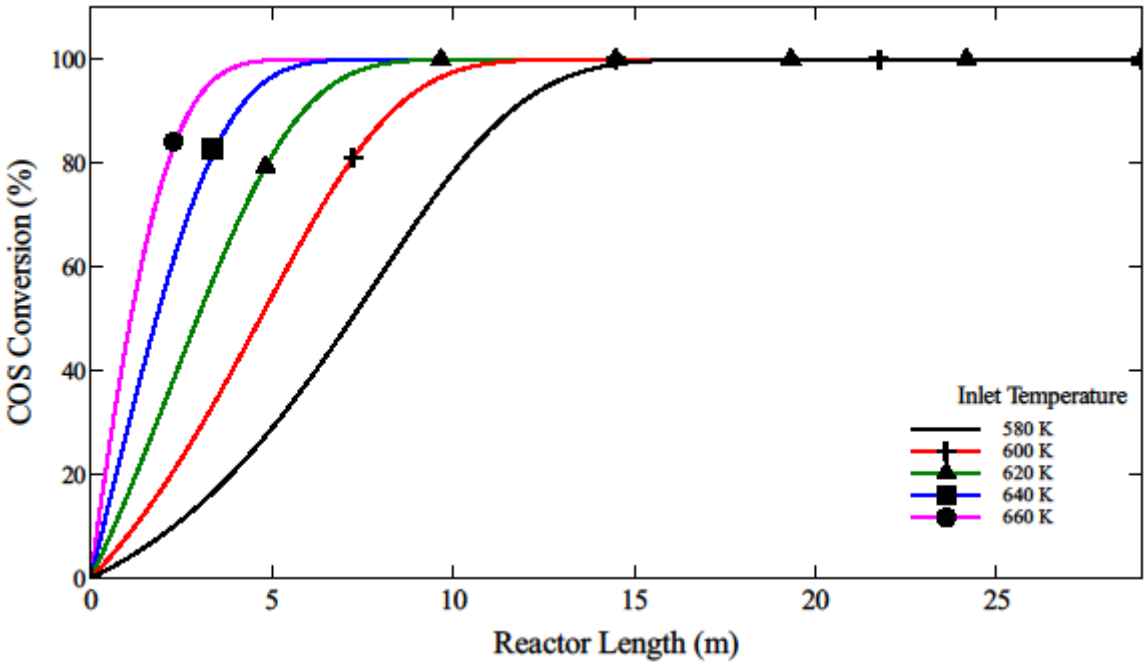

Figure 12. COS conversion profiles for different inlet gas temperatures

Figure 12 shows that high conversion is achieved at temperatures around the inlet operating temperature of 620 K and the COS conversion is not sensitive to the inlet temperature as the studied inlet temperatures are high enough to bring the COS hydrolysis reaction to completion. Although the magnified view in Figure 11 shows that an increase in the temperature results in a slightly lower conversion of CO, the reactor initially shows inverse response to step increase in inlet temperature as shown in Figure 13. Figure 13 is generated by introducing a step increase in the inlet temperature from 620 to 640 K. When the inlet

temperature rises, it takes some time for the temperature in the rest of the reactor to increase. So, initially the CO conversion increases due to higher reaction rate, but decreases later as the reaction temperature rises pushing the equilibrium to the left.

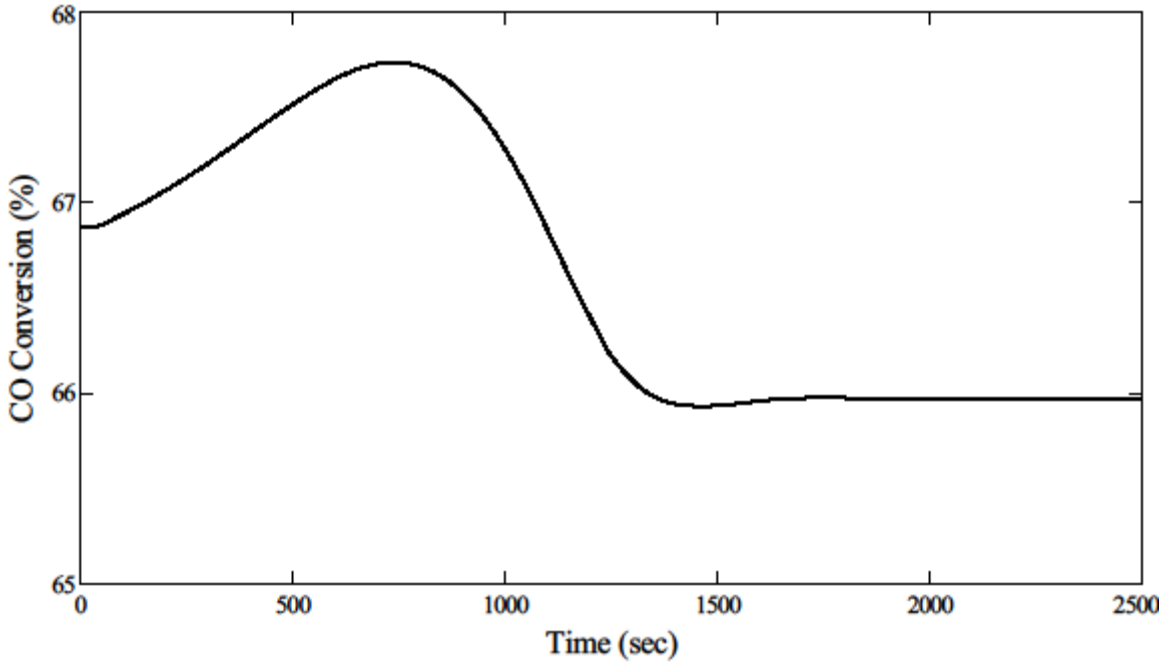

Figure 13. CO conversion transient for a step change in inlet temperature from 620 to 640 K

Figure 14 shows the dynamic response of gas temperature at the outlet of the reactor for the mentioned step increase in the inlet temperature. When the inlet temperature increases, more CO is consumed in the area near the inlet of the reactor, thus, the CO conversion increases initially as seen in Figure 13. This causes the CO concentration to reduce in the rest of the reactor, which at the same time reduces the reaction rate. Since reaction rate is decreased, less heat is generated by the exothermic reactions, thus, the temperature decreases initially. However, as the catalyst temperature slowly increases due to the higher heat input from the front end, the temperature increases. The COS conversion remains unchanged as the reactor temperature remains high enough to bring the reaction to completion in the early region of the reactor.

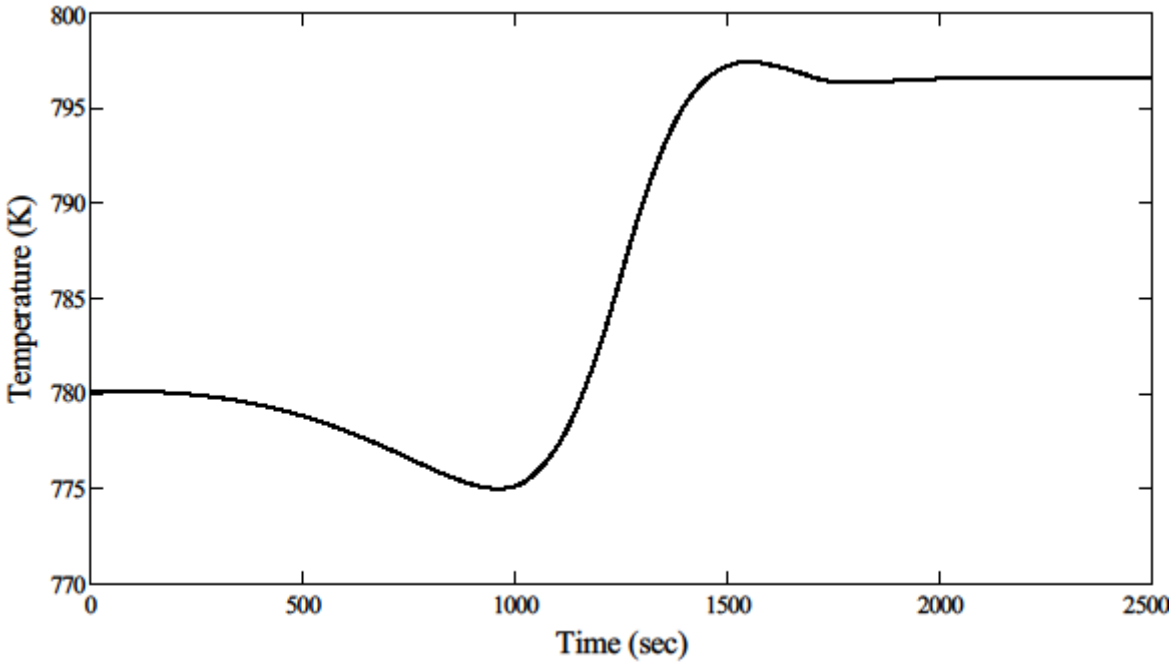

Figure 14. Temperature transient at the outlet of the reactor for a step change in inlet temperature from 620 to 640 K

In IGCC plants, additional steam is added to the syngas feed to achieve the desired conversion of CO. However, the required steam is extracted from the steam turbine.[31] Therefore, the production of electricity from the steam turbines gets reduced. It is therefore important to design the H_2O/CO ratio at the inlet of the WGS reactors appropriately by considering an optimal CO conversion in the WGS reactor system. Figure 15 show this relation between CO conversion and H_2O/CO ratio. In Figure 15, increasing the molar ratio of steam to CO at constant dry flow rate (2,661 mol/s) increases the CO conversion until it reaches a maximum at a steam-to- CO ratio of about 4. However, increasing the ratio requires higher flow rate of steam, consequently, higher flow rate at the inlet to the reactor. Increasing the flow at the same residence time and superficial velocity requires higher reactor volume. This can be seen in Figure 16a and Figure 16b where the reactor diameter and the flow are non-dimensionalized with respect to the values in Table 4. Thus, higher conversion must be weighed with respect to the capital cost of the reactor and the amount of steam taken from the steam cycle. Since the partial pressure of steam is in the denominator of Eqn. (25), it seems that increasing the steam content will reduce the COS hydrolysis rate. However, the COS conversion is not greatly affected by the amount of steam present in the syngas. This is because the system's temperature is high enough to bring the COS hydrolysis to completion.

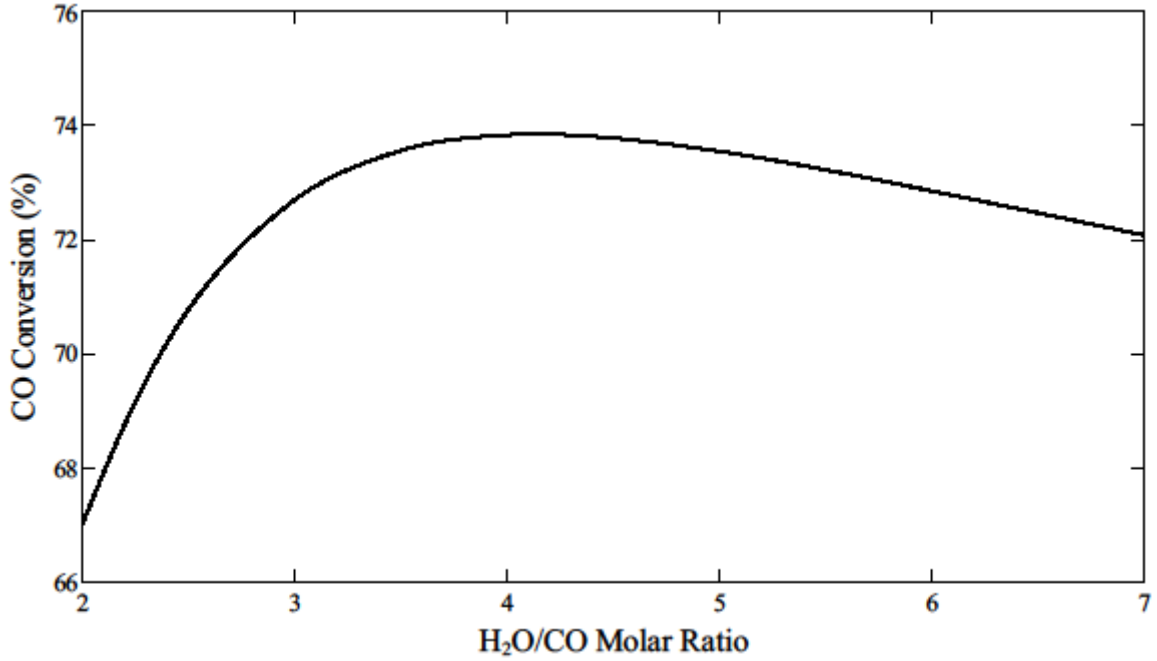

Figure 15. CO conversion profile for different steam/CO molar ratio

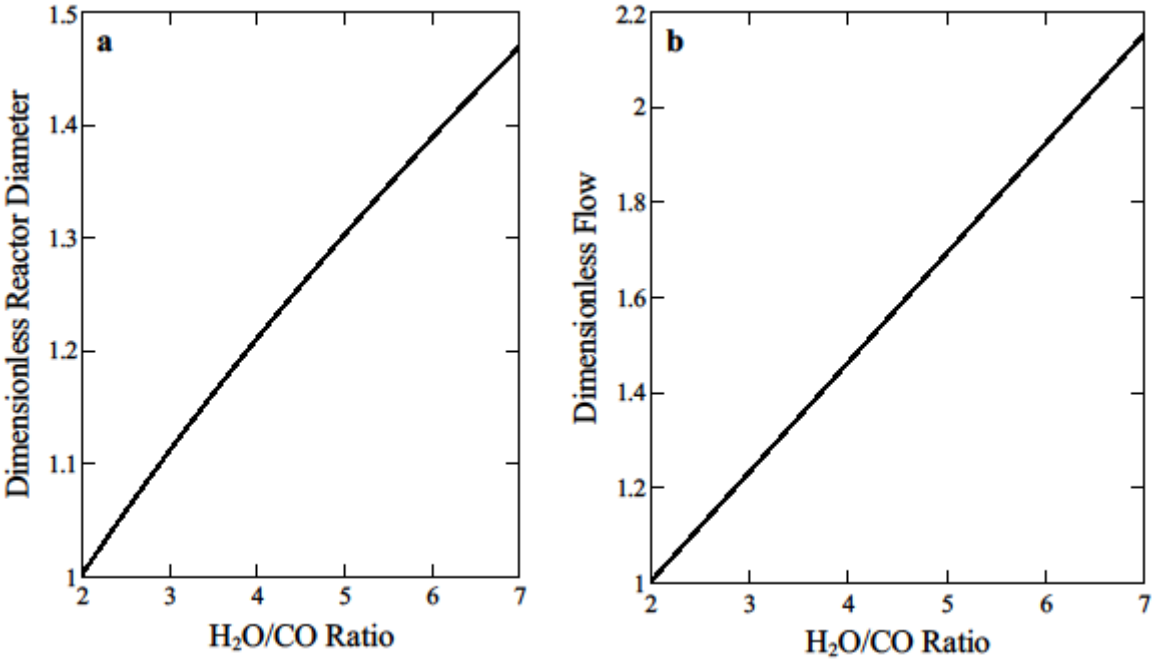

Figure 16. Required (a) Diameter (b) Flow at different steam/CO molar ratios

The catalyst deactivation due to sintering can lower the conversion in a sour WGS reactor. Figure 17 show the effect of catalyst deactivation on CO conversion for different inlet temperatures over the catalyst lifetime of 60 months (5 years).[77] From an optimization perspective, it can be argued that a lower inlet temperature would result in fairly acceptable conversion as can be seen in Figure 11 since lowering the temperature from 620 to 580 K will only decrease the conversion by approximately 1%. In return, the excess heat can be recovered to increase the efficiency of the steam cycle and the power generation.

However, Figure 17 shows that at lower inlet temperatures, catalyst deactivation has substantial effect on the conversion of CO during the lifetime of the catalyst. Figure 17 shows that the CO conversion reduces drastically over time at lower temperatures. However, COS conversion remains at completion for the range of inlet temperature studied. Figure 18 shows the COS conversion along the reactor at different inlet temperatures after the period of 5 years. As seen in Figure 18, since the length and temperature are high enough for the range of temperature studied, the COS conversion remains at completion even in the presence of the catalyst deactivation. Although, as can be seen in Figure 18, the COS conversion along the reactor is drastically reduced at lower temperatures, this effect is compensated by the length of the reactor. Therefore, there is a trade-off between the efficiency of steam cycle and the extent of the reactions over catalyst lifetime. However, from the design perspective, the effect of catalyst deactivation can be compensated by overdesigning the reactor.

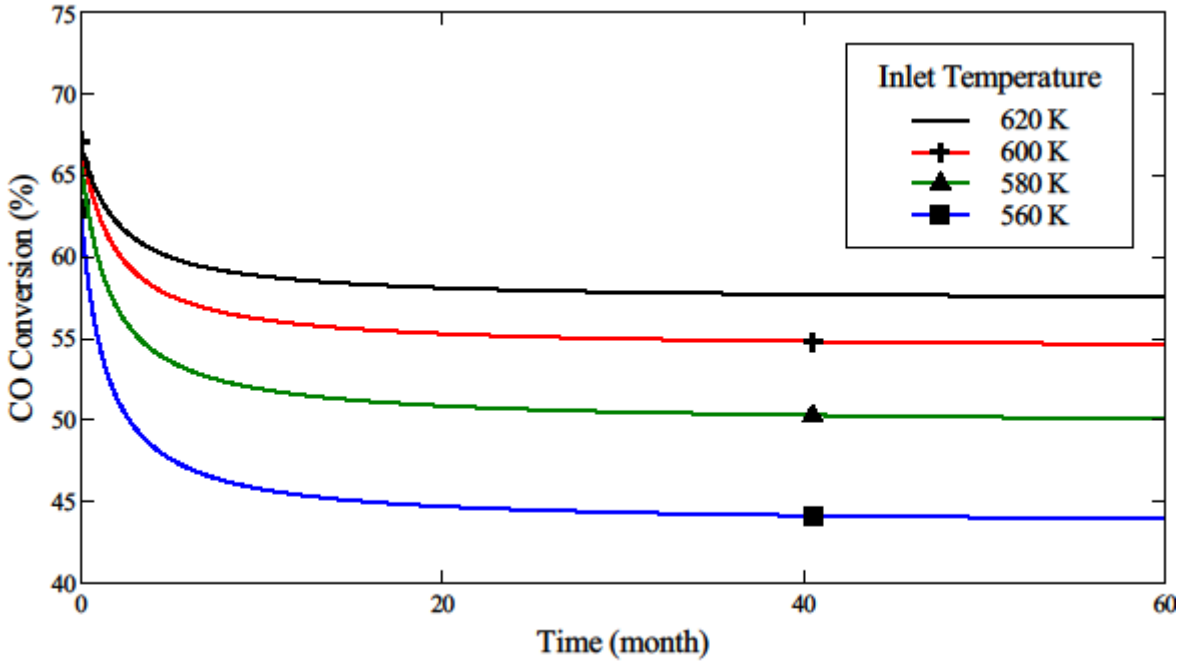

Figure 17. Effect of catalyst deactivation over time on CO conversion

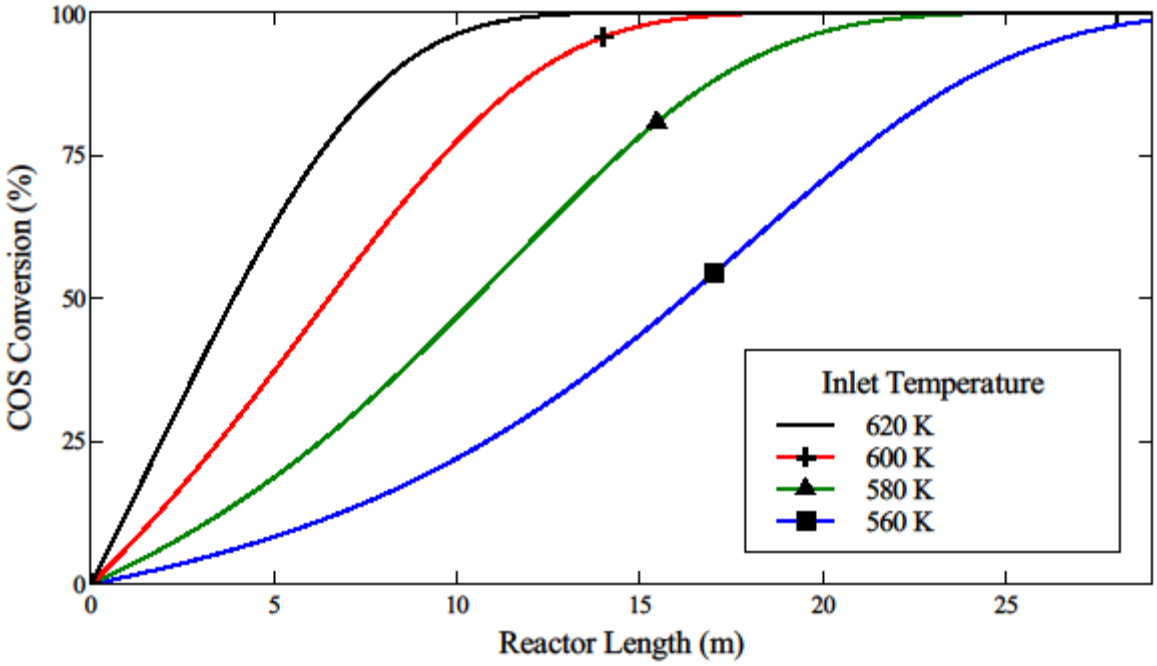

Figure 18. COS conversion along the reactor after the catalyst lifetime of 5 years

2.1.6 Conclusions

A 1-D dynamic model of a sour water gas shift reactor has been developed. The available experimental data for a sour WGS reactor have been reconciled to obtain consistent data. The proposed data reconciliation procedure uses the reactor model to reconcile the data while simultaneously extracting the rate constant. A minimization problem is solved for each run of the experimental work and the corresponding rate constant is obtained. The Arrhenius plot yields the pre-exponential factor and activation energy for the WGS reaction.

A simulation study under typical conditions of a sour WGS reactor as part of an IGCC plant is performed. The effects of different parameters on the performance of the reactor are investigated and results are presented. This study shows that the reactor should be designed with due consideration of the desired CO conversion as the WGS reaction is found to reach equilibrium further down the reactor. The study shows that the *L/D* ratio of the reactors should be appropriately designed by considering the pressure drop across the reactors as the efficiency of the AGR unit downstream of the WGS reactor is affected by the outlet pressure from the shift reactor system. For the range of inlet temperatures studied, i.e., 580-660 K, the COS conversion is found to be not affected by the feed temperature. In addition, even though an increase in the temperature results in slightly lower CO conversion, the reactor shows inverse response to a step increase in the syngas inlet temperature. At constant flow, as the steam-to-CO ratio increases, the CO conversion reaches a maximum at steam-to-CO ratio of about 4 while the COS conversion remains at its highest value for the range of steam-to-CO studied. It is observed that the CO and COS conversions are not significantly affected by the catalyst deactivation if the inlet temperature is sufficiently high.

2.2 Gasification Process

The gasifier is considered to be the heart of the IGCC power plant. Coal is converted to syngas, mainly CO and hydrogen, which is cooled in the radiant syngas cooler (RSC) and sent to the shift reactors before being processed in the acid gas removal section of the plant.

An entrained flow gasifier is considered in this section. The coal is crushed and mixed with water to form slurry. The coal slurry, along with oxygen or oxygen enriched air is fed into the gasifier. Entrained flow gasifiers typically operate at very high temperatures to achieve high carbon conversions[84]. Due to the high temperatures, the ash associated with the coal melts and gets deposited onto the gasifier wall to form a flowing layer of molten slag. The layer of slag can penetrate into the refractory wall and can cause degradation of the refractory at an accelerated rate[85,86]. Refractory degradation is one of the leading issues that impact economic viability of the entrained-flow gasifiers[87].This causes change in the thermo-physical properties of the refractory material eventually leading to spalling which could result in irreversible damage to the equipment. Therefore, refractory degradation due to penetration of slag into the refractory and spalling of the refractory wall are considered to be the primary faults in the gasifier.

Another fault of interest is the rapid increase in the thickness of the slag layer on the refractory wall of the gasifier. The viscosity of slag is a strong function of temperature and at lower temperatures; the slag layer could rapidly increase thereby choking the exit of the gasifier exit. This could reduce the volume available in the bulk of the gasifier and under extreme circumstances, lead to a sudden increase in the pressure within the gasifier.

A gasifier model with slag flow has been developed, which captures the physics of the gasifier unit, along with the processes of slag formation and detachment from the char particle, transport and deposition on the gasifier wall and the formation of a slag layer on the gasifier wall. This model is then used in a degradation model in order to obtain data on the degradation of the refractory. The time scales for the gasifier mechanisms are very different from the degradation processes, and thus these models are solved separately.

2.2.1 Modeling

A number of papers have investigated the flow of slag on the gasifier wall[88,89,90,91,92]. All these papers have considered that a fraction of the char particles hits the flowing slag layer on the wall of the gasifier. A fraction of these char particles stick to the wall and continue to react. As a result, the ash contained in these char particles melts contributing to the slag layer. Since it is assumed that the ash remains attached to the reacting char particles in the bulk of the gasifier, a shrinking core model is considered to describe the kinetics[89,91,93,94]. In the shrinking core model, the ash contained in the char particles is assumed to form a solid shell around the unreacted carbon core. The overall size of the char particle remains unchanged while its density decreases as the core shrinks.

However, due to the very high operating temperature of the entrained-flow gasifiers, it is expected that the ash gets molten in such environments as suggested by a number of researchers[95,96,97]. There are several papers that have reported that for combustion systems, liquid slag does exist as droplets in the bulk[98,99,10,101]. Depending upon the composition of the ash content in coal, the melting points of ash can vary greatly. Ash from the Illinois #6, Pittsburgh #8, and PRB coals for most of the seams is expected to have a melting temperature lower than 1350°C[102]. The exit temperature from the entrained flow gasifiers is typically 1350-1600°C. The temperature immediately after the devolatilization section in which the combustion reactions take place, often exceed the outlet temperatures by a few hundred degrees. Therefore, for a major section of the gasifier, the temperature would exceed the melting point of the ash in an entrained flow gasifier.

Since slag is highly non-wetting on the surface of carbon[103,104] when the ash melts, it is likely that it will agglomerate into one or several slag droplets rather than spread over the surface of the char particle. Several papers[105,106,107] in the literature have shown, using SEM, the existence of liquid slag droplets on the char surface but there is hardly any work that has modeled this phenomenon.

If the slag exists in the form of droplets on the char surface rather than as a solid shell around the unreacted char particle, then the widely-used shrinking core model (SCM) does not seem physically correct. Rather, a shrinking particle model (SPM) would be more physically realistic representation. Unlike the shrinking-core model that assumes the diameter of the char particle to be constant[108], the shrinking-particle model considers the char particle to shrink while the slag droplet(s) would build up on the particle's surface. Eventually the slag droplets may detach from the char surface moving into the gasifier bulk. More included mineral matter gets exposed on the surface leading to the formation of new droplets. This suggested mechanism is shown in Figure 19.

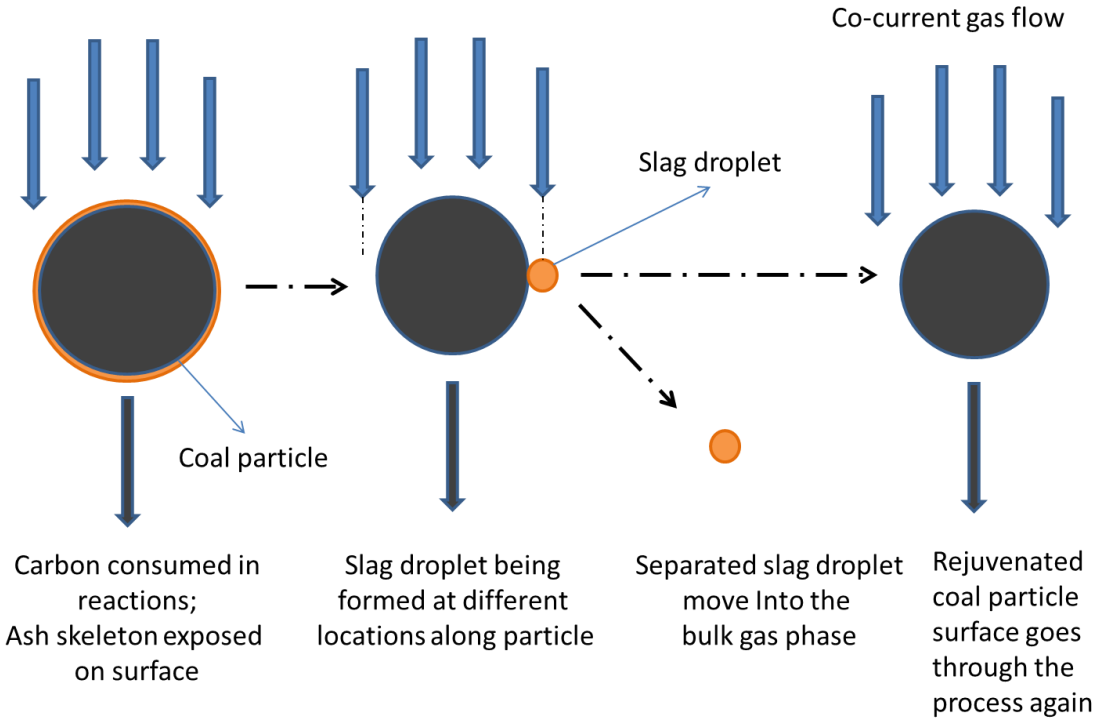

Figure 19. Slag formation and detachment.

Very few papers in the area of modeling look into the process of slag detachment. The dominant mechanism for the addition of ash to the slag flow layer on the refractory is assumed to be due to the impaction of char particles. However, deposition of slag due to char impaction may not be the only mechanism by which slag gets added to the flowing slag layer on the wall. A fraction of these slag droplets that separate into the bulk of the gasifier can also get deposited on the wall in addition to the char particles.

The deposition rate of char particles and slag droplets depends on their size, density, and the bulk flow conditions[109,110,111,112]. The size distribution of the slag droplets in the bulk of the gasifier is difficult to estimate as the mechanisms for detachment of the slag droplets are complicated and depend on several variables such as solids temperature, coal type, ash composition, ash quantity, coal particle size, rate of heating of char particle, feed nozzle design, profile of transport variables, probability of attrition, and so on. Experimental studies using drop tube furnaces show that the size distribution of the slag droplets also strongly depends on the mechanism by which they get detached from the char particles[113]. Condensation of volatile components of the ash content is expected to result in the formation of sub-micron slag droplets[114]. Char particles from certain coal types can readily break up due to the rapid volumetric increase of carbon and volatile materials within the coal particle. This mechanism can lead to the formation of slag droplets of the order of a few microns[99]. Shedding can also be a dominant mechanism

when the temperature of the solids is much higher than the melting point of the ash. The size of the liberated slag droplets also depends on the conversion rate of the char particles. In the limiting case, complete coalescence can take place where all the ash content within a coal particle coalesces to form a single slag droplet[99,109,113,115]. This case is similar to the dominant assumption of no ash separation in the existing literature. During rapid reaction, the char surface recedes rapidly and the molten ash minerals do not have sufficient residence time on the surface to coalesce. Under these circumstances, the minerals inside the char matrix, also known as the included minerals, would detach from the coal particle without coalescing[107,109]. Between the two limiting cases, slag droplets can separate after they partially coalesce[109]. Therefore, a particle size distribution (PSD) of detached slag droplets would be expected in the bulk. The deposition of char particles, as well as slag droplets, has not been considered in the open literature to the best of the authors' knowledge and there is rarely any information on the contribution of slag deposition to the net slag deposit on the wall and how this deposition flux is affected by the size of the slag droplets.

The existing literature shows that slag layer models have been developed and implemented in gasifiers and combustors[88,89,91,92,116-124]. However, slag deposition flux to the wall is difficult to model and a number of assumptions are often made. Deposition flux is typically assumed to be constant[88,125] or set to a fraction of the total solid flow rate entering the gasifier[120]. Another common assumption is to consider a fixed profile for slag deposition along the wall[123] during steady state and dynamic simulations. Obviously, these assumptions are somewhat arbitrary and difficult to justify especially during transient operation of the gasifier. A number of authors have developed CFD models[91,118,119] that track particle trajectories to calculate the net amount of slag deposition on the wall. However, it is computationally intractable to extend these rigorous models to perform dynamic simulations on a commercial-scale gasifier.

As noted before, since the slag layer thickness is an important variable, the objective of this study is to obtain a better estimate of the slag layer thickness as the operating conditions are changed. Therefore, the dynamic effect of a number of key variables such as coal flow rate and O_2/coal ratio on the slag layer is evaluated. In addition, when the coal switching takes place, there can be a significant impact on the slag layer depending on the type of the coal, unless the operating conditions are changed appropriately. Therefore, a study has been conducted to observe the effect of coal switching. These simulations will help to determine the conditions under which the flowing slag layer thickness will increase rapidly.

From the previous discussion, a shrinking-particle model seems more physically correct for the region where the gasifier bulk temperature well exceeds the ash melting temperature. However, in the early region of the gasifier, where the bulk temperature remains lower than the ash melting temperature, a shrinking-core model seems more appropriate. Therefore, in this work, we have developed a novel first principles, one-dimensional, non-isothermal, pressure-driven dynamic model for a downward-firing, entrained-flow, slurry-fed, oxygen-blown (GEE-Texaco type) gasifier using a hybrid shrinking-core-shrinking-particle reaction model. A novel sub-model for slag formation on the char surface and detachment into the bulk is included in the present work. Slag deposition and slag layer models have been developed and integrated into the novel gasifier model where slag deposition due to char impaction and slag droplet impaction have been considered. It is desired that the models should be reasonably accurate yet computationally tractable so that the dynamic model can be used for estimation and control studies. First the model development is described followed by a number of studies conducted using the model.

2.2.1.1 Background and description

The shrinking-core model used in this work has been previously presented by Kasule[93,126] et al. and is used for the early region of the gasifier where the bulk temperature is below the ash melting temperature. Details of that model can be found in the work of Kasule et al. It should be noted that in entrained-flow gasifiers, burners are designed to promote swirling motion at the top of the gasifier that results in quick evaporation of water and the subsequent devolatilization step followed by combustion of the liberated volatile matter leading to a significant temperature peak. The high carbon residue formed after this process is called char. From that region to the exit of the gasifier, the solids temperature remains well

above the melting point of ash. Therefore the shrinking particle model is applied to that region. Figure 20 shows the regions where shrinking core and shrinking particle models are applied.

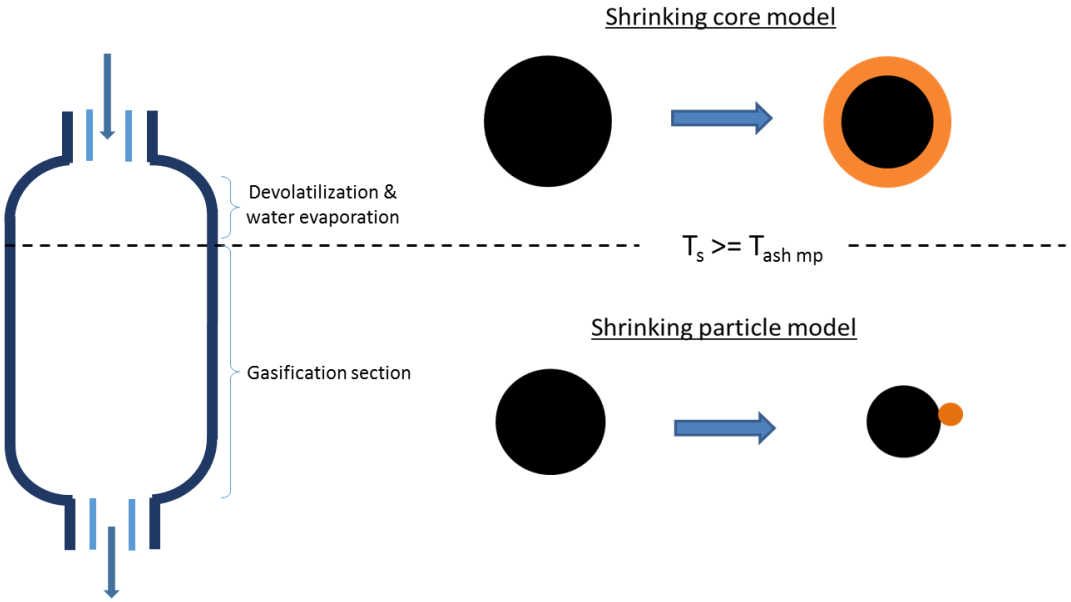

Figure 20. Hybrid shrinking core shrinking particle (HSCSP) model.

A PSD is considered for the detached slag droplets. A model is developed to calculate the deposition flux for both char particles and slag droplets, both of which contribute to the slag flow along the wall that eventually leaves the gasifier from the bottom. A schematic of the proposed model is shown in Figure 21.

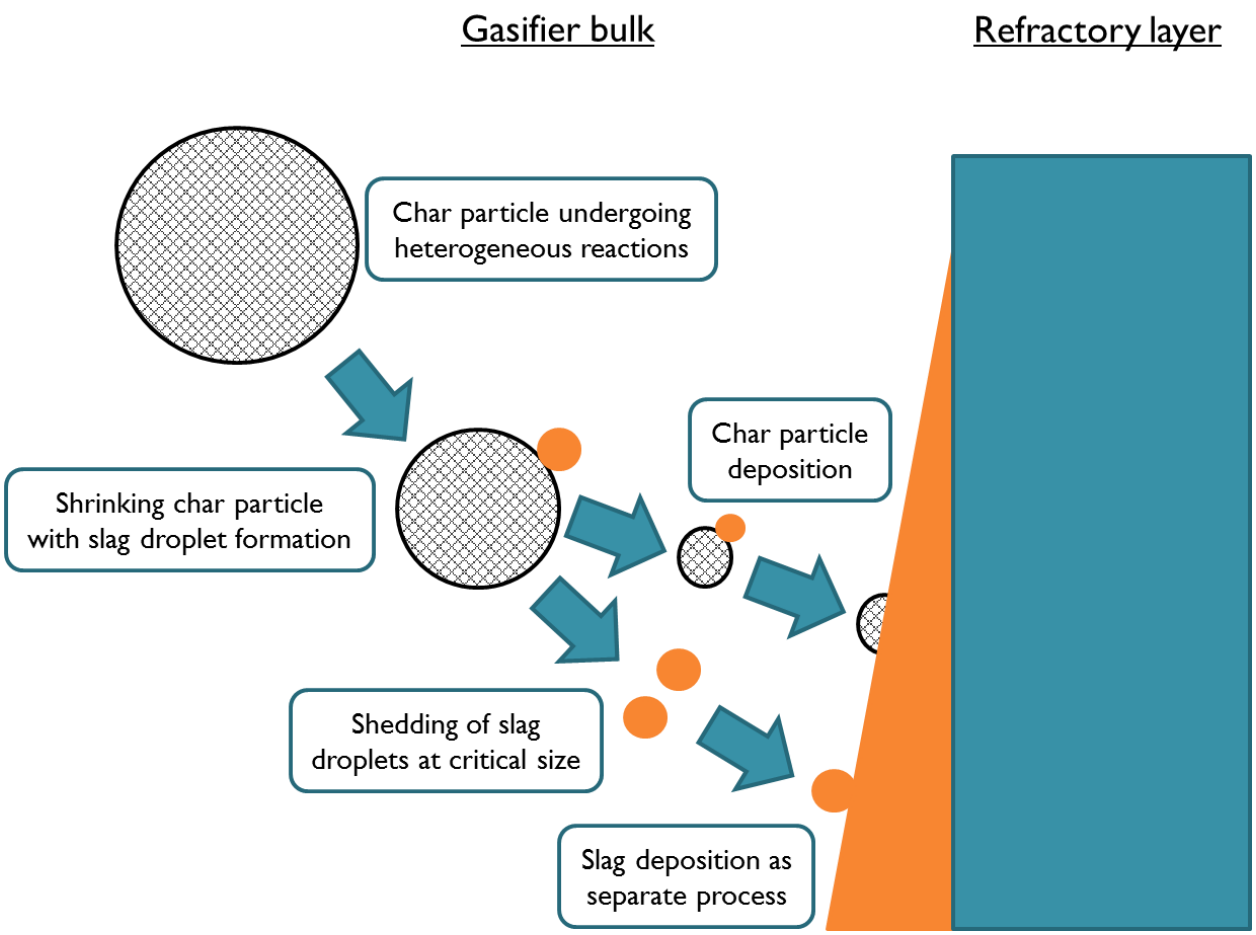

Figure 21. Schematic of the formation mechanism of slag droplets and their deposition on the wall along with char particles and the subsequent formation of a slag layer on the gasifier wall.

The following assumptions have been made in developing the gasifier model with slag flow:

1. Char particles and slag droplets are spherical.
2. Radial distribution of char particles and slag droplets is uniform.
3. The constituents of the coal particle are assumed to be uniformly distributed. Slag separation occurs uniformly for all char particles.
4. No particle-particle interaction; system is assumed to be sparse.
5. Excluded minerals, or minerals not associated with the char particles, are not considered in this study.
6. The char particle and detached slag droplet velocity are assumed to be equal and solved for using a single momentum balance equation. For entrained flow gasifiers, it is found that the volume fraction of solids is very small, less than one percent[94]. Furthermore, the solid particle sizes considered are < 100 microns in diameter and for such systems, the differences in gas and solid velocities are found to be very small[127]. The detached slag droplets are smaller than the char particles and therefore would tend to flow at the gas velocity. The solid phase velocity calculated on the basis of the char particle and slag droplets can be expected to be even closer to the gas velocity and therefore the error in calculating the solid velocity using a single momentum balance equation is assumed to be small.
7. The capture efficiency for char and slag droplets at the wall is assumed to be unity when the solids temperature exceeds the melting point of ash. The assumption for the char particles has been made

based on the observation of the results from the present model that when the char particles impact the wall, they already contain substantial amounts of slag. Therefore, it is likely that the impacting slag droplets will be fully captured.

8. Slag layer properties including thermal conductivity, specific heat, and density are assumed to be constant.
9. Due to the small thickness of the slag layer, a linear temperature profile is assumed in the slag layer.
10. The slag layer viscosity is assumed to be constant along the slag layer thickness.
11. The momentum equation for the slag layer is solved analytically and used in the model.

Both the solid and gas phases are modeled as continuous phases. A particle model is developed to account for the slag droplets that are attached to the char particles and for the detached slag droplets that exist in the bulk and is integrated with the continuous phase model. Both, the continuous and the particle models are solved integrated and solved simultaneously. A schematic of the integration is shown in Figure 22.

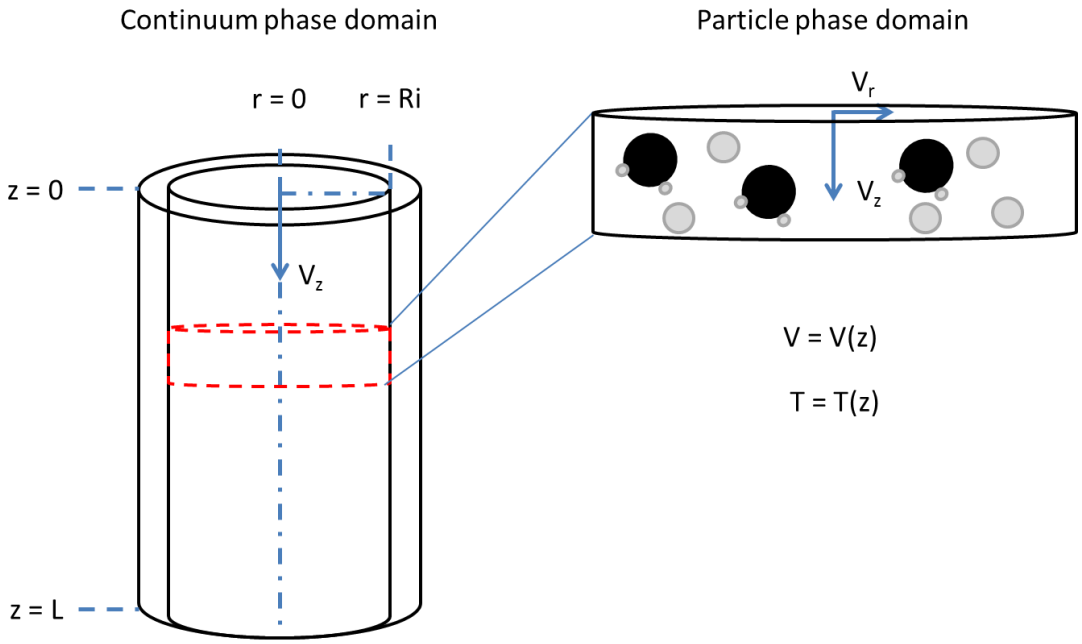

Figure 22. Continuum phase domain for solid and gas integrated with the particle phase domain.

A few notations need to be described before presenting the model. The gas phase volume fraction is denoted as ε. The volume fraction of the detached slag droplets is represented by ε_{sd}. The volume fraction of the attached slag droplets is denoted by ε_{sa}. A particle size distribution is considered, where the detached slag droplets are divided into four size bins depending on the diameters of the slag droplets: 1-10, 10-20, 20-30 and greater than 30 μm. The volume fractions of these bins in the bulk are denoted by $\varepsilon_{d,1}$, $\varepsilon_{d,2}$, $\varepsilon_{d,3}$, and $\varepsilon_{d,4}$, respectively. Figure 23 shows the schematic representation of the notations used in this work.

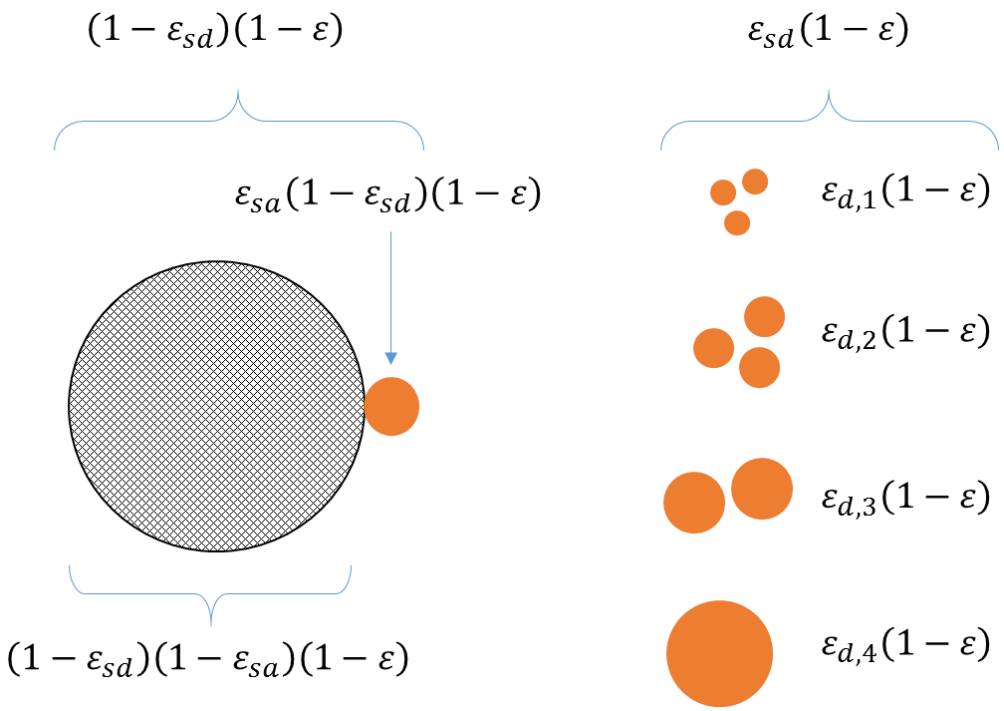

Figure 23. Schematic representation of the notations for denoting solids fractions in the continuum model.

The overall mass balance of the solid phase is modeled by Eqn. (106) . Solids are lost to the gas phase due to the heterogeneous reactions and due to the deposition of char particles and slag droplets onto the wall. These loss mechanisms are represented by the second and third terms on the right hand side of Eqn. (37), respectively.

$$\frac{\partial\left(\rho_{s,avg}(1-\varepsilon)\right)}{\partial t} = -\frac{\partial\left(\rho_{s,avg}(1-\varepsilon)U_s\right)}{\partial x} - (1-\varepsilon)(1-\varepsilon_{sa})(1-\varepsilon_{sd})\Gamma_{s-g} - \frac{4\,m_{dep}}{D_i} \quad (37)$$

Here, $\rho_{s,avg}$ is the average density of the solid phase comprising of the char particles and slag droplets, U_s is the solid phase velocity, Γ_{s-g} is the sum of all heterogeneous reaction rates, m_{dep} is the net deposition flux to the wall considering deposition of both char particles and slag droplets and D_i is the internal diameter of the gasifier. The term $(1-\varepsilon)(1-\varepsilon_{sa})(1-\varepsilon_{sd})$ represents the volume fraction occupied by the char particles.

Eqn. (38) shows the gas phase mass conservation equations.

$$\frac{\partial\left(\rho_g\varepsilon\right)}{\partial t} = -\frac{\partial\left(\rho_g\varepsilon U_g\right)}{\partial x} + (1-\varepsilon)(1-\varepsilon_{sa})(1-\varepsilon_{sd})\Gamma_{s-g} - m_{rg} + m_{mg} \quad (38)$$

ρ_g are the average gas density, U_g are the gas velocity, the recirculation effect in the gas phase is captured by the terms m_{rg}, which is the mass of gas that leaves the control volume (CV) because of recirculation, and m_{mg}, which is the mass of gas that gets added to a CV due to recirculation. These terms are calculated by the following equations:

$$m_{rg} = \dot{m}_{recir}/A_R L_2 \quad (39)$$

$$m_{mg} = \dot{m}_{recir}/A_R L_1 \quad (40)$$

$$\dot{m}_{recir} = \alpha\, \dot{m}_{in} \tag{41}$$

where A is the cross section area, L_2 is the length of the zone from where the recirculating gas is removed and L_1 is the length of the zone where the gas is added into the bulk gas stream, α is the recirculation ratio and $\dot{m}_{in}$ is the inlet gas stream. A schematic of the recirculation model is shown in Figure 24.

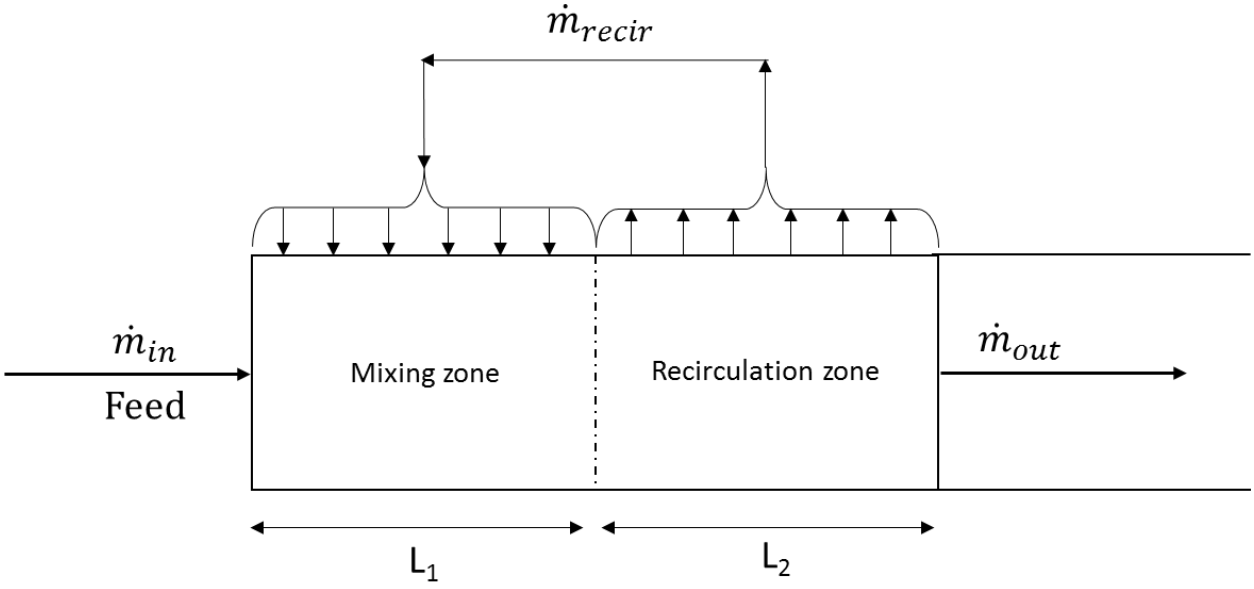

Figure 24. Schematic of the recirculation model.

Eqn. (42) and (43) show the species conservation equations for the solid and gas phases, respectively.

$$\frac{\partial\left((1-\varepsilon)(1-\varepsilon_{sa})(1-\varepsilon_{sd})\rho_{ch}X_{s,j}\right)}{\partial t} = -\frac{\partial\left((1-\varepsilon)(1-\varepsilon_{sa})(1-\varepsilon_{sd})\rho_{ch}U_s X_{s,j}\right)}{\partial x} + (1-\varepsilon)(1-\varepsilon_{sa})(1-\varepsilon_{sd})r_{s,j} \tag{42}$$

$$\frac{\partial\left(\varepsilon\rho_g y_{g,i}\right)}{\partial t} = -\frac{\partial\left(\varepsilon\rho_g U_g y_{g,i}\right)}{\partial x} + \varepsilon\, r_{g,i} - m_{rg}y_{g,i} + m_{mg}y_{g,i,avg} \tag{43}$$

The volume fraction corresponding to the char particle volume, shown in Figure 23 is used in Eqn. (42) for each of the terms. The last two terms in Eqn. (43) correspond to the recirculation of gas species out of and into the control volume similar to the overall gas balance equation. $y_{g,i}$ is the mass fraction of the species i. $y_{g\,i,avg}$ denotes the average mass fraction of species i in the circulating flow. Details of the recirculation model can be found in the work of Kasule et al[93].

The gas phase density is calculated by assuming ideal gas law in the form given by Eqn. (44).

$$\rho_g = \frac{P}{RT_g}.\frac{1}{\sum_{i=1}^{N}\left({}^{y_i}/_{MW_i}\right)} \tag{44}$$

In Eqn. (44), N is the total number of gaseous species and y_i and MW_i are the mass fraction and molar weight of the i[93] gaseous species.

As the char undergoes reactions, slag associated with the matrix becomes free and forms slag droplets that are attached to the surface of the char particle. The ash is assumed to be homogeneously distributed in the coal particle. Based on the mass fraction of the ash and carbon, the amount of ash that gets exposed on the surface per mass of carbon reacting can be calculated. The mass conservation equation for the attached slag droplets is given by Eqn. (45).

$$\rho_{sl}\frac{\partial((1-\varepsilon)(1-\varepsilon_{sd})\varepsilon_{sa})}{\partial t} = -\rho_{sl}\frac{\partial\left((1-\varepsilon)(1-\varepsilon_{sd})\varepsilon_{sa}U_s\right)}{\partial x} + (1-\varepsilon)(1-\varepsilon_{sa})(1-\varepsilon_{sd})\Gamma_{s-g}\omega_{ash} - \sum_{n=1}^{4} p_{sl,n}M_{cd,n} \quad (45)$$

Here, ρ_{sl} is the slag density, ω_{ash} is the ratio of ash to carbon mass fraction, $p_{sl,n}$ is the number of slag droplets detached per unit volume per unit time from the char surface corresponding to the size bin *n* and $M_{cd,n}$ is the mass of the slag droplet of critical diameter corresponding to the size bin *n*. The second term on the right side of Eqn. (45) represents the rate of formation of the slag droplets due to the heterogeneous reactions. The final term represents the sum of the rates of detachment of slag droplets into their respective size bins.

Detached slag droplets belong to one of the four size bins. The mass conservation equation for the slag droplets in each of the bins is given by Eqn. (46).

$$\rho_{sl}\frac{\partial\left((1-\varepsilon)\varepsilon_{sd}\varepsilon_{d,n}\right)}{\partial t} = -\rho_{sl}\frac{\partial\left((1-\varepsilon)\varepsilon_{sd}\varepsilon_{d,n}U_s\right)}{\partial x} + p_{sl,n}M_{cd,n} - \frac{4\,m_{sl,dep,n}}{D_i} \quad (46)$$

$m_{sl,dep,n}$ is the deposition flux of the slag droplets in bin size *n*. Eqn. (46) is written for three of the four bins. In addition, a summation equation shown in Eqn. (47) is written.

$$\sum_{n=1}^{4}\varepsilon_{d,n} = 1 \quad (47)$$

The overall detached slag mass conservation equation is shown in Eqn. (48).

$$\rho_{sl}\frac{\partial((1-\varepsilon)\varepsilon_{sd})}{\partial t} = -\rho_{sl}\frac{\partial\left((1-\varepsilon)\varepsilon_{sd}U_s\right)}{\partial x} + \sum_{n=1}^{4} p_{sl,n}M_{cd,n} - \frac{4\sum_{n=1}^{4} m_{sl,dep,n}}{D_i} \quad (48)$$

The continuum model tracks the mass of slag droplets in the bulk based on $p_{sl,n}$ and $m_{sl,dep,n}$.

2.2.1.2 Particle model

For calculating the term $p_{sl,n}$ used in the continuum model, a particle model is required. This model tracks the growth of the slag droplets on the char particle and helps to identify the locations of detachment and the detachment rate into each of the bin sizes. A particle size distribution is used as an input to the model and is assumed to be constant throughout the length of the gasifier. In the present framework, it is also assumed that the ash content of all the char particles in a control volume is constant and the growth and detachment phenomena of slag droplets from a char particle are similar for all char particles in the same control volume.

The number of slag droplets that belong to bin size *n* that could detach from the char surface is termed as $w_{det,n,i}$. After the slag droplets detach, the residual mass left behind gets added to the slag generated in the next control volume. This mass of remaining slag is denoted by $M_{sr,n,i}$. $M_{sr,n,i}$ and $w_{det,n,i}$ are calculated using Eqn. (49)-(50).

$$w_{det,n,i} = \left\lfloor \frac{\omega_{ash,i}\Gamma_{s-g,i}V_{ch,i}\tau_{p,i} + M_{sr,n,i-1}}{M_{cd,n}} \right\rfloor \quad (49)$$

$$w_{det,n,i}V_{cd,n}\rho_{sl,i} + M_{sr,n,i} = \omega_{ash}\Gamma_{s-g,i}V_{ch,i}\tau_{p,i} + M_{sr,n,i-1} \quad (50)$$

Here, $\omega_{ash,i}$ is the ratio of ash to carbon mass fraction, $\Gamma_{s-g,i}$ is the sum of all heterogeneous reactions on the carbon of the char particle, $V_{ch,i}$ is the char particle volume, $V_{cd,n}$ is the detachment volume of the slag in size bin *n* and $M_{cd,n}$ is its corresponding mass.

The total slag mass that could possibly separate from the char surface per unit volume of the reactor for each of the size bins is denoted by $M_{sl,poss,n,i}$ and is calculated using Eqn. (51). Based on the PSD, the total mass of slag that does finally separate into each of the bin sizes in a CV is calculated using Eqn. (52).

$$M_{sl,poss,n,i} = w_{det,n,i}N_{ch,i}M_{cd,n} \quad (51)$$

$$M_{sl,sep,n} = M_{sl,poss,n,i}\, fr_n \quad (52)$$

Here, fr_n is the input to the model and is the fraction of mass present in bin size *n* over the total slag mass in the bulk. The sum of fr_n for all bin sizes is unity. $N_{ch,i}$ is the number of char particles per unit volume in the CV and is calculated using Eqn. (46), which is obtained directly from the definition of the volume fractions.

$$N_{ch,i}V_{ch,i} = (1-\varepsilon_i)(1-\varepsilon_{sa,i})(1-\varepsilon_{sd,i}) \quad (53)$$

Finally, the slag detachment rate into each of the bins is calculated using Eqn. (54)-(55).

$$p_{sl,n,i}M_{cd,n}\tau_{p,i} = M_{sl,sep,n} \quad (54)$$

$$\tau_{p,i} = \frac{\Delta x}{U_{s,i}} \quad (55)$$

where, $\tau_{p,i}$ is the residence time of the particles in a CV. Eq. (53)-(54) are the key equations for connecting the continuum and particle models. Eqn. (49)-(52) and Eqn. (54) are written for each of the bin sizes. Additional equations are written for the shrinking char particles as shown in Eqn. (56)-(57).

$$M_{ch,i} = V_{ch,i}\,\rho_{ch} \quad (56)$$

$$M_{ch,i} = M_{ch,i-1} - \Gamma_{s-g,i}V_{ch,i}\,\tau_{p,i}\,(1+\omega_{ash}) \quad (57)$$

A figure showing the important equations and exchange of information between the continuum model and the particle model is shown in Figure 25. The continuum and particle model equations are solved simultaneously.

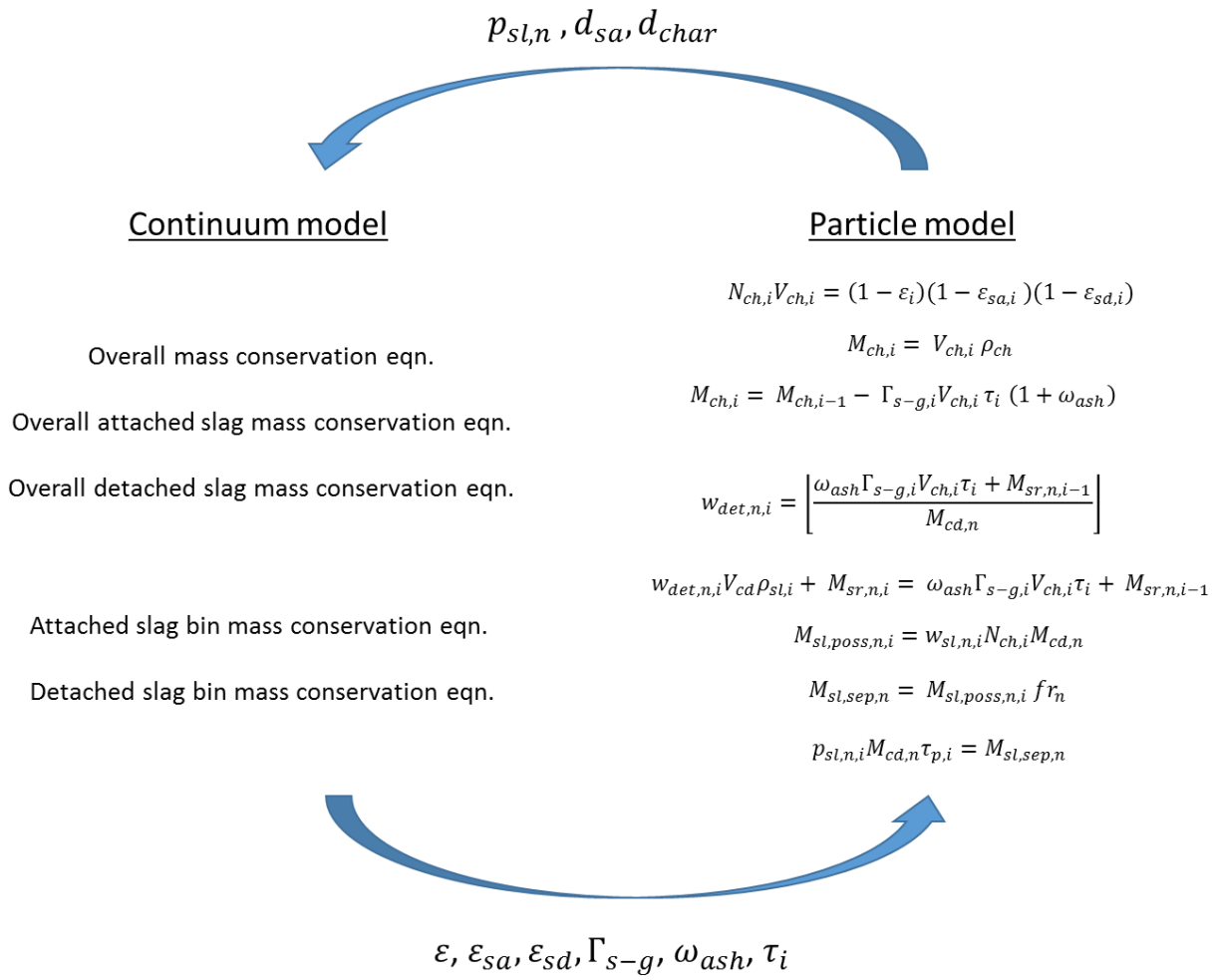

Figure 25. Transfer of information between the particle model and continuum model.

2.2.1.3 Momentum balance equation

It is assumed that the velocities of the slag droplets, both attached and detached, are the same as the char particle since the system is found to be dilute in terms of solid concentration and the difference in gas and solid velocities are found to be inconsiderate. This assumption has been made mainly for simplicity and ensures the computational expense remains tractable for a dynamic model. But certainly, the model can be easily enhanced by relaxing this assumption. Under this assumption, momentum balances are required only for the gas phase and the overall solid phase and these balances are shown in Eqn. (58) and (59), respectively.

$$\frac{d(\varepsilon\rho_g U_g^2)}{dx} = -\varepsilon\frac{dP_t}{dx} + \varepsilon\rho_g g - (1-\varepsilon)f_s \tag{58}$$

$$\frac{d((1-\varepsilon)\rho_{s,avg}U_s^2)}{dx} = -(1-\varepsilon)\frac{dP_t}{dx} + (1-\varepsilon)\rho_{s,avg}g + (1-\varepsilon)f_s \tag{59}$$

where, f_s is the drag force per unit volume of particles, U_s and U_g are the solid and gas phase velocities respectively, P_t is the total pressure in the system. The drag force is calculated using the equation from Arastroopour and Gidaspow[128] as;

$$f_s = \frac{3C_D\rho_g(1-\varepsilon)^{-2.65}(U_g - U_s)\left|U_g - U_s\right|}{4d_{avg}} \tag{60}$$

where the C_D is the drag coefficient taken from Rowe and Henwood[129]. This is given as

$$C_D = \begin{cases} \frac{24}{Re}[1 + 0.15Re^{0.687}]\,; Re < 1000 \\ 0.44; \qquad\qquad Re \geq 1000 \end{cases} \tag{61}$$

The Reynolds number is given as

$$Re = (1-\varepsilon)\rho_g d_{avg}\frac{\left|U_g - U_s\right|}{\mu_g} \tag{62}$$

where, μ_g, is the viscosity of the gas phase and d_{avg} is the weighted average diameter of the slag droplets and char particles, calculated on the basis of their respective volume fractions.

2.2.1.4 Energy balance equation

The energy balance equations for the gas and solid phases are shown in Eqn. (63) and (64). The temperature of the slag droplets and the char particle are assumed to be equal. This is done mainly for simplicity and keeping the computational expense tractable for a dynamic model. The model can be easily enhanced by relaxing this assumption.

$$\begin{aligned} &\frac{\partial\left(\varepsilon\rho_g C_{p,g}T_g\right)}{\partial t} + \frac{\partial\left(U_g\varepsilon\rho_g C_{p,g}T_g\right)}{\partial x} \\ &\qquad = \frac{\pi D_i}{A_R}\left\{h_{w-g}\left[T_w - T_g\right]\right\} \\ &\qquad - (1-\varepsilon)\frac{6}{d_{char}}\left\{e_g F_{g-s}\sigma\left[T_g^4 - T_s^4\right] + h_{g-s}\left[T_g - T_s\right]\right\} \\ &\qquad + \sum_{\substack{gas-phase \\ reactions \\ j}} \varepsilon\left(-\Delta H_{rxn,j}\right)r_j \; - \; m_{rg}h_{rg} + m_{mg}h_{mg} \end{aligned} \tag{63}$$

$$\begin{aligned} &\frac{\partial\left((1-\varepsilon)\rho_{s,avg}C_{p,avg}T_s\right)}{\partial t} + \frac{\partial\left(U_s(1-\varepsilon)\rho_{s,avg}C_{p,avg}T_s\right)}{\partial x} \\ &\qquad = \frac{\pi D_i}{A_R}F_{w-s}[T_w^4 - T_s^4] + (1-\varepsilon)\frac{6}{d_{char}}\left(e_g F_{g-s}\sigma\left[T_g^4 - T_s^4\right] + h_{g-s}\left[T_g - T_s\right]\right) \\ &\qquad + \sum_{\substack{solid-phase \\ reactions \\ k}} (1-\varepsilon)\left(-\Delta H_{rxn,k}\right)r_k \end{aligned} \tag{64}$$

where F_{g-s} and F_{w-s} are the view factors between gas-solid and wall- solid, respectively. In the gas phase energy balance equation, $m_{rg}h_{rg}$ is the enthalpy leaving and $m_{mg}h_{mg}$is the enthalpy entering the control volume due to recirculation. $\Delta H_{rxn,j}$ and $\Delta H_{rxn,k}$ are the heat of reaction for the homogeneous and heterogeneous reactions, respectively. The heat of reactions and kinetic parameters have been taken from the literature cited in Kasule et al[93]. The authors could not find the heat of fusion for the ash in Illinois #6 coal, however, based on the limited literature, it seems that the heat of fusion for ash in coal[130,131] is usually very small in comparison to the heat of reaction of the heterogeneous reactions. Therefore, the heat of fusion is not explicitly considered in this model. Furthermore, ash transformation reactions are not considered separately, but are assumed to take place spontaneously along with the char

conversion reactions. Due to this assumption, the latent heat of fusion for ash can be readily included in the energy balance equations by modifying the heat of reaction for the heterogeneous reactions. In the solid phase energy balance equation, $C_{p,avg}$is the average specific heat calculated using the weighted average of the void fractions of char, slag droplets attached and slag droplets in the bulk. Eqn. (65)-(66) show how h_{rg} and h_{mg} are calculated.

$$h_{rg} = \sum_{i=}^{N} y_i \int_{298}^{T} C_{p,i} dT \tag{65}$$

$$h_{mg} = \frac{1}{m} \sum_{k=1}^{r} h_{rg,k} \tag{66}$$

where *N* is the number of components in the gas phase, *r* is the number of control volumes in the recirculation zone and *m* is the number of control volumes in the mixing zone.

Eqn. (67)-(69) are used for the calculation of the average density and specific heat that is used in the momentum and energy balance equation for the solid phase.

$$\rho_{s,avg} = \varepsilon_{sd}\rho_{sl} + (1-\varepsilon_{sd})\varepsilon_{sa}\rho_{sl} + (1-\varepsilon_{sd})(1-\varepsilon_{sa})\rho_{ch} \tag{67}$$

$$d_{avg} = \varepsilon_{sd} d_{cr} + (1-\varepsilon_{sd})\varepsilon_{sa} d_{sa} + (1-\varepsilon_{sd})(1-\varepsilon_{sa}) d_{ch} \tag{68}$$

$$\rho_{s,avg} C_{p,avg} = \varepsilon_{sd}\rho_{sl} C_{p,slag} + (1-\varepsilon_{sd})\varepsilon_{sa}\rho_{sl} C_{p,slag} + (1-\varepsilon_{sd})(1-\varepsilon_{sa})\rho_{ch} C_{p,ch} \tag{69}$$

2.2.1.5 Reaction rates

The gasifier can be divided into several reaction zones based on the dominant reactions/processes that occur in the solids. These reactions/ processes include drying, devolatilization, combustion, and gasification. The first three of these processes tend to occur much earlier in the gasifier, and result in a dramatic increase in the solid temperature. Gasification reactions are slower and continue till the end of the gasifier. In both shrinking core and shrinking particle models, all reactions are considered at all locations.

Water vapor evaporation, devolatilization and the homogeneous reactions are modeled in the same manner as shown in Kasule et al[93]. Water evaporation is modeled similar to the work of Rao et al.[132] A point to note is that the water in the slurry and the moisture content is considered together in calculation of the evaporation rate. For devolatilization, the products and kinetic parameters for the reaction / processes given by Syamlal and Bisset[133] are used in the model.

The overall reaction rate for the shrinking core model is given by:

$$K_{overall} = \frac{1}{\frac{1}{k_{diff}} + \frac{1}{k_{ash}}\left(1 - \frac{1}{Y}\right) + \frac{1}{k_s Y^2}} \tag{70}$$

where *Y* is the ratio of the diameters of unreacted core and the char particle, and k_{diff}, k_{ash} and k_s are the gas film diffusion coefficient, ash diffusion coefficient and surface reaction coefficient respectively.

In contrast to the shrinking-core model, the shrinking particle model considers no resistance due to ash. The overall rate constant for a shrinking particle model is given by:

$$K_{overall} = \frac{1}{\frac{1}{k_{diff}} + \frac{1}{k_s}} \tag{71}$$

It can be noted that all rate constants are in the units of $g.cm^{-2}.atm^{-1}s^{-1}$. The expressions for the coefficients are taken from the work of Wen and Chaung[134]. Typically, a conversion factor of $6/d_{char}$ is used to give the overall reaction rate constant in terms of volumetric units. For the present model, the surface reaction rate constant term cannot be evaluated at a shrinking particle size since the reaction rate would tend to infinity as the diameter of the char particle shrinks to zero. The surface reaction rate constant is instead converted to volumetric units by evaluating the factor $6/d_{char}$ at the fixed char particle size. The particle size used by Wen and Chaung[134] had considered while developing these kinetics was 350µm.

2.2.1.6 Slag transport and deposition

While most of the slag droplets that are detached into the bulk remain in the gas phase, some of the droplets and char particles in the vicinity of the wall can impact the molten slag layer and get captured as shown in Figure 26. The deposition flux of the impacting particles and droplets is a key input required for the slag layer sub-model. The deposition flux depends on the number density of the particles and droplets as well as the deposition velocity.

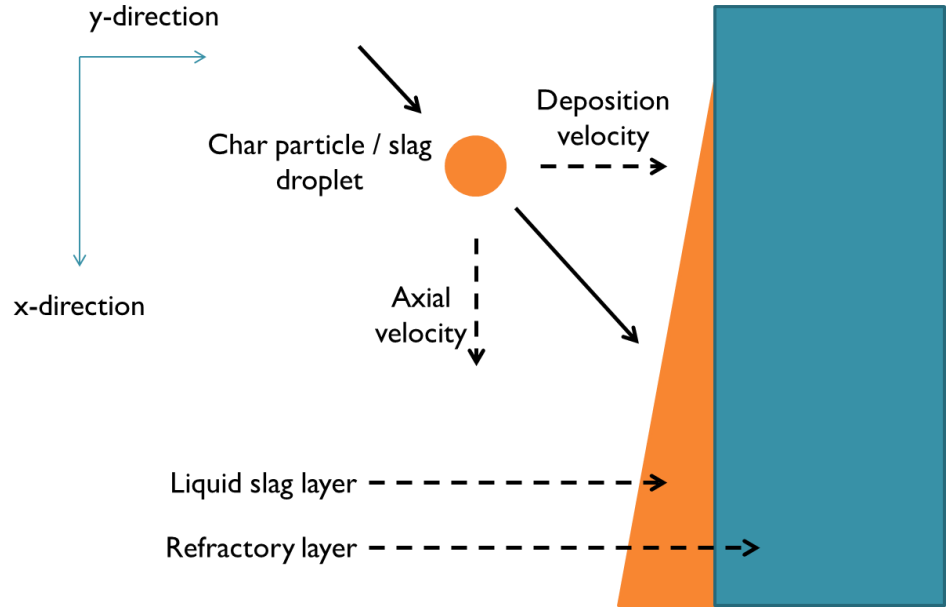

Figure 26. Schematic showing the slag droplet deposition on the gasifier wall.

Since the present model is a 1-D model of the slagging gasifier, an analytical expression is required in order to calculate the velocity of the char particles and slag droplets. Experimental and computational works are available in the open literature where the transport and deposition of solid particles or liquid droplets suspended in a flowing fluid are studied. The results are usually presented in the form of a dimensionless velocity as a function of dimensionless relaxation time graph[110,111,112,121,122] as seen in Figure 27. The relaxation time is a function of flow conditions as well as particle density and size and is calculated using Eqn. (72).

$$\tau_+ = \frac{\rho_p {d_p}^2 u_*^2}{18\rho_g \vartheta^2} \tag{72}$$

In Eqn. (72), ρ_p is the particle density, d_p is the particle diameter, u_* is the fluid friction velocity, ρ_g is the gas phase velocity and ϑ is the kinematic viscosity. The deposition velocity is calculated using Eqn. (73).

$$V_{dep} = V_{dep+} u_* \tag{73}$$

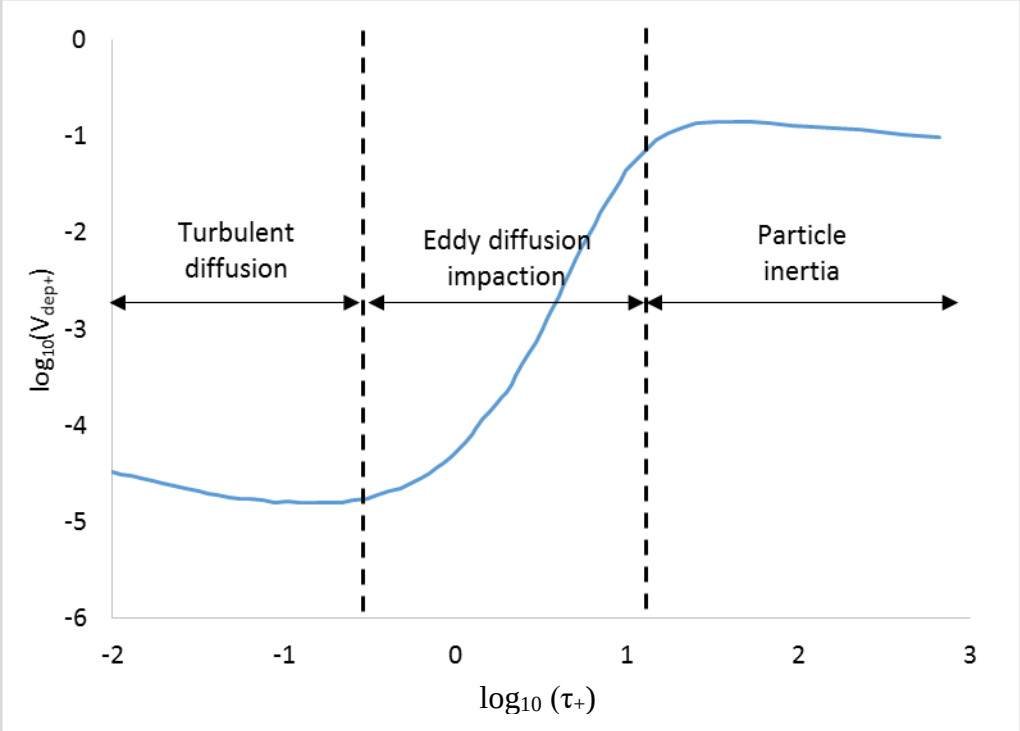

Figure 27. General plot showing the relation between the Vdep + and τ+ redrawn from Guha[114].

As seen in Figure 27, the dominant deposition mechanism(s) and deposition velocity can vary greatly depending on the value of τ_+. Particles that are a few microns in size fall in the regime where the deposition is mainly due to turbulent diffusion. In this case, the deposition velocity is small. Larger particles with higher relaxation time deposit due to eddy diffusion impaction. In this regime, the deposition velocity increases rapidly with increase in particle size. Deposition velocity levels out as the relaxation time increases further. In this third regime, particle inertia is the dominant deposition mechanism.

A few authors[111,121,122]have used correlations between the dimensionless relaxation time and dimensionless velocity to calculate the deposition rate in combustors and gasifiers. In the present study, the correlations proposed by Wood[110] are used to calculate the deposition velocity of the char particles and the slag droplets of different sizes.

For particles depositing due to turbulent diffusion and eddy diffusion impaction, V_{dep+} is given by Eqn. (74).

$$V_{dep+} = \frac{3\sqrt{3}}{29\pi}\left(\frac{D_p}{\vartheta}\right)^{2/3} + 4.5\times10^{-4}\,{\tau_+}^2 \tag{74}$$

where, D_p is the particle diffusivity and is given by;

$$D_p = \frac{kT}{3\pi\mu d_p} \tag{75}$$

In Eqn. (75), k is the Boltzmann's constant, T is the absolute temperature and μ is the gas phase viscosity. The dimensionless deposition velocity for particles that deposit due to particle inertia can be calculated

using Eqn. (76). The dimensionless deposition velocity is assumed to be constant and independent of particle size[110].

$$V_{dep+} = 0.175 \tag{76}$$

The fluid friction velocity and friction factor can be calculated using Eqn. (77)-(78) for the current range of fluid Reynolds number and are taken from Haaland[135].

$$u^* = \left(\frac{f}{2}\right)^{.5} \bar{u} \tag{77}$$

$$\frac{1}{\sqrt{f}} = -1.8 log_{10}\left[\left(\frac{\varepsilon_*/_D}{3.7}\right)^{1.11} + \frac{6.9}{Re}\right] \tag{78}$$

In the present work, it is assumed that the molten slag layer has a smooth surface and the term associated with surface roughness in Eqn. (78) i.e. $\left(\varepsilon_*/_D\right)$ is set to zero.

Using Eqn. (74)-(78), the deposition velocity of the slag droplets in different bin sizes and the char particles can be calculated. For the current flow conditions, it is found that the slag droplets of the size 1-10 microns deposit due to turbulent diffusion and eddy diffusion impaction with values for τ_+ less than 15. The slag droplets in the larger bin sizes have τ_+ values ranging from 50 to 400, depending upon location in the gasifier and size droplet sizes. Droplets in these size bins fall in the particle inertia dominant regime. The char particles enter the gasifier at a size of 100 microns which correspond to τ_+ as high as 1000. As the char particles react, they shrink in size and can exit the gasifier with τ_+ values lower than 50. As a result the char particles also fall in the particle inertia dominant regime and therefore have the same deposition velocity as the larger slag droplets as shown in Eqn. (76).

The deposition flux terms used in Eqn. (37), (46) and (48) are calculated using Eqn. (79)-(81).

$$m_{sl,dep,n} = \frac{(1-\varepsilon)\varepsilon_{sd}\varepsilon_{d,n}\rho_{sl}V_{dep,n}}{2} \tag{79}$$

$$m_{ch,dep} = \frac{(1-\varepsilon)(1-\varepsilon_{sa})(1-\varepsilon_{sd})\rho_{char}V_{dep.char}}{2} \tag{80}$$

$$m_{dep} = m_{ch,dep} + \sum_{n=1}^{4} m_{sl,dep,n} \tag{81}$$

Here, $V_{dep,n}$ is the slag deposition velocity for different bin sizes and $V_{dep,char}$ is the char particle deposition velocity. The slag deposition velocity is calculated using the Sauter mean diameter of the size range of the bins.

2.2.1.7 Slag flow model

It is important to ensure that the wall temperature in a refractory-lined entrained flow gasifier be high enough to avoid the formation of a solid slag layer. Slag solidification can lead to a rapid reduction in the available volume for reactions in the gasifier and can eventually clog the equipment. The maximum viscosity for slagging gasifiers is considered to be 250 Poise to avoid build-up of the slag layer[101]. To simulate the dynamics of the slag layer on the wall, a liquid slag layer sub-model is incorporated into the gasifier model described previously. A linear temperature profile across the slag thickness, i.e., in the radial direction is assumed. An analytical expression for the momentum balance is used and the mass and energy balance equations are solved using continuum equations. Several heat transfer mechanisms have been considered in the energy balance equation of the slag layer including convective heat transfer between the gas and the slag layer, conductive heat transfer between the refractory wall and the slag layer and the radiative heat interaction between various sections of the inside wall of the gasifier, and the solid

particles in the gasifier bulk, with the slag layer. Such an involved heat balance equation for the slag layer has not been considered previously in the literature to the best of the author's knowledge. A schematic of the slag model is shown in Figure 28.

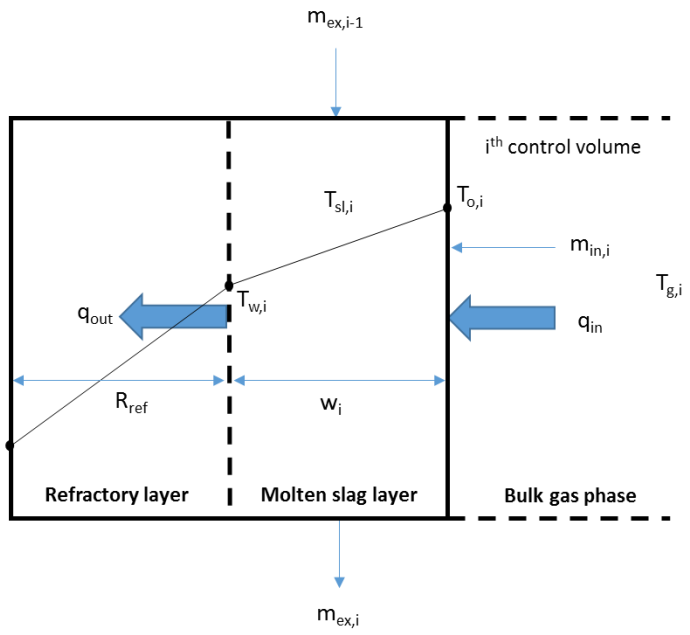

Figure 28. Schematic of the mass, momentum and energy interactions in the slag layer.

The mass balance equation is shown in Eqn. (82)[88].

$$\rho_{sl}\pi D_i \Delta x \frac{dw_i}{dt} = m_{in,i} + m_{ex,i-1} - m_{ex,i} \tag{82}$$

$m_{in,i}$ is the mass deposition rate onto the control volume, $m_{ex,i}$ is the mass flow rate of slag flowing out of the control volume and $m_{ex,i-1}$ is the mass flow rate of slag flowing into the control volume and w_i is the slag layer thickness. $m_{ex,i}$ is calculated using Eqn. (83)[136].

$$m_{ex,i} = \frac{1}{3}\frac{\pi D_i {\rho_{sl}}^2 g {w_i}^3}{\eta_{sl,i}} \tag{83}$$

$\eta_{sl,i}$ is the viscosity of the slag in the slag flow layer and g is acceleration due to gravity.

The expression for viscosity is calculated by the BCURA S [85] correlation[137] using Eqn. (84)-(85).

$$log_{10}\eta_{sl} = 4.468s^2 + \frac{12650}{T_{sl}} - 7.44 \tag{84}$$

$$s = \frac{SiO_2}{SiO_2 + Fe_2O_3 + CaO + MgO} \tag{85}$$

where, s is known as the silica ratio.

A slag layer heat balance equation is derived and shown in Eqn. (86).

$$\rho_{sl} w C_{p,sl,i} \pi D_i \Delta x \frac{dT_{sl,i}}{dt} = q_{in,i} - q_{out,i} + m_{in,i} C_{p,sl,i}\left(T_{s,i} - T_{sl,i}\right) + m_{ex,i-1} C_{p,sl,i}(T_{sl,i-1} - T_{sl,i}) \tag{86}$$

where $C_{p,sl,i}$ is the specific heat, $q_{in,i}$ is the sum of the energies flowing into the slag layer from the bulk side of the gasifier, $q_{out,i}$ is the heat conducted to the refractory, $T_{sl,i}$ and $T_{sl,i-1}$ are the temperatures of the slag layer in the current and previous control volume, respectively, and $T_{s,i}$ is the temperature of the incoming slag droplet, which is assumed to be equal to the solid phase temperature. $q_{in,i}$ is calculated using Eqn. (87)-(92). The heat transfer mechanisms considered in this work are similar to Kasule et al.[93].

$$q_{in,i} = \pi D_i \Delta x. \left[q_{conv,sl-g} + q_{rad,sl-p} + q_{rad,sl-b} + q_{rad,sl-top} + q_{rad,sl_i-sl_{allp\neq l}}\right] \quad (87)$$

$$q_{conv,sl-g} = h_{sl-g}\left(T_o - T_g\right) \quad (88)$$

$$q_{rad,sl-p} = F_{sl-p}\sigma_{sl-p}(T_o^4 - T_s^4) \quad (89)$$

$$q_{rad,sl-b} = F_{sl-b}\sigma_{sl-b}(T_o^4 - T_o(end)^4) \quad (90)$$

$$q_{rad,sl-top} = F_{sl-top}\sigma_{sl-top}(T_o^4 - T_w(0)^4) \quad (91)$$

$$q_{rad,sl_i-sl_{all,a\neq l}} = \sum_a e_{sl} F_{sl_i-sl_a}\left(T_{o_i}^4 - T_{o_a}^4\right) \quad (92)$$

Here, $q_{conv,sl-g}$ is the transfer due to convection from the gas phase in the bulk, $q_{rad,sl-p}$is the radiation heat transfer between the particles to the slag layer, $q_{rad,sl-b}$ and $q_{rad,sl-top}$ are the radiation heat transfer between the slag layer and the top and bottom wall of the slagging gasifier respectively and $q_{rad,sl_i-sl_{all,a\neq l}}$is the radiation heat transfer between different control volumes of the slag layer. *F* represents the view factor for the corresponding radiation heat flux terms. The equations for the friction factors are shown in Eqn. (72)-(75) and were obtained from Siegel and Howell[138].

$$F_{sl-p} = \left[\left(\left(z_{sl-p}/D_i\right)^2 + 0.5\right)/\sqrt{\left(z_{sl-p}/D_i\right)^2 + 1}\right] - \left(z_{sl-p}/D_i\right) \quad (93)$$

$$F_{sl-b} = \left[((z_{sl-b}/D_i)^2 + 0.5)/\sqrt{(z_{sl-b}/D_i)^2 + 1}\right] - (z_{sl-b}/D_i) \quad (94)$$

$$F_{sl-top} = \left[\left(\left(z_{sl-top}/D_i\right)^2 + 0.5\right)/\sqrt{\left(z_{sl-top}/D_i\right)^2 + 1}\right] - \left(z_{sl-top}/D_i\right) \quad (95)$$

$$F_{sl_i-sl_{all,a\neq l}} = 1 - \left[1 - \left[\left(2(z_{sl-b}/D_i)^3 + 3(z_{sl-b}/D_i)\right)/(2(z_{sl-b}/D_i)^2 + 1)\right]^{1.5}\right] dz \quad (96)$$

z is the distance between the surfaces. T_o in Eqn. (87)-(92) is the temperature at the hot face of the slag layer and is given by Eqn. (97)[87].

$$T_o = 2T_{sl} - T_w \quad (97)$$

$q_{out,i}$ is obtained using Eqn. (98).

$$q_{out,i} = 2\pi\Delta x.(T_o - T_w)\lambda_{sl} \quad (98)$$

2.2.2 Computational Approach

The slagging gasifier model, the slag transport and deposition model, and the model for the slag layer are integrated and solved using Aspen Custom Modeler® (ACM)[139]. In this formulation, $w_{det,n,i}$ is an integer variable making it difficult to solve the problem in software like ACM. In order to obtain a solution, an offline calculation is first done to obtain initial values of $w_{det,n,i}$ for the solver. This approach worked for obtaining steady state solutions, however, for a dynamic simulation, this approach is not feasible. The error in results is assessed by assuming that the detachment process is continuous rather than discrete for a number of cases. The error was found to be acceptable for slag droplets with detachment diameters of 1-10 microns. Therefore, the resulting error in calculation of the deposition flux is expected to be small

since only a fraction of the detached droplets are deposited. The assumption of continuous detachment of slag droplets can also be extended to larger slag droplets if the deposition velocities of these droplets and char particles are the same. This is because the total amount of slag deposited is calculated by summing up the slag deposition due to impaction of both char particles and slag droplets. As mentioned previously, as both large slag droplets and char particles belong to the particle inertia dominated regime, their deposition velocities are expected to be similar.

Due to the assumption of continuous detachment, Eqn. (45) is replaced by Eqn. (99).

$$\varepsilon_{sa} = 0 \tag{99}$$

The slag mass does not remain on the surface and continually detaches into the slag size bins in the bulk according to the particle model. The slag volume fraction in each bin is calculated using Eqn. (100). The total detached slag fraction can be calculated by summing up Eqn. (100) for all size bins and is given as Eqn. (101). Therefore, Eqn. (46) and (48) are replaced by Eqn. (100) and (101).

$$\rho_{sl}\frac{\partial\left((1-\varepsilon)\varepsilon_{sd}\varepsilon_{dn}\right)}{\partial t} = -\rho_{sl}\frac{\partial\left((1-\varepsilon)\varepsilon_{sd}\varepsilon_{dn}U_s\right)}{\partial x} + (1-\varepsilon)(1-\varepsilon_{sa})(1-\varepsilon_{sd})\Gamma_{s-g}\omega_{ash}fr_n - \frac{4*m_{sl,dep,n}}{D_i} \tag{100}$$

$$\rho_{sl}\frac{\partial((1-\varepsilon)\varepsilon_{sd})}{\partial t} = -\rho_{sl}\frac{\partial\left((1-\varepsilon)\varepsilon_{sd}U_s\right)}{\partial x} + (1-\varepsilon)(1-\varepsilon_{sa})(1-\varepsilon_{sd})\Gamma_{s-g}\omega_{ash} - \frac{4*\sum_{n=1}^{4}m_{sl,dep,n}}{D_i} \tag{101}$$

It should be noted that by using larger number of bins or a detailed particle size distribution and more accurate calculation of deposition velocities, especially in the particle inertia regime, a more accurate value for the slag thickness can be obtained. However considering both accuracy and computational tractability for a dynamic simulation, the authors believe that the current approach is reasonable.

The dimensions of the gasifier used in the present model are taken from the literature for the TECO gasifier[140]. The dimensions along with the operating conditions are shown in Table 5. The base coal type used in the steady state and dynamic simulation of the slagging gasifier model is Illinois #6. A dynamic run where the coal type is changed from Illinois #6 to Pittsburgh #8 is also simulated. The proximate and ultimate analyses for both the coal types are shown in Table 6.

Table 5. Model parameters and input conditions

Parameters/Conditions	Value
Gasifier parameters	
Length (m)	6.62
Internal diameter (m)	1.79
Operating conditions	

Coal slurry flow rate (kg/hr)	220,438
Particle diameter (μm)	100
Water to coal ratio	0.4115
O_2 to coal ratio	0.8347
Inlet Temperature (°C)	29.85
Inlet Pressure (bar)	28.33
Recirculation ratio	1.5

Table 6. Proximate and Ultimate analysis of Illinois #6 and Pittsburgh #8 coal [As-Received (wt %)]

Analyses	Illinois #6	Pittsburgh #8
Proximate analysis		
Fixed Carbon	44.19	52.38
Ash	9.99	9.17
Volatile matter	34.70	35.82
Moisture	11.12	2.63
Ultimate analysis (DAF)		
C	63.75	73.15
H	4.50	4.97
O	6.88	6.22
N	1.25	1.46
S	2.51	2.36
Silica ratio	0.5266	0.6105

The control structure for the dynamic runs is shown in Figure 29.

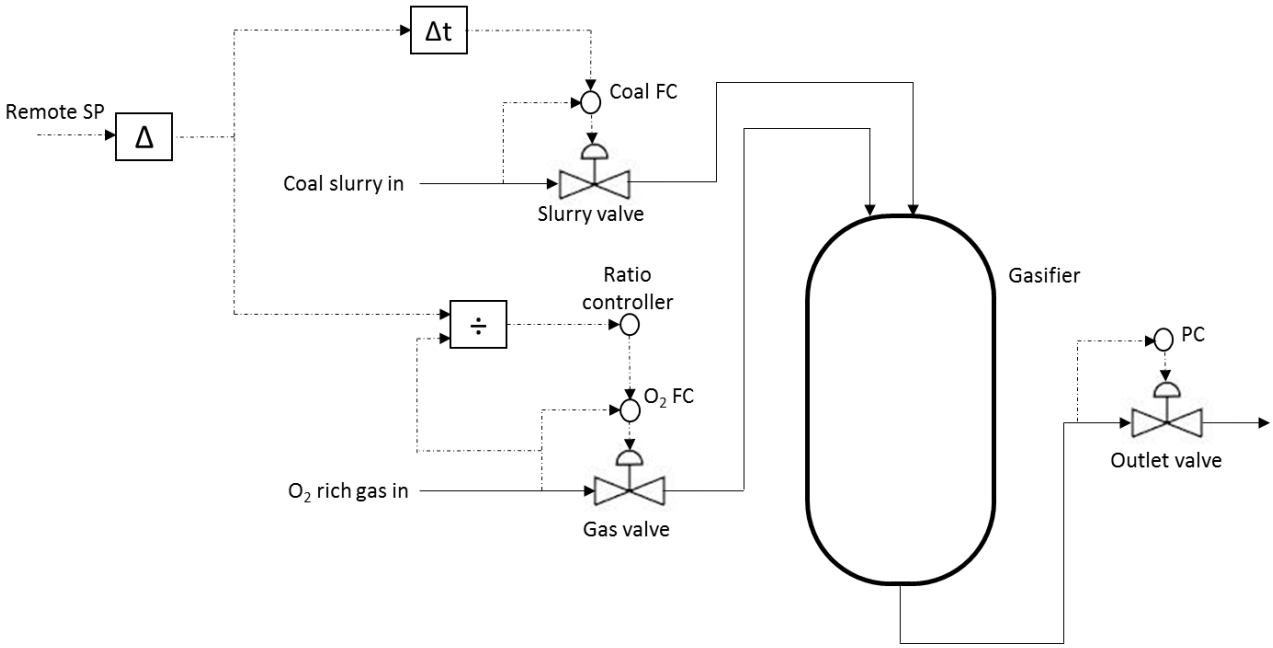

Figure 29. Control structure implemented to simulate dynamic runs for the slagging gasifier.

To avoid an oxygen-rich environment in the gasifier when the coal flow needs to be increased, first the coal flow is increased and then oxygen flow is increased. While decreasing the coal flow, first oxygen flow is increased. An O_2/coal ratio controller is used to generate the setpoint for the oxygen flow controller. The gasifier pressure is controlled by a valve in the exit line. It should be noted that for an IGCC plant, the gasifier pressure is controlled depending on the control strategy that is used. For a gas-turbine-lead-gasifier-follow strategy, the gasifier pressure is controlled by manipulating the slurry flowrate to the gasifier. For the gasifier-lead-gas-turbine-follow strategy the gasifier pressure is controlled by manipulating the syngas flow to the gas turbine. The current control system setup mimics the later strategy, but the pressure controller is placed right at the gasifier outlet as the balance of the plant is not considered in this study.

2.2.3 Results and Discussions

The results from the HSCSP model are summarized below. These include the validation of the data as compared to the TECO power plant[140], comparison with the traditional shrinking-core model, profiles of key variables and a sensitivity analysis on the detachment diameter.

2.2.3.1 Model Validation

In this section, the results were obtained assuming complete coalescence of slag droplets, which should closely resemble the results from the shrinking-core model assuming no slag detachment. This is compared first with the industrial data of TECO power plant[140]. The gasifier configuration of the TECO power plant and the operating conditions are shown in Table 7.

Table 7. Validation data from TECO power plant[140]

Conditions	TECO
Gasifier configuration[141]	

Internal diameter (cm)	179
Length (cm)	662
Operating conditions	
Coal feed rate (kg/s)	40
Coal particle size (µm)	100
Oxygen/coal ratio	0.82806
Water/coal ratio	0.4108
Pressure (atm)	26

The data from the TECO power plant are available for the clean syngas that is downstream of the radiant syngas cooler (RSC). In the RSC, steam is produced by utilizing the energy in the gasifier exit stream. It has been reported that certain gas-phase reactions, such as the water-gas shift reaction, continue to take place in the initial section of the RSC[93]. Therefore, for comparing the results with the TECO Power plant, a simple model of the RSC was developed in Aspen Plus.

The RSC is modeled using a plug flow reactor. This model is implemented in a similar manner as done in the work of Kasule[93]. A constant cooler temperature of 609 K was assumed.

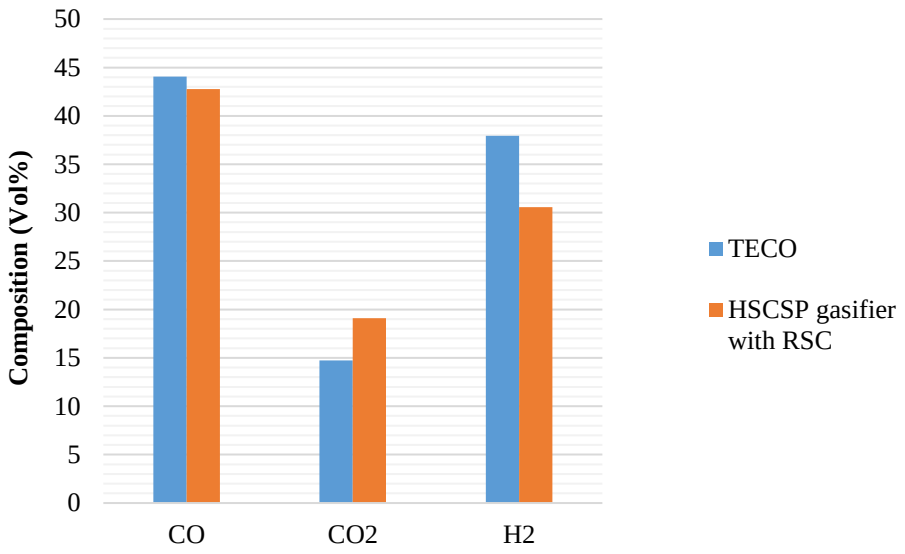

Figure 30. Comparisons of the mole fractions of CO2, CO, H2 and ¬¬H2O (on dry basis) at the exit of the RSC with TECO data.

Figure 30 shows that the results from the HSCSP model shows a good qualitative agreement with the TECO data.

2.2.3.2 Shrinking core vs HSCSP model

The results from this work are compared with the shrinking-core model developed by Kasule et al.[93] For a fair comparison, feed composition, flow rates, pressures, and O_2/Coal ratio are set to be the same in both the models.

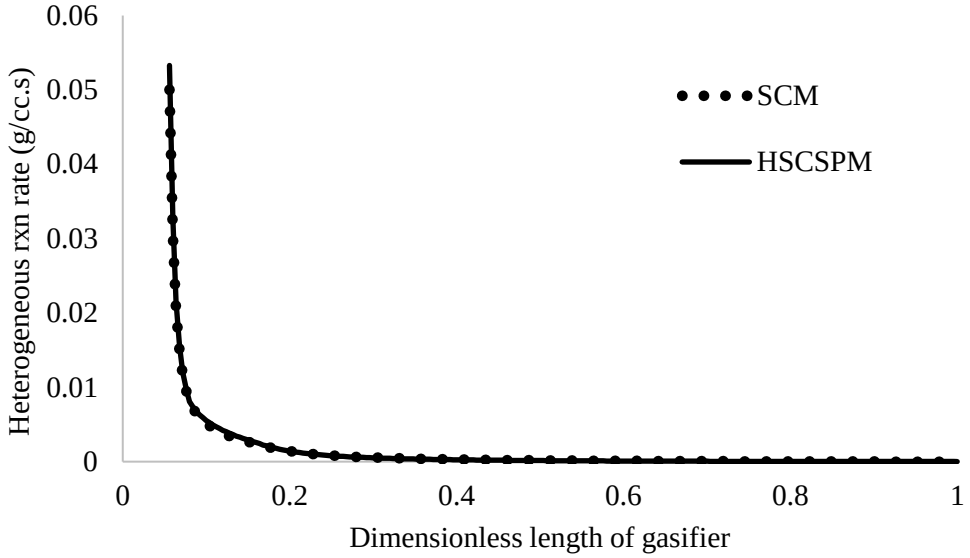

Figure 31. Comparison of the reaction rates between the shrinking particle model and hybrid shrinking core-shrinking particle model.

Figure 31 shows the heterogeneous reaction rates for both the models after combustion of char takes place, i.e., in the region where the SPM is applied. In the SCM, the overall reaction rate is limited by the resistance due to the ash layer which is zero for the SPM model. Furthermore, the diffusion resistance of a shrinking particle would be lower than that calculated in the SCM. However, the volume of the particle keeps decreasing in the SPM. Overall, there is hardly any difference in the heterogeneous reaction rate as shown in Figure 31.

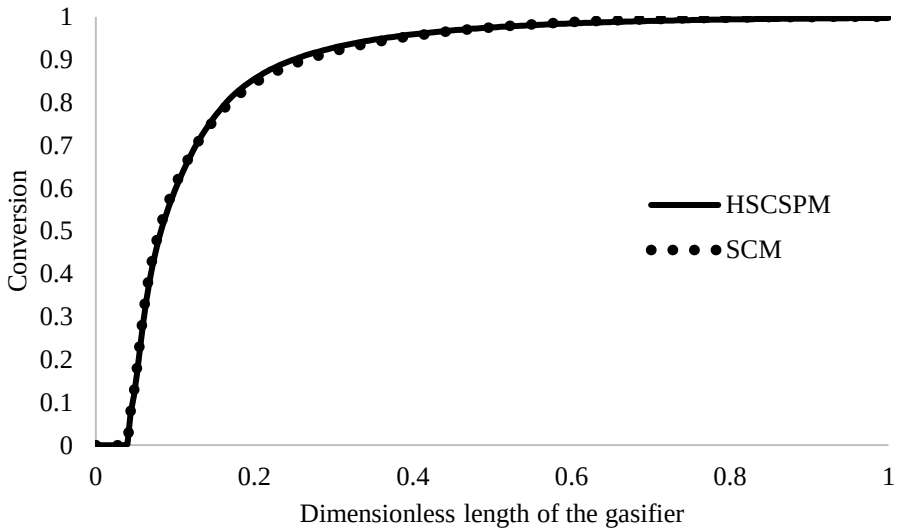

Figure 32. Comparison of carbon conversion of carbon between the gasifier model and the complete coalescence model.

Figure 32 compares carbon conversion obtained in this work to that obtained using the SCM. In both the cases, a significant amount of carbon gets converted very early in the reactor followed by slower conversion, which is mainly due to the gasification reactions.

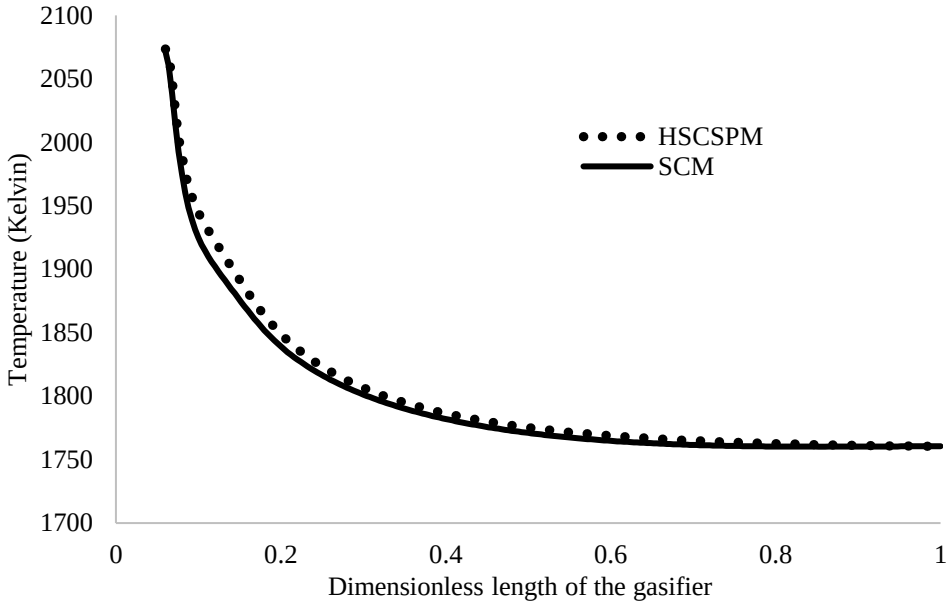

Figure 33. Comparison of solids temperature profiles between the shrinking core and HSCSP model.

Figure 33 compares the temperature of the char particle using the SCM with the HSCSP model developed in this work. As mentioned earlier, in the initial region of the gasifier up to the point when the bulk temperature exceeds the ash melting temperature the HSCSP model considers shrinking core assumption and therefore, the solid and gas temperatures closely match that from the SCM in this region. Therefore in Figure 33, the solids temperature profile beyond this initial region is compared. The solids temperature from the HSCSP model is found to be little higher towards the beginning of this section. However, towards the end, both models reach similar conversion and the exit temperatures are the same. The gas temperature also follows the same trend (not shown here).

Comparing the mole fractions at the exit of the gasifier for the SCM and HSCSP models in Table 8, we see that there is very little difference between the two models.

Table 8. Comparison between outlet mole fractions of SCM and HSCSP models

Component	SCM	HSCSPM
CO_2	0.22396	0.22531
CO	0.47236	0.47052
H_2	0.01848	0.01842
H_2O	0.20823	0.20883

2.2.3.3 Complete coalescence scenario

In this scenario, it is assumed that the slag droplets are not detached from the char particles. Figure 34 shows that even though the char conversion is high, the char particle still exits at some finite size that exits the gasifier. The slag droplet attached to the char particle grows rapidly initially when the conversion is high. It begins to level off towards the end due to the decrease in conversion rate.

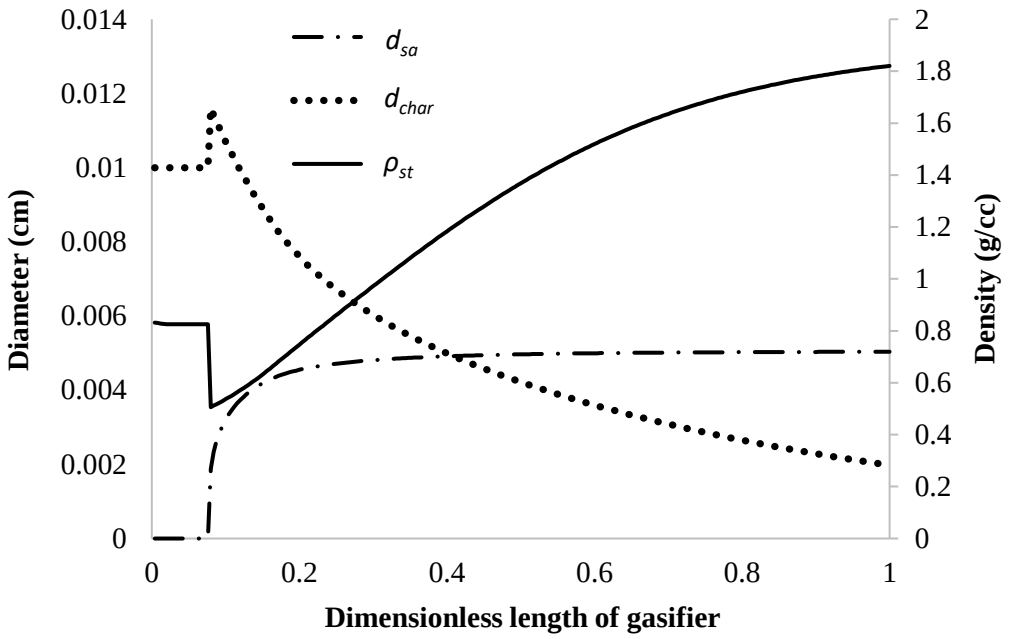

Figure 34. Variation of diameter of char particles, attached slag droplets, and average density of the char-slag system along the gasifier.

Figure 34 shows the profiles for the diameters and densities in the zone where the SPM is applied, i.e., after the bulk temperature increases beyond the ash melting temperature. Figure 34 also shows that the average density calculated using Eqn. (67) keeps increasing along the gasifier as char content continues to decrease while slag content keeps increasing, which is because the slag droplets have higher density than the char particles. In contrast, in the SCM, the density keeps decreasing as mass disappears while the volume of the char particle remains constant.

2.2.3.4 Model Validation – Slag Deposition and Flow

Data for the slag layer of a commercial scale slagging gasifier are scarce in the open literature as it is extremely difficult, if not impossible, to obtain using current measurement technology. Therefore, for model validation one option is to consider the computational models published in this area. While some CFD models[88,91,92] have been developed for upward-firing, membrane-cooled slagging gasifiers, very little information exists on slag layer thickness or deposition rate for refractory-walled downward-firing gasifiers. Table 9 shows validation of the present slagging gasifier model under steady state conditions. Two variables, deposition % and slag layer thickness, are compared with the results available in two references[88,142] that have developed CFD models. However, as noted before, these CFD models consider char deposition as the only mechanism for slag deposition.

Bockelie et al.[91] have simulated a CFD model of a downward-firing commercial scale gasifier fed with Illinois #6 coal using similar operating conditions as the current work. The fraction of solid mass flow entering the gasifier that subsequently gets deposited is reported in their work. As Bockelie et al.[91]considered only char deposition, a complete coalescence case (i.e., no slag detachment) is considered for our model so that the results from our model can be compared with the work of Bockelie et al.[91]. As seen in Table 9, the fraction of the total solid mass entering the gasifier that gets deposited is comparable for both the models. In the current model, 2% of the total solid mass entering the gasifier gets deposited onto the walls of the gasifier. It should be noted that the dimensions of the gasifier in our work are somewhat different than the work of Bockelie et al.[91], where the *L*/*D* ratio was considered to be 2.

Monaghan and Ghoniem[142] developed a dynamic, reduced order model for a commercial scale gasifier. Using a silica ratio similar to their work, the current model shows that the slag layer thickness is expected

to be much lower as seen in Table 9. One reason for this difference between our results and the work of Monaghan and Ghoniem[142] is due to the difference in the estimated slag layer temperature. The average refractory wall temperature in the current model is about 120°C higher than the work of Monaghan and Ghoniem[142] leading to a decrease in the slag layer thickness. This could be due to difference in the operating conditions and the energy conservation model. The energy conservation model used in this work is similar to the comprehensive model developed by Kasule et al.[93], which considers additional radiative heat transfer mechanisms in between the wall segments. When the refractory wall temperature in the present model was reduced to similar values in the work of Monaghan and Ghoniem[142], it was found that the slag layer thickness increased from 3.1 to 4.5 mm. Another reason for the difference in slag layer thickness is because Monaghan and Ghoniem[142] assumed that 10% of total solid mass entering the gasifier is deposited on the wall while the current model makes no such assumption.

Table 9. Comparison of the results from this work with the existing literature[91,142]

Source	Inlet coal flowrate (kg/h)	Gasifier diameter (m)	Gasifier length (m)	Deposition %	Slag layer thickness (mm)
Bockelie et al.[91]	125,000	-	-	2.7	-
Monaghan & Ghoniem[142]	113,586	2.74	8.31	10	6-7
Present model	156,251	1.79	6.62	2.02	3.11

2.2.3.5 Steady State Simulation Results

Effect of PSD. Combustion or gasification conditions are often simulated using drop-tube furnaces. The ash resulting from these tests is segregated on the basis of its size and mass. A wide variation in PSD is observed depending on the coal type, coal particle size, gas flow rates, temperatures and other operating conditions in experimental wor[107,143-149]. The mechanisms for the formation of droplets of different sizes differ and depending upon the conditions, some mechanisms may be dominant. Some tests show the presence of ash particles in the millimeter range which can form due to melting of larger excluded ash particles. In the present study, a PSD of slag droplets that form only due to the liberation of included slag droplets has been considered[150]. The gas-solid system in the gasifier is assumed to be dilute and therefore the formation of large slag droplets due to the collision of two or more char particles is not considered. In the present model, slag droplets of the largest size can form when most or all of the ash initially present in the char particle separates as a single slag droplet. Smaller slag droplets of sizes between 1-10 microns can form due to liberation or shedding of included ash while partial coalescing of the included ash before separation would result in slag droplets with sizes between the two size ranges.

Based on the slag droplet sizes that can be expected from detachment of included ash, the PSD is divided into four bin sizes. It is difficult to obtain a good estimate of the fraction of the slag droplets in each size bin along the gasifier. Since there is significant uncertainty in the estimated fraction of slag droplets in each bin, it was necessary to perform sensitivity studies by changing these fractions. Three different cases shown in Table 10 were evaluated. In Table 10, the variables fr_1, fr_2, fr_3 and fr_4 denote the mass fraction of the total slag in the 1-10 microns, 10-20 microns, 20-30 microns, and 30+ microns size bins, respectively. Obviously, for the complete coalescence case, denoted by case CC, all these fractions are zero.

Table 10. Simulated particle size distributions

PSD case	fr_1	fr_2	fr_3	fr_4
SD35-10	0.35	0.30	0.25	0.10
SD60-10	0.60	0.20	0.10	0.10
SD5-50	0.05	0.15	0.30	0.50
CC	0	0	0	0

Case SD35-10 is used as a base case for the model. The cases SD60-10 and SD5-50 are considered as limiting cases where the majority of the slag mass is considered to be in the small and large size bins, respectively.

Figure 35 shows the char and slag droplet deposition fluxes separately as well as the slag layer thickness profile along the gasifier for the base case PSD. It should be noted that for char particles impacting the gasifier wall, the char flux only represents the ash being added to the slag layer and the carbon continues to burn at the same rate as in the bulk of the gasifier.

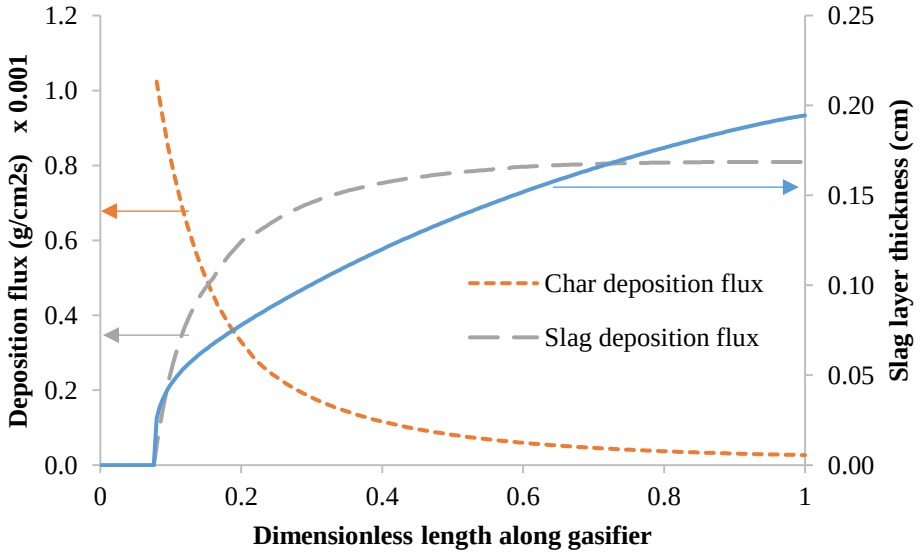

Figure 35. Deposition flux and slag layer thickness profile for base case PSD.

Figure 35 shows that the slag layer thickness rapidly increases in the initial section of the gasifier and that slag addition due to the impact of char particles is the dominant mode of slag addition in this section. This is because the deposition velocity in the initial section is high and also because very little ash has separated as slag droplets from the char particles into the bulk of the gasifier. As a result, the amount of ash content in the impacting char particles is high. As the char particles react, increasing amounts of slag droplets are separated into the bulk and slag deposition becomes the dominant mode of slag addition to the layer. Towards the end of the gasifier, char impact adds little to the growth of the slag layer. In total, about 82% contribution to the slag layer comes from slag droplet impact and the rest from char impact. As stated previously, no slag is assumed to deposit onto the wall in the shrinking core section of the model.

Figure 36 shows the slag droplet deposition flux and the slag layer thickness for Case SD5-50 (PSD with higher mass fraction of larger particles) and for Case SD60-10 (PSD with higher mass fraction of smaller

particles). The char deposition flux, not shown here, was found to be identical for the PSD cases. Even though the number density of the smaller slag droplets is higher, the deposition velocity and mass of the smaller slag droplets are lower in comparison to the larger slag droplets. Initially the slag layer thickness profile is similar since ash deposition due to char impaction is dominant. The profile begins to differ as the ash deposition begins to dominate. However the slag layer thickness does not differ appreciably.

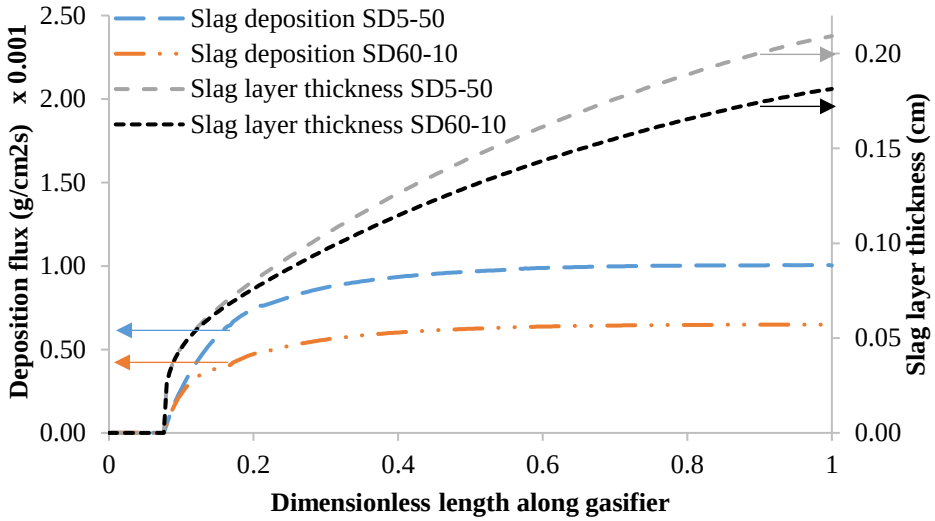

Figure 36. Slag droplet deposition flux and slag layer thickness for cases SD-5-50 and SD 60-10.

Figure 37 shows the slag layer thickness profile for the Case CC in comparison to the base case. The difference in slag layer thickness is small.

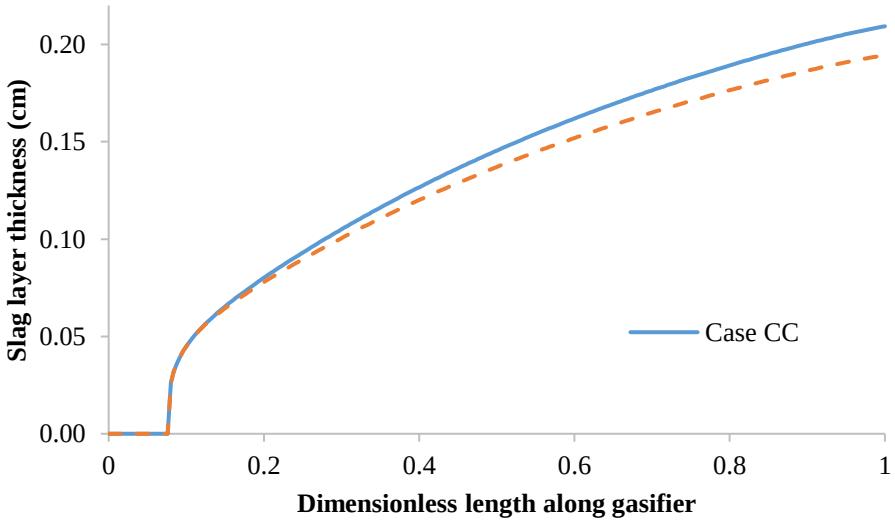

Figure 37. Comparison of the slag layer thickness for Case CC and base case.

From Figure 35-37, it was found that the PSD did not have a significant effect on the slag layer thickness for the range of slag droplet sizes that were considered in this study. However, since it is has been shown that the ash can separate from char particles as slag droplets and these droplets could vary in sizes, the inclusion of a PSD for the detached slag droplets would be a more physically realistic representation of

the system. To the best of the author's knowledge, the present formulation has not been done previously and this work could be useful to evaluate the deposition flux and slag layer thickness for the various cases at other operating conditions. For the subsequent runs, the base case PSD is used.

Effect of change in input conditions. Disturbances in the O_2 or coal flow rate can result in the slag layer temperature dropping below its critical viscosity, leading to thickening of the slag layer. The effect of change in O_2/coal ratio on the slag layer thickness can be seen in Figure 38.

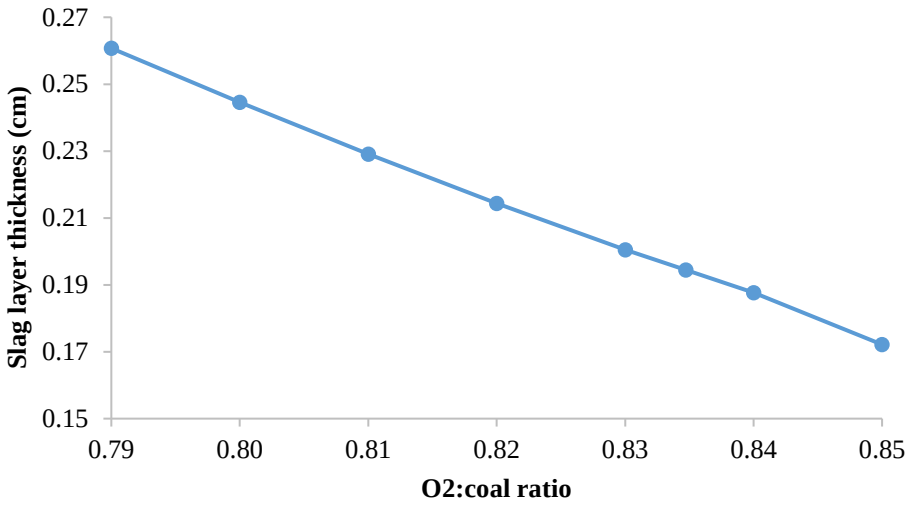

Figure 38. Effect of change in O2/coal ratio on slag layer thickness at gasifier exit.

Changes in the O_2/coal ratio affect the gasifier bulk temperature and thus the slag layer temperature resulting in a change in its viscosity. With a change in the ratio from 0.79 to 0.85, it is seen that the slag layer thickness decreases by approximately 35%.

The effect of change in the O_2/coal ratio on the maximum and minimum slag temperatures and carbon conversion is shown in Figure 39. The maximum temperature occurs near the gasifier inlet while the minimum temperature occurs at the exit.

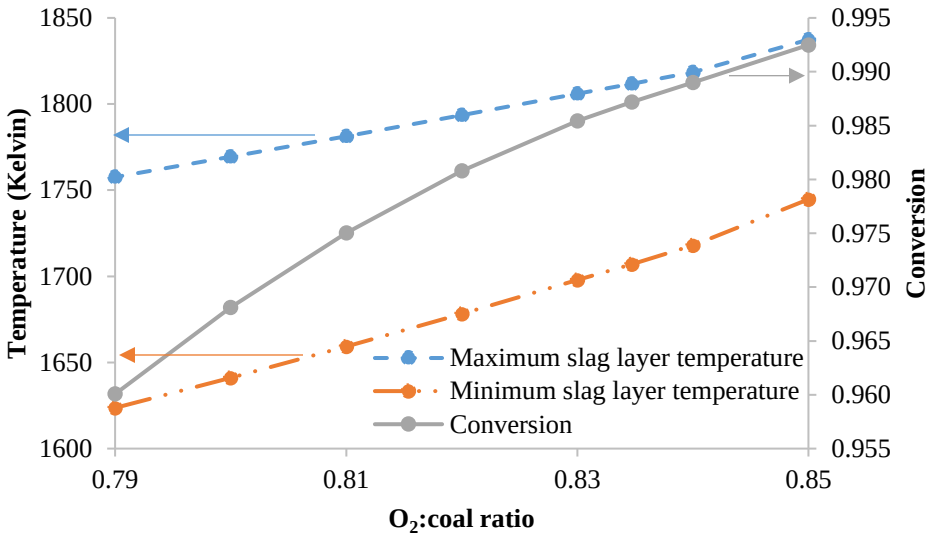

Figure 39. Variation of the maximum and minimum slag layer temperature due to change in O_2/Coal feed ratio.

For Illinois #6 the fluid temperature was found to be 1600 K in a reducing environment[135]. If the O_2/coal ratio is decreased below 0.79, the slag may cease to flow because of the lower temperature and higher slag viscosity. Even though it is observed in Figure 38 and Figure 39 that a higher O_2/coal ratio results in higher carbon conversion and lower slag layer thickness, the resulting high temperature has strong detrimental effect on the refractory life. Thus the O_2/coal ratio should be optimally controlled by evaluating these tradeoffs.

2.2.3.6 Effect of change in ash composition

The composition and amount of ash can vary widely between coal types as well as for the same coal from different seams. Since the viscosity at a given temperature strongly depends on the ash composition, ash composition needs to be carefully considered during gasifier operation. In Table 11, the silica ratio of Illinois #6 coal from different authors is presented. A silica ratio of 0.527 is used as a base case and is calculated for "Lab No. Christian c-10142" taken from a report of Illinois #6 coal[150].

Table 11. Silica ratios calculated for Illinois #6 coal taken from literature

Source	Silica ratio
Present model	0.527
McCollor et al.[151]	0.627
Nowok[152]	0.690
Cho et al.[153]	0.700

The coal composition in this study is kept constant in order to assess the effect of changing only the silica ratio. The effect of silica ratio on slag layer thickness and exit viscosity can be seen in Figure 40 for the base case operating conditions shown in Table 5.

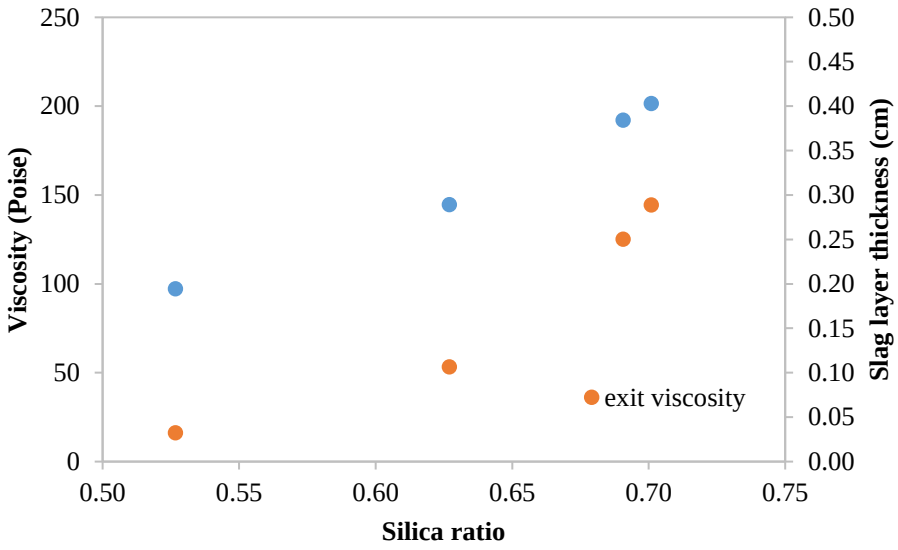

Figure 40. Effect of silica ratio on exit viscosity and slag layer thickness.

It can be seen that there is a strong variation in slag layer thickness and viscosity due to a change in the silica ratio. Under the present operating conditions, the exit slag temperature is found to be about 1417^0C. Figure 40 shows that even though all operations in the given range are feasible, the slag layer thickness can be more than double depending on the silica ratio.

2.2.3.7 Dynamic Simulation Results

Change in coal slurry flowrate: To study the effect of change in the gasifier throughput on slag layer thickness, the coal slurry flow rate was ramped up by 10% for a duration of 10 minutes. The oxygen rich air flow rate also is ramped by the ratio controller to maintain the desired O_2/coal ratio. The change in the flow rates is shown in Figure 41. The slag layer thickness is found to increase by about 6%. This increase happens due to two reasons. First, the overall mass flux of char particles and slag droplets to the wall increases. Second, there is also a small change in the slag layer viscosity due to a decrease in the temperature of the slag layer at the exit of the gasifier. The transient temperature profiles of the temperature of the slag layer and the wall at the end of the gasifier are shown in Figure 42. While the slag layer temperature is responsive to the O2/coal ratio entering the gasifier, the wall temperature has a much slower dynamic response. The final temperature is lower, but by a small amount.

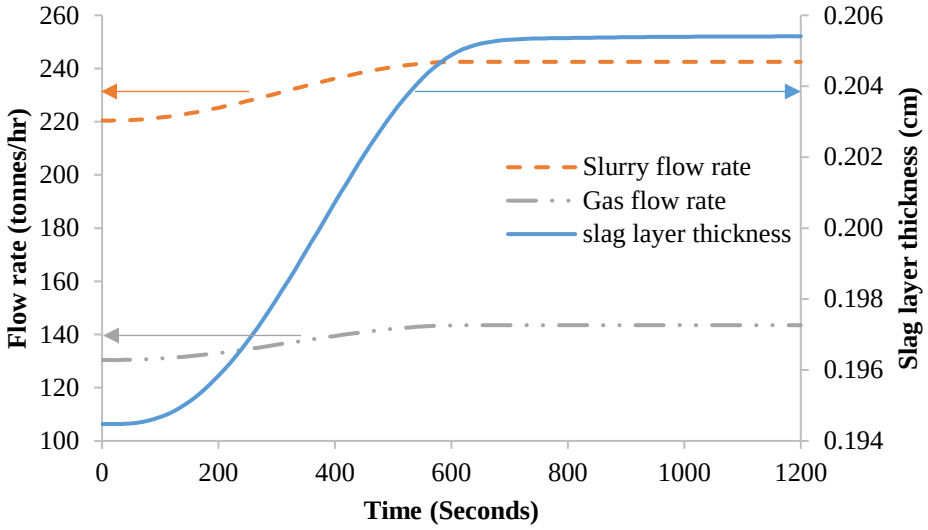

Figure 41. Effect of ramp change in coal slurry flow rate on slag layer thickness at final CV.

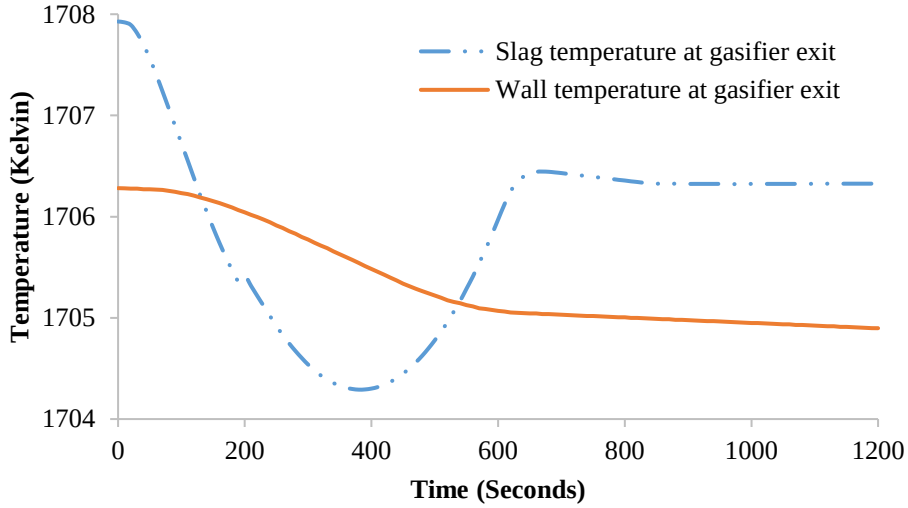

Figure 42. Effect of ramp change in coal slurry flow rate on slag layer temperature at final CV.

2.2.3.8 Coal feed switch

In this study, the coal feed to the gasifier is changed from Illinois #6 to Pittsburgh #8 over a period of 1 hour. The coal switch is initiated after 30 seconds of operation, and is achieved by ramping the normalized ultimate and proximate analysis parameters. These parameters for the two coals have been reported in Table 6. The O_2/coal ratio and the coal/water ratio is left unchanged to observe the effect of only the change in the coal type. It should be noted that usually during a coal switch, the O_2/coal ratio and coal/water ratio are normally adjusted and if these ratios are adjusted, the results would vary. The silica ratio is also ramped accordingly. For Pittsburgh #8 coal, the silica ratio is calculated on the basis of ash composition available in a report from the U.S. DOE's National Energy Technology Laboratory[102].

Figure 43 shows the change in the mole fraction and carbon conversion due to switching the coal. The carbon conversion decreases from about 99% to 93%.

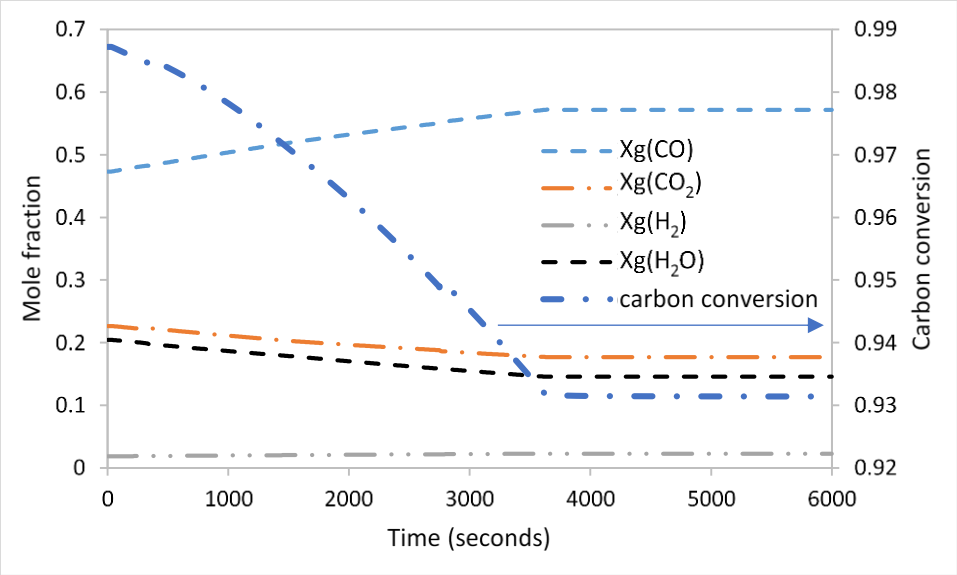

Figure 43. Change in outlet gas composition and carbon conversion during coal switch from Illinois #6 to Pittsburgh #8 coal.

Figure 44 shows the trend of char and slag droplet deposition fluxes as well as the slag layer thickness profile before and after the coal switch from Illinois #6 to Pittsburgh #8. The drop in conversion means that less ash is being separated from the char particle and this ash is depositing on the slag layer with the deposition velocity of the char particles. A decrease in the slag droplet deposition flux is due to a decrease in the number density of slag droplets in all the bins and the decrease in ash content of Pittsburgh #8 coal as can be seen from Table 6.

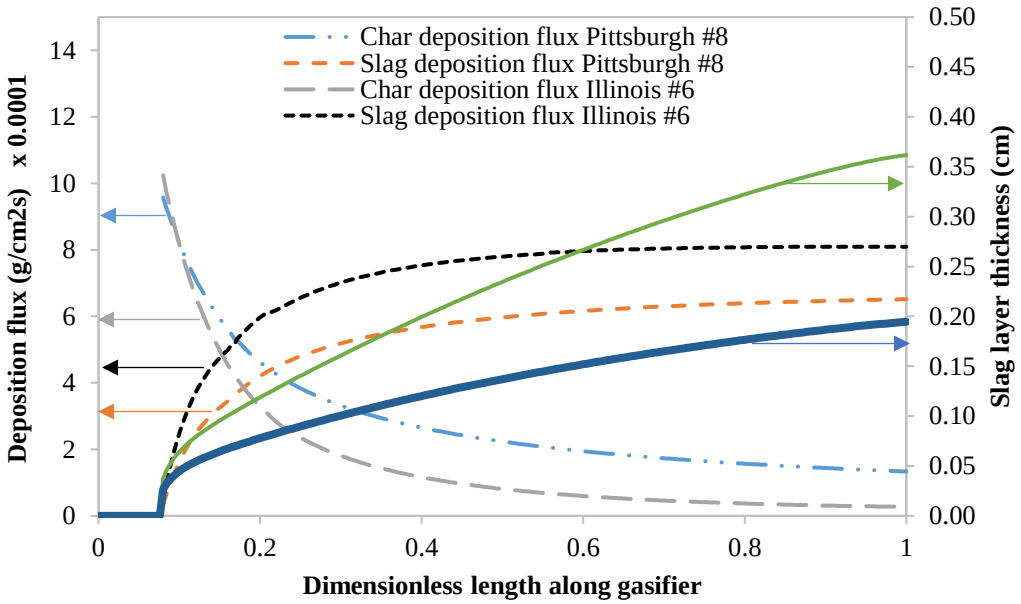

Figure 44. Deposition flux before and after change of coal from Illinois #6 to Pittsburgh #8.

Although the net deposition flux decreases by 5% after the coal switch, the slag layer thickness increases tremendously. Figure 45 shows the slag temperature profile and the viscosity profile along the gasifier before and after the change has been implemented. For Pittsburgh #8 coal ash, the fluid temperature is

found to be around 1600K in a reducing environment[102]. It can be seen that the slag temperature approaches this temperature at the end of the coal switch. Due to the large decrease in slag layer temperature, and the change in the ash composition as the coals are switched, the viscosity increases significantly.

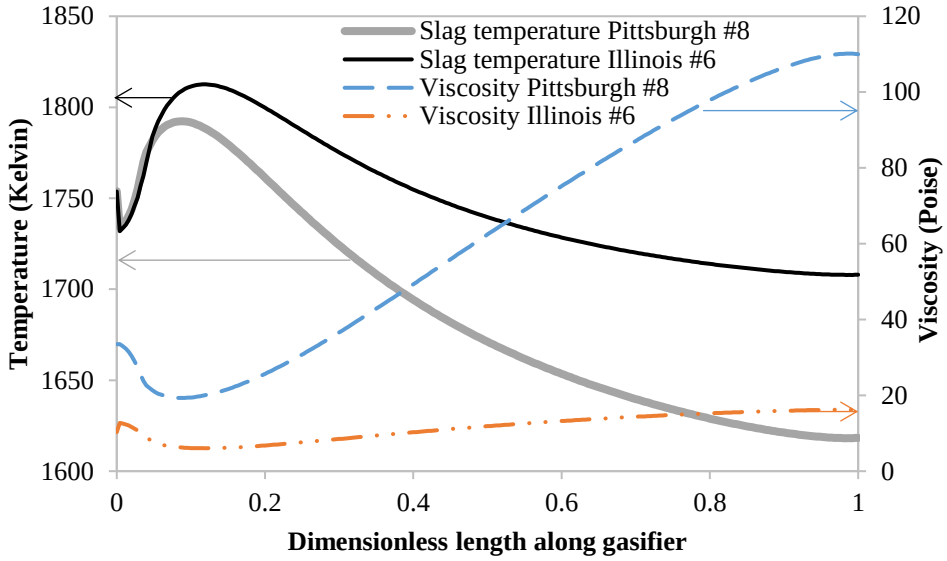

Figure 45. Slag layer temperature and viscosity profile before and after the coal switch.

Manipulating the O_2/coal ratio can alleviate the issue of high slag layer thickness as observed before. The O_2/coal ratio can be changed to control the gasifier exit temperature or to control carbon conversion, if it can be estimated. Kasule et al.[126] have implemented the later control strategy. Their work shows that the O_2/coal ratio for the Pittsburgh #8 coal for same carbon conversion as the Illinois #6 coal is about 0.9. For this O_2/coal ratio, the slag temperature at the exit of the gasifier is found to be around 1703 K, which is slightly higher than that for the Illinois #6 coal. The slag layer thickness for these conditions reduces to 0.25mm.

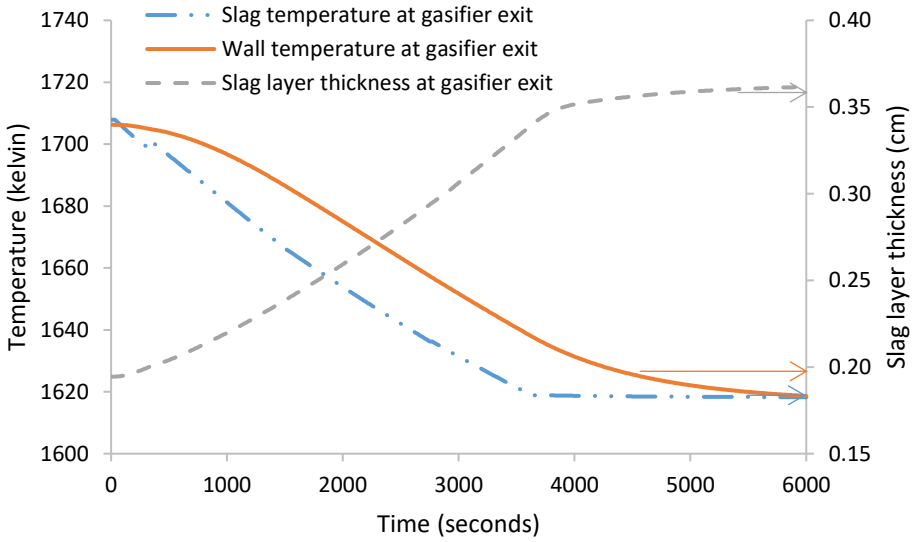

Figure 46. Transient response of slag layer and wall temperature and slag thickness at gasifier exit.

An interesting difference between the temperature time scales of the slag layer and the wall is observed in Figure 46 using the base case O_2/coal ratio. Even though the final wall and slag layer temperatures are similar, the dynamics of the slag temperature is faster. As mentioned earlier, the deposition flux of slag to the wall remains almost the same. Therefore, the increase in slag layer thickness is mainly due to the decrease in slag viscosity. Therefore, the slag layer thickness dynamics have a similar time constant as the slag temperature dynamics.

2.2.4 Fault Simulation

Refractory degradation is one of the key issues highlighted in the operation of gasifiers in the literature. Replacement of refractory bricks is done every 3 months to 2 years. The replacement is expensive and also results in the downtime of the entire power plant. Due to the harsh operating condition inside a slagging gasifier, direct, in-situ measurements of either the transport variables or refractory degradation are not possible with current state-of-the-art technology. Non-destructive tests to assess the life of the refractory layer online do not provide reliable answers due to the interference of the slag layer.

Several mechanisms have been identified that contribute to the degradation of the refractory layer. Ash is one of the components of coal that melts within the gasifier and is known to deposit on the refractory layers as slag. The slag can directly interact with the refractory layer through corrosion and erosion of the brick. Another way through which the slag results in degradation of the refractory is through a process known as compressive spalling. Slag penetrates into the brick thereby changing the mechanical properties of the section that is penetrated. The slag penetrated section also has a different thermal expansion coefficient which results in a strain being developed. The penetrated region begins to buckle after a certain depth and can ultimately spall.

Refractory degradation can also take place in the absence of slag through mechanisms such as creep and thermal fatigue. These are generally slow processes, taking place over periods of months, however they could become dominant in high temperature operation. They lead to formation of micro-cracks that can change material properties such as the Young's modulus, maximum tensile stress, etc. resulting in the weakening of the material. Thermal shock is an example of a fast mechanism where sudden change in temperature could result in immense build-up of stresses near the hot face surface. This is analogous to quenching of a material, which results in the formation of cracks and defects on or near the surface.

For the project, slag penetration and spalling as a result of compressive spalling have been identified as the main methods of degradation of the refractory layer and are modeled and simulated as faults. A slag penetration model is first developed to identify the location that is most susceptible the degradation mechanism. A refractory degradation model is developed for this location using the compressive spalling mechanism to calculate the time and depth at which the first spall is expected to occur. The time scale for the refractory degradation is in months or years, while the gasifier reactions dynamics take place in seconds. Due to this difference in time scales, the two models are not integrated. The gasifier model is simulated and the results from the simulation are used in the refractory degradation model.

2.2.4.1 Model

The gasifier refractory is made up of several layers. The innermost layer is the high chrome layer. Refractory containing up to 95% chrome is used. The purpose of the layer is to withstand high thermal shocks and attrition. Following this layer, there is the castable alumina layer. This layer is thicker than the chrome refractory layer. The third layer consists of silica bricks. The purpose of this layer is that of insulation. The final layer is the metal layer of the gasifier unit.

In order to simulate the process of slag penetration into the refractory, a dynamic model would be required. As the slag penetrates deeper into the refractory, the rate of penetration will change due to the decreasing temperature and/or change in gasifier operating conditions. In order to identify the location in

the gasifier where refractory degradation due to slag penetration would occur the fastest, a 2D model for the concentration profile and heat transfer in the refractory was developed. The gasifier refractory layers are modeled as composite cylinders and the heat balance equation is written for all layers. The concentration equation is solved only for the first layer, viz. the high chrome layer as this layer is the most susceptible to spalling due to slag penetration because it is directly in contact with the slag.

The inner hot wall temperature profile is taken from the gasifier model results shown earlier at a base case steady state condition. The refractory layer thickness is kept the same as the gasifier model. It is assumed that the slag penetration and refractory degradation model do not have a significant effect on the gasifier model, and thus the exchange of information is only from the gasifier model to the refractory degradation model.

The heat balance equation is given as Eqn. (102).

$$\rho_{ch} C_{p,ch} \frac{dT_{ch}}{dt} = k_{ch} \left[\frac{1}{r} \frac{d}{dr} \left(r \frac{dT_{ch}}{dr} \right) + \frac{d^2 T_{ch}}{dz^2} \right] \tag{102}$$

Here, ρ_{ch} is the density of the chrome layer, $C_{p,ch}$ is the specific heat, k_{ch} is the thermal conductivity and T_{ch} is the temperature in the chrome layer. Equations similar to Eqn. (102) are written for the remaining three layers as well.

The concentration equation is given in Eqn. (103).

$$\frac{dC_{slag}}{dt} = D_{eff} \left[\frac{1}{r} \frac{d}{dr} \left(r \frac{dC_{slag}}{dr} \right) + \frac{d^2 C_{slag}}{dz^2} \right] \tag{103}$$

Here, C_{slag} is the concentration of slag in the refractory and D_{eff} is the diffusivity of slag in the high chrome layer. Diffusion is a function of the temperature[84], and for this case, an average penetration front temperature is selected at which the concentration of slag in the refractory brick pores is 30%.

A time evolution video was made for slag penetration into the high chrome wall along the gasifier length that shows the slag concentration at different locations. This was presented in the AIChE as part of the presentation. Snapshots of the video at different times are shown below in Figure 47.

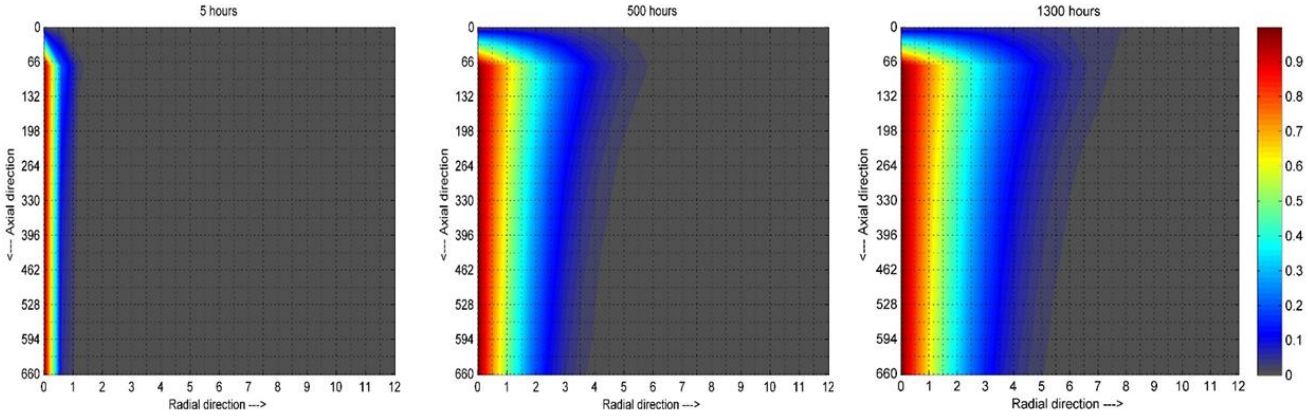

Figure 47. Slag penetration into the high chrome refractory at different time instances.

The dimensions of the wall chosen for this study are 660 cm length and 12 cm thickness of the high chrome layer. The 2D model has cylindrical coordinates. In the first 10% of the gasifier length, no slag is assumed to be on the wall of the refractory. At 5 hours, the slag penetration into the refractory appears to be uniform. At 500 hours, it can be seen that the slag penetration at a distance of about 66 cm from the gasifier inlet is highest. This is because, the wall temperature is very high at this location and diffusion variable is a function of temperature. After significant penetration into the refractory however, the slag penetration rate in the radial direction decreases as the temperature reduces. Some diffusion in the axial direction is seen after this point.

The location where slag penetration takes place the fastest is selected for the refractory degradation simulation. The wall temperature at this location is found to be 1800 Kelvin. The steady state temperature profile is shown in Figure 48.

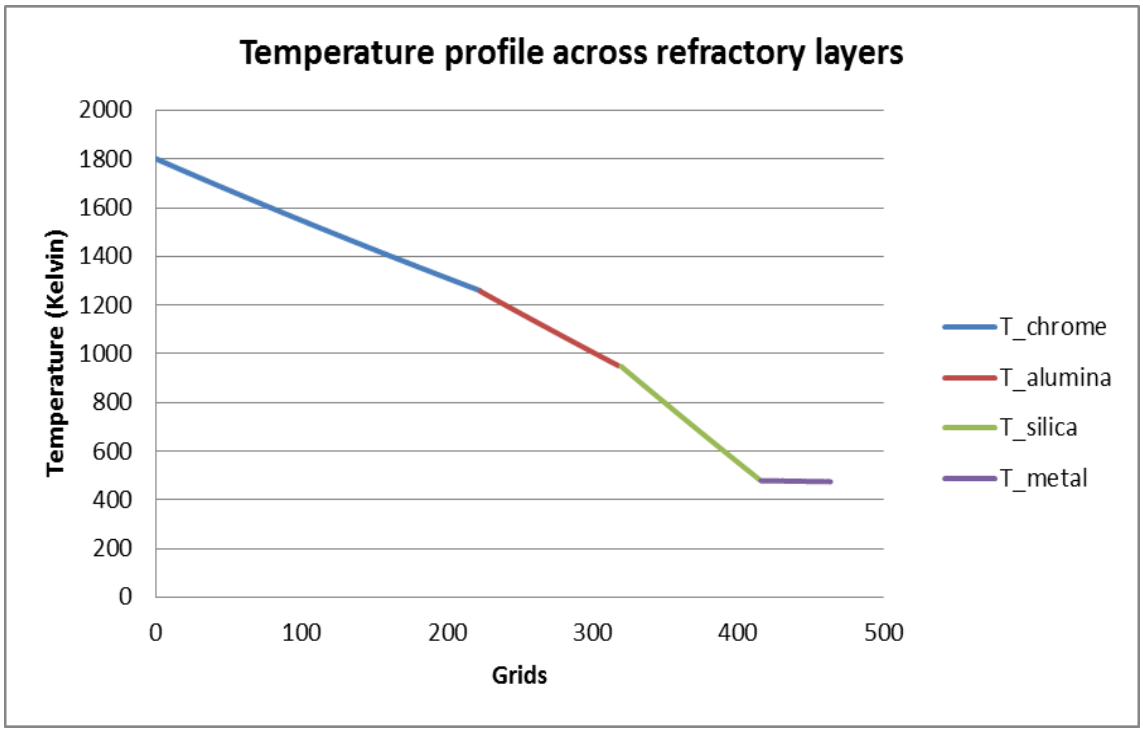

Figure 48. Steady state temperature profile along the refractory across the four layers.

2.2.4.2 Compressive Spalling model

The model equations for refractory degradation due to spalling have been taken from the work of Williford[87]. Compressive spalling occurs due to slag penetration and exchange of Fe ions in the slag with the chromium ions in the refractory. Slag diffuses in the pores in the first layer and the exchange of ions renders the diffused material to have different properties. Due to this, there is a thermal expansion mismatch that eventually leads to spalling.

The slag penetration depth is calculated using the concentration equation at the location where the slag concentration is 30%. The minimum distance required for spalling is given in Eqn. (104).

$$h_{min} = \frac{\Gamma\, \varphi^2 (1 - \gamma_p)}{E\, {\Delta\varepsilon_{total}}^2} \tag{104}$$

where, Γ is the toughness, φ is a dimensionless parameter, γ_p is the Poisson's ratio, E is the Young's modulus of the penetrated region and $\Delta\varepsilon_{total}$ is the total differential strain caused by differential growth and differential thermal expansion of the penetration in comparison to the refractory. $\Delta\varepsilon_{total}$ is given as:

$$\Delta\varepsilon_{total} = \Delta\varepsilon_g + \Delta\varepsilon_{th} \tag{105}$$

where, $\Delta\varepsilon_g = \frac{\Delta V_{Cr}}{3V_{Cr}}$ and $\Delta\varepsilon_{th} = \Delta\alpha\Delta T$ in which $\Delta\alpha$ is the difference in thermal expansion coefficients between the slag and refractory and ΔT is the temperature gradient between the refractory inner wall and the slag penetration front.

When the slag penetration depth exceeds the minimum depth at which spalling can occur, a spall is assumed to take place. In order to test the refractory degradation model, four cases were simulated. The first was a base case where the gasifier is operated at a design inlet flow rate of 60,000 gm/sec of coal slurry. The second case is when thermal cycling is done in the gasifier. For maintenance purposes, the gasifier feed is oscillated in a sinusoidal manner. This could also be done in response to the variation in demand of power during day and night. To simulate a cycle, the coal slurry is varied within 10% of its base case value with a time period of 1 hour as can be seen in Figure 49.

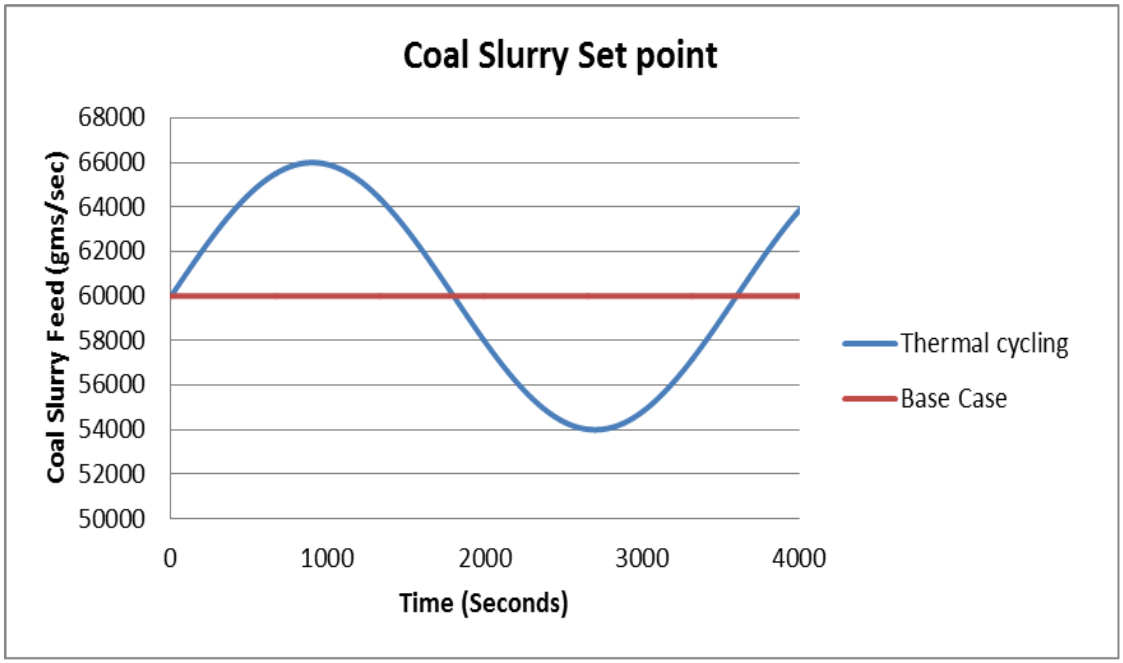

Figure 49. Coal slurry set point variation in the gasifier model.

The temperature variation at the same position is recorded for the two cases. The temperature profile for the oscillating case of coal feed is fit to a sinusoidal curve. The temporal temperature profiles are then used as an input to the degradation model. Two other case studies were also simulated where a high and low fixed temperature values were assumed as the hot face temperature.. The high temperature value of 1850 K and low temperature value of 1775 K are used in these cases. The temperature profiles for the four cases used in the refractory degradation model are shown in Figure 50.

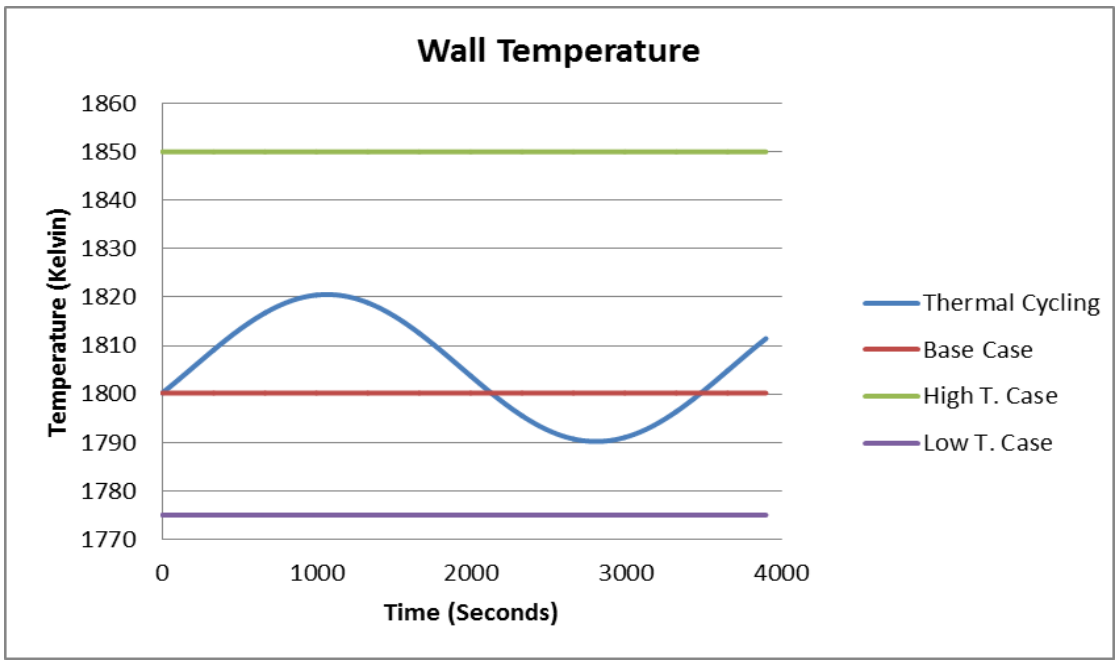

Figure 50. Wall temperature at the grid point selected for simulating degradation.

From Figure 50, it can be seen that although in the second case the inlet flow rate of the coal slurry is fluctuated by 10%, the wall temperature at the selected grid does not vary more than 15°C on average. The refractory degradation model is simulated for all four cases and the results are plotted in Figure 51.

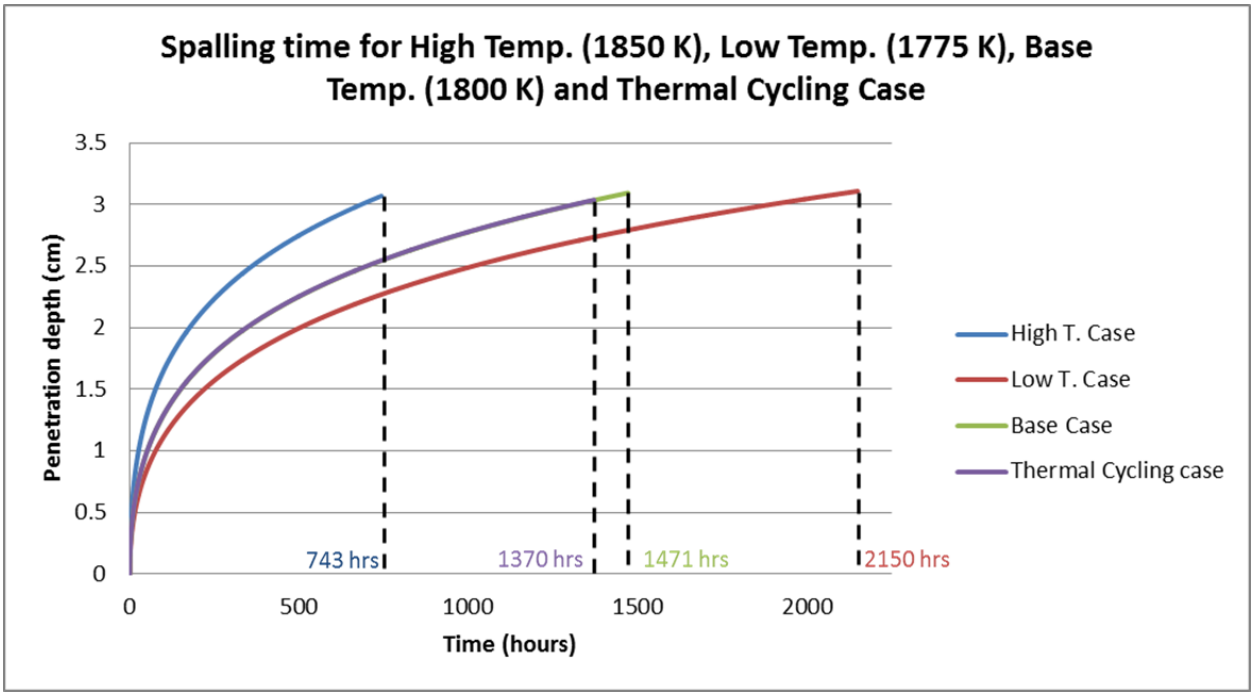

Figure 51. Time for first spall for the four cases.

From Figure 51, it can be seen that the time for the first spall to occur when the base case wall temperature is 1800 K is around 1471 hr. For the thermal cycling case, the curve seems to closely flow that of the base case but the first spall occurs around 100 hr sooner. This could be because of a faster diffusion front. The effect of thermal cycling can be better captured if creeping and fatigue are considered in the refractory layer. For the case of high temperature, spalling occurs at 743 hr. In the low temperature case, spalling occurs much later. However, due to its proximity to the critical viscosity temperature, such low temperature is avoided to prevent any solid slag build up on the wall of the refractory that could eventually lead to clogging of the gasifier.

2.3 Gasification Island

The gasification island model is developed for the two-tier sensor placement method. It consists of the sour water gas shift reactor (SWGSR) combined with the Selexol unit. In the IGCC plant, the water gas shift reaction is performed using two reactors operating at different temperatures. This allows for more residence time for the equilibrium reactions and to reduce the amount of SO_2 in the reactor outlet. The outlet of the first reactor is fed to the second reactor, after which it is sent through a series of heat exchangers until finally being sent to the Selexol unit.

In order to set-up the gasification island model, the SWGSR model and the Selexol model were first modified before they were integrated. The SWGSR model was enhanced to consider two trains consisting of two reactors in series with an intermediate cooler. The control system of the Selexol model was modified to ensure it was stable in the operating region of interest. Variables to be recorded were carefully selected so as to completely capture the fault progression through the simulation, while at the same time, reducing the memory load of the program to prevent slowing of the simulation.

The SWGSR was modeled in MATLAB while the Selexol model was developed in Aspen Plus Dynamics. The SWGSR was not modeled using Aspen because, the in-house library reactor models in Aspen do not allow for simulating faults such as reduction in catalyst surface area, drop in catalyst porosity or catalyst activity etc. Plant level simulations on the other hand, are fairly easy to simulate using a process modeling software such as Aspen Plus or Aspen Dynamics. This brings forth the challenge of running two models in two different platforms, making them communicate and solve in a coupled manner.

Sensor placement in a two-tier setting can help identify potential sensors that can detect faults at different levels. In this case, sensor placement using fault data from fault simulation in the gasification island may show sensors in the SWGSR that are sensitive to faults at both levels, viz. the SWGSR as well as the Selexol plant or vice versa. This study can help reduce the total number of sensors required to detect the faults if the sensor placement was done separately at both tiers.

2.3.1 Model Development

The first step was to develop the two-stage SWGS reactor in MATLAB which give the same output as its APD counterpart in the IGCC plant wide model. The initial reactor model was designed to run at different operating conditions as the APD SWGS reactors and thus had to be modified. In order to accommodate the large flow rate, the reactors were designed as a two-train system. The rate of reaction equation for the shift reaction used in the SWGSR model shown earlier is different from the APD case and is derived by data reconciliation. The COS hydrolysis reaction rate expression was changed to the expression used by APD to match the conversion of H_2S and COS. The first stage is designed to match the outlet composition of the water gas components in Aspen Plus Dynamics. The second stage of the reactor was developed independently using the outlet composition from the first stage and the inlet temperature from the APD model. The reactor was sized in order to achieve equilibrium at about 90% of the length and the valve

coefficients were set so as to match the flowrates. Both stages were run independently until they achieved steady state.

Once steady state was achieved in each of the stages, the code for the two stages was compiled into a one m-file and the SWGS reactor system was solved as a single unit. The system representation can be seen in Figure 52 below.

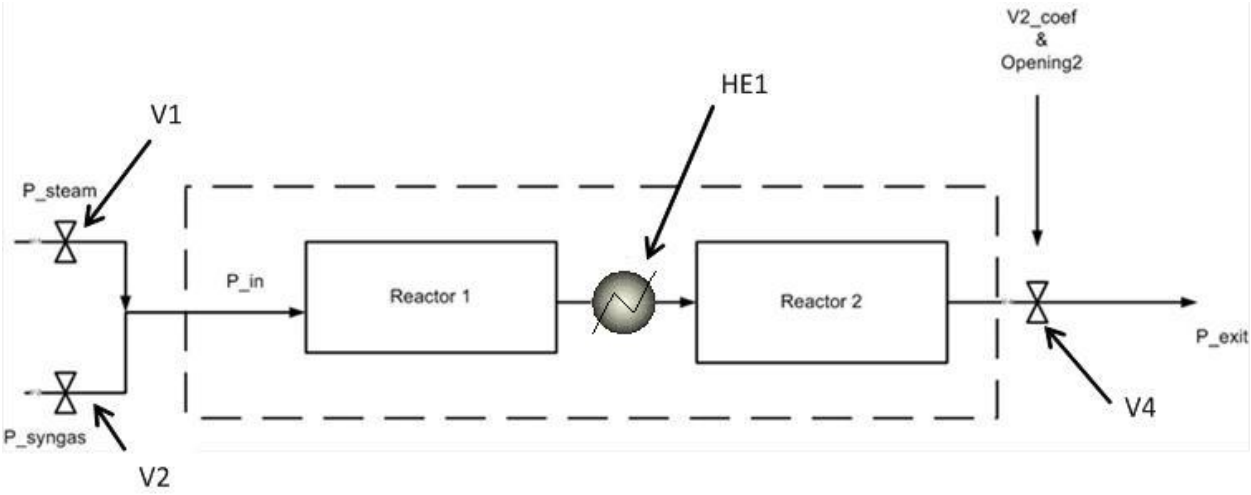

Figure 52. Schematic representation of the Sour Water Gas Shift Reactor system developed in MATLAB.

Once this system achieved steady state, work started on integrating the MATLAB model with Aspen Plus Dynamics. There is not much data in the literature about such integration between the MATLAB and APD to solve such a coupled system. The Matlab and APD files are integrated using SIMULINK. Using a Aspen Modeler Block in Simulink, the outlet variables from Matlab simulation, viz. Temperature, Composition and Pressure were sent to the inlet of the Aspen Plus Dynamics model.

In order to ensure the models in both the software are squared, an outlet valve V4 as can be seen from Figure 52. Due to the coupled pressure-flow dynamics of the entire plant, the boundary conditions for pressure at the output of the MATLAB model and the pressure at the input of the APD models are not static, but dynamic and must be synchronized. A valve is added to the entrance stream in the Aspen simulation such that the valve coefficient and valve opening of the exit valve V4 of the MATLAB model and the entrance valve for the APD model are kept exactly the same to ensure they have the same flow rates. The value for the pressure variable, P_{exit}, in MATLAB is sent from APD, and the pressure before valve V4 is sent to APD as the inlet pressure to the first valve. A schematic of the exchange of information across the platforms is shown in Figure 53.

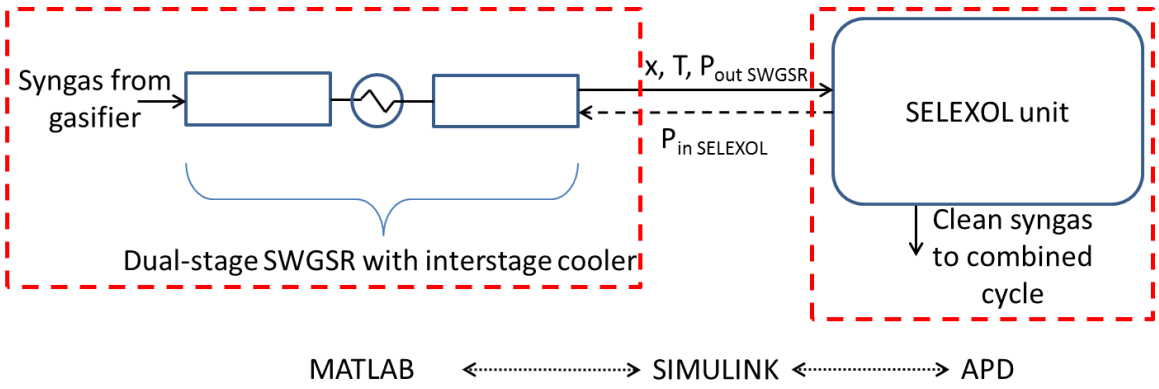

Figure 53. Exchange of information between the SWGSR in MATLAB and the Selexol model in APD.

The algorithm for the process flows is: the MATLAB solver solves for a fixed time step. This time span along with the outlet variables are sent to the APD model via SIMULINK. The APD model then solves, using a variable step solver, for the same timespan and sends back exit pressure value, P_exit, to MATLAB and so on. A few profiles are shown below.

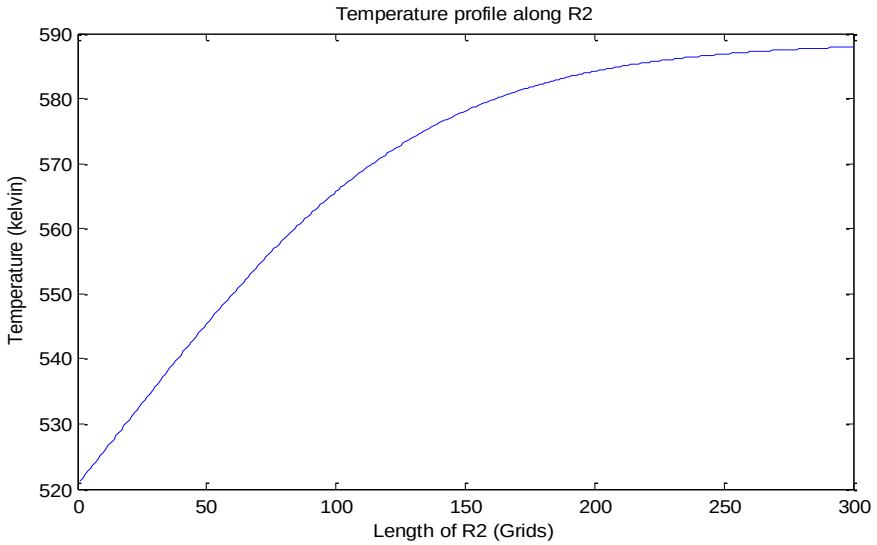

Figure 54. Temperature profile along reactor R2.

The process fluid enters reactor R2 after being cooled in the heat exchanger. Figure 54 shows that the temperature begins to level out at the end of R2 as the shift reaction approaches equilibrium.

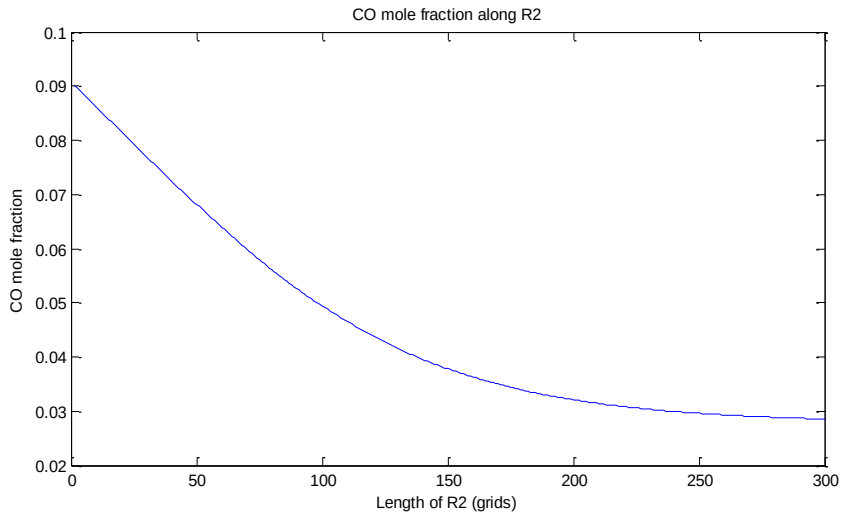

Figure 55. Profile of CO mole fraction along the length of reactor R2.

As the WGS reaction reaches equilibrium towards the end of R2, mole fraction of CO changes negligibly towards the end of R2. The spatial profile of CO in R2 is shown in Figure 55.

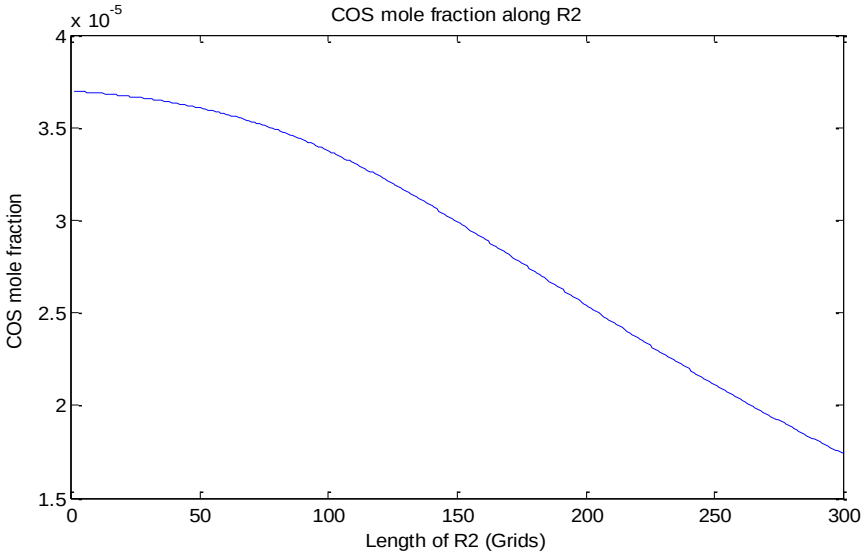

Figure 56. Plot of COS mole fraction along R2.

The mole fraction of COS in the entering syngas stream is 1.38 x 10^{-4} and reduces to 1.7 x 10^{-5} at the end of R2 as can be seen in Figure 56. It should be noted that even though COS mole fraction at the inlet is small, it is important to convert it to H_2S so that it can be captured in the acid gas removal unit for satisfying the overall emission requirements of sulfur.

2.3.2 Study of Fault Effects

Before simulating the faults in the gasification island, it is important to implement the control configuration as would be expected in an actual operating plant. In the WGS reactor system, the syngas flowrate is maintained for producing the desired amount of power by the integrated gasification combined cycle (IGCC) plant. In addition, the CO/H_2O ratio at the inlet of the WGS reactor system is maintained by manipulating the steam flowrate to the reactors. These two controllers have been coded in MATLAB for manipulating valves V1 and V2. The controllers were then tuned for satisfactory response.

The integrated system is used to simulate some typical faults. As an example, the results due to change in porosity of the first reactor, R1, will be presented below. This fault is expected to happen in a WGS reactor system as part of an IGCC plant since tar or soot that are generated in the gasifier but can escape the scrubber could enter the reactor and clog the pores of the catalyst. As a result of this, the reaction rate goes down and yield could suffer. For this fault, it is assumed that the unwanted material is captured by the first reactor alone, and thus only the porosity of R1 is ramped down. This is done at a rate of 25% decrease in porosity over a period of 12 hours. The response of this fault is shown as follows. It should be noted that in real-life, such faults can happen over much longer period of time, but here a much faster rate is considered in order to study the capability of the integrated models.

2.3.2.1 Effect on Reactor R1

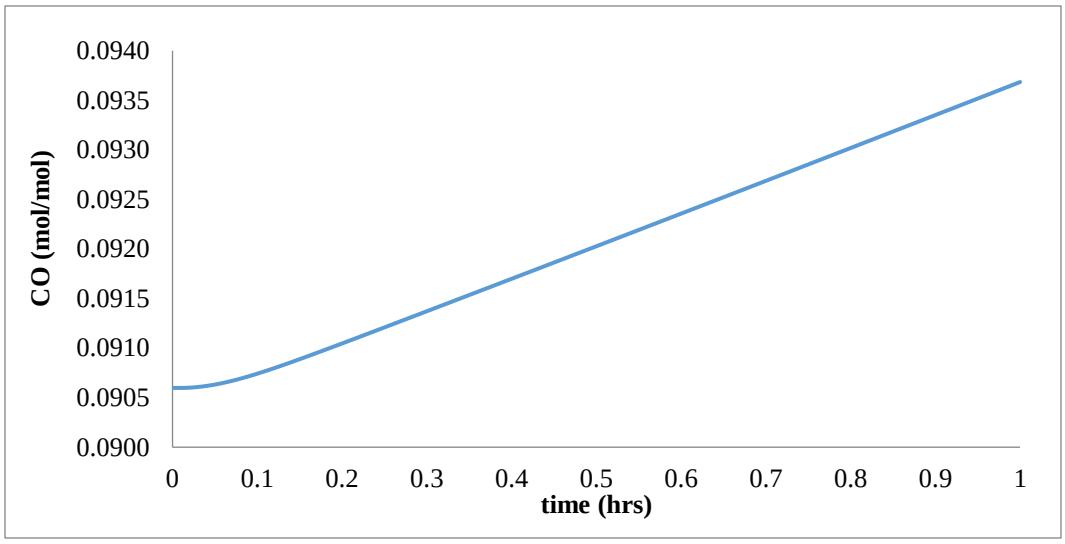

Figure 57. CO at the end of R1 as a result of a ramp change in the porosity.

Figure 57 shows that CO composition at the end of R1 increases as time progresses. As the catalyst pores get clogged and the porosity decreases, the extent of WGS reaction reduces, and thus the amount of CO consumed reduces.

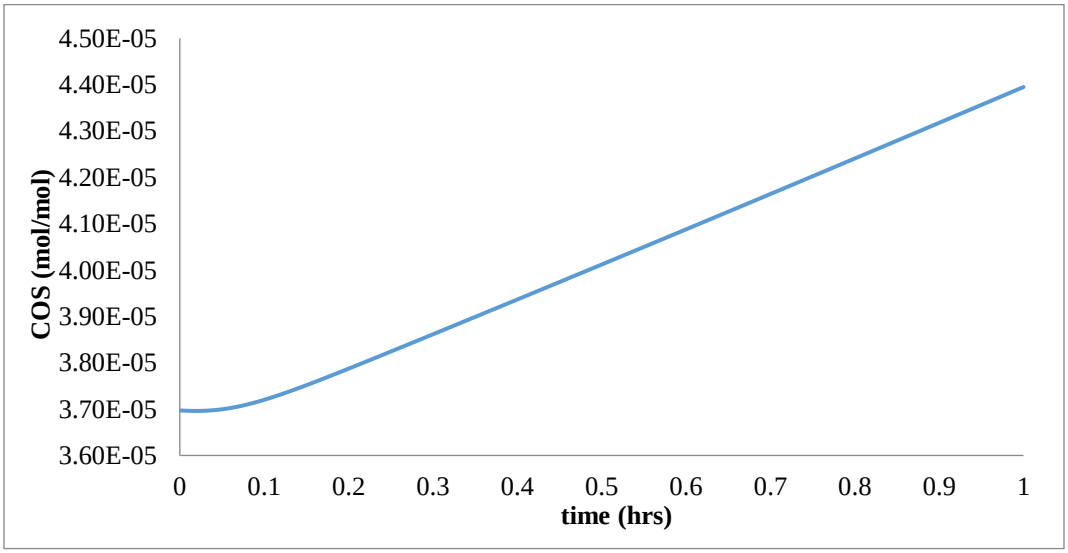

Figure 58. COS at the end of R1 as a result of a ramp change in porosity.

The rate of COS hydrolysis also gets affected due to the fault. The amount of COS converted reduces due to the reduction in porosity. Therefore, the COS mole fraction at the end of the reactor R1, increases, as can be seen from Figure 58.

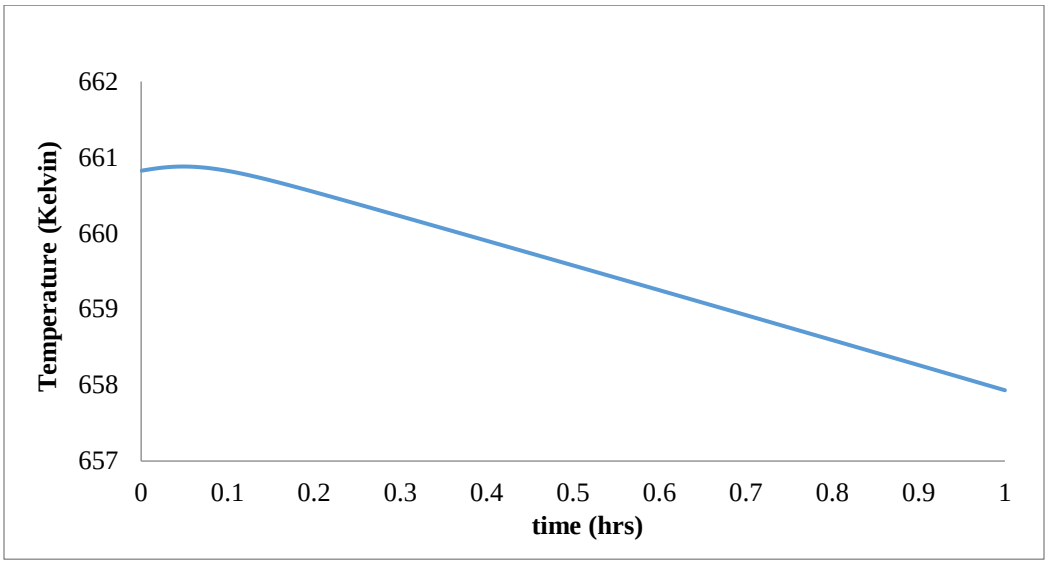

Figure 59. Temperature at end of R1 as a result of a ramp change in porosity.

The WGS reaction is an exothermic reaction. The reaction does not reach equilibrium in the first reactor. As the extent of reaction decreases in reactor R1, the temperature at the exit also reduces. This can be seen in Figure 59.

2.3.2.2 Effect on Reactor R2

Allowances have been provided in the design of the second reactor, R2, to accommodate acceptable deterioration in the performance of R1. Due to lower extent of WGS reaction in R1, the partial pressure of CO at the inlet of R2 increases. As a result, higher conversion of CO takes place in R2. The WGS reaction still approaches equilibrium, but it does so at different conditions as compared to what it had prior to the fault due to changes in the inlet conditions.

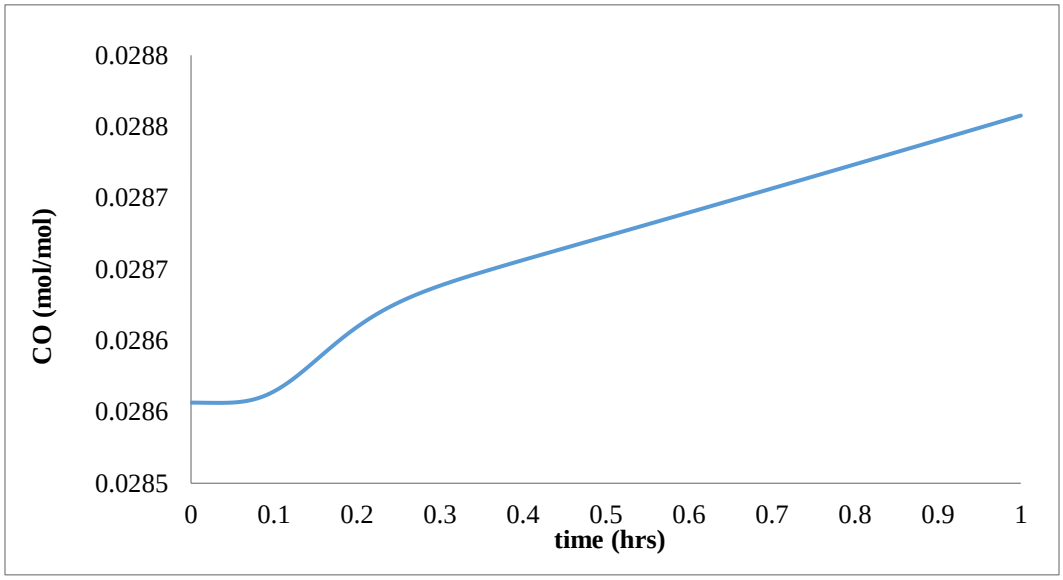

Figure 60. CO mole fraction at end of R2 as a result of ramp change in porosity.

From Figure 60, it can be seen that the effect of the fault in R1 has very small impact on the overall conversion at the outlet of R2.

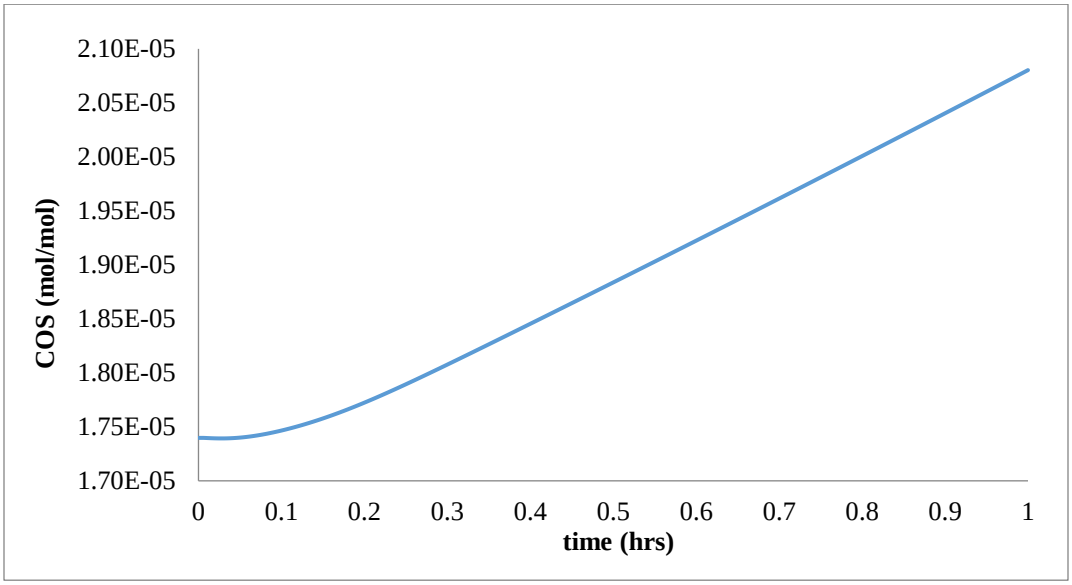

Figure 61. COS mole fraction at end of R2 as a result of ramp change in porosity.

As seen in Figure 61, COS seems to show stronger response than CO but the overall change in COS conversion is still negligible.

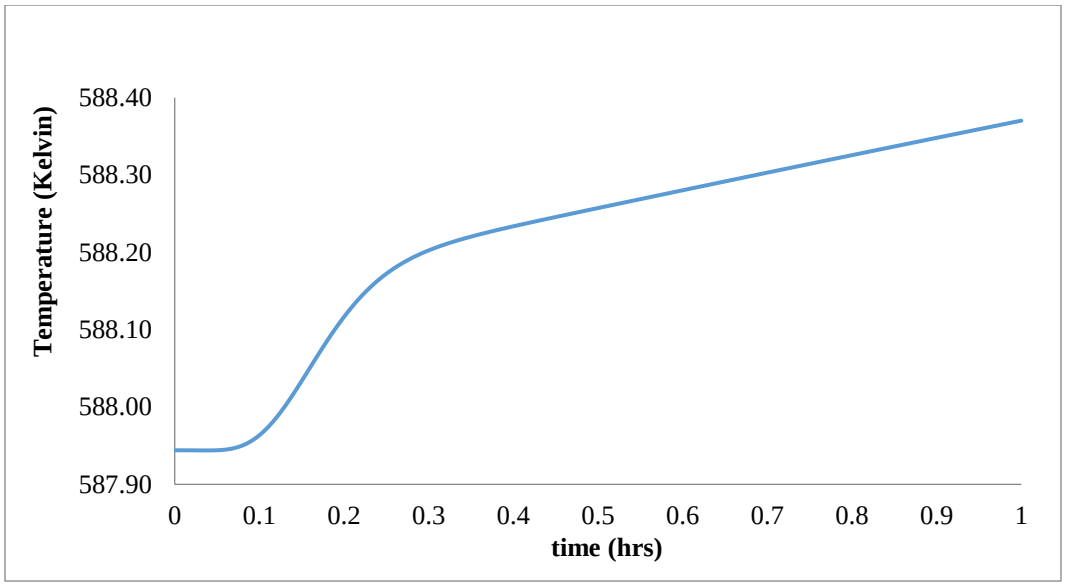

Figure 62. Temperature response at the exit of R2 as a result of ramp change in porosity.

Due to the increase in inlet CO composition, more reaction takes place in the R2. Being exothermic, as more reaction takes place, the temperature at the exit of the reactor, increases as shown in Figure 62.

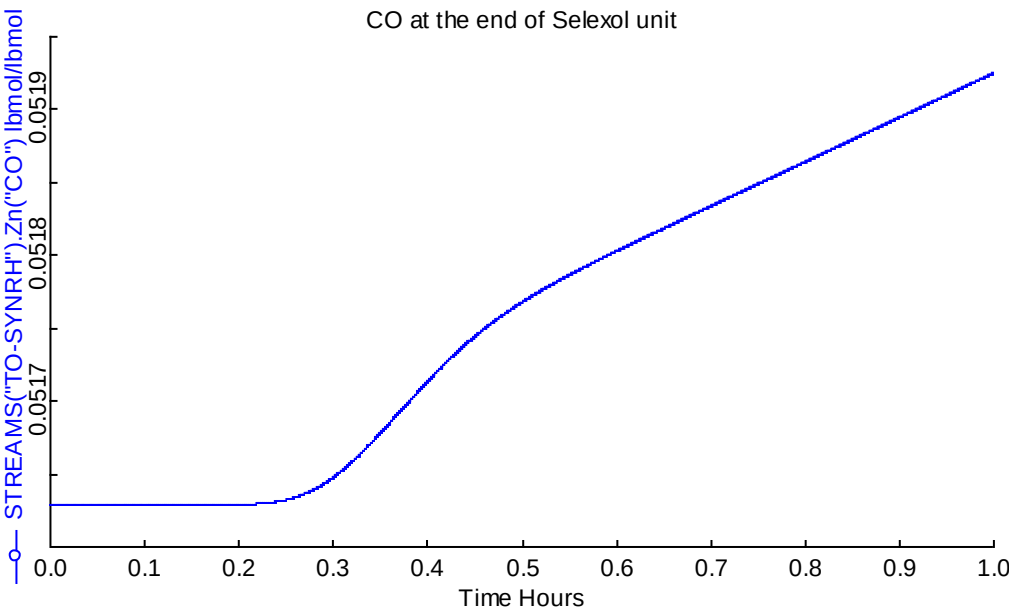

Figure 63. CO response at the exit of the Selexol unit as a result of ramp change in porosity.

The CO increase as a result of the ramp change in porosity is also reflected at the end of the Selexol plant. Figure 63 is a plot that shows CO mole fraction increases due to this fault. However, it takes around 12 – 13 minutes for this effect to be seen. The changes in the mole fractions of other components are very small to be detected clearly by a measuring device.

3 Model Simplification and Order Reduction

3.1 Scaling Analysis

The detailed 1D model of WGS reactor consists of PDEs, solution of which is computationally intensive. Therefore reduced order models, which approximate the detailed model with good computational efficiency, might become critical, particularly when such models are used in online optimization. In this section, such a reduced order model that is derived using scaling analysis and method of characteristics is described. Scaling analysis is a systematic way to identify important phenomena in a system for the given parameters and inlet conditions. This will help in retaining only these phenomena resulting in a simplified model. In literature, there are works which use scaling to simplify models and to identify the correlation between process performance and dimensionless groups. For example, Dahl et al.[154] used scaling analysis to get insight into the behavior of fluid aerosol reactor without performing actual simulations. Kopaygorodsky et al.[155], used scaling analysis to identify key differences between the approximation of conventional pressure swing adsorption and ultra-rapid pressure swing adsorption. Kaisare et al.[156], used scaling analysis to identify phenomena occurring at varying scales in a reverse flow reactor. Balaji et al.[157], have used scaling analysis for reverse flow reactor and have shown ways of simplifying the model equations. Rao et al.[158], have used scaling analysis for pulsed pressure swing adsorber to identify useful correlations in terms of dimensionless numbers. Rezvanpour et al.[159] studied electro hydrodynamic atomization process using scaling analysis to simply the model and to find correlation relating efficiency with single dimensionless number involving parameters of the process. Baldea et al.[160] used scaling analysis to auto thermal reactors to identify a non-stiff model by separating fast and slow time scales. Krantz et al.[161,162], described this scaling analysis in his book for various transport and reaction process.

This study closely follows the methodology of Krantz et al.[161,162] to derive appropriate dimensionless model for WGS reactor. The scaling analysis in this study differs from the rest of the literature in the manner in which the reaction terms are handled. This becomes important because with the present scaling methodology, approximating the nonlinearity in the reaction kinetics would result in unrealistic scales. This study also compares the scales obtained from scaling analysis with that of actual scales from simulation of the corresponding detailed model. This demonstrates that scaling is proper and the resulting reduced order model is appropriate. Further, in the scaling of the unsteady model, we introduce a new scale combining length and time scale which characterizes the velocity dynamics of a variable. This scale helps in assessing the quasi- steady assumption for some of the variables. The reduced order model obtained from scaling analysis consists of hyperbolic PDE coupled with ODEs. Hyperbolic PDE models can be further reduced using a recently developed technique using method of characteristics. Munusamy et al.[163,164], used this technique to reduce the hyperbolic PDE model describing fixed bed and plug flow reactor. In this study, we follow this technique to further reduce the computational load in simulating WGS reactor.

3.1.1 Scaling of WGS reactor model equations:

Systematic scaling of model equations results in identifying phenomena with different scales. It provides a way for model simplification through approximation. These scales represent the characteristic values for the given parameters and operating conditions. Krantz[161] has described scaling of model equations in detail in his book, where scales are obtained by forming dimensionless groups which vary in the order of 1. In this study we follow similar approach to that of Krantz[161], but differ in the manner in which the characteristic reaction terms are found.

The procedure for scaling involves introducing scale values for each of the variables involved to make these variables dimensionless. Introduction of these scales and dimensionless variables will result in dimensionless equations. Scales can be obtained appropriately by making the dimensionless variables to vary in the order of 1.

Following are the scales introduced for the variables in the model for water gas shift reactor

$$C_i^{\varphi} \equiv \frac{C_{i,r-}C_i}{C_{i,s}} \; ; T_g^{\varphi} \equiv \frac{T_g - T_{g,r}}{T_{g,s}} \quad ; \quad T_{cat}^{\varphi} \equiv \frac{T_{cat} - T_{cat,r}}{T_{cat,s}}$$
$$C^{\varphi} \equiv \frac{C - C_r}{C_s}; \quad P^{\varphi} \equiv \frac{P_r - P}{P_s}; \quad z^{\varphi} \equiv \frac{z}{z_s} \tag{106}$$

In the above definition, variables with subscript 'r' represent reference variables, variables with subscript 's' represent scaling variables and the variables with superscript φ represent the dimensionless variables. Reference and scale variables need to be chosen such that the variables vary between 0 and 1. Additional scales are introduced for nonlinear terms such as derivatives and reaction rate terms.

$$\left(\frac{dC_i}{dz}\right)^{\varphi} \equiv \frac{1}{C_{i,zs}}\frac{dC_i}{dz} \; ; \left(\frac{dC}{dz}\right)^{\varphi} \equiv \frac{1}{C_{zs}}\frac{dC}{dz}$$
$$; \left(\frac{dT_g}{dz}\right)^{\varphi} \equiv \frac{1}{T_{g,zs}}\frac{dT_g}{dz}; \; \left(\frac{d^2T_{cat}}{dz^2}\right)^{\varphi} \equiv \frac{1}{T_{cat,zzs}}\frac{d^2T_{cat}}{dz^2} \tag{107}$$
$$\left(\frac{dP}{dz}\right)^{\varphi} \equiv \frac{1}{P_{zs}}\frac{dP}{dz} \; ; \; r_{wgs}{}^{\varphi} \equiv \frac{r_{wgs}}{r_{wgs,s}}; \quad r_{hyd}^{\varphi} \equiv \frac{r_{hyd}}{r_{hyd,s}}$$

The derivative scales introduced above can be approximated using the scaling definition for each individual variable in the derivative. Similar approximations for the reaction scale by introducing the scaling definition of each individual variable in the reaction kinetics would result in wrong scaling for the reaction term. In literature, this scale is either assumed to be the maximum reaction rate or the rate is found by introducing maximum values for the variables in the reaction rate. Both the approximations for reaction scale will result in errors while obtaining the reduced order model. Appropriate scaling of reaction terms will be discussed in section 3.1.1. The approximate derivative scales are given below

$$C_{i,zs} \equiv \frac{C_{i,s}}{z_s} \; ; \; C_{zs} \equiv \frac{C_s}{z_s} \; ; \; T_{g,zs} \equiv \frac{T_{g,s}}{z_s} \; ; \; T_{g,zs} \equiv \frac{T_{cat,s}}{z_s^2} \; ; \; T_{g,zs} \equiv \frac{T_{cat,s}}{z_s^2} \; ; \; P_{zs} \equiv \frac{P_s}{z_s} \tag{108}$$

In addition to derivative terms, scales for the other nonlinear terms are approximated as below

$$\left(\frac{r_i}{u}\right)_s \equiv \frac{r_{i,s}}{u_{\min}} \; ; \; \left(u^2\right)_s \equiv u_s^2 \tag{109}$$

In this approximation we use $\frac{1}{u_{\min}}$ as the scale for the variable $\frac{1}{u}$, because this will be the maximum and hence will make the variable to vary at most to 1.

Introducing the above scaling definitions into the model equation and dividing the coefficient of one of the terms results in following dimensionless model equation. For the first four equations, we divide the coefficient of the derivative terms to form the dimensionless equation. For these equations it is assumed that variation of the corresponding variables over the length of the reactor is significant. In the equation for catalyst energy balance, we divide the coefficient of one of the reaction terms to form the dimensionless equation. This is because we assume that the heat generated from this reaction is the main source for energy which is convected to gas phase and conducted through the catalyst bed. Scaling analysis will confirm the validity of this assumption.

Component balance: (where i = 1 to 6)

$$\left(\frac{dC_i}{dz}\right)^{\varphi} = \frac{y_i C_{zs}}{C_{i,zs}}\left(\frac{dC}{dz}\right)^{\varphi} + \left(\frac{r_i}{u}\right)_s \frac{(1-\varepsilon)}{C_{i,zs}}\left(\frac{r_{wgs,i}}{u}\right)^{\varphi} \tag{110}$$

Total balance:

$$\left(\frac{dC}{dz}\right)^{\varphi} = -\left(\frac{C}{T}\right)\frac{T_{zs}}{C_{zs}}\left(\frac{dT_g}{dz}\right)^{\varphi} + \left(\frac{C}{P}\right)\frac{P_{zs}}{C_{zs}}\left(\frac{dP}{dz}\right)^{\varphi} \tag{111}$$

Pressure drop equation:

$$\left(\frac{dP}{dz}\right)^{\varphi} = \frac{1}{P_{zs}}\frac{\rho\left(u^2\right)_s}{d_{cat}}\left(\frac{1-\varepsilon}{\varepsilon^3}\right)1.75\left(u^2\right)^{\varphi} + \frac{1}{P_{zs}}\frac{u_s(1-\varepsilon)^2\mu 150}{d_{cat}^2\varepsilon^3}u^{\varphi} \tag{112}$$

Gas phase energy balance:

$$\left(\frac{dT_g}{dz}\right)^{\varphi} = \frac{h_f a_c z_s}{Cp_g G\varepsilon}\left(\frac{T_{cat,s}}{T_{g,s}}T_{cat}^{\varphi} - T_g^{\varphi}\right) \tag{113}$$

Catalyst phase energy balance:

$$\frac{K_{cat}T_{zzs}}{r_{wgs,s}\Delta H_{R,wgs}}\left(\frac{d^2T_{cat}}{dz^2}\right)^{\varphi}=\frac{h_f a_c T_{cat,s}}{(1-\varepsilon)r_{wgs,s}\Delta H_{R,wgs}}\left(\frac{T_{cat,s}}{T_{g,s}}T_{cat}^{\varphi}-T_g^{\varphi}\right)-r_{wgs}^{\varphi}-\frac{r_{hyd,s}\Delta H_{R,hyd}}{r_{wgs,s}\Delta H_{R,wgs}}r_{hyd}^{\varphi} \quad (114)$$

The boundary conditions are made dimensionless as follows

$$z^{\varphi}=0 \quad ; \quad C_i^{\varphi}=\frac{C_{i,r}-C_{i,in}}{C_{i,s}} \quad ; \quad T_g^{\varphi}=\frac{T_{g,in}-T_{g,r}}{T_s}$$

$$T_{cat}^{\varphi}=\frac{T_{g,in}-T_{cat,r}}{T_s} \; ; \; P^{\varphi}=\frac{P_{in}-P_r}{P_S} \quad (115)$$

$$z^{\varphi}=\frac{L}{z_s} \quad ; \frac{dT_{cat}^{\varphi}}{dz^{\varphi}}=0$$

3.1.2 Calculation of scales and reference factors

The scales and reference factors in the above dimensionless equation can be found by confining the dimensionless variables to vary between 0 and 1. In particular, the reference factors are found by equating the boundary conditions to 0. For example, the reference factor for the concentration variable is found as below

$$C_i^{\varphi}=\frac{C_{i,r}-C_{i,in}}{C_{i,s}}=0 \text{, this implies } C_{i,r}=C_{i,in} \quad (116)$$

In a similar manner, reference factors for other variables can be found and it will be equal to the boundary values of the corresponding variables. The scale factors can be found by equating appropriate dimensionless variable to 1. For example, consider the equation for species balance (Eqn. (110)), where there are two dimensionless groups.

$$\pi_1=\frac{y_i C_{zs}}{C_{i,zs}} \quad \text{and} \quad \pi_2=\left(\frac{r_i}{u}\right)_s\frac{(1-\varepsilon)}{C_{i,zs}}=\frac{r_{i,s}(1-\varepsilon)}{u_{in}C_{i,zs}} \quad (117)$$

Once C_{zs} and $r_{i,s}$ are known, one can find the derivative scale for concentration C_i by equating either of these dimensionless groups to 1. The dimensionless group which gives maximum value for the corresponding scale can be equated to 1. The resulting scale can be substituted into the other dimensionless group and if the resulting value is much less than 1 then the term involving this dimensionless group contributes less to the characteristic derivative scale and hence can be neglected for the condition considered.

3.1.3 Calculation of reaction rate scale

Calculation of characteristic scale for reaction rate can be tricky for exothermic reactions in a tubular or fixed bed reactor where reaction rate varies along the length of the reactor. A scale should be a representative value, which, when it divides the actual value makes it to vary in the order of 1. Also, the value of the scale should be close to the reaction rates occurring over entire length of the reactor. For exothermic reactions, the rate varies along the length such that it attains a maximum value at some point in the reactor. This is because concentration drops along the length of the reactor which reduces the reaction rate and temperature increases due to release of heat which in turn increases the reaction rate. For sufficiently high temperature, this maximum can occur at the inlet of the reactor and for others it can

occur at a small distance from inlet of the reactor. Typical reaction rate variation is shown in the Figure 64.

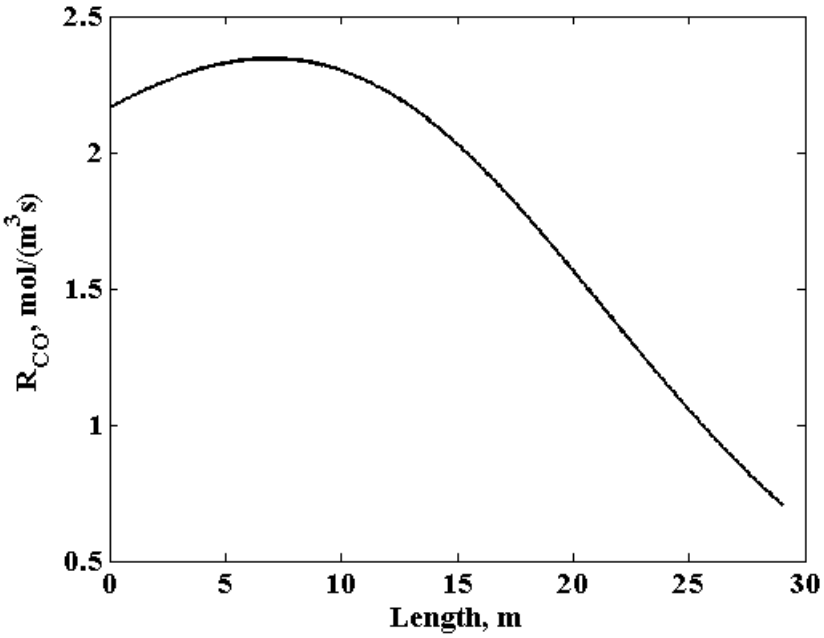

Figure 64. Typical variation of exothermic reaction rate along the length of the reactor.

In the literature, the characteristic reaction rate is found by substituting the maximum temperature and maximum concentration in the reaction kinetic term.[161,162] For exothermic reactions, maximum temperature and maximum concentration are rarely going to occur at the same point in the reactor. So substitution of these values will give unrealistic maximum reaction rates. This will lead to erroneous calculation of other scales. In a mass transfer limited reaction, this reaction scale is based upon mass transfer coefficient.[157]

The proper scale for reaction rate which can make the corresponding dimensionless reaction rate order of 1 would be the maximum reaction rate occurring in the reactor. It is difficult to obtain this rate without performing actual simulations of the given detailed model. So this reaction rate scale can be approximated to be

- Reaction rate based on inlet condition which is a reasonable approximation for this maximum rate. In this study, we have used this inlet rate to be the characteristic rate to obtain the other scales.
- Reaction rate obtained using simulation of simplified model. One can obtain a simplified model by assuming velocity to be constant, neglecting any mass transfer or heat transfer resistance, neglecting pressure drop, assuming only 1D variation, etc. This means that we assume reaction to be the main cause for the variation of concentration and temperature along the length of the reactor. Kaisare et al.[156] have suggested in their paper the use of simulation data for obtaining the reaction scale.

3.1.4 Calculation of scales based on inlet reaction rate

Consider the dimensionless species balance equation Eqn. (110). In this equation, we have two dimensionless terms as mentioned in the previous paragraph. Let's assume the contribution of the second

dimensionless term to be important for the concentration gradient, so this group is equated to 1, to find length scale over which the reaction occurs

$$\pi_2 = \left(\frac{r_i}{u}\right)_s \frac{(1-\varepsilon)}{C_{i,zs}} = \frac{r_{i,s}(1-\varepsilon)}{u_{in}C_{i,zs}} = 1 \tag{118}$$

This dimensionless group can be inferred as

$$\pi_2 = \frac{r_{i,s}(1-\varepsilon)}{u_{in}C_{i,zs}} = \frac{Generation/Consumption\ of\ species\ due\ to\ reaction}{Transport\ of\ species\ by\ axial\ convection} \tag{119}$$

This means that the species generated (or consumed) from reaction is made equal to that transported by axial convection based on inlet velocity. The other dimensionless groups present in this equation indicate the change in species concentration is due to change in pressure and temperature along the length of the reactor. The importance of this dimensionless group can be found from its value by inserting the concentration scale C_s from total balance equation.

Let's also assume there is complete conversion in the reactor and take C_{is} to be equal to C_{in}. With this assumption, we can calculate the characteristic length scale as follows

$$z_s = \frac{r_{i,in}(1-\varepsilon)}{u_{in}C_{i,in}} \tag{120}$$

If the length scale obtained above is greater than the length of the reactor (L), then it indicates that the reaction is slow and there is no complete conversion. Then one can find the characteristic change in the concentration by making the length scale to be length of the reactor. Thus,

$$C_{i,s} = \frac{r_{i,in}(1-\varepsilon)}{u_{in}L} \tag{121}$$

From Eqn. (113), we can make $T_{g,s} = T_{cat,s}$, so that the dimensionless temperature difference between catalyst and gas phase can be of order 1. The temperature change in a reactor is directly proportional to the rate of heat release from the reaction. In order to find the scale for the temperature change, we need to relate this to the heat of reaction. From Eqn. (113) and (114) we see that this relation is present in one of the terms in Eqn. (114).

$$\pi_4 = \frac{h_f a_c T_{cat,s}}{(1-\varepsilon) r_{wgs,s} \Delta H_{R,wgs}} \tag{122}$$

The above dimensionless term multiplies the temperature difference and this cannot be used to calculate the temperature scale. Instead, this term can be used to verify the equality of the temperatures between gas phase and catalyst phase. This is because in order for the term $\pi_4\left(T_{cat}^{\varphi} - T_g^{\varphi}\right)$ to be in the order 1, higher the value of π_4 implies lower the value of $\left(T_{cat}^{\varphi} - T_g^{\varphi}\right)$, which implies that both the temperatures are equal and vice versa. Next, the term which multiplies the second derivative of temperatures can be used. If we assume conduction is not an important phenomenon compared to axial convection of heat then this term also cannot be used. So in order to find the temperature scale we can combine the energy balance for gas phase and catalyst phase by using the temperature difference terms in these equations as follows

$$K_{cat}\frac{d^2T_{cat}}{dz^2}=\frac{Cp_gG\varepsilon}{(1-\varepsilon)}\frac{dT_g}{dz}-r_{wgs}\Delta H_{R,wgs}-r_{hyd}\Delta H_{R,hyd} \tag{123}$$

Eqn. (123) can be made dimensionless using the scaling definition as follows

$$\frac{(1-\varepsilon)K_{cat}T_{zzs}}{Cp_gG\varepsilon T_{zs}}\left(\frac{d^2T_{cat}}{dz^2}\right)^{\varphi}=\left(\frac{dT_g}{dz}\right)^{\varphi}-\frac{r_{wgs,s}\Delta H_{R,wgs}(1-\varepsilon)}{Cp_gG\varepsilon T_{zs}}r_{wgs}^{\varphi}-\frac{r_{hyd,s}\Delta H_{R,hyd}(1-\varepsilon)}{Cp_gG\varepsilon T_{zs}}r_{hyd}^{\varphi} \tag{124}$$

From the above equation, we can find the temperature scale by equating the following dimensionless group to 1,

$$\pi_5=\frac{r_{wgs,s}\Delta H_{R,wgs}(1-\varepsilon)z_s}{Cp_gG\varepsilon T_s}=1 \tag{125}$$

The above dimensionless group implies that the rate of heat generated per unit volume from water gas shift reaction is equal to rate of heat convected by the gas in axial direction. In the above equation, we have assumed water gas shift reaction to be an important source of heat and we have selected the dimensionless group involving this reaction. We can verify this assumption by substituting the resulting scales into the other terms.

Similarly one can find the pressure scale from the Eqn. (112) by equating following dimensionless group to 1,

$$\pi_6=\frac{L}{P_s}\frac{\rho(u^2)_s}{d_{cat}}\left(\frac{1-\varepsilon}{\varepsilon^3}\right)1.75=1 \tag{126}$$

In the above term, since pressure variation is seen over the entire length of the reactor, the appropriate length scale for finding pressure scales will be the actual length of the reactor. This also assumes that the Reynolds number is high enough that the contribution of second term in Eqn. (112) is lesser than the first. For lower Reynolds number we need to make the other dimensionless group to 1 to find the pressure scale. Further, the velocity scale in Eqn. (126) is represented in terms of temperature and pressure scale as

$$u_s=\frac{G\varepsilon R(T_{in}+T_s)}{(P_{in}-P_s)}$$

This represents the maximum velocity due to increase in temperature and decrease in pressure. Similarly, the total concentration scale can be found from either of the dimensionless term which gives the maximum value for this scale. The variable values present in these groups can be assumed to be the inlet values as the ratio of these values are maximum at the inlet. For example, consider the first group,

$$\pi_7=\frac{CT_s}{TC_s}=\frac{C_{in}T_s}{T_{in}C_s}=1 \tag{127}$$

In the above equation, the ratio $\frac{C}{T}$ can be assumed to be the ratio of the inlet values as $\frac{C_{in}}{T_{in}}$. Once the necessary scales are found as described above, then one can substitute these values in other dimensionless groups. If the value of these dimensionless groups is much less than 1, it indicates its contribution is less in the corresponding equation and hence can be ignored. In the model equation for WGS reactor, based on the value of the following groups, one can neglect the corresponding phenomena

For neglecting conduction phenomena,

$$\pi_8 = \frac{K_{cat} T_{zzs}}{r_{wgs,s} \Delta H_{R,wgs}} \approx \frac{K_{cat} T_s}{r_{wgs,s} \Delta H_{R,wgs} L^2} << 1 \quad (128)$$

For neglecting the heat contribution due to hydrolysis reaction term

$$\pi_9 = \frac{r_{hyd,s} \Delta H_{R,hyd}}{r_{wgs,s} \Delta H_{R,wgs}} << 1 \quad (129)$$

Similarly one can decide on the significance of heat transfer between gas and catalyst phase and can make both the temperatures equal.

3.1.5 Reduced order model of WGS reactor

A reduced order model for WGS reactor can be obtained using scaling analysis by neglecting the terms with contribute less when compared to others in an equation. This model will be an approximate representation of the corresponding detailed model for the given parameter and inlet conditions. Table 12 reports the typical parameters and inlet conditions for the reactor.

Table 12. Parameters and inlet conditions for WGS reactor

Parameter	Value
Length of the reactor L, (m)	29
Porosity of bed, ε	0.38
Heat transfer coefficient, h_f $\left(\frac{W}{m^2 K}\right)$	10^2
Heat of reaction - WGS, ΔH_{wgs} $\left(\frac{J}{mol}\right)$	3.85×10^4
Heat of reaction - Hyd, ΔH_{wgs} $\left(\frac{J}{mol}\right)$	3.1×10^4
Density of gas, ρ_g $\left(\frac{mol}{m^3}\right)$	20.5
Viscosity of gas mixture, μ_g $\left(\frac{N-s}{m^2}\right)$	0.25×10^{-4}
Specific heat of gas, Cp_g $\left(\frac{J}{mol-K}\right)$	35
Density of catalyst, ρ_{cat} $\left(\frac{kg}{m^3}\right)$	650
Specific heat of catalyst, Cp_{cat} $\left(\frac{J}{kg-K}\right)$	880

Specific area per unit volume of catalyst $a_c, \frac{m^2}{m^3}$	1.69×10^3
Conductivity of catalyst, $K\left(\frac{W}{m-K}\right)$	35
Diameter of catalyst, $d_{cat}\ (m)$	0.0035

Inlet condition

Molar flow, $\left(\frac{mol}{s}\right)$	
CO	1128
COS	0.4410
CO_2	435
H_2	1070
H_2O	2240
H_2S	22.78
Inlet temperature, $T\ (K)$	620
Inlet pressure, $P\ (Pa)$	5.86×10^6

The stoichiometric relation from reaction can be used to avoid species balance for all the species except for the key reactant. This is valid when species are transported mainly by convection and not by diffusion both in the axial and in radial direction. Then the transport of all other species can be exactly described by the variation of key reactant participating in each reaction. In the WGS reactor model, we consider two main reactions, water gas shift and hydrolysis reaction taking place in the reactor.

$$\gamma_{CO}CO + \gamma_{H_2O}H_2O \Leftrightarrow \gamma_{CO_2}CO_2 + \gamma_{H_2}H_2$$

$$\gamma_{COS}COS + \gamma_{H_2O}H_2O \Leftrightarrow \gamma_{CO_2}CO_2 + \gamma_{H_2S}H_2S$$

Considering CO and COS to be key reactants, we can write the variation of other species using stoichiometry as follows

$$y_{h_2} = y_{h_{2,in}} + \frac{\gamma_{h_2}}{\gamma_{CO}}\left(y_{CO,in} - y_{CO}\right) \tag{130}$$

$$y_{h_2s} = y_{h_2s_{,in}} + \frac{\gamma_{h_2s}}{\gamma_{COS}}\left(y_{COS,in} - y_{COS}\right) \tag{131}$$

$$y_{CO_2} = y_{CO_{2,in}} + \frac{\gamma_{CO_2}}{\gamma_{CO}}\left(y_{CO,in} - y_{CO}\right) + \frac{\gamma_{CO_2}}{\gamma_{COS}}\left(y_{COS,in} - y_{COS}\right) \tag{132}$$

$$y_{h_2o} = y_{h_2o_{,in}} - \frac{\gamma_{h_2o}}{\gamma_{CO}}\left(y_{CO,in} - y_{CO}\right) + \frac{\gamma_{h_2o}}{\gamma_{COS}}\left(y_{COS,in} - y_{COS}\right) \quad (133)$$

The value of various dimensionless groups discussed in the previous section is found based on the parameters and inlet condition given in Table 12. Based on these values we can decide on approximating the model equations by neglecting terms which are much less than 1.

Table 13. Values of dimensionless group for the WGS reactor model

Dimensionless group	Value
$\pi_1 = \frac{y_{co} C_s z_s}{C_{co,s} L}$	0.41
$\pi_2 = \frac{r_{co,s}(1-\varepsilon) z_s}{u_{in} C_{co,s}} = 1$	$z_s = 29$ *and* $C_{co,s} = 180.54 < C_{co,in}$
$\pi_3 = \frac{h_f a_c z_s}{C p_g G \varepsilon}$	606.90
$\pi_4 = \frac{h_f a_c T_{cat,s}}{(1-\varepsilon) r_{wgs,s} \Delta H_{R,wgs}}$	606.90
$\pi_5 = \frac{r_{wgs,s} \Delta H_{R,wgs}(1-\varepsilon) z_s}{C p_g G \varepsilon T_s} = 1$	$T_s = 185.8$
$\pi_6 = \frac{L}{P_s} \frac{\rho(u^2)_s}{d_{cat}} \left(\frac{1-\varepsilon}{\varepsilon^3}\right) 1.75 = 1$	$P_s = 2.94 \times 10^5$
$\pi_7 = \frac{C_{in} T_s}{T_{in} C_s} = 1$	$C_s = 320.6$
$\pi_8 = \frac{K_{cat} T_s}{r_{wgs,s} \Delta H_{R,wgs} L^2}$	9.27×10^{-5}
$\pi_9 = \frac{r_{hyd,s} \Delta H_{R,hyd}}{r_{wgs,s} \Delta H_{R,wgs}}$	1.8×10^{-3}
$\pi_{10} = \frac{L}{P_s} \frac{u_s (1-\varepsilon)^2 \mu 150}{d_{cat}^2 \varepsilon^3}$	6.2×10^{-2}
$\pi_{11} = \frac{C_{in} P_s}{P_{in} C_s}$	0.1781
$\pi_{12} = \frac{y_{\cos} C_s z_{s,\cos}}{C_{\cos,s} L}$	7.1×10^{-2}

$$\pi_{13} = \frac{r_{\cos,s}(1-\varepsilon)z_{s,\cos}}{u_{in}C_{\cos,s}} = 1 \qquad z_{s,\cos} = 6.88 \; and \; C_{co,s} = 0.963 = C_{\cos,in}$$

Based on the values of dimensionless group present in Table 13, we can decide on retaining or neglecting some of the phenomenon to obtain a reduced order model. The length scale for water gas shift reaction is equal to length of the reactor and the concentration scale is less than the inlet concentration, this implies there is no complete conversion in the reactor. On the other hand hydrolysis reaction goes to completion and this occurs at 23% of the length of the reactor.

The dimensionless group π_1 and π_{12} represent the variation of C_{CO} and C_{COS} due to the variation of total concentration which in turn depends on temperature and pressure variation in the reactor. Though π_1 is in the order of 1, π_{12} is much less than 1, indicating that C_{COS} variation is mainly due to reaction and this is also seen from the complete conversion of C_{COS} well within the reactor. So we can neglect this term from the species balance of C_{COS}.

The value of dimensionless groups π_3 and π_4 are much higher than 1 and they both multiply the dimensionless temperature difference term. As mentioned previously, the value of the dimensionless group which multiplies dimensionless temperature difference will indicate whether this difference is significant or can be made equal.

$$\pi_3 = \frac{h_f a_c z_s}{C p_g G \varepsilon} >> 1 \quad \text{and} \quad \pi_4 = \frac{h_f a_c T_{cat,s}}{(1-\varepsilon) r_{wgs,s} \Delta H_{R,wgs}} >> 1 \tag{134}$$

Since π_3 multiplies $T_{cat,s} - T_{g,s}$, if π_3 >>1 then it implies that $T_{cat}^{\varphi} - T_g^{\varphi}$ <<1, so that $\pi_3\left(T_{cat}^{\varphi} - T_g^{\varphi}\right)$ will be in the order of 1 and hence both the temperatures can be made equal and vice versa. The dimensionless group π_3 implies the ratio of rate of heat transfer from catalyst to rate of heat convected along axial direction by the flowing gas. Similarly π_4 indicates the ratio of rate of heat transfer from catalyst to gas phase to rate of heat generation from reaction. A large value of this dimensionless group indicates that the heat generated from reaction is convected by the flowing gas. This in turn verifies the assumption of π_5 equal to 1 while finding the temperature scale. From the value of these dimensionless groups in Table 13, catalyst and gas phase temperatures can be safely assumed to be equal.

The scale of total concentration change C_s is found by assuming that temperature is the dominant cause for this variation by equating π_7 to 1. From π_{11} which is in order 1, we see that C_s also depends on pressure variation. So we cannot neglect any term from the total concentration balance.

The value of dimensionless group π_8 indicates that its contribution in the energy balance equation is negligible. The dimensionless group π_8 represents

$$\pi_8 = \frac{K_{cat} T_s}{r_{wgs,s} \Delta H_{R,wgs} L^2} = \frac{Heat\ conducted\ \ per\ unit\ voulme}{Heat\ generated\ per\ unit\ voulme} << 1 \tag{135}$$

This infers transport of heat by conduction through catalyst in axial direction is negligible. Resistance for conduction R_{cond} through catalyst bed can be given by

$$R_{cond} = \frac{L}{K_{cat}(1-\varepsilon)A_c} \tag{136}$$

where A_c is the cross sectional area of the reactor. The resistance for conduction increases with length of the reactor. So for the length considered, this resistance is higher and hence this contribution is negligible compared to heat transport by convection along axial direction.

The dimensionless group π_9 represents the ratio of rate of heat generation per unit volume by hydrolysis reaction to water gas shift reaction. Small value of this group indicates that this term in the energy balance equation can be safely neglected. The dimensionless number π_9 is much less than 1 and it indicates that Reynolds number is high enough to neglect the contribution of the second term in pressure drop equation.

3.1.6 Reduced order model after scaling

A reduced order model is obtained after removing terms as discussed previously. The simplifications described require us to re-derive the energy balance by assuming instantaneous transfer of heat from catalyst to gas phase and neglecting any conduction. The new energy balance is given as

$$\frac{dT}{dz} = \frac{1}{GCp_g}\left(\frac{1-\varepsilon}{\varepsilon}\right) r_{wgs}\Delta H_{R,wgs} \tag{137}$$

Reduced order model for the given parameter and inlet condition is given below

Component balance: (CO)

$$\frac{dC_{Co}}{dz} = y_{Co}\frac{dC}{dz} + r_{CO}\frac{1-\varepsilon}{u} \tag{138}$$

Component balance: (COS)

$$\frac{dC_{\cos}}{dz} = r_{\cos}\frac{1-\varepsilon}{u} \tag{139}$$

Total balance:

$$\frac{dC}{dz} = -C\left(\frac{1}{T}\frac{dT}{dz} - \frac{1}{P}\frac{dP}{dz}\right) \tag{140}$$

Pressure drop equation:

$$\frac{dP}{dz} = \frac{\rho u^2}{d_{cat}}\left(\frac{1-\varepsilon}{\varepsilon^3}\right)1.75 \tag{141}$$

Energy balance:

$$\frac{dT}{dz} = \frac{1}{GCp_g}\left(\frac{1-\varepsilon}{\varepsilon}\right) r_{wgs}\Delta H_{R,wgs} \tag{142}$$

3.1.7 Comparison of simulation results from reduced order model with that of detailed model

The reduced order model obtained through scaling analysis is tested by comparing the simulation results with that of detailed model. The percentage change in the average values of the variables between detailed and reduced order model and the computational time taken are considered as the metrics for comparison. These metrics represent the closeness of the reduced order model and its computational efficiency compared to the corresponding detailed model. For example, the average change in the temperature over the length of the reactor between two models is given by

$$T_{avg,error} = \frac{\left|\frac{1}{L}\int_0^L T_{\det ailed}dz - \frac{1}{L}\int_0^L T_{reduced}dz\right| \times 100}{\frac{1}{L}\int_0^L T_{\det ailed}dz} \tag{143}$$

In the above equation, the integral is calculated numerically based on the profile values of the corresponding variables. Computational load is measured in terms of time taken for simulation using tic-toc command in MATLAB. Table 14 shows the values for these metrics and the values shows that error percentage is small enough that one can consider reduced order model is a good approximation for the given parameters and inlet conditions. On the other hand, the computational load is considerably lower and it is reduced by about 97.8% of the load required for the detailed model, which can make the use of this model preferred of several applications.

Table 14. Metric for comparing reduced and detailed model simulation

Variable/Model	Metric	Value (%)
Concentration of CO	$C_{co,avg,error}$	0.3045
Concentration of COS	$C_{\cos,avg,error}$	5.02
Temperature	$T_{avg,error}$	0.0132
Pressure	$P_{avg,error}$	0.1340
Detailed model	Computational load, s	74.86
Reduced order model	Computational load, s	0.96

In the figure below, we show the profile of two of the variables between these two models. Figure 65-66 show the profile of COS and temperature along the length of the reactor, respectively. From the temperature profile one can observe there is increase in catalyst temperature very near to the inlet of the reactor. This is because at a small enough lengths, conduction dominates over convection, hence there is rise in catalyst temperature and also we see difference between catalyst and gas phase temperature. This length where conduction is important can be approximately given by,

$$\delta_{cond} = \sqrt{\frac{K_{cat} T_s}{r_{wgs,s} \Delta H_{R,wgs}}} = 0.23 \qquad (144)$$

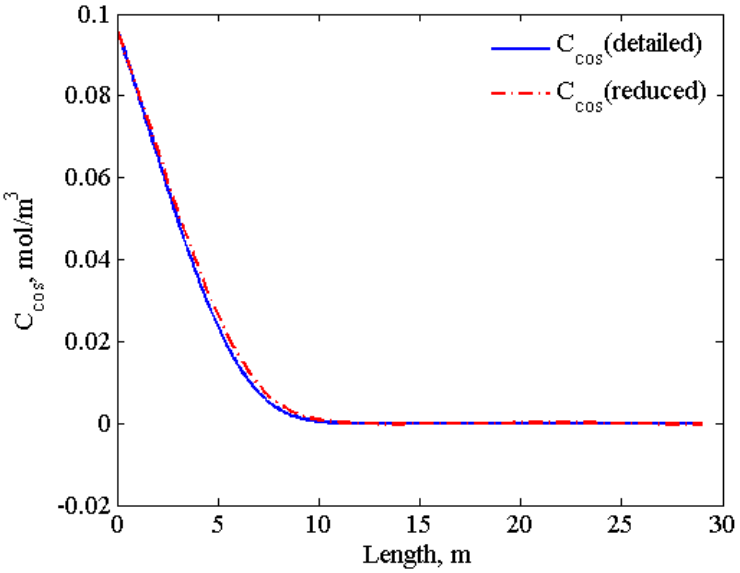

Figure 65. Concentration profile of COS from detailed and reduced model for WGS reactor.

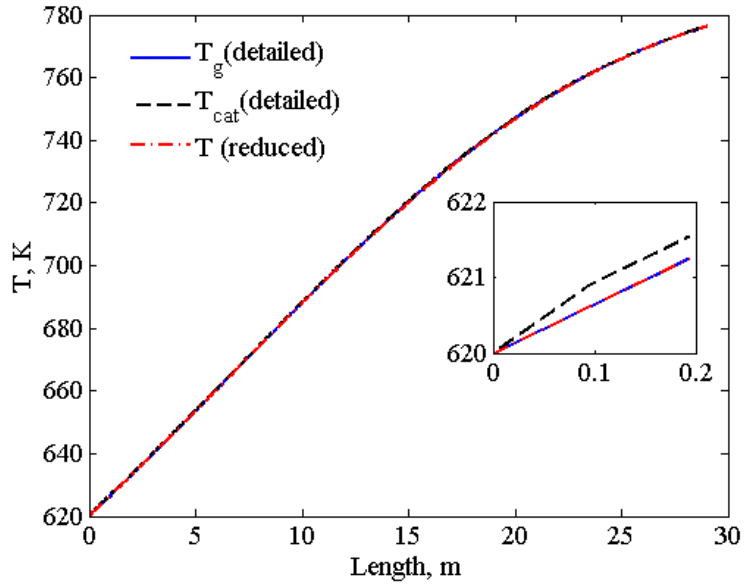

Figure 66. Temperature profile from detailed and reduced model for WGS reactor.

3.1.8 Comparison of scales with actual simulation

The scales can be thought of as maximum values which makes the dimensionless variable to take value at most of 1. These scales can be approximately calculated without performing any simulation, based on the inlet and parameter values. However if the detailed model is simulated then the exact values of these scales can be calculated based on the simulation results. In this section, we compare the approximate scales obtained in the previous section with the exact ones obtained through simulation.

In the steady state model of WGS, maximum gradient of a variable can be calculated by considering the dimensionless variables taking maximum value of 1 in the corresponding dimensionless equation. For

example, consider dimensionless species balance, Eqn. (110). The maximum concentration gradient can be found from this equation as follows,

$$1 \approx \frac{y_i C_{zs}}{C_{i,zs}} + \left(\frac{r_i}{u}\right)_s \frac{(1-\varepsilon)}{C_{i,zs}} \qquad \Rightarrow \qquad \left(\frac{dC_i}{dz}\right)_{\max} \approx y_i C_{zs} + \left(\frac{r_i}{u}\right)_s (1-\varepsilon) \tag{145}$$

In Eqn. (145), we see the maximum gradient depends on two terms $y_i C_{zs}$ and $\left(\frac{r_i}{u}\right)_s (1-\varepsilon)$. These two terms can be calculated either approximately as detailed in the previous sections or can be calculated from values of simulation.

The idea behind calculating scales approximately is to assume one of the terms in Eqn. (145) dominates in contributing to the maximum gradient. This is done by equating one of the corresponding dimensionless groups to 1. In a similar way one can calculate all other relevant scales by assuming one of the terms dominates in each of the corresponding dimensionless equation. The obtained scales are then substituted in the other dimensionless group to see whether they are of order 1 or much less than 1 or much greater than 1. If the value of the resulting dimensionless group is much less than 1, we can neglect this term resulting in model simplification, if it is of order 1, then it equally contributes to the gradient and hence needs to be retained. If the value is much greater than 1, then our assumption of selecting dominating dimensionless group is wrong and we need to equate this dimensionless group to 1 and test the other dimensionless groups.

The maximum value of a variable from simulation can be taken as scale for the corresponding variable. For example, maximum temperature change $(T_{\max} - T_{in})$ can be taken as the scale for temperature T_s. Then this scale can be substituted into the dimensionless group to identify which terms are important to be retained or not important to be neglected. For example consider again Eqn. (145). In this equation, the maximum value of y_i i.e. y_{in} can be substituted and the maximum value of total concentration gradient can be calculated from total balance equation and substituted, maximum of ratio $\left(\frac{r_i}{u}\right)$ from simulation can be substituted in the second term. Then this will give the maximum value of the concentration gradient. Based on the percentage of contribution of each term, one can decide on retaining or neglecting the terms.

$$\left(\frac{dC_i}{dz}\right)_{\max} \approx y_{i,in} C_{zs} + \left(\frac{r_i}{u}\right)_{\max} (1-\varepsilon) \tag{146}$$

Table 15 shows the scales for WGS reactor calculated from simulation and through scaling analysis and it is seen that they are close to each other.

Table 15. Exact values and approximate values of the scales

Variable scales	Actual values from simulation	Approximate value through scaling analysis
$C_{co,s}$	246.33	246.33
$C_{\cos,s}$	0.0963	0.0963
$r_{co,s}$	2.34	2.17

$r_{\cos,s}$	0.0053	0.0049
u_s	0.2817	0.296
T_s	156.26	185.79
P_s	2.31×10^5	2.94×10^5

In Table 16, we show the dimensionless equation of WGS reactor in the limit of dimensionless variables taking the value of 1. This results in a simple algebraic equation containing the maximum values. In values under simulation, each value represents the actual value that is obtained through simulation. For example, in the first equation, 9.024 represents the maximum gradient of C_{co}, 2.79 represents maximum value of $y_{co}C_{zs}$ and 6.33 represents the maximum value of $\left(\frac{r_{co}}{u}\right)_s(1-\varepsilon)$. In the values under scaling analysis, values on the right hand side of the equation (2.54 and 6.23) represent the one that obtained by substitution of appropriate scales. It is seen that all the values of the equation obtained from simulation and from scaling analysis are again close to each other. Table 15 and Table 16 confirm that reduced order model obtained from scaling analysis is based on realistic scales and hence will be a good approximate model.

Table 16. WGS reactor dimensionless equations are shown as algebraic equations with their corresponding values from simulation and scaling analysis

Equation	Values through simulation	Values through scaling analysis
$\left(\frac{dC_{co}}{dz}\right)_s \approx y_{co}C_{zs}+\left(\frac{r_{co}}{u}\right)_s(1-\varepsilon)$	$9.024\approx2.79+6.33$	$8.77=2.54+6.23$
$\left(\frac{dC_{\cos}}{dz}\right)_s \approx y_{\cos}C_{zs}+\left(\frac{r_{\cos}}{u}\right)_s(1-\varepsilon)$	$0.0158\approx11\times10^{-4}+0.0149$	$0.015=9.95\times10^{-4}+0.014$
$C_{zs}\approx-\left(\frac{C}{T}\right)_s T_{zs}+\left(\frac{C}{P}\right)_s P_{zs}$	$12.19\approx11.05+1.52$	$13.03=11.06+1.97$
$P_{zs}\approx\frac{\rho(u^2)_s}{d_{cat}}\left(\frac{1-\varepsilon}{\varepsilon^3}\right)1.75+\frac{u_s(1-\varepsilon)^2\mu150}{d_{cat}^2\varepsilon^3}$	$0.98\times10^4\approx0.92\times10^4+604.2$	$1.079\times10^4=1.015\times10^4+634.84$
$T_{zs}\approx\frac{(1-\varepsilon)K_{cat}T_{zzs}}{Cp_gG\varepsilon}+\frac{r_{wgs,s}\Delta H_{R,wgs}(1-\varepsilon)}{Cp_gG\varepsilon}+\frac{r_{hyd,s}\Delta H_{R,hyd}(1-\varepsilon)}{Cp_gG\varepsilon}$	$6.93\approx3.5\times10^{-4}+6.93+0.013$	$6.423=5.94\times10^{-4}+6.41+0.012$

3.1.9 Scaling of unsteady WGS model

Scaling can be done for unsteady model using the definitions introduced above. In addition to the scales for steady state model, we need to introduce one more scale which characterizes the unsteady nature of the model. We define this scale as 'velocity of dynamics of a variable'. Following is the unsteady model of WGS reactor,

Component balance:

$$\frac{\partial C_i}{\partial t} = -GR\frac{T_g}{P}\frac{\partial C_i}{\partial z} - C_i GR\left[\frac{1}{P}\frac{\partial T_g}{\partial z} - \frac{T_g}{P^2}\frac{\partial P}{\partial z}\right] + \left(r_{wgs,i} + r_{hyd,i}\right)\frac{1-\varepsilon}{\varepsilon} \tag{147}$$

Pressure drop equation:

$$\frac{dP}{dz} = \frac{\rho u^2}{d_{cat}}\left(\frac{1-\varepsilon}{\varepsilon^3}\right)\left(1.75 + \frac{150}{\mathrm{Re}}\right) \tag{148}$$

Gas phase energy balance:

$$\frac{\partial T_g}{\partial t} = \frac{1}{\rho_g Cp_g}\left[-Cp_g G\frac{\partial T_g}{\partial z} + \frac{h_f a_c}{\varepsilon}\left(T_{cat} - T_g\right)\right] \tag{149}$$

Catalyst phase energy balance:

$$\frac{\partial T_{cat}}{\partial t} = \frac{1}{\rho_{cat} Cp_{cat}}\left[K_{cat}\frac{\partial^2 T_{cat}}{\partial z^2} - \frac{h_f a_c}{1-\varepsilon}\left(T_{cat} - T_g\right) + r_{wgs}\Delta H_{R,wgs} + r_{hyd}\Delta H_{R,hyd}\right] \tag{150}$$

In the dimensionless model Eqn. (151) and (152), we have introduced the new scales $V_{c,s}$, $V_{T_{cat,s}}$ and $V_{T_{g,s}}$ which characterize the dynamics of concentration and temperature. Reaction scale for this can be the maximum of two inlet rates corresponding to two steady states before and after the introduction of dynamics or can be obtained by simulating the simplified version of the corresponding unsteady model.

Dimensionless species balance:

$$\frac{\varepsilon V_{c,s}}{u}\left(\frac{\partial C_i}{\partial t}\right)^{\varphi} = -\left(\frac{\partial C_i}{\partial z}\right)^{\varphi} - \frac{C_i}{T}\frac{T_{zs}}{C_{i,zs}}\left(\frac{\partial T_g}{\partial z}\right)^{\varphi} + \frac{C_i}{P}\frac{P_{zs}}{C_{i,zs}}\left(\frac{\partial P}{\partial z}\right)^{\varphi} + \frac{r_{i,s}\left(1-\varepsilon\right)}{uC_{i,zs}}\left(\frac{r_i}{u}\right)^{\varphi} \tag{151}$$

Dimensionless combined energy balance:

$$\begin{aligned}\frac{V_{T_{cat}s}\rho_{cat}Cp_{cat}(1-\varepsilon)}{Cp_g G\varepsilon}\left(\frac{\partial T_{cat}}{\partial t}\right)^{\varphi} &= \frac{K_{cat}(1-\varepsilon)T_{zzs}}{Cp_g G\varepsilon}\left(\frac{\partial^2 T_{cat}}{\partial z^2}\right)^{\varphi} - \frac{V_{T_g s}\rho_g}{G}\left(\frac{\partial T_g}{\partial t}\right)^{\varphi} - \left(\frac{\partial T_g}{\partial z}\right)^{\varphi} \\ &+ \frac{(1-\varepsilon)r_{wgs,s}\Delta H_{R,wgs}}{Cp_g G\varepsilon T_{zs}} r_{wgs}^{\varphi} + \frac{(1-\varepsilon)r_{hyd,s}\Delta H_{R,hyd}}{Cp_g G\varepsilon T_{zs}} r_{hyd}^{\varphi}\end{aligned} \tag{152}$$

The scales $V_{c,s}$, $V_{T_{cat,s}}$ and $V_{T_{g,s}}$ can be obtained by equating the dimensionless group multiplying the unsteady term to 1.

$$V_{c,s} = \frac{u_{in}}{\varepsilon} = 0.57\,; \qquad V_{T_{cat}s} = \frac{Cp_g G\varepsilon}{\rho_{cat} Cp_{cat}(1-\varepsilon)} = 0.023\,; \qquad V_{T_g s} = \frac{G\varepsilon}{\rho_g} = 29.62 \qquad (153)$$

Based on the values of the scales, dynamics of gas phase temperature is faster compared to catalyst temperature. But from π_3 and π_4, it is seen that $T_g = T_{cat}$, this means that dynamics of gas phase temperature is limited by the catalyst temperature dynamics. On comparing the velocity of dynamics of temperature with that of concentration, one can observe that concentration dynamics is about 25 times faster. This implies we can safely assume the concentration variation to be quasi steady. We can remodel the energy balance by considering the both catalyst and gas phase temperature to be equal and its dynamics is governed by that of catalyst temperature.

$$\frac{\partial T}{\partial t} = \frac{\varepsilon}{\left(\varepsilon\rho_g Cp_g + (1-\varepsilon)\rho_{cat} Cp_{cat}\right)}\left(-GCp_g \frac{\partial T}{\partial z} + \left(\frac{1-\varepsilon}{\varepsilon}\right) r_{wgs}\Delta H_{R,wgs}\right) \qquad (154)$$

From scaling analysis, we see that the dynamics of detailed of model of WGS reactor for the given parameter and inlet conditions is governed mainly by temperature dynamics. The coupled parabolic and hyperbolic PDE model becomes only hyperbolic PDE model which can be further simplified using recently developed model reduction techniques through method of characteristics. The computational load of simulating this model is about 40 seconds, which is about 75% reduction compared to the corresponding detailed model. Table 17 shows the summary of relevant properties for comparison between the detailed and reduced model. Figure 67 shows the dynamic response of outlet temperature for a step change in inlet temperature from 620 to 640 K.

Table 17. Summary of detailed and reduced order model

Properties	Detailed model	Reduced model
No. of PDEs	8	1
No. of ODEs	1	3
No. of algebraic equations	0	4
Types of problem solved	IVP & BVP	Only IVP
Steady state simulation time, sec	96	1
Dynamic simulation time, sec	130	40
Further order reduction can be achieved by	POD+MOC	MOC

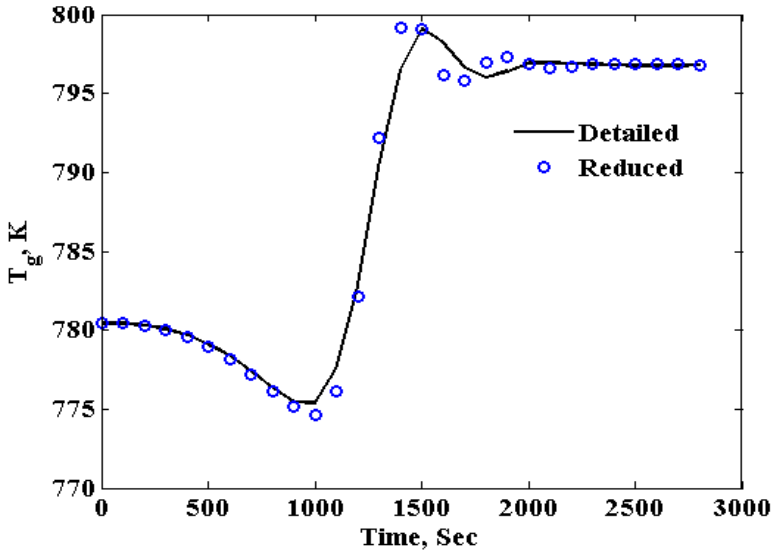

Figure 67. Dynamic response of outlet gas temperature for a step up of 20 degrees in the inlet gas temperature from detailed and reduced order model.

3.2 Method of Characteristics

Model reduction using method of characteristics is a recently developed technique to reduce the model described by hyperbolic PDE.[163,164] This method has been applied to a model consisting of hyperbolic PDEs like fixed bed reactor and plug flow reactor. Here, we can employ this technique to the hyperbolic PDE model of WGS reactor obtained from scaling analysis.

Method of characteristics is a method which converts partial differential equations to a set of ordinary differential equations. This is possible by finding a relation between two independent variables (z,t) and these results in equations having single independent variable (ODEs). The relation between the two independent variables is given by the equation of the lines called characteristic lines in $(z-t)$ plane. The resulting ODEs for the dependent variables are solved along these characteristic lines. The accuracy of the solution obtained from MOC depends on the density of characteristic lines in the solution surface.[163,164]

Consider the following equation which is similar to the reduced order model of WGS reactor:

$$\lim_{\alpha\to 0} \alpha \frac{\partial \phi_1}{\partial t} = -\psi_1 \frac{\partial \phi_1}{\partial z} + F_1(\phi_1, \phi_2) \tag{155}$$

$$\frac{\partial \phi_2}{\partial t} = -\psi_2 \frac{\partial \phi_2}{\partial z} + F_2(\phi_1, \phi_2) \tag{156}$$

Here $\phi_1 \in R^{n_1}$, $\phi_2 \in R^{n_2}$ and $t, z \in R$. In the above equation ϕ_1 corresponds to quasi steady variables such as concentration and pressure in the reduced WGS reactor model and ϕ_2 corresponds to temperature variable. The variable ϕ_1 is assumed to vary instantaneously and the variable ϕ_2 is assumed to vary with finite rate. In these equations as α tends to zero, equation for ϕ_1 is assumed to be quasi steady. The model exhibits characteristic lines with two slopes given by two different time scale behavior of the variables. One set of characteristic lines is assumed to be with a slope zero as α tends to zero and

the other set of characteristic lines have finite slope given by the value of $\frac{1}{\psi_2}$. The value of ψ_2 in the reduced WGS reactor model corresponds to $\frac{\varepsilon Cp_g G}{\varepsilon\rho_g Cp_g + (1-\varepsilon)\rho_{cat} Cp_{cat}}$.

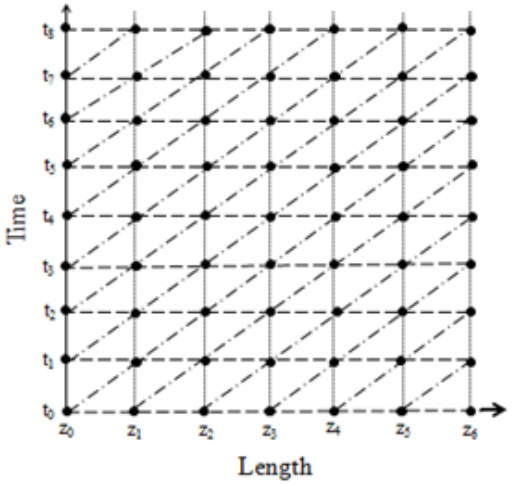

Figure 68. Schematic figure showing the characteristic lines in (*z*-*t*) plane.

The characteristic lines are schematically represented in the Figure 68 where the horizontal line with slope zero and slanting lines with finite slope represent these characteristic lines. These lines are represented by $t_a\left(z;z^0,t^0\right)$ and $t_b\left(z;z^0,t^0\right)$ where $\left(z^0,t^0\right)$ represents the starting point of these lines. For example, the points $\left(z_0,t_0\right)$, $\left(z_1,t_0\right)$, $\left(z_1,t_1\right)$ etc. as shown in Figure 68 represent these starting points.

Based on the model equations Eqn. (155) and (156), using the concept of method of characteristics, equations for the characteristic lines starting from the point $\left(z^0,t^0\right)$ are given by,

$$\frac{dt_a}{dz}\left(z;z^0,t^0\right)=\lim_{\alpha\to 0}\frac{\alpha}{\psi_1} \tag{157}$$

$$\frac{dt_b}{dz}\left(z;z^0,t^0\right)=\frac{1}{\psi_2} \tag{158}$$

Similarly, equations for the dependent variables are given by,

$$\frac{d\phi_1}{dz}\left(z,t_a\left(z;z^0,t^0\right)\right)=\frac{F_1\left(\phi_1,\phi_2\right)}{\psi_1} \tag{159}$$

$$\frac{d\phi_2}{dz}\left(z,t_b\left(z;z^0,t^0\right)\right)=\frac{F_2\left(\phi_1,\phi_2\right)}{\psi_2} \tag{160}$$

The above equations represent the steady state model for ϕ_1 and ϕ_2 which is solved along respective characteristic lines and the solution of each of these equations requires information of simultaneous variation of both the variables ϕ_1 and ϕ_2. Since this information is only partially available, i.e. only ϕ_1 along $t_a\left(z;z^0,t^0\right)$ and only ϕ_2 along $t_b\left(z;z^0,t^0\right)$, some sort of approximation is needed. This is

addressed by an approximation where for the solution of one variable, the available information of the other variable in another characteristic line is approximated. The approximation involved is schematically shown in Figure 69. Arrows in the figure shows the direction of approximation.

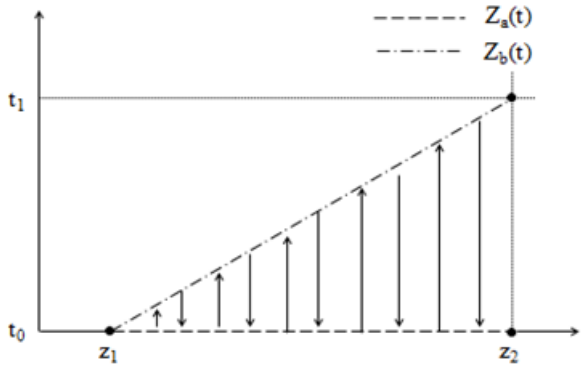

Figure 69. Schematic figure showing the approximation involved in the solution of dependent variable along characteristic lines.

Thus starting from the information at (z_0, t_0), Eqn. (159) and (160) are solved to find the value of ϕ_1 at (z_1, t_0) and ϕ_2 at (z_1, t_1). This procedure is repeated for all the points in a plane to obtain the solution of the corresponding hyperbolic PDE model. Figure 70 shows the dynamic response of outlet gas temperature from detailed and reduced order model from MOC. The computational load is further reduced to 6 seconds from 40 seconds taken by the model obtained from scaling analysis. Hence the original computational load of 130 seconds using detailed model is reduced to 6 seconds using reduced order model through scaling analysis and method of characteristics.

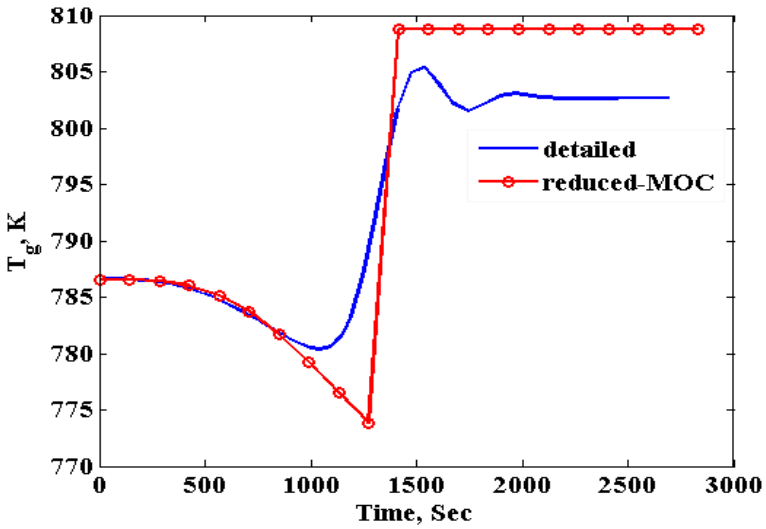

Figure 70. Dynamic response of outlet gas temperature for a step up of 20 degrees in the inlet gas temperature from detailed and reduced order model.

3.3 In-Situ Adaptive Tabulation

Sensor network design for water-gas shift reactor (WGSR) involves repeated simulation of its model equations inside extended Kalman filter (EKF). Direct numerical simulation of the current detailed model in EKF which is called by genetic algorithm during the design of sensor network is computationally intensive. Use of scaling analysis on the original detailed model of WGSR resulted in a simplified model with computational reduction by about 60%. To further reduce the computational burden, in situ adaptive tabulation (ISAT) is currently investigated.

ISAT is a tabulation method developed by Pope[165] and is used for the computationally efficient simulation of nonlinear equations through efficient storage and retrieval of solution data. This has been used for computational reduction of simulating detailed chemistry in reactive flow calculations (Pope 1997), for simulation of heterogeneous reaction[166,167], for computational reduction during online implementation of nonlinear model predictive control[168], for dynamic simulation of large scale flowsheet[169], etc.

ISAT is a storage and retrieval method, where solutions of DAE are stored in the form of a binary tree. This step is called 'Addition' during which the DAE model is numerically simulated (called as 'Direct integration (DI)'.) During this step, no computational advantage is realized and is done offline. Once sufficient data is added to the table or after sufficient time of addition of data to the table, one can retrieve the solution from the table during which higher computational efficiency can be realized.

The working of ISAT is represented in Figure 71. The left hand side figure shows the normal numerical integration to find the solution and this direct integration is done as many times as the model is called during sensor network design. The right hand side figure shows similar direct integration along with 'retrieval' of the stored solution from the ISAT table. In this case, the number of times the direct integration is performed will be less and is dependent on the density of the data in the table. Hence using ISAT for sensor network design will result in higher computational efficiency.

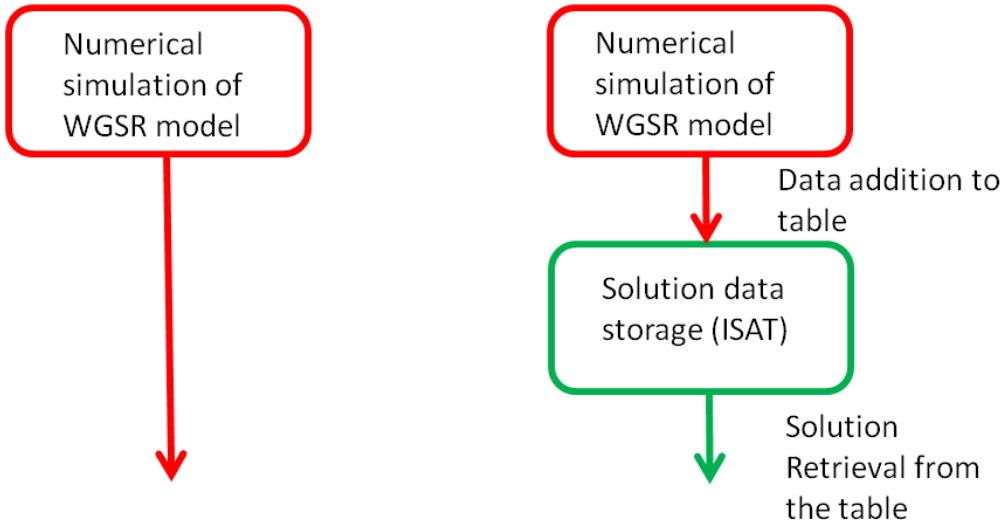

Figure 71. Concept of direct integration and ISAT when the model is solved several times.

3.3.1 Algorithm

The ISAT algorithm is explained by the following simple 2-state problem as given below. In this we consider a 2-state problem with an objective of solving the equations several times for different initial conditions.

$$\frac{d\phi_1}{dt} = f_1(\phi_1, \phi_2) \quad ; \quad \phi_1(t = t_0) = \phi_{10} \tag{161}$$

$$\frac{d\phi_2}{dt} = f_2(\phi_1, \phi_2) \; ; \quad \phi_2(t = t_0) = \phi_{20} \tag{162}$$

One way to accomplish the above objective is numerically integrate the Eqn. (161) and (162) for each of the initial conditions which would be computationally intensive. The other way would be to use storage and retrieval method such as ISAT, which is explained below. ISAT algorithm typically involves three main steps:

3.3.1.1 Addition

In this step, solution data is added to the table. In ISAT, this data is called a record which holds four main pieces of information

- Initial condition or input and for the 2-state problem, this corresponds to $s_0 = \begin{bmatrix} \phi_{10} \\ \phi_{20} \end{bmatrix}$
- Final solution value or output at desired sampling instant Δt and this is given as $s_f = \begin{bmatrix} \phi_{1f} \\ \phi_{2f} \end{bmatrix}$
- Sensitivity matrix which holds the information about the sensitivity of output with respect to input. This is given by

$$A = \begin{bmatrix} \frac{\partial \phi_{1f}}{\partial \phi_{10}} & \frac{\partial \phi_{1f}}{\partial \phi_{20}} \\ \frac{\partial \phi_{2f}}{\partial \phi_{10}} & \frac{\partial \phi_{2f}}{\partial \phi_{20}} \end{bmatrix}$$

This sensitivity information matrix is used in the linear equation for the calculation of output for the inputs within the 'region of accuracy'. Due to this region of accuracy, ISAT requires only finite number of solution data points to be added to cover the whole of operating region. The nonlinear solution surface can be thought as approximated to be several 'linear' regions where following linear equation can be used.

$$s_{q,f}^{l} = s_f + A(s_{q,0} - s_0) = s_f + Ax \tag{163}$$

where x represents $(s_{q,0} - s_0)$. In the above equation , s_0 and s_f come from the added record to the ISAT table, $s_{q,0}$ is the new query point, which is within the region of accuracy of s_0. Thus one can see that for the points within the region of accuracy of added points in the table, one can calculate the output using the linear equation without resorting to computationally intensive nonlinear numerical integration.

- Ellipsoid of accuracy (EOA) or region of accuracy: As seen before, EOA is required, which defines a region around the added point in the table. One way to find this region is to define an accuracy ε for the solution from linear equation compared to actual solution from direct integration, i.e. $\varepsilon = s_{q.f} - s_{q,f}^{l}$. The region should be in such a way that it covers all the initial points $s_{q,0}$ whose final solution $s_{q,f}$ when found through linear equation will at most have error of ε.

In practice, to avoid complexity[165], only an estimate of this region is found initially. This estimate is improved during 'growth' phase where the region is expanded. This initial estimate is found as follows

Let us define the solution from 'constant approximation' for the solution of query point $s^0_{q,f} = s^c_{q,f} = s_f$. The error in solution between this constant approximation and the linear approximation is bounded to ε.

$$s^c_{q,f} - s^l_{q,f} \le \varepsilon \quad \Rightarrow Ax \le \varepsilon \tag{164}$$

Squaring the above equation by multiplying with the transpose, we get

$$x^T A^T Ax = \varepsilon^T \varepsilon \quad \Rightarrow \quad x^T Mx = \mathrm{E} \tag{165}$$

In Eqn. (165), M represent EOA. The major and minor axis of the ellipse is given by singular value of M.
Following figure represents the addition of this record in the solution space

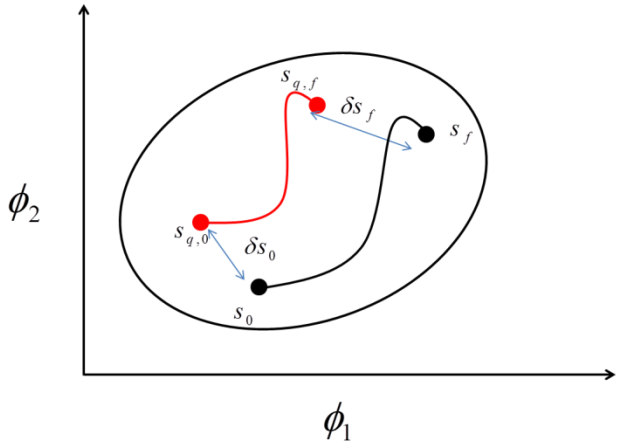

Figure 72. Addition of record in a solution space.

3.3.1.2 Growth

In this step, initial estimate of EOA is grown whenever the following condition is satisfied

$$x^T Mx > \mathrm{E} \text{ and } \left(s_{q.f} - s^l_{q,f}\right)^T \left(s_{q.f} - s^l_{q,f}\right) \le \mathrm{E} \tag{166}$$

This condition implies that whenever a new query point is outside EOA but the solution from the linear equation is within the specified accuracy in comparison with the solution from the actual numerical integration, then EOA is grown and this results in a modified M. The details of the growth step involves concepts from linear algebra and can be found in the literature. Following figure shows the growth of initial EOA to final grown EOA which encompasses the initial EOA and the query point.

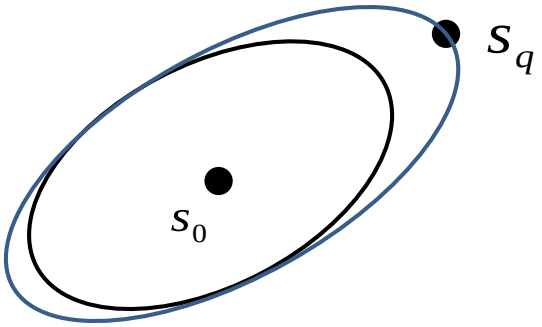

Figure 73. Growth of EOA where grow EOA encompasses the initial EOA and the query point.

3.3.1.3 Retrieval

This is the most important step for the computation reduction, where a linear equation is used for the retrieval of the solution. So whenever $x^T Mx \leq \mathrm{E}$ or $x^T M_{\mathrm{mod}ified} x \leq \mathrm{E}$, retrieval can be performed.

Once sufficient records are added to the table, for any new query point, the first step is to search for the closest record. Once the closest record is found and the condition $x^T Mx \leq \mathrm{E}$ or $x^T M_{\mathrm{mod}ified} x \leq \mathrm{E}$ is satisfied, retrieval is performed, otherwise either growth to modify EOA or new record corresponding to the query point is added to the table. Thus one can see that during initial phase there will be more addition and growth, which are computationally intensive as actual numerical integration is required. After sufficient data is added to the ISAT table, one can realize more retrieval leading to computational efficiency.

3.3.2 Binary tree structure

Binary tree structure is an efficient way to find the closest record which is necessary to determine addition, growth or retrieval from the ISAT table. During addition of record to the ISAT table, this binary tree structure is formed. This tree has node from which two braches come out and these branches either hold another node or record. The first node in the tree is called the root node, which can have child node. The child node can have further children nodes as one traverses the tree. This tree is schematically represented in the following Figure 74.

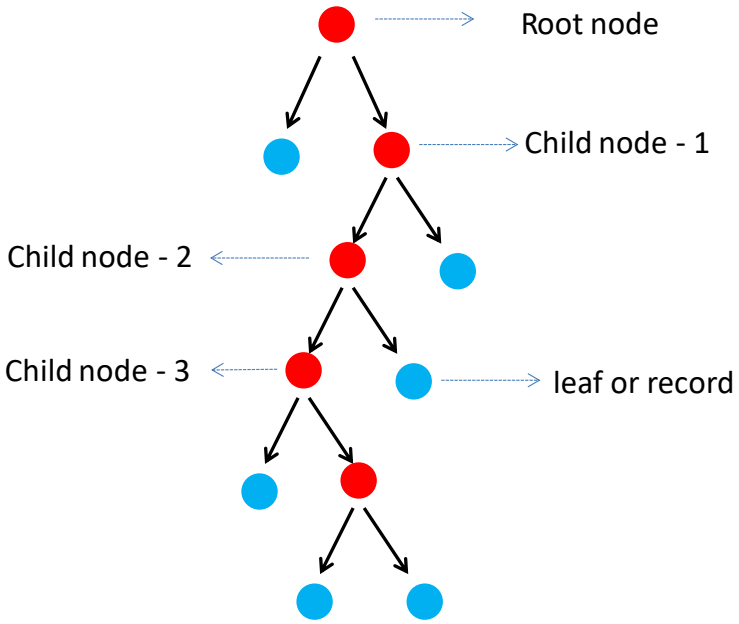

Figure 74. Binary tree showing nodes and leaves.

Each of the nodes in the binary tree holds information, which will help in deciding whether to take the left branch or right branch while searching for the closest record.

$$v = s_{0,1} - s_{0,2}\,;\ \alpha = v^T\left(\frac{s_{0,1} + s_{0,2}}{2}\right) \tag{167}$$

Considering two records (whose corresponding initial points are $s_{0,1}$ and $s_{0,2}$) are already present, when third point $s_{0,3}$ is encountered, one has to decide which among $s_{0,1}$ and $s_{0,2}$ is close to $s_{0,3}$. One way is sequentially check with each of the points in the table, which is time consuming. Another way is to use the binary tree structure as follows

$v^T s_{0,3} < \alpha \quad \Rightarrow$ take left branch, otherwise take right branch

Using binary tree structure takes only $O(\log_2(N))$ operations compared to $O(N)$ operations in a sequential search, thus improving the search time. Here, N represents the number of data points in the table. In a search space of this binary tree represented as in Figure 75, a 3 record addition is shown. In Figure 75, the dotted line represents the cutting plane given by $v^T\phi = \alpha$, where ϕ is the new query point.

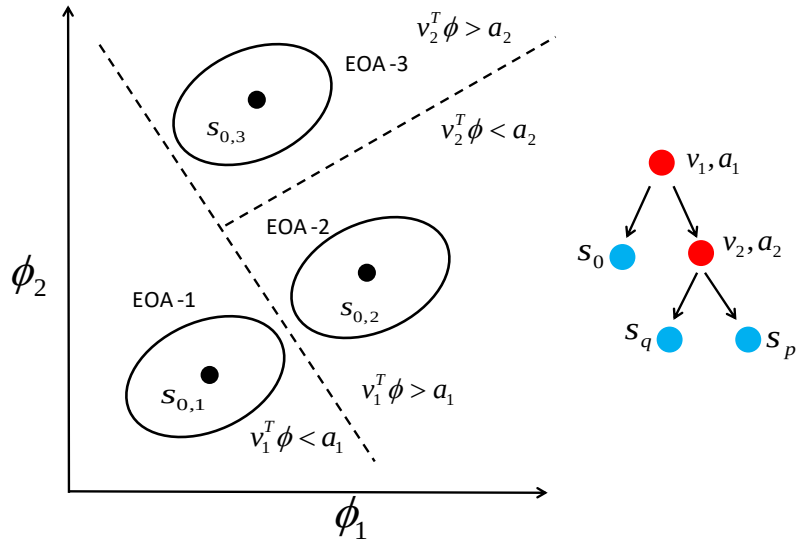

Figure 75. Binary tree shown in search space where represent a new query point . Corresponding binary tree structure is shown on the right hand side.

3.3.3 ISAT for WGSR model

ISAT algorithm is used in the dynamic simulation of simplified WGSR model obtained after scaling analysis. On the computational aspect, using ISAT, the computational load during retrieval of output takes only 0.0027 seconds compared 0.12 seconds for the corresponding direct numerical integration. This shows the significant benefit of using ISAT. Figure 76 shows the open loop dynamic simulation result from ISAT with only retrieval compared with direct integration of WGSR model.

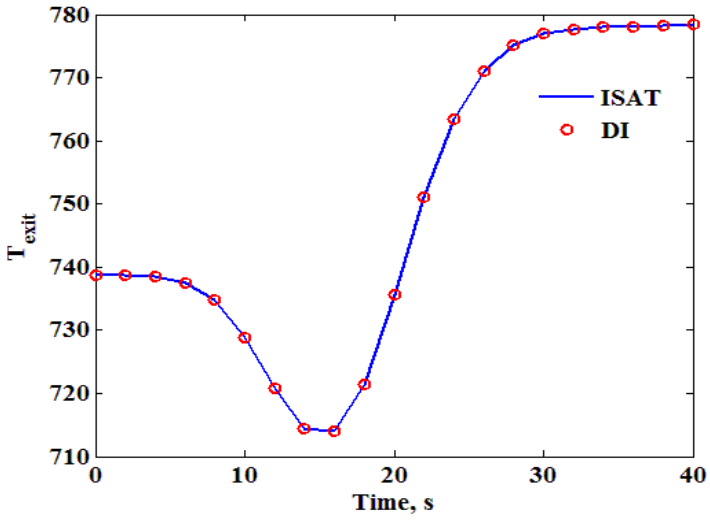

Figure 76. Dynamic simulation of WGSR model using ISAT with retrieval and direct integration (DI).

3.4 Conclusion

The simulation of mathematical model of WGS reactor is computationally expensive. In this study we have shown the use of scaling analysis and method of characteristics for computationally efficient simulation of WGS reactor model. In the scaling analysis we have used inlet reaction rate as the reaction

scale as opposed to using the rate based on maximum temperature and concentration suggested in the literature. Comparison of scales with the actual ones obtained from simulation, confirms the scales are realistic and the resulting reduced order model is reliable. The scaling analysis resulted in an approximate model involving hyperbolic PDEs which is further approximated using recently developed techniques involving method of characteristics. The simulation results shows that the obtained reduced order model is a good approximation for the detailed model with higher computationally efficiency.

Simulation of WGSR model is performed several times during sensor network design inside EKF. Currently, the computational load involved during the design is intensive. Usage of ISAT proves to be computationally efficient in such similar scenarios and hence the use of this algorithm is investigated. Initial results from application of ISAT to WGSR are encouraging and further work is needed to test its effectiveness inside EKF during sensor network design.

4 System-Level Sensor Placement

4.1 Introduction

Highly integrated and complex processes and advancements in control technologies for controlling these processes have increased the necessity of cost-effective automated diagnostic systems that can efficiently detect, identify and diagnose abnormalities and their origins as they propagate in the process. The diagnostic systems traditionally use underlying mathematical models and the on-line measurement from sensors specific to the process. As a fault enters a system, it affects the process variables, which deviate from normal operating conditions. Diagnostic systems compare the response of the process variables with respect to a reference model in the presence of faults in order to detect fault symptoms and monitor the performance of the process which depends crucially on the location of the sensors that capture the behavior of process variables. However, it is not economically viable and practically possible to measure all the process variables. Therefore, designing a cost-effective sensor network based on various criteria, e.g. observability, reliability, diagnosability, etc., poses a unique problem for process engineers. Several techniques have been reported in the literature, such as fault trees, cause-effect diagraphs, fuzzy logic-based methods, neural network, principal component analysis, qualitative trend analysis, support vector machines, hidden Markov model-based methods, and multivariate analysis techniques for sensor placement for fault diagnosis. For a broader discussion on available techniques, interested readers are referred to the review articles by Kramer and Mah[170], Bagajewicz[171], Frank et al.[172], Venkatasubramanian et al.[173]and Ould Bouamama et al.[174]

Generally, the diagnostic systems are categorized into quantitative model-based, qualitative model-based and process history based techniques[173]. The model-based techniques are centered around fundamental first-principal mathematical equations of the process, whereas the process history techniques rely on the analysis of long-time acquired process data.[173] Cause and effect models such as the directed graph (DG) and signed directed graphs (SDG) are popular qualitative model-based techniques that have been studied in the context of sensor placement for fault diagnosis (FD) by many researchers. The DG representation is one where the nodes (representing process variables and root causes) are connected by arcs. The SDG is a DG where a positive or negative sign is associated with each arc. In both the representations, the direction of the arcs are from 'cause' nodes to the 'effect' nodes.[173] Iri et al.[175] were first to use SDG representation for FD where they used SDG representation to identify the origin of failure for the available set of measurements. While the various fault observability and resolvability criteria for graph models used by the researchers are fundamentally analogous, e.g. diagnostic observability means at least one variable corresponding to the actual fault is estimated correctly[176,177], this study follows the definition by Raghuraj et al.[178] Fault observability means that at least one of the sensors in the network can observe the fault, and fault resolution means that the fault can be uniquely identified from other faults by the sensor network.

The problem of sensor placement (SP) was first tackled by Lambert[179] using a fault tree representation based on failure probabilities. Chang et al.[180] adopted the concept of observability and resolution and proposed a sensor placement method to minimize the number of sensors while ensuring the observability and highest resolution. Raghuraj et al.[178] incorporated the concept of fault observability and resolution into DG representation of the process and proposed an approach to identify the optimal location of the sensors. Bhushan and Rengaswamy[181] extended the work of Raghuraj et al.[178] to SDG analysis for FD and continued the work by taking into account additional quantitative information such as fault occurrence probabilities, sensor failure probabilities and sensor costs.[182] Bhushan and Rengaswamy[183] presented their framework by formulating the problem as a mixed integer linear programming (MILP) formulation by using the bipartite matrix for various fault diagnostics and reliability criteria. Bagajewicz et al.[184] formulated the problem as an MILP formulation for simultaneous process monitoring and fault detection and resolution. Recent efforts in cause-effect modellings are centered around incorporating useful concepts or adding more information that improve the FD by DG and SDG models. Kolluri and Bhushan[185] improved the FD capability by introducing the sensor network audit while minimizing unreliability of fault detection and ensuring fault observability and resolution. Bhushan et al.[186], Yang et al.[187] and Gao et al.[188] incorporated robustness, false alarm rates and qualitative trend analysis into SDG, respectively. Recently, Chen and Chang[189] enhanced the SDG algorithm by considering the sequence in which the faults propagates throughout the process. In their work, the problem is posed as a binary integer linear programming (BILP) formulation with sensor pairs as additional decision variables.

In almost all of the works using cause-effect models, the sensor network design is obtained by considering the qualitative simulation of the process; numerical solutions are used to verify the sensor network. However, the problem of spurious solutions, which refers to the solutions that are not realizable physically, inherent in qualitative models might reduce the efficacy of the sensor placements, particularly for complex processes. On the other hand, optimization solutions involving large-scale first-principles models for sensor placement might still be intractable. As a result, a compromise might be to directly utilize the numerical solution of the process models in the traditional sensor placement algorithms. We believe that this approach while keeping the sensor placement algorithms still tractable will also enhance the specificity of these algorithms. In this work, the SDG algorithm is enhanced by taking advantage of available numerical data and the relationship among the variables. We adapt the DG and SDG philosophy under the assumption that a numerical solution is available and propose magnitude ratio (MR) – ratio of the changes in a pair of process variables in response to a fault – to improve sensor placements for FD. The sensor placement problem is posed as a BILP formulation by using the bipartite matrix while ensuring observability and maximum possible resolution. Moreover, we generalize this idea of magnitude ratio to the realistic case of multiple process variables and multiple faults. We also study the fault evolution sequence (FES) – sequence in which a pair of sensor variables deviate from their nominal values in response to a fault - for improvements in the sensor placements for FD.

4.2 Sensor Placement Approach

To facilitate the use of MR and FES information in a SP algorithm, a set of artificial sensors, which correspond to pair-wise sensors from the original list of sensors are defined. In MR algorithm, artificial sensors represent the magnitude ratio of the corresponding pairs; and in FES algorithm, artificial sensors represent the sequence in which the corresponding pairs respond to the faults as the faults propagate in the system. We believe these enhancements not only improve the capability of the SP algorithms, but they can be viewed as independent components of a more general and complex SP problem that is decomposed into simple, yet efficient components.

Theoretically, the SP problem can be thought of as an optimization problem that requires minimization of the cost of the sensor network while satisfying the underlying mathematical equations and constrained to some fault diagnosis performance metrics. However, the major drawbacks to this theoretical view are: (*i*) solving such minimization problems for large complex systems is

computationally expensive, (*ii*) the underlying mathematical equations must be embedded within the optimizer and might require solution to a mixed-integer non-linear programming problem, (*iii*) it is in general non-obvious and difficult to define fault diagnosis performance metrics, and (*iv*) finally, simple engineering interpretation of the results might be difficult. We believe that one way to resolve these drawbacks is to decompose the underlying mathematical model into smaller and simpler interacting building blocks of information such as DG, SDG, FES and MR. By doing this, the resultant optimization problem can be solved easily as the underlying complex mathematical equations are removed from the optimizer. The complexity of optimization problem can be reduced to solving an integer linear programming problem. Further, the sensor placement results can be easily interpreted. Moreover, further improvements can be achieved by adding more information components to the model description. One such example could be qualitative trends or "signatures" that faults leave in the measured variables.

Another interpretation of this approach is that the sensor placement problem is simplified and efficiently solved through the use of appropriate features. The DG and SDG develop qualitative features, whereas FES is a purely temporal feature. Clearly, none of these are quantitative features. The MR is probably the simplest quantitative feature that one could include in the sensor placement algorithm; this has not been attempted before. We will show that the inclusion of this feature can help in both better resolvability and also in deriving more cost-effective sensor placements with the same level of performance.

4.3 SDG and FES Algorithms in the Presence of Numerical Simulations

In a process system, a change in one variable can cause one or more variables to change significantly. These cause-effect (CE) relations among the variables are very useful for diagnosing faults in the system. The optimum number and locations of sensors for diagnosis of a process can be identified through an algorithmic approach when process simulation is available. Such an approach is detailed next. First, the total number of faults (*M*) that one is interested in diagnosing is chosen. Then under the assumption of occurrence of one fault at a time, fault simulations are performed. Next, the candidate sensor locations (*N*) are chosen. Fault sets - which are a set of all the sensors that respond to the occurrence of a fault - are generated. Due to large differences in the magnitude and direction of change of the process variables in response to the occurrence of a fault, it is important to use a threshold value for each process variable while developing the fault sets. A variable should be included in a fault set whenever that process variable deviates beyond the threshold limit. The extent of deviation in a particular process variable depends on its actual operating value, type, operating condition, noise and disturbances. For simplicity, we have considered the threshold limit on the process variables as ±2σ variation of the sensor that measures the variable where σ is the standard deviation, e.g. 2 °F for temperature sensors.[190] If the variable changes from its nominal value beyond the ±2σ of the sensor that measures the variable, the variable is assumed to be changed from its nominal value.

All the faults are introduced at the same operating condition. No disturbance is introduced into the system during fault simulations. In DG, if a variable changes beyond its operating limit, a "1" is assigned, otherwise "0" is assigned, i.e. $R_{DG} \in \{0,1\}$. This operation returns a row vector for each fault with the dimension of $1 \times N$ and performing this operation for M faults will return matrix A^{DG} with the dimension of $M \times N$. In SDG, "1" is assigned if the variable changes beyond the upper limit and "-1" if it changes beyond the lower limit. If the variable stays within its limits, "0" is assigned. Note that the deviations are based on the incipient response of the process, thus, if a variable response changes during the course of the fault evolution, e.g. "1" then after some time "-1", only the initial response is considered, i.e. "1". Therefore, $R_{SDG} \in \{-1,0,1\}$. Considering all the faults, the matrix A^{SDG} of dimension $M \times N$ is obtained. The constraint matrix is constructed by augmenting the observability (A^{obs}) and resolution matrices (A^{res}), $A = \begin{bmatrix} A^{obs} \\ A^{res} \end{bmatrix}$. For observability, since only observing the fault is required and not the direction, $A^{obs} = A^{DG}$. For resolution, symmetric difference sets of the form $A_{ij}^{res} = A_i^{SDG} \cup A_j^{SDG} - A_i^{SDG} \cap A_j^{SDG}$ for each

pair of faults results in matrix A^{res} with the dimension ${}^{M}C_2 \times N$.[182,183,191] However, it is possible that some of the faults may produce deviation in the same direction for the same set of variables. In that case, the corresponding rows in the observability matrix are the same. If q rows are same in the observability matrix, the resolution matrix will have ${}^{q}C_2$ number of rows with zero elements. Therefore, those faults cannot be resolved.

A binary integer programming problem for sensor placement is formulated for minimizing the sensor cost subjected to fault observability and resolution considering all the process variables as decision variables. A binary decision variable is assigned to each process variable; if the decision variable takes a value of "1" then a sensor is placed to measure that variable and a "0" value implies that the variable is not measured. The constraint matrix, **A,** in the optimization problem represents the coefficient matrix obtained by DG and SDG. Since for observability and resolution at least one sensor must be picked by the optimizer, the *b* vector represents the constant vector of unity with $(M + {}^{M}C_2)$ rows.

$$min \sum_{j}^{N} w_j x_j \tag{168}$$

Subject to:

$$Ax^T \geq b$$

and x_j binary

w_j is weight for the sensor for j =1,…,N

where

$$A = \begin{bmatrix} 1 & 0 & 0 & 1 & \cdots & 1 \\ 0 & 0 & 1 & 1 & \cdots & 1 \\ \vdots & \vdots & \vdots & \vdots & \ddots & \vdots \\ 0 & 1 & 0 & 1 & \cdots & 1 \end{bmatrix}_{(M+{}^{M}C_2-{}^{q}C_2)\times N} \qquad b = \begin{bmatrix} 1 \\ 1 \\ \vdots \\ 1 \end{bmatrix}_{(M+{}^{M}C_2-{}^{q}C_2)\times 1}$$

The sign of the variables' response to a fault and the sequence in which the variables respond to a fault can be utilized to enhance the fault resolution. The FES algorithm, proposed by Chen and Chang[189], takes into account the sequence in which fault propagates through the process. This is the first work where this approach was proposed. In their work, sensors are paired together and assumed as a pseudo-sensor to obtain the sequence information. Since the work of Chen and Chang[189]is based on qualitative analysis without numerical simulations and the current work assumes that numerical solutions are available, an algorithmic approach for FES had to be developed. This is described below.

After a set of *M* faults are modeled individually, the sequence in which sensors capture the changes in the process variables for each fault is determined by the time elapsed from a reference time, which is set before any variable goes beyond the threshold limit. As soon as a variable goes beyond the threshold limit, it is added to the sequence. To pair the sensors, ${}^{N}C_2$ combinations are considered as the available pairs and a base sequence is assumed for each pair as $\{S_i,S_j\}$ where $j > i$ and S represents the corresponding sensor. The pairs used in this study are of the form of P_{ij} , where P_{ij} is the pseudo-sensor assigned to the sequence of sensors S_i and S_j. This will result in the generation of $\frac{N(N-1)}{2}$ pseudo-sensors as pairs. If the sequence of any pair (P_{ij}) is in the same sequence as the base pairs, "1" is assigned to that pair variable, if the pair is in the opposite sequence of the base pairs, "-1" is assigned and for all others "0" is assigned to the pair variables. However, it would not be possible in practice to determine the sequence

of pairs of variables if the time elapsed between the responses is short. Thus, a threshold time is defined to determine if responses can be arranged in the sequence. If the difference in response time of the pair is greater than the time threshold then it will take the values as described, otherwise, "0" is assigned to distinguish them from pairs that can be practically assumed in sequence. Therefore, $P \in \{-1,0,1\}$. This operation will return a matrix with dimension $M \times {}^{N}C_2$. Figure 77 shows the flowchart of FES algorithm in presence of numerical solution. In this flowchart, G is the measurement value, t is the time elapsed from a reference time until the sensor magnitude (measured value) goes beyond the threshold limit, T_i and T_j are the operational threshold limit, and T_t is the time threshold.

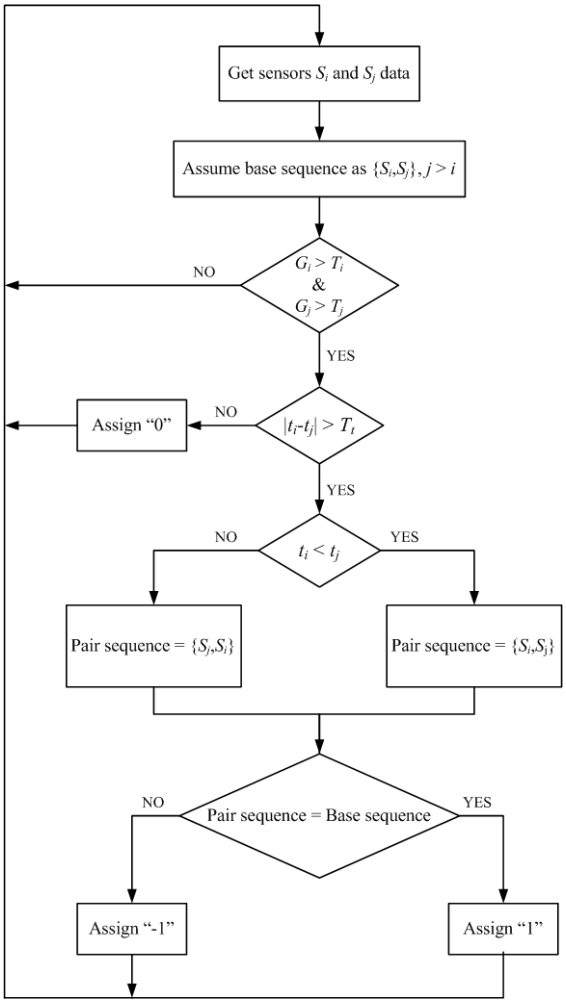

Figure 77. Flowchart of FES algorithm in presence of numerical solution

4.4 Sensor Placement Using Magnitude Ratio

Qualitative reasoning, in general, predominantly focuses on the behavior of single process variables and neglects relationship among process variables.[192] Other than the information available from single variables, partial information such as absolute value ranges, relative orders of magnitudes and approximate numerical values can be utilized.[192] Qualitative reasoning disregards such available information and practices reasoning at a very abstract level. Thus, the focus is on the signs exclusively and practical use of numerical values is excluded. Explicit use of numerical information in conjunction with qualitative reasoning makes such reasoning more applicable for engineering systems. Such reasoning has been reported in the work of Mavrovouniotis and Stephanopolous[192], and Raiman[193] for FD. In their

work, the order of magnitude reasoning is discussed through the definition of three relations among quantities: A is negligible in relation to B, A has the same sign and is close to B, and A has the same sign and order of magnitude as B. Although this approach uses quantitative information of the variables, it cannot relate numbers to order of magnitude relations; and order of magnitude reasoning contains no extra information when full numerical solutions are available.[192] Therefore, a somehow similar reasoning is proposed that take advantage of the available numerical data. The magnitude ratio can be thought as reasoning by A>>B or A≅B≅1, where, A and B represent the ratio of normalized magnitude of the sensors. To better understand this idea, consider the example in Table 18. SDG algorithm cannot distinguish between F_1 and F_2, but, we can examine the ratio of the sensors and see if we can distinguish between these faults. Figure 78 shows the ratio of $S_1$to S_2 for each fault. Note that the magnitude of each sensor is normalized by its steady state value. The magnitude ratio for fault F_1 is much higher than that of F_2's. This indicates that the sensor S_1 is much more affected than S_2, or vice versa, for F_1 compared to F_2. Therefore, this way we can distinguish between faults F_1 and F_2.

Table 18. SDG example

Fault	**Sensor**	
	S_1	S_2
F_1	1	-1
F_2	1	-1

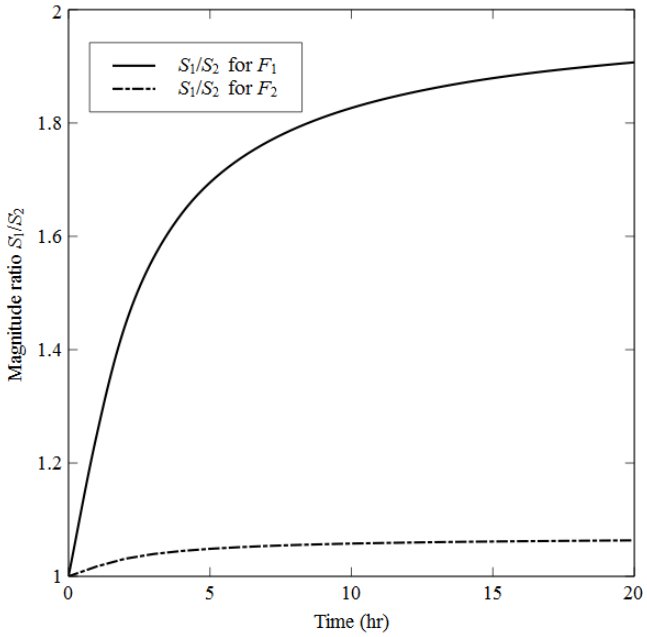

Figure 78. Magnitude ratio for example in Table 18

Generally, the extent that a variable is affected by a fault gives an insight into the propagation of the fault through the process. Although both quantitative and qualitative analysis shows that changes in variables can be utilized, as in DG and SDG, some variables are affected more by a fault while others are less affected. While this information is neglected in DG, SDG and FES, magnitude ratio can uncover such information from the relationship between pairs of variables. The magnitude ratio of a pair of sensors, S_i and S_j, is written as:

$$r_{ij} = \frac{G_i / G_{i,SS}}{G_j / G_{j,SS}} \tag{169}$$

where G_i and G_j are the magnitude of the sensors S_i and S_j and are normalized by their steady-state values $S_{i,SS}$ and $S_{j,SS}$, respectively. Note that both S_i and S_j must at least go beyond their threshold limit to be considered for further analysis. The magnitude ratio, r_{ij}, is initially at "1". After a fault is introduced to the system, R_{ij} changes from its steady state ("1"), and can change in either direction. Recall that the pair P_{ij} is assigned to the sensors S_i and S_j, here, if $r_{ij} \gg 1$, P_{ij} is assigned "1", if $r_{ij} \ll 1$, P_{ij} is assigned "-1" and P_{ij} is assigned "0" if otherwise. For this, a threshold is required to satisfy the inequalities. Therefore, the threshold value is tuned for maximum fault resolvability by a sensitivity analysis of the upper threshold value. Note that the lower threshold is calculated as the inverse of the upper threshold. If a variable is at "0" initially - like the error in a controller - P_{ij} is assigned "0". Eventually, $P \in \{-1,0,1\}$ and after simulation of M faults, the operation will return a matrix with dimension $M \times {}^{N}C_2$, same as in the FES algorithm. Figure 79 shows the flowchart of MR algorithm. In this flowchart, T_{MR} is the MR threshold value.

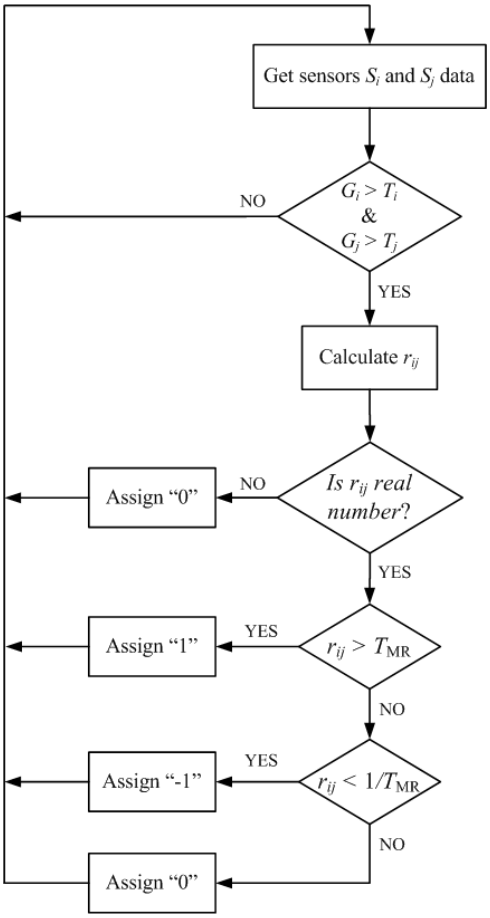

Figure 79. Flowchart of MR algorithm

4.5 Constraint matrix for FES and MR

Similar to the resolvability problem of SDG, ${}^{M}C_2$ pseudo-faults with corresponding symmetric differences of fault sets is constructed using the information provided by the P matrix. This results in an ${}^{M}C_2 \times {}^{N}C_2$ matrix that contains the fault resolution by FES or MR. The constraint matrix for SDG, before removing any zero rows, have $(M + {}^{M}C_2) \times N$ dimension with first M rows representing the observability and the following ${}^{M}C_2$ rows representing the fault resolution. To add the resolution by FES or MR, the constraint matrix is augmented by ${}^{N}C_2$ columns which consist of two blocks. An $M \times {}^{N}C_2$ block of zeros is generated for observability, since FES and MR do not contribute to fault observability. In addition, an ${}^{M}C_2 \times {}^{N}C_2$ block is generated by performing symmetric difference set on FES matrix (resulting in A^{FES} matrix) or MR matrix (resulting in A^{MR} matrix). The new augmented constraint matrix is treated as in SDG where rows that are the same and the rows that contain only zeros should be removed. Note that in order to solve the optimization problem, these rows must be removed from the constraint matrix A and the constant vector b.

After construction of the new augmented constraint matrix, the optimization problem has $N + {}^{N}C_2$ decision variables, including the sensors and pseudo-sensors. However, to ensure consistency between the sensors and corresponding pseudo-sensors, the following constraint should be added to the optimization problem (augmented constraint matrix) for each pseudo sensor:[189]

$$\begin{aligned}&(1-x_i)+(1-x_j)+x_{ij}\geq 1\\&(1-x_{ij})+\ x_i\geq 1\\&(1-x_{ij})+x_j\geq 1\end{aligned}\qquad(170)$$

where x_{ij} is the pseudo-sensor corresponding to the sensors x_i and x_j in the decision variables. Eqn. (170) implies that per each pair of sensors, three linear inequality constraints must be added to the optimization problem constraints; therefore, the constraint matrix and the constant vector must augment with the consistency matrix, A^{cons}, with the dimension of $(3\times{}^{N}C_2)\times(N+{}^{N}C_2)$ and a vector of unity with the dimension of $(3\times{}^{N}C_2)\times 1$, respectively.

4.6 Formulation Summary

4.6.1 Optimization Problem

The optimization problem in Eqn. (168) is summarized as:

$$min\sum_{j}^{N} w_j x_j \qquad(171)$$

Subject to:

$$Ax^T\geq b$$

x_j binary

where

$$A=\begin{bmatrix}A^{obs} & 0_{M\times {}^{N}C_2}\\ A^{res} & 0_{{}^{M}C_2\times {}^{N}C_2}\\ 0_{{}^{M}C_2\times N} & A^{*}\\ & A^{cons}\end{bmatrix}_{(M+{}^{M}C_2+3\times {}^{N}C_2-{}^{q}C_2)\times(N+{}^{N}C_2)}\qquad b=\begin{bmatrix}1\\1\\\vdots\\1\end{bmatrix}_{(M+{}^{M}C_2+3\times {}^{N}C_2-{}^{q}C_2)\times 1}$$

where $A^{*}=A^{FES}$ for FES algorithm and $A^{*}=A^{MR}$ for MR algorithm. Note that a joint FES and MR algorithm can be obtained by $A^{*}=A^{FES\,\&\,MR}=\ A^{FES}\cup A^{MR}$.

4.6.2 Solution Approach

The sensor network design is posed as a BILP and can be solved by a number of commercially available optimization software. In this work, the optimization problem is formulated in MATLAB and the solution is obtained by the CPLEX optimization toolbox integrated in MATLAB.

4.7 Network Decomposition

As mentioned before, using the qualitative approach in presence of numerical solution reduces the complexity of optimization problem into solving an integer linear programming problem. However, complexity still exists with respect to the processing of the signed directed graph, especially as the size of

the system increases. One of the main issues is the memory limitations of computers for storage and computations. A computing machine is not only limited by the amount of information it can store for a particular problem, for a simple example, the augmented FES-MR matrix or constraint matrix, it is also limited by the amount of memory available for computations, resulting in slower computations due to low availability of memory. Therefore, diagraph-based causal models are vulnerable to such complexities though the problem is defined as a linear optimization problem.

Generally, in graph theory, a system can be depicted by a set of vertices and edges that connect the vertices. Vertices can represent the system variables or any aspect of a system, for example sources and clients in a wireless network or variables in diagraph-based fault detection, while the edges represent the relationship between the vertices. Mathematical efforts in graph theory have been made to reduce the computational complexities by reducing the problem into smaller components, through "graph partitioning" techniques. In graph partitioning, one tries to decompose the graph into smaller sub-systems with specific properties. However, very little work exists in graph partitioning that considers fault detection as an objective. Almost all of the works in the area of graph partitioning focus solely on minimizing the number of edges between the sub-systems. However, it is not intuitive for one to think that the same reasoning holds while considering fault detection. Although, it is intuitive that the solution to the decomposed graph can be sub-optimal compared to the solution to the original graph, this compromise might be acceptable due to the complexity reduction achieved by decomposition.

The graph partitioning problem is classified as a NP-hard (non-deterministic polynomial-time hard) problem. In computational complexity theory, NP-hard problems are a class of problems, whose solutions cannot be found in polynomial time and hence are generally obtained by heuristic algorithms. Developing graph partitioning algorithms that fits the fault detection context might be complex. However, an initial understanding of the impact of graph partitioning on different aspects of fault detection such as the trade-offs between the fault detection, optimality and computation speed can be developed through sensitivity analysis.

Since different systems have different properties with different possible decompositions, thus, the study includes a Monte Carlo simulation of a pool of random systems with similar properties and different decomposition. The random systems are constructed by a bottom-up design. In this approach, initially random sub-systems are generated; and the overall system is obtained by cross-connecting the sub-systems. Certain constraints on the overall system, such as total connectivity, are handled at the sub-system level which ensures the constraint satisfaction at overall level.

For simplicity, each random system represents a directed graph (DG). More complex systems can be achieved if the edges not only represent the direction but are also associated with real or integer quantities. Directed graph is the most widely used causal model, a popular technique in model-based analysis for fault detection. For simplicity, in this work, fault detection is performed by only considering the directed graph (DG) algorithm. In DG formulation for a process where vertices represent the variables and edges represent the relation between the variables, one tries to find a network of sensors with minimum cost that satisfies the fault detection constraints. Sensor placement is formulated as a binary integer linear programming problem constrained by the required fault detection and resolution. A thorough study of DG algorithm can be found in previous sections. It is worth mentioning that a major part of the DG analysis is to find the initial response table (IRT). The initial response table is a matrix of binary values that represents from each vertex what other vertices can be reached directly or indirectly. Using the IRT and the optimization constraints, fault detection and resolution matrices can be obtained. Therefore, IRT is critical to fault detection and must be consistent with the system of interest. While generating a random system, the IRT is obtained using the DG matrix that represents the system.

This section is organized as follows: In subsection 1, the method for generating the random systems is thoroughly explained. In subsection 2, fault detection in the presence of system decomposition is explained.

4.7.1 Method

4.7.1.1 Assumptions

As mentioned before, random system generation is performed in a bottom-up process where, first, sub-systems are generated and the overall system is obtained by cross-connecting the sub-systems. Generating random systems for fault detection requires some basic assumptions that must be met by the random systems.

1. Faults in the system are presented by independent nodes. Fault nodes are the only nodes that have no inward edge.
2. All the nodes must be connected to at least one other node.
3. There is no self-connection in the system.

A mathematical representation of a directed graph is through the use of a node adjacency matrix. Rows and columns of node adjacency matrix represent the vertices and each $(i,j)^{th}$ entry is assigned "1'' if there is a directed edge; and "0" otherwise. Figure 80 shows an example of the node adjacency matrix for the corresponding DG.

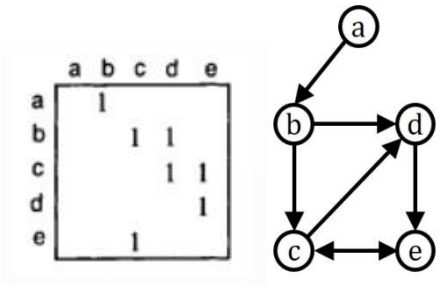

Figure 80. Representation of adjacency matrix

Generating random systems requires some parameters to be provided in advance. These parameters include:

a. Number of sub-systems (N_s):
   A scalar that represent the total number of sub-systems.
b. Number of nodes (N_n):
   A $1\times N_s$ vector where each array in the vector represents the number of nodes in each sub-system.
c. Number of edges (N_e):
   A $1\times N_s$ vector where each array in the vector represents the number of edges in each sub-system.
d. Number of cross-connection edges (N_{ce}):
   A $1\times N_s(N_s\text{-}1)/2$ vector of values where each array represents the number of edges between each pair of sub-systems.
e. Number of faults (N_f):
   A $1\times N_s$ vector where each array in the vector represents the number of faults in each sub-system.
f. Number of fault edges (N_{fe}):
   A $1\times N_f$ vector where each array in the vector represents the total number of output edges of the faults in each sub-system.

It should be mentioned that all the parameters must be positive integers and must follow the mentioned assumptions, for example, $N_{fe}\geq N_f$, otherwise, there will be at least a fault node without any edges.

4.7.1.2 Algorithm

In order to explain the algorithm, first, a logical reachability matrix must be defined. Each $(i,j)^{th}$ entry in the adjacency matrix shows the number of ways possible to go from i^{th} node to the j^{th} node with distance of one. Considering the squared matrix of adjacency matrix, each $(i,j)^{th}$ entry in the squared adjacency matrix shows the number of ways possible to go from i^{th} node to the j^{th} node with distance of two; and so on for higher powers of the adjacency matrix. The reachability matrix is defined as the sum of all powers of the adjacency matrix up to $N_n{}^{th}$ power. Each array in this special matrix shows the total number of ways to go from i^{th} to j^{th} node with any distance. Since we are only interested if there is any connection between two nodes by any distance, the reachability matrix is transformed into a logical form where the non-zero arrays in the reachability matrix are assigned "1". It should be noted that self-connections, if any, must be converted to zero for further analysis.

The algorithm follows these steps for each sub-system:

1. Initialize the adjacency matrix
2. Randomly pick N_e arrays in adjacency matrix and assign "1" (Self-connections excluded)
3. Check if constraints are satisfied
    a. All nodes are connected: Sum of each row of logical reachability matrix is equal to N_n-1
    b. All nodes have at least one input edge: Sum of each column of adjacency matrix is greater or equal to one
4. Randomly connect the faults
    a. For each fault, the number of output edges are determined randomly
    b. For each output edge of each fault, a node without input from the same fault is randomly determined

Steps 2 and 3 are repeated until a system that satisfies the constraints is achieved. After performing the algorithm for each sub-system, sub-systems are randomly cross-connected as per N_{ce} without overlapping edges. For each cross-connection, one node in each corresponding sub-systems are randomly chosen and the direction of the edge is chosen as random.

The main drawback of this algorithm is that finding appropriate sub-systems that satisfy the constraints gets harder for larger number of nodes and lower number of edges. Therefore, a second algorithm is introduced when a system is not found within a reasonable number of iterations. The algorithm is as follows:

1. Randomly choose two nodes from the pool of available nodes and connect them. Mark the node at the end of the directed edge as current node and place it in the pool of visited nodes
2. Define probability parameter β for each sub-system:
    a. With chance of β, connect the current node to a randomly chosen node from the pool of available nodes. Mark the chosen node as current node and place it in the pool of visited nodes
    b. Otherwise, randomly choose a node from the pool of visited nodes and connect it to a randomly chosen node from the pool of available nodes and place the second node in the pool of visited nodes

It should be noted that step 2 is performed until N_e number of connections are made. Other than the fact that the second algorithm is faster, another advantage of it lies in the choice of value for parameter β. Higher values of β result in systems analogous to recycle process systems while lower values result in systems analogous to spanning tree systems.

4.7.1.3 Initial Response Table calculation

After generating the random sub-systems with fault nodes and cross-connecting the sub-systems, the overall system is achieved. The total DG matrix that includes the fault nodes for the overall system can be obtained by augmenting the fault DG (FDG) matrices with augmented system DG matrices. As shown below, the total DG matrix contains four blocks. The zero blocks are due to the assumption that faults have no input edges. The FDG block is made by augmenting the fault adjacency matrices of all sub-

systems. Similarly, DG block is made by augmenting the adjacency matrix of all sub-systems' DG. After calculating the logical reachability matrix of the total DG matrix, the FDG block of the logical reachability matrix will represent the IRT.

$$\begin{array}{c} \\ F \\ X \end{array} \begin{array}{c} \begin{array}{cc} F & X \end{array} \\ \begin{bmatrix} [0] & \text{FDG} \\ [0] & \text{DG} \end{bmatrix} \end{array}$$

4.7.2 Fault detection for decomposed system

While performing fault detection for each sub-system, one can either ignore that there are faults outside the sub-system (in other sub-systems) and assume they cannot affect the sub-system through the inward cross-connection, or, we can find a simple way to mitigate the effects and bring these faults into consideration. Clearly, the former will cause some information loss due to the naïve approximation, while the latter add more information to the system and may improve fault detection. The latter can be realized by simply assuming that all the inward cross-connections as a pseudo-fault inside the sub-system. This way all the inward cross-connections are assumed to be coming from a single node marked as a pseudo-fault. While one may argue that each inward cross-connection can act as a single pseudo-fault and add more information to the system, the drawback to this assumption is that large number of pseudo-faults can further complicate the fault detection and may compromise the speed for very little additional information. Therefore, the approach taken in this work is based on assuming all the inward cross-connections from other sub-systems as coming from a single pseudo-fault. The pseudo-fault is then added to the system as a node and considered in fault detection. Figure 81 shows an example of how the pseudo-fault is considered in a sub-system. In this example, red nodes indicate the faults while black nodes indicate the graph nodes. The effect of faults F1 and F2 in sub-system 1 are passed to sub-system 2 through the dashed edges, which represent the cross-connection between the sub-systems. The cross-connections in Figure 81 are then replaced by a pseudo-fault (yellow node) and the pseudo-fault is connected to the same nodes, marked as SP1 and SP2 in sub-system 2.

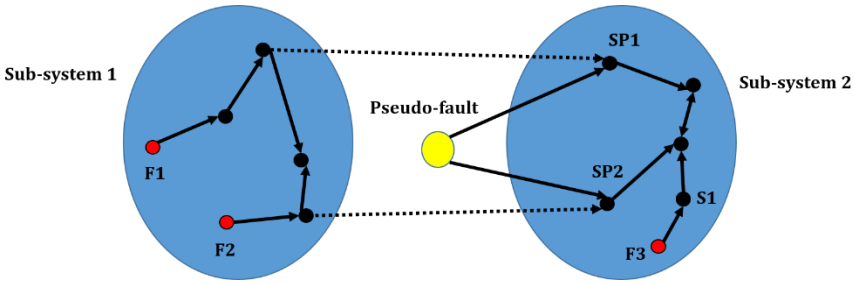

Figure 81. Pseudo-fault representation for two sub-systems.

The main issues that arise in the pseudo-fault approach are the existence of multiple solutions in fault detection and the information loss due to decomposition. As an example, consider performing fault detection for sub-system 2, where we want to resolve between fault F3 and the pseudo-fault. The multiple solutions which are available for fault resolution are S1, SP1 and SP2 nodes. Assume the cost of placing sensors on all the nodes are the same, thus, placing a sensor on each of the nodes can be the solution to our sensor placement problem. However, due to information loss by decomposition, each solution can have different impact on the fault detection of overall system. If S1 is picked as the solution and implemented on the overall system, fault pairs (F3,F1) and (F3,F2) can be resolved. If SP1 is picked as the solution and implemented on the overall system, although fault pair (F3,F1) can be resolved, fault pair (F3,F2) cannot be resolved. Similarly, if SP2 is picked as the solution and implemented on the overall system, although fault pair (F3,F2) can be resolved, fault pair (F3,F1) cannot be resolved. Therefore,

since no extra information is available about the overall system, multiple solutions with different overall fault resolution may exist. One way to overcome this issue is to pick the nodes affected by the faults but not the pseudo fault, for example, S1 in Figure 81. This ensures total resolution from the faults out of the sub-system.

In the original fault detection method, fault resolution is based on the set difference of the nodes affected by the fault that are being resolved. If A is a set of nodes affected by fault f_1 and B is set of nodes affected by f_2, then, set difference S is defined as: $S = A \cup B - A \cap B$. In the new approach, when resolving between a fault (as set A) and the pseudo-fault (as set B), symmetric difference is replaced by $S_{new} = A - A \cap B$. This ensures that the fault is resolved from all the other faults outside the sub-system. However, there may be cases when resolving between a fault and the pseudo-fault where $S_{new} = \emptyset$ and $S \neq \emptyset$. In this case, S contains at least a solution and can be used over S_{new}.

5 Distributed Sensor Placement

5.1 State Estimation Development

5.1.1 Introduction

Differential-algebraic equation (DAE) systems often arise in modeling of physical and mechanical systems, such as robotics, chemical processes, electrical circuits and so on. DAE systems which are also called descriptor systems, can be viewed as ordinary differential equations (ODEs) that are constrained by the algebraic equations. In general, both the differential and algebraic equations can be linear or nonlinear. Although the dynamic behavior is modeled by ODEs, the presence of algebraic constraints results in some complications while solving the DAE systems. State estimation of linear and nonlinear ODEs have been studied thoroughly in literature and several techniques are present for state estimation including but not limited to Kalman filter (KF), extended Kalman filter (EKF) Unscented Kalman filter (UKF), Ensemble Kalman filter(EnKF), particle filters and etc.[197] The Kalman filter is an estimator of linear stochastic ODEs where the term “stochastic” represents the presence of process and measurement noises. Kalman filter is optimal when the noise is assumed as Gaussian white noise. Although the Kalman filter is optimal for linear systems, an extension of KF is sub-optimal when applied to non-linear systems.[198] The idea of extended Kalman filter (EKF) is based on local linearization of the non-linear equations and application of the linear Kalman filter framework. At first glance, it seems that by converting the DAE to an implicit ODE, state estimation can be performed using the KF or EKF framework as it is done for implicit ODE systems. However, unlike ODE systems, there is a necessity for generation of consistent initial guesses that respect the algebraic constraints. Further, DAEs are characterized by the index of the system, which is the number of differentiations that are required to convert a DAE system into fully implicit ODEs. As a result, state estimation techniques for ODEs cannot be directly extended to DAE systems.[199]

The index of a DAE represents the difficulty in the numerical treatment of such systems. DAEs of index-zero and one are considered to be the easiest for numerical treatment compared to higher index systems. The systems considered in this work are all assumed to be index-1 DAEs.[200] A literature search indicates extensive work on applying KF to linear DAEs, see[201-206], though there is very little work on implementation of EKF on non-linear DAEs.[197,207]

For applying EKF to DAE systems, Becerra et al.[207] proposed a modified EKF for DAE systems. In their approach, the DAE is converted to implicit ODE and the non-linear equations are linearized locally, then, the Kalman filter is performed at each sampling time while the error covariance matrix is updated for differential states. A disadvantage of this approach is that the effect of prior algebraic state estimates and measurements from algebraic states are ignored and updated algebraic state estimates are obtained by solving the algebraic equations after updated differential state estimates are computed.[197] Further, measurements of the algebraic states cannot be directly included in this framework. To address these disadvantages, in our previous work, an approach was proposed that takes into consideration the effect of prior algebraic states and accommodates the measurements from the algebraic states in the framework.[197]

One of the difficulties in state estimation of DAEs is that derivative of white noise may show up in state estimates. However, derivative of white noise is not well-defined.[208] For linear systems, researchers have proposed different approaches to address this problem. For instance, Campbell[209] suggested the use of band limited noise filter and in turn compromised the optimality of the Kalman filter. Schon et al.[210] explained the transformation of the DAE into a state space form and the conditions under which the derivative of white noise in algebraic equations can be avoided in state-space form. Darouach et al.[202] avoided the presence of white noise derivative by decomposing the filtering problem into two subproblems: (i) computing the estimates and error covariance of differential states, and (ii) using them in computation of estimates and error covariance of algebraic states.

In almost all of the works that consider the EKF for non-linear DAEs, the algebraic equations are noise-free and the process noise is considered only in the differential equations. The reason is that when differentiating the algebraic equations to convert the DAE to an implicit ODE, white noise will be differentiated, if present in the algebraic equations. Therefore, algebraic equations must be certain for differentiation to be meaningful. However, in practice, algebraic equations are not always exact and they might themselves be uncertain equations. This is particularly true when simplifying correlations are used in the modeling framework. Moreover, when extra information such as exact state equality constraints are available for the system, current EKF formulations cannot handle such information. Thus, EKF must be modified to include such constraints. In this work, we address these issues by proposing a modification to the EKF to handle constrained DAEs of index-1 with uncertainties in both differential and algebraic equations.

In the proposed work, the error covariance matrix is written as a 4-block matrix with separate square blocks for differential and algebraic variables, respectively. Since the DAE is of index-1, the algebraic equations are written in terms of the differential variables and the error covariance in the corresponding covariance matrix are updated by linear or non-linear transformation of the error covariance of the differential equations. This avoids the differentiation of algebraic equations and makes the filter practical. The following sections are organized as follows. First, the currently available state estimation techniques for DAEs in the absence of uncertainties in algebraic variables are reviewed. Then, the EKF formulation is modified to account for exact equality constraints. We also discuss how this avoids the differentiation of algebraic equations. Finally, the performance of the proposed work on two examples, a simple example system and the system of interest, water gas shift reactor are described.

5.1.2 State estimation of DAE systems

5.1.2.1 Problem formulation

Consider the following stochastic nonlinear discrete-time DAE system with discrete measurements sampled at intervals of Δt

$$\begin{aligned} x_{k+1} &= x_k + \int_{k\,\Delta t}^{(k+1)\,\Delta t} f\big(x(t), z(t)\big)\, dt + \omega_{k+1} \\ g(x_{k+1}, z_{k+1}) &= 0 \\ y_{k+1} &= h(x_{k+1}, z_{k+1}) + \nu_{k+1} \\ \omega &\sim N(0, Q) \qquad \nu \sim N(0, R) \end{aligned} \tag{172}$$

where $x_{k+1} \in \mathbb{R}^{m\times 1}$ and $z_{k+1} \in \mathbb{R}^{p\times 1}$ are the differential and algebraic states at interval (k+1), respectively; and $Q \in \mathbb{R}^{m\times m}$ and $R \in \mathbb{R}^{p\times p}$ are known covariance matrices.

5.1.2.2 Propagation

Let $\hat{x}_{k|k}$ and $\hat{z}_{k|k}$ be the updated differential and algebraic states estimates at time $t = k\Delta t$ using the information available up to and including k^{th} measurement sample, respectively. The predicted states, $\hat{x}_{k+1|k}$ and $\hat{z}_{k+1|k}$, are obtained by integrating the DAE system in Eqn. (172). Let $P_{k|k}$ be the error

covariance matrix of updated estimates, the predicted error covariance, $P_{k+1|k}$, is obtained by first linearizing the nonlinear system in Eqn. (172) around the updated differential and algebraic states ($\hat{x}_{k|k}$ and $\hat{z}_{k|k}$) and second, differentiating the algebraic equations in Eqn. (172) to convert the DAE into a continuous implicit ODE. Therefore, augmenting the resulting system as:

$$\begin{bmatrix}\dot{x}\\ \dot{z}\end{bmatrix} = \begin{bmatrix} A & B \\ -D^{-1}CA & -D^{-1}CB \end{bmatrix}\begin{bmatrix}x\\ z\end{bmatrix} = A^{aug}x^{aug} \quad \textbf{(}173\text{)}$$

where superscript *'aug'* represents the augmented form (i.e. $x^{aug} = \begin{bmatrix}x\\ z\end{bmatrix}$) and the Jacobian matrix around the $\hat{x}_{k|k}$ is evaluated as

$$J = \begin{bmatrix} A & B \\ C & D \end{bmatrix} = \begin{bmatrix} \frac{\partial f}{\partial x} & \frac{\partial f}{\partial z} \\ \frac{\partial g}{\partial x} & \frac{\partial g}{\partial z} \end{bmatrix}_{\hat{x}_{k|k},\hat{z}_{k|k}} \quad (174)$$

The transition matrix, calculated as $\Phi = \exp(J\Delta t)$, is used to obtain the predicted error covariance by

$$P_{k+1|k} = \phi P_{k|k}\phi^T + \Gamma Q_{k+1}\Gamma^T \quad (175)$$

where

$$\Gamma = \begin{bmatrix} I \\ -D^{-1}C \end{bmatrix} \quad (176)$$

5.1.2.3 Correction

In the update step of EKF, the augmented states are updated as

$$\hat{x}^{aug}_{k+1|k+1} = \hat{x}^{aug}_{k+1|k} + K_{k+1}\left(y_{k+1} - h\left(\hat{x}^{aug}_{k+1|k}\right)\right) \quad (177)$$

Only the differential part of the estimated augmented states are retained and the algebraic part is obtained by solving

$$g\left(\hat{x}_{k+1|k+1}, \hat{z}_{k+1|k+1}\right) = 0 \quad (178)$$

The updated covariance matrix is obtained by

$$P_{k+1|k+1} = (I - K_{k+1}H_{k+1})P_{k+1|k} \quad (179)$$

where in the update step, H_{k+1} is the linearized measurement model evaluated at $\hat{x}^{aug}_{k+1|k}$ and K_{k+1} is the Kalman gain matrix calculated by

$$\begin{aligned} K_{k+1} &= P_{k+1|k}H^T_{k+1}\left(H_{k+1}P_{k+1|k}H_{k+1} + R_{k+1}\right)^{-1} \\ &= \left({P^a_{k+1|k}}^{-1} + C^T R^{-1} C\right)^{-1} C^T R^{-1} \end{aligned} \quad (180)$$

Note that these equations are written for augmented system except for Eqn. (178) where the algebraic part is only calculated.

5.1.3 Equality constrained state estimation of uncertain nonlinear DAEs

In practice, not all the algebraic equations that describe the behavior of a physical system are exact and additional information about the dynamic system may be available. If the algebraic equations are not exact, uncertainties must be considered in these equations to more closely represent the real behavior. Therefore, one could model uncertainties in the algebraic equations also as Gaussian random variables with known statistical properties. Moreover, if additional information about the system represents an equality constraint, which the system variables must satisfy, then this information must be incorporated into the estimation framework. To the best of our knowledge no work exists for estimation of such systems in the literature. In this section, we propose enhancements to the EKF approach for DAE systems to address this class of problems. We believe this class of systems is quite common in all engineering disciplines and particularly in chemical engineering, where the DAE models are likely to be uncertain in addition to the presence of exact equality constraints arising out of flow balances and summation of mole fractions.

Most efforts in constrained Kalman filtering involves linear systems with optimal filtering while non-linearities in the system result in sub-optimal and complicated filtering.[198] Therefore, approximation is inevitable in filtering non-linear systems while they remain sub-optimal. Although there is no extensive investigation on constrained Kalman filtering of non-linear models due to their sub-optimal nature and complications, we make the assumptions that handling constraints in Kalman filtering of non-linear models can be done similar to their linear counterparts due to their linear approximations. There are several ways in which equality constraints can be incorporated into the linear Kalman filter. An attractive approach is to substitute the constraints into the model equations. This approach has an advantage of reducing the constrained problem to a simpler unconstrained problem with lower computational load of the Kalman filter. However, a major disadvantage is that this method will sacrifice the physical meaning of the variables, especially in systems expressing the detailed phenomena taking place in a process. Study on constrained filtering has shown that projecting the unconstrained estimates of the Kalman filter on the constraint surface accommodates ease of implementation, low computational cost and flexibility compared to other approaches for both linear and non-linear systems.[198]

5.1.3.1 Problem formulation

The system of interest in this section is as shown in Eqn. (181).

$$
\begin{aligned}
& x_{k+1} = x_k + \int_{k\,\Delta t}^{(k+1)\,\Delta t} f\big(x(t), z(t)\big)\, dt + G\omega_{k+1} \\
& g(x_{k+1}, z_{k+1}) + \gamma_{k+1} = 0 \\
& y_{k+1} = h(x_{k+1}, z_{k+1}) + \nu_{k+1} \\
& \omega \sim N(0, Q) \qquad \nu \sim N(0, R) \qquad \gamma \sim N(0, W) \\
& subject\ to: E x_{k+1}^{aug} = b
\end{aligned}
\tag{181}
$$

where in addition to the assumptions for system described in Eqn. (172), $G \in \mathbb{R}^{m\times m}$ is a known matrix with rank(G) = $l < m$, $E \in \mathbb{R}^{l\times m+n}$ is the equality constraint with rank(E) = l which can be split into $E = [E_x \quad E_z]$ where $E_x \in \mathbb{R}^{l\times m}$ satisfies $E_x G = 0_{l\times m}$ and $E_z = 0_{l\times n}$, $b \in \mathbb{R}^{l\times 1}$ is a vector of equality constraint values and $W \in \mathbb{R}^{n\times n}$ is a known covariance matrix. The estimation algorithm described previously is not a valid framework for the defined system. The main issue is that the white noise is not differentiable; therefore, the system cannot be converted into an implicit ODE as shown in Eqn. (173).

Remark 2.1: Assume rank(E) = m+n, then for all $k \geq 1$ the system is fully constrained and the updated states are calculated as $x_{k+1} = E^{-1}b$.

Proof: If rank(E) = m+n, then E is square and invertible. Therefore, the constraint equation has unique answer as $x_{k+1} = E^{-1}b$.

5.1.3.2 Propagation

Let $\hat{x}_{k|k}$ and $\hat{z}_{k|k}$ be updated differential and algebraic state estimates, respectively, at k^{th} time instant and P_k be the error covariance of the states. States are propagated by solving the DAE from k^{th} time instant to k+1$^{\text{th}}$ time instant to get $\hat{x}_{k+1|k}$ and $\hat{z}_{k+1|k}$. In what follows, the superscripts *'c'* and *'st'* represent the corrected and standard form, respectively. In order to propagate the covariance matrix, the DAE system is linearized around the $\hat{x}_{k|k}$ and $\hat{z}_{k|k}$ as

$$\dot{x} = Ax + Bz \tag{182}$$

$$Cx + Dz = 0 \tag{183}$$

where the coefficient matrix of linearized form is simply the Jacobian evaluated at the operating point, $\hat{x}_{k|k}, \hat{z}_{k|k}$, similar to Eqn. (173). Solving Eqn. (183) in terms of z and rewriting the Eqn. (182) results

$$z = -D^{-1}Cx \tag{184}$$

$$\dot{x} = (A - BD^{-1}C)x \tag{185}$$

Based on differential and algebraic variables, the error covariance matrix can be split into

$$P_{k+1|k} = \begin{bmatrix} P^{xx}_{k+1|k} & P^{xz}_{k+1|k} \\ P^{zx}_{k+1|k} & P^{zz}_{k+1|k} \end{bmatrix} \tag{186}$$

The error covariance of differential states is calculated as

$$P^{xx}_{k+1|k} = \phi P^{xx}_{k|k} \phi^T + GQG^T \tag{187}$$

where Φ is the transition matrix of differential states and is obtained as

$$\phi = e^{(A - BD^{-1}C)\Delta t} \tag{188}$$

The error covariance of algebraic states is propagated as

$$P^{zz}_{k+1|k} = (D^{-1}C)P^{xx}_{k+1|k}(D^{-1}C)^T + D^{-1}WD^{-1^T} \tag{189}$$

Since the algebraic states are linear transformation of the differential states, the error covariance between differential and algebraic states is propagated as a linear transformation of the error covariance of differential states as

$$P^{xz}_{k+1|k} = P^{xx}_{k+1|k}(D^{-1}C)^T \tag{190}$$

$$P_{k+1|k}^{zx} = (D^{-1}C)P_{k+1|k}^{xx} \tag{191}$$

5.1.3.3 Correction

The updated augmented state estimates are obtained by solving the following minimization problem

$$\begin{aligned}\underset{\hat{x}_{k+1|k+1}^{a,c}}{min} \left(\hat{x}_{k+1|k+1}^{aug,c} - \hat{x}_{k+1|k}^{aug}\right)^T {P_{k+1|k}}^{-1} \left(\hat{x}_{k+1|k+1}^{aug,c} - \hat{x}_{k+1|k}^{aug}\right) \\ + \left(y_{k+1} - C\hat{x}_{k+1|k+1}^{aug,c}\right)^T R^{-1} \left(y_{k+1} - C\hat{x}_{k+1|k+1}^{aug,c}\right)\end{aligned} \tag{192}$$

subject to the state constraints

$$E\hat{x}_{k+1|k+1}^{aug,c} = b \tag{193}$$

where $\hat{x}_{k+1|k+1}^{aug,c}$ is the augmented updated state estimates (i.e. $\hat{x}_{k+1|k+1}^{aug,c} = \begin{bmatrix}\hat{x}_{k+1|k+1}^{c} \\ \hat{z}_{k+1|k+1}^{c}\end{bmatrix}$) that satisfies the state constraints.

Remark 2.2: In the absence of any constraints, the optimization problem is similar to the problem investigated in the work of Vachhani et al.[211] and the solution to the optimization problem for all $k \geq 1$ is given by standard KF.

Proof: The proof is described in the work of Vachhani et al.[211]

The optimization problem is solved using the standard Lagrange multiplier technique, where the Lagrangian is defined as

$$\begin{aligned}L\left(\hat{x}_{k+1|k+1}^{aug,c}, \lambda\right) = \left(\hat{x}_{k+1|k+1}^{aug,c} - \hat{x}_{k+1|k}^{aug}\right)^T {P_{k+1|k}}^{-1} \left(\hat{x}_{k+1|k+1}^{aug,c} - \hat{x}_{k+1|k}^{aug}\right) \\ + \left(y_{k+1} - H\hat{x}_{k+1|k+1}^{aug,c}\right)^T R^{-1} \left(y_{k+1} - H\hat{x}_{k+1|k+1}^{aug,c}\right) + \lambda^T \left(E\hat{x}_{k+1|k+1}^{aug,c} - b\right)\end{aligned} \tag{194}$$

The necessary conditions for $\hat{x}_{k+1|k+1}^{a,c}$ minimizing Eqn. (194) are

$$\frac{\partial L}{\partial \hat{x}_{k+1|k+1}^{aug,c}} = 2{P_{k+1|k}}^{-1} \left(\hat{x}_{k+1|k+1}^{aug,c} - \hat{x}_{k+1|k}^{aug}\right) - 2H^T R^{-1} \left(y_{k+1} - H\hat{x}_{k+1|k+1}^{aug,c}\right) + E^T\lambda = 0 \tag{195}$$

$$\frac{\partial L}{\partial \lambda} = E\hat{x}_{k+1|k+1}^{aug,c} - b = 0 \tag{196}$$

Solving Eqn. (195) for $\hat{x}_{k+1|k+1}^{a,c}$ after some manipulations yields

$$\begin{aligned}\hat{x}_{k+1|k+1}^{aug,c} = \hat{x}_{k+1|k}^{aug} + \left({P_{k+1|k}}^{-1} + H^T R^{-1} H\right)^{-1} C^T R^{-1} \left(y_{k+1} - H\hat{x}_{k+1|k}^{aug}\right) \\ - \frac{1}{2}\left({P_{k+1|k}}^{-1} + H^T R^{-1} H\right)^{-1} E^T\lambda\end{aligned} \tag{197}$$

Following the definition of Kalman gain matrix, K_{k+1}, in Eqn. (180) and matrix inversion lemma[212] we have

$$
\begin{aligned}
&\left[{P_{k+1|k}}^{-1} + H^T R^{-1} H\right]^{-1} \\
&\quad = \left[{P_{k+1|k}}^{-1} + H^T R^{-1} H\right]^{-1} \left[I + H^T R^{-1} H P_{k+1|k} - H^T R^{-1} H P_{k+1|k}\right] \\
&\quad = \left[{P_{k+1|k}}^{-1} + H^T R^{-1} H\right]^{-1} \left[\left[{P_{k+1|k}}^{-1} + H^T R^{-1} H\right] P_{k+1|k} - H^T R^{-1} H P_{k+1|k}\right] \\
&\quad = P_{k+1|k} - \left[{P_{k+1|k}}^{-1} + H^T R^{-1} H\right]^{-1} H^T R^{-1} H P_{k+1|k} \\
&\quad = P_{k+1|k} - K_{k+1} H P_{k+1|k} \\
&\quad = P_{k+1|k+1}
\end{aligned}
\tag{198}
$$

Substituting Eqn. (198) into Eqn. (197) and using the state update in Eqn. (177) we have

$$
\hat{x}^{aug,c}_{k+1|k+1} = \hat{x}^{aug}_{k+1|k+1} - \frac{1}{2} P_{k+1|k+1} E^T \lambda \tag{199}
$$

Substituting Eqn. (199) into Eqn. (196) and solving for Lagrangian multiplier, λ, we get

$$
\lambda = 2\left(E P_{k+1|k+1} E^T\right)^{-1} \left(E \hat{x}^{aug}_{k+1|k+1} - b\right) \tag{200}
$$

Substituting the value of Lagrangian multiplier from Eqn.(200), the states are updated in the presence of equality constraints as

$$
\hat{x}^{aug,c}_{k+1|k+1} = F \hat{x}^{aug}_{k+1|k+1} + b' \tag{201}
$$

where

$$
F = \left(I - P_{k+1|k+1} E^T \left(E P_{k+1|k+1} E^T\right)^{-1} E\right) \tag{202}
$$

$$
b' = P_{k+1|k+1} E^T \left(E P_{k+1|k+1} E^T\right)^{-1} b \tag{203}
$$

where $P_{k+1|k+1}$ is the KF covariance matrix calculated similar to Eqn. (179). Using the state propagation matrix, for covariance matrix update we have

$$
\begin{aligned}
&P^c_{k+1|k+1} \\
&= F P_{k+1|k+1} F^T \\
&= \left(I - P_{k+1|k+1} E^T \left(E P_{k+1|k+1} E^T\right)^{-1} E\right) P_{k+1|k+1} \left(I - P_{k+1|k+1} E^T \left(E P_{k+1|k+1} E^T\right)^{-1} E\right)^{\mathrm{T}} \\
&= P_{k+1|k+1} - P_{k+1|k+1} \left[P_{k+1|k+1} E^T \left(E P_{k+1|k+1} E^T\right)^{-1} E\right]^T \\
&\qquad - P_{k+1|k+1} E^T \left(E P_{k+1|k+1} E^T\right)^{-1} E P_{k+1|k+1} \\
&\qquad + P_{k+1|k+1} E^T \left(E P_{k+1|k+1} E^T\right)^{-1} E P_{k+1|k+1} \left[P_{k+1|k+1} E^T \left(E P_{k+1|k+1} E^T\right)^{-1} E\right]^T \\
&= P_{k+1|k+1} - P_{k+1|k+1} E^T \left(E P_{k+1|k+1} E^T\right)^{-1} E P_{k+1|k+1}
\end{aligned}
\tag{204}
$$

$$
\begin{aligned}
&-P_{k+1|k+1}E^T\left(EP_{k+1|k+1}E^T\right)^{-1}EP_{k+1|k+1} \\
&+P_{k+1|k+1}E^T\left(EP_{k+1|k+1}E^T\right)^{-1}\left(EP_{k+1|k+1}E^T\right)\left(EP_{k+1|k+1}E^T\right)^{-1}EP_{k+1|k+1} \\
&= P_{k+1|k+1} - P_{k+1|k+1}E^T\left(EP_{k+1|k+1}E^T\right)^{-1}EP_{k+1|k+1} \\
&\quad -P_{k+1|k+1}E^T\left(EP_{k+1|k+1}E^T\right)^{-1}EP_{k+1|k+1} + P_{k+1|k+1}E^T\left(EP_{k+1|k+1}E^T\right)^{-1}EP_{k+1|k+1} \\
&= P_{k+1|k+1} - P_{k+1|k+1}E^T\left(EP_{k+1|k+1}E^T\right)^{-1}EP_{k+1|k+1} \\
&= \left(I - P_{k+1|k+1}E^T\left(EP_{k+1|k+1}E^T\right)^{-1}E\right)P_{k+1|k+1} \\
&= FP_{k+1|k+1}
\end{aligned}
$$

Remark 2.3: Assume that equality constraint, E, in Eqn. (181) can be split into $E = \begin{bmatrix} E_x \\ E_z \end{bmatrix}^T$ where $E_x \in \mathbb{R}^{l\times m}$ is left eigenvector(s) of Φ that satisfies $E_xG = 0_{l\times m}$, $E_xf_x = 0_{m\times 1}$ and $E_z = 0_{l\times n}$ where f_x is the differential equations of the DAE system represented by Eqn. (181). Also assume that for a given $k = 1$, $E\hat{x}^{aug,c}_{k+1|k+1} = b$ and $EP^c_{k+1|k+1} = 0_{l\times m+n}$. Then, for all $k \geq 2$, $x^{aug,c}_{k+1|k+1} = \hat{x}^{aug}_{k+1|k+1}$ and $P^c_{k+1|k+1} = P_{k+1|k+1}$.

Proof: By multiplying the differential equations in DAE system of Eqn. (181) by E we get

$$
\begin{aligned}
Ex^{aug}_{k+1} &= E_xx_k + \int_{k\,\Delta t}^{(k+1)\,\Delta t} E_xf_x\big(x(t),z(t)\big)\,dt + E_xG\omega_{k+1} + E_zz_{k+1} \\
&= b + 0_{l\times 1} + 0_{l\times 1} + 0_{l\times 1} \\
&= b
\end{aligned}
\tag{205}
$$

Since E_x is the left eigenvector(s) of Φ, then we can write $E_x\Phi = \lambda E_x$ where λs are the eigenvalues of the corresponding eigenvectors. Multiplying Eqn. (186) by E then yields

$$
\begin{aligned}
EP_{k+1|k} &= \begin{bmatrix} E_xP^{xx}_{k+1|k} + E_zP^{zx}_{k+1|k} \\ E_xP^{xz}_{k+1|k} + E_zP^{zz}_{k+1|k} \end{bmatrix}^T \\
&= \begin{bmatrix} \left(E_x\phi P^{xx}_{k|k}\phi^T + E_xGQG^T\right) + E_z(D^{-1}C)P^{xx}_{k+1|k} \\ E_xP^{xx}_{k+1|k}(D^{-1}C)^T + \left(E_z(D^{-1}C)P^{xx}_{k+1|k}(D^{-1}C)^T + E_zM\right) \end{bmatrix}^T \\
&= \begin{bmatrix} \left(\lambda E_xP^{xx}_{k|k}\phi^T + 0_{l\times m}\right) + 0_{l\times m} \\ 0_{l\times n} + (0_{l\times n} + 0_{l\times n}) \end{bmatrix}^T \\
&= 0_{l\times(m+n)}
\end{aligned}
\tag{206}
$$

Lemma 2.1: let $\boldsymbol{\nu}$ be a left eigenvector of the square matrix U with a corresponding eigenvalue λ. Then, $\nu e^{U\Delta t} = e^{\lambda\Delta t}\nu$.

Proof: To prove this, we can write $U\Delta t = U\Delta t - \lambda I\Delta t + \lambda I\Delta t$, therefore

$$
\begin{aligned}
\nu e^{U\Delta t} &= \nu e^{U\Delta t - \lambda I\Delta t + \lambda I\Delta t} \\
&= \nu e^{(U-\lambda I)\Delta t + \lambda I\Delta t} \\
&= \nu e^{(U-\lambda I)\Delta t}e^{\lambda\Delta t} \\
&= \nu\left(I + (U-\lambda I)\Delta t + \frac{(U-\lambda I)^2\Delta t^2}{2!} + \cdots\right)e^{\lambda\Delta t} \\
&= \left(\nu I + \nu(U-\lambda I)\Delta t + \frac{\nu(U-\lambda I)^2\Delta t^2}{2!} + \cdots\right)e^{\lambda\Delta t}
\end{aligned}
\tag{207}
$$

$$= (\nu I + 0 + 0 + \cdots)e^{\lambda \Delta t}$$
$$= e^{\lambda \Delta t}\nu$$

Therefore, in Eqn. (206) E_x is already the left eigenvector(s) of (A-$BD^{-1}C$). Multiplying Eqn. (201) and (204) by E yields

$$\begin{aligned} E\hat{x}_{k+1|k+1}^{aug,c} &= EF\hat{x}_{k+1|k+1}^{aug} + Eb' \\ &= E\left(I - P_{k+1|k+1}E^T\left(EP_{k+1|k+1}E^T\right)^{-1}E\right)\hat{x}_{k+1|k+1}^{aug} \\ &\quad + EP_{k+1|k+1}E^T\left(EP_{k+1|k+1}E^T\right)^{-1}b \\ &= (E-E)\hat{x}_{k+1|k+1}^{aug} + b \\ &= b \end{aligned} \tag{208}$$

$$\begin{aligned} EP_{k+1|k+1}^{c} &= EFP_{k+1|k+1} \\ &= E\left(I - P_{k+1|k+1}E^T\left(EP_{k+1|k+1}E^T\right)^{-1}E\right)P_{k+1|k+1} \\ &= (E-E)P_{k+1|k+1} \\ &= 0_{l\times(m+n)} \end{aligned} \tag{209}$$

Giving Eqn. (208)-(209), from Eqn. (205)-(206) we have $x_{k+1|k+1}^{aug,c} = \hat{x}_{k+1|k+1}^{aug}$ and $P_{k+1|k+1}^{c} = P_{k+1|k+1}$. Therefore, if the assumptions hold, the correction step in Eqn. (201) and (204) has to be performed only once at $k = 1$ and for all $k \geq 2$ the corrected states given by Eqn. (177) already satisfies $E\hat{x}_{k+1|k+1}^{aug} = b$.[213]

5.2 Distributed Sensor Placement Problem Formulation

5.2.1 Introduction

In the past decades, process monitoring for safety and optimal operation has been a vast area for researchers to develop techniques for control, optimization, fault detection, condition monitoring and etc. With growing scale and complexity of the processes, mathematical models cannot be solely used and information from sensors as an alternate source of information is necessary. The problem of sensor placement is defined as finding optimal locations throughout the process for maximum possible information to be acquired. Most important constraints involved are the feasibility of placing sensors and cost and redundancy of the sensors. For example, in a fixed-bed reactor, it is not feasible to directly measure the temperature of the catalyst. Sensor redundancy includes placing multiple sensors at the same location to handle the probability of the sensor failure. Also, clustering sensors in an area may result in significantly less information compared to if they were distributed. Therefore, optimizing sensor placement is important for maximizing the profit from the process and reducing the risk of health and environmental issues.

Sensor placement has been studied for different tasks such as parameter estimation[214-221], state estimation[222-233] and fault detection[234] that deals with distributed parameter systems (DPS). Distributed parameter systems represent the dynamical systems governed by partial differential equations (PDE). A common idea in sensor placement is the idea of choosing sensors that optimize some performance criteria. Many contributions in literature can be found that consider the steady-state behavior of the systems[235], including the sensor placement by qualitative analysis[236-238]. Although many efforts on sensor placement belong to linear DPS, various optimality criteria are either developed or adapted from linear systems to account for nonlinear systems. A common metric used in sensor placement involves the use of empirical

Sensor placement has been applied in different tasks such as parameter estimation [214-221], state estimation[222-233] and fault detection[234] that deals with distributed parameter systems (DPS). Distributed parameters systems represent the dynamical systems governed by partial differential equations (PDE). A most common technique in sensor placement is by optimizing performance criteria. Many contributions in literature can be found that consider the steady-state behavior of the systems[235], including the sensor placement by qualitative analysis[236-238]. Although many efforts on sensor placement belong to linear DPS, various optimality criteria either developed or reinstated from linear systems to account for nonlinear systems. A common metric used in sensor placement involves the use of empirical observability Grammian proposed by Muller and Weber[239]. This includes evaluation of different aspects of the observability matrix such as smallest eigenvalue, determinant, trace of the inverse, condition number, spectral norm and smallest singular value[222,233,239-245]. Different criteria in sensor placement has been also proposed based on the geometric approach[223,246], measurement cost[232,247], sensor failure[248,249], max-min optimization[250], posterior Cramer-Rao lower bound[249] and so on.

Despite the information from common observability matrix, efforts in state estimation have been made in defining metrics for sensor placement that considers trace, determinant, variance and norm of the error covariance matrix of the Kalman filter[228-231,244,245,251-254]. Colantuoni and Padmanabhant[230], Kumar and Seinfeld[231] and Omatu et al.[227] consider minimization of the trace of the error covariance as the metric in their sensor placement work and proposed an iterative optimization procedure for sensor placement for a tubular reactor. Harris et al.[229] performed the sensor placement for a tubular reactor while minimizing the trace and determinant of the error covariance matrix. Alvarez et al.[244] approached the problem by developing a variable measurement structure for the tubular reactor with minimum variance as the optimality index. Morari and O'Dowd[253] considered optimality criteria as minimization of the error caused by the unobservable subspace and Morari and Stephanopoulos[254] extended the criteria to also include the minimization of the estimation error.

In most of the works mentioned above, sensor placement is performed for steady state condition. In the cases where dynamical systems are considered, sensor placement is performed by linearizing the nonlinear equations around the steady-state point. This reduces the complexity of the nonlinear equations to linear form and the sensor placement can be performed as if the system is linear. This is due to the reason that solving the nonlinear equations in the sensor placement frameworks is cumbersome. However, this is not always applicable for two reasons. First, since the previous works on sensor placement always consider the system is represented by PDE, it is not always possible to have the system as fully implicit PDE (or ordinary differential equations, ODE). For example, as the system in this work is represented by differential and algebraic equations (DAE), it is not possible to differentiate the equations to get ODE since the white Gaussian noise in algebraic equations cannot be differentiated. Second, in terms of fault detection, if a fault occurs in the process it will significantly move the system from steady-state condition and will result in the system reaching a new steady-state condition. Therefore, the linearized system or the assumption of the dynamics around the initial steady-state condition is no longer valid. These drawbacks of the classical sensor placement approaches necessitate the use of nonlinear models in the sensor placement framework.

The most important drawback of using nonlinear models in sensor placement is the computational burden and tractability of the calculations caused by nonlinear models in state estimation. A recent work in use of nonlinear model in extended Kalman filter (EKF) is reported in the work of Olanrewaju and Al-Arfaj[228] in which the sensor placement problem is not extensively addressed. One way to address the tractability of use of detailed nonlinear models is to use simplified or reduced models. However, it is not clear how much this will affect the computational burden and how close will the sensor placement results are to that of detailed models. To our best knowledge, no one has investigated the suitability of the simplified models in sensor placement.

In this work, a sensor placement framework is developed that makes use of EKF for state estimation. For simplicity, the optimality index is chosen as the accuracy of the state estimates by minimizing the error between the true solution and the state estimates. The infinite dimensional model of the reactor is discretized along the reactor axis by finite element method and the discrete points on the reactor are the locations where sensors can be placed. The sensor placement is performed by genetic algorithm (GA) where the genes are assumed to be measurement models and each measurement model represents a vector of binary decision variables in which if a sensor is placed, the decision variable will take a value of "1" and a value of "0" otherwise. The GA evolves while minimizing the objective function and the optimal measurement model as the result of the optimization is obtained. The optimal measurement model is then the optimal sensor placement when projected on the discretized locations.

5.2.2 Summary of WGS Model simplification

The detailed reactor model represents complex equations that must be solved. A simplified model of the reactor has been developed in section 3.1. Model simplification retains the most important phenomena occurring in the reactor by means of scaling analysis. In the scaling analysis, dimensionless groups are formed using the parameters and inlet condition values. The decision on retaining or discarding the phenomenon in the reactor is made by analyzing the values of the dimensionless groups where the phenomenon with least values can be discarded from model equations. Through this analysis, it is observed that the model can be represented by only a single differential equation which combines the energy balance for gas and catalyst phases while the rest of the equations are algebraic. The temporal differential mass balance equation can be reduced to algebraic equation where it is sufficient to solve the algebraic equation only for one species and the rest of the species can be calculated on side from the result of other equations. The simplified model is expressed by following equations:

Mass balance:

$$\frac{dC_{H_2O}}{dz} = -y_{H_2O}C\left(\frac{1}{T}\frac{dT}{dz} - \frac{1}{P}\frac{dP}{dz}\right) + r_{CO}\frac{1-\varepsilon}{u} \tag{210}$$

Energy balance:

$$\frac{\partial T_g}{\partial t} = \frac{\varepsilon}{\varepsilon\rho C_P + (1-\varepsilon)\rho_{cat}C_{P,cat}}\left(-GC_P\frac{\partial T_g}{\partial z} + r_{CO}\Delta H_R\frac{1-\varepsilon}{\varepsilon}\right) \tag{211}$$

Momentum balance:

$$\frac{dP}{dz} = \frac{\rho u^2}{d_{cat}}\left(\frac{1-\varepsilon}{\varepsilon}\right)\left(1.75 + \frac{150}{Re}\right) \tag{212}$$

5.2.3 EKF for simplified model

In a mathematical view of the simplified model, part of the differential equations are decoupled from the original system and assumed to be algebraic through the analysis shown in previous sections. Although the corresponding states represent the states of the original system, they have no effect on the internal states of the simplified model and can be treated as exogenous states with corresponding exogenous equations. In view of DAEs, these exogenous equations can be either part of the DAE system as algebraic equations or be used outside the DAE model and computed independently. A simple drawback of assuming the exogenous equations as part of the DAE is that since exogenous equations do not impose a constraint on the system, though they have to be solved at each integration step in the propagation step of

the filter. Therefore, this poses a burden on the DAE solvers and hence complicating the computations. Another drawback is that in the propagation step of the filter, the updated states at the next time step are only required while the path that these states take to the final states can be neglected. For these reasons, the decoupled algebraic equations are treated as independent exogenous equations. The overall simplified system is presented by

$$
\begin{gathered}
DAE\begin{cases} x_{k+1} = x_k + \int_{k\,\Delta t}^{(k+1)\,\Delta t} f\big(x(t), z(t)\big)\, dt + \omega_{2,k} \\ g(x_{k+1}, z_{k+1}) = \gamma_{k+1} \end{cases} \\
s_{k+1} = U x_{k+1}^{A} + J s_k + \Gamma_{k+1} \\
y_{k+1} = h(x_{k+1}, z_{k+1}, s_{k+1}) + \nu_{k+1} \\
\omega \sim N(0, Q_2) \qquad \nu \sim N(0, R) \quad \gamma \sim N(0, W) \quad \Gamma \sim N(0, \Omega) \\
subject\ to: E x_{k+1}^{aug} = b
\end{gathered}
\tag{213}
$$

where s_{k+1} is the vector of exogenous states and U and J are the coefficient matrices of the linearized exogenous equations around the state updates, x_{k+1}^{A} and s_k, respectively. Here, $x_{k+1|k}^{A}$ is the augmented internal states, $x_{k+1|k}^{A} = \begin{bmatrix} x_{k+1} \\ z_{k+1} \end{bmatrix}$, and x_{k+1}^{aug} is the augmented internal and exogenous states, $x_{k+1}^{aug} = \begin{bmatrix} x_{k+1}^{A} \\ s_k \end{bmatrix}$. Also, here, the exogenous states do not depend on their initial states, therefore, $J = \mathbf{0}$. Note that $\omega_{2,k}$ is assumed uncorrelated with ν, γ and Γ; and since the exogenous equations are decoupled from the differential equations, G matrix that correlates the noise in mole fractions is omitted, however, a white noise term, Γ_{k+1}, is assumed in the exogenous equations. Although omitting G may have effect on the quality of the state estimates, it is not easy mathematically to account for the correlated noise in the mole fractions when considering the simplified model.

The modification made to the original system requires modifications of the filter equations as well. The new filter formulation follows the same process as for DAEs while adding the presence of the exogenous states. In the propagation step, the DAE model can be solved again by the DAE solvers from instant k to $k+1$, while the exogenous states are computed using the updated internal states to obtain the updated exogenous states. The updated error covariance matrix is calculated by splitting the matrix for internal and the exogenous states as

$$
P_{k+1|k}^{aug} = \begin{bmatrix} P_{k+1|k}^{x^A x^A} & P_{k+1|k}^{x^A s} \\ P_{k+1|k}^{s x^A} & P_{k+1|k}^{ss} \end{bmatrix} \tag{214}
$$

where $P_{k+1|k}^{x^A x^A}$ is the error covariance matrix of the simplified DAE and is derived using general derivation explained in section 5.1. This results in equations similar to equations derived in Section 5.1.3 with the exception that the simplified model has now modified process noise covariance ($\omega \sim N(0, Q_2)$. The other blocks in $P_{k+1|k}^{aug}$ can be calculated by

$$
P_{k+1|k}^{x^A s} = P_{k+1|k}^{x^A x^A}\, U^T \tag{215}
$$

$$
P_{k+1|k}^{s x^A} = U\, P_{k+1|k}^{x^A x^A} \tag{216}
$$

$$
P_{k+1|k}^{ss} = U\, P_{k+1|k}^{x^A x^A}\, U^T + \Omega \tag{217}
$$

Eqn. (215)-(217) can be proved simply by taking similar approach as for filtering of the DAE systems. Therefore, for the sake of brevity we have omitted the mathematical proofs. In the correction step of the filter, the corrected states can be calculated similar to the Eqn. (201)-(204).

Although considering noise in exogenous equations may results in better quality estimates since the original states are not noise free, it raises the need for the presence of constraint in the formulation. However, another approach would then be to remove the noise from the exogenous equations. Since the exogenous equations automatically satisfy the constraint, therefore, the constraint in Eqn. (213) can be removed and the correction step reduces to use of standard EKF correction step. It is not clear to what extent this can affect the quality of state estimates and the SP results. Removing the noise term from exogenous equations may or may not be compensated by tuning the error covariance matrix Q_2 in the filtering.

5.2.4 Genetic algorithm

In the GA, the genes represent the binary measurement models that can be used by EKF for state estimation. The fixed population of GA evolves by the elitist selection strategy where a portion of the population is considered as the elite genes and carries over to the next generation. The rest of the population are obtained based on the tournament selection where fitness values of 2 randomly chosen genes are compared against each other and the gene with highest fitness is considered as the winner. This selection is repeated until two winner genes are selected for crossover and mutation- the GA operators for obtaining the two children from parent genes. Since in our work the number of measurements (sensors) are fixed for a particular study, the crossover and mutation on the winner genes are repeated until at least one of the children has the same number of fixed measurements. The tournament selection results in obtaining two children per each run, therefore, this process must be repeated until a new population is generated. The objective of the GA is to minimize the error between actual data and the state estimates and the objective function is given by

$$\min \sum_{i=2}^{k_T} \sum_{j=1}^{n_T} \left(\frac{x_{actual,(i,j)} - \hat{x}_{estimated,(i,j)}}{x_{actual,(i,j)}} \right)^2 \tag{218}$$

subject to: EKF of WGSR for k_T time instants and n_T variables

It should be noted that the summation in Eqn. (218) is over all the estimated values for all time instants while the initial state estimates are discarded and summation start from $i = 2$. This assumption will be justified later when we study the effect of initial error covariance of the states.

6 Interpretation of Results

6.1 System-Level Sensor Placement

In this section, four illustrative case studies are used to demonstrate the performance of FES and MR algorithms. A set of predefined faults are simulated in each case while assuming no disturbances exist in the system. Table 19 shows the sensors' cost assumed in all three cases which are normalized by the cost of flow sensor.[190] In all three cases, MR algorithm is performed for three different levels of MR threshold value as low, medium and high with values 1.1, 1.5 and 2, respectively. Results are compared for FES and MR algorithms individually and jointly. Detail tabulated results for the SDG, FES and MR algorithms are provided in the supporting documents. Also, sensitivity analysis of the MR threshold value is performed for each case study and the results are included in the supporting document.

Table 19. Type and cost of each sensor used in all case studies[190]

Sensor type	Cost
Temperature sensor	0.1
Pressure sensor	0.5
Flow sensor	1
Level sensor	1
Concentration sensor	10

6.1.1 CSTR Case Study

The CSTR system used in the work of Bhushan and Rengaswamy[181] is considered in this work for application of FES and MR algorithms. For more details of the process, interested readers are referred to their work.[181] Figure 82 shows the schematic of the CSTR system. Table 20 and Table 21 show lists of measured variables and simulated faults in the CSTR system. Faults are simulated one by one and measured variables are stored for later implementation of FES and MR algorithms. As seen in Table 21, all faults except U and C_d can change in both directions with "+" representing increase and "-" decrease in the fault. The heat transfer coefficient, U, and the catalyst activity, C_d can only decrease due to nature of the fault. Therefore, these faults are unidirectional and can only change in "-" direction.

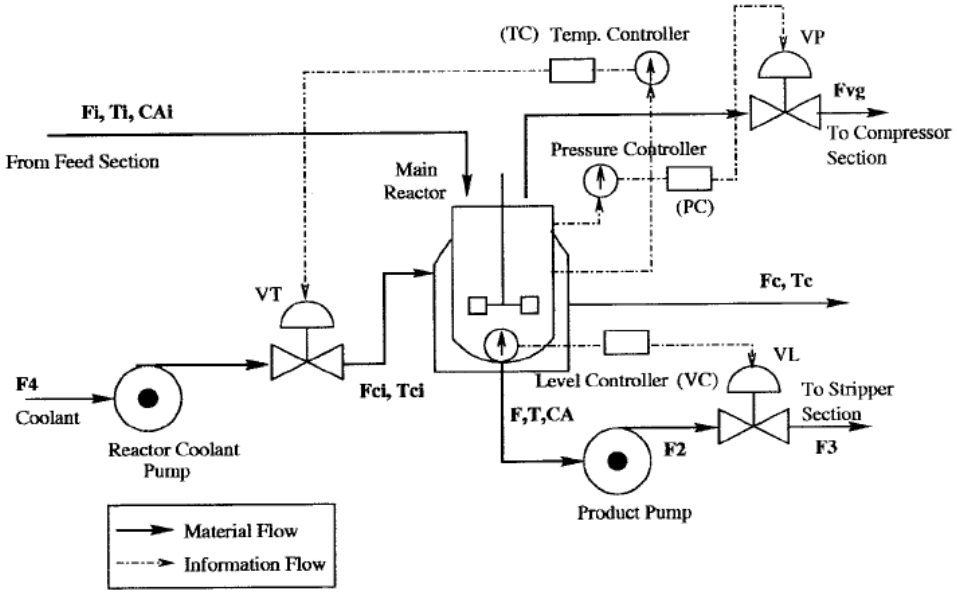

Figure 82. Schematic of the CSTR system[182]

Table 20. List of measured variables in CSTR system

Sensor no.	Measured variable	Description	Sensor no.	Measured variable	Description
s1	C_A	CSTR Outlet concentration	s5	VL	Level controller valve opening

s2	T_c	Coolant outlet temperature	s6	*VT*	Temperature controller valve opening
s3	*F*	CSTR outlet flow rate	s7	*VP*	Pressure controller valve opening
s4	F_c	Coolant flow rate			

Table 21. List of simulated faults and the corresponding affected sensors in CSTR system

Fault	Description		Affected sensors
1	C_{Ai}^{+}	Inlet concentration	s1,s2,s4,s6,s7
2	C_{Ai}^{-}		s1,s2,s4,s6,s7
3	T_i^{+}	Inlet temperature	s4,s6,s7
4	T_i^{-}		s4,s6,s7
5	F_i^{+}	Inlet flow rate	s1,s3,s4,s5,s6,s7
6	F_i^{-}		s1,s3,s4,s5,s6,s7
7	T_{Ci}^{+}	Coolant outlet temperature	s4,s6,s7
8	T_{Ci}^{-}		s2,s4,s6,s7
9	*U*	Heat transfer coefficient	s4,s6
10	C_d	Catalyst deactivation	s1,s2,s4,s6,s7

Table 22. Results of applying different algorithms to CSTR system

Algorithm(s)	MR threshold level	Selected sensors	Sensor network cost	Irresolvable fault sets
SDG		s1,s2,s6,s7	10.7	[3,7]
FES		s2,s6,s7	0.7	[3,7]
MR	Low	s1,s2,s6,s7	10.7	[3,7]
	Medium	s2,s6,s7	0.7	[ ]
	High	s2,s6,s7	0.7	[3,7]

	Low	s2,s6,s7	0.7	[3,7]
FES & MR	Medium	s2,s6,s7	0.7	[ ]
	High	s2,s6,s7	0.7	[3,7]

Both FES and MR algorithms are run individually and in combination. Although both algorithms are associated with SDG, for illustration, SDG is also performed individually and results are shown in Table 22. FES algorithm has less number of variables measured compared to SDG, thus, decreasing the capital cost of the network. However, there is still a fault set that cannot be resolved by FES. At low MR threshold level, MR algorithm shows no improvement over the associated SDG algorithm and the results are the same as if the SDG is performed individually. The combination of both MR and FES algorithms take advantage of the FES as it has lower sensor network cost. At medium MR threshold level, MR algorithm chooses the same sensors as FES but it can resolve all the faults, thus, the algorithm shows improvement in terms of fault resolvability compared to FES algorithm. The combination of both algorithms takes advantage of the MR algorithm as it can resolve all the faults. At high MR threshold level, although MR algorithm again chooses the same sensors as FES, it cannot resolve all the faults. The combination of both algorithms uses the same sensors as if the MR or FES performed individually since the sensor network cost and number of irresolvable faults is the same for both algorithms. Table 21 and 23 show the affected variables and variables that can be used for fault resolution, respectively. The fault resolution of MR algorithm shown in Table 23 is shown only for medium MR threshold level (value of 1.5). In Table 23 and the upcoming tables for fault resolution, each single sensor (i.e. s1) represent the sensor that can individually resolve the corresponding pair of faults and each sensor pair (i.e. $P_{1,2}$ which represents pair s1 and s2) represent pairs of sensors that can resolve the corresponding pair of faults.

Table 23. Fault resolution by SDG, FES and MR in CSTR system

Fault	Resolution sensors			Fault	Resolution sensors		
	Single	Pair			Single	Pair	
		FES	MR			FES	MR
[1,2]	s1,s2,s4,s6,s7			[3,10]	s1,s2,s4, s6,s7	$P_{1,4}$, $P_{1,6}$, $P_{1,7}$, $P_{2,4}$, $P_{2,6}$, $P_{2,7}$	$P_{1,4}$, $P_{1,6}$, $P_{1,7}$, $P_{2,4}$, $P_{2,6}$, $P_{2,7}$
[1,3]	s1,s2	$P_{1,2}$, $P_{1,6}$, $P_{1,7}$, $P_{2,4}$, $P_{2,6}$, $P_{2,7}$, $P_{4,6}$, $P_{4,7}$, $P_{6,7}$		[4,5]	s1,s3, s5,s7	$P_{1,3}$, $P_{1,4}$, $P_{1,5}$, $P_{1,6}$, $P_{1,7}$	
[1,4]	s1,s2,s4,s6,s7	$P_{1,2}$, $P_{1,6}$, $P_{1,7}$, $P_{2,4}$, $P_{2,6}$, $P_{2,7}$, $P_{4,6}$, $P_{4,7}$, $P_{6,7}$		[4,6]	s1,s3,s4, s5,s6	$P_{1,3}$, $P_{1,4}$, $P_{1,5}$, $P_{1,6}$, $P_{1,7}$	
[1,5]	s2,s3,s4,s5,s6	$P_{1,2}$, $P_{1,3}$, $P_{1,4}$, $P_{1,5}$, $P_{1,6}$, $P_{1,7}$, $P_{2,4}$, $P_{2,6}$, $P_{2,7}$, $P_{4,6}$, $P_{4,7}$, $P_{6,7}$		[4,7]	s4,s6,s7		$P_{4,7}$, $P_{6,7}$
[1,6]	s1,s2,s3,s5,s7	$P_{1,2}$, $P_{1,3}$, $P_{1,4}$, $P_{1,5}$, $P_{1,6}$, $P_{1,7}$, $P_{2,4}$, $P_{2,6}$, $P_{2,7}$, $P_{4,6}$, $P_{4,7}$, $P_{6,7}$		[4,8]	s2		$P_{2,4}$, $P_{2,6}$, $P_{4,7}$, $P_{6,7}$
[1,7]	s1,s2	$P_{1,2}$, $P_{1,6}$, $P_{1,7}$, $P_{2,4}$, $P_{2,6}$, $P_{2,7}$,	$P_{4,7}$, $P_{6,7}$	[4,9]	s4,s6,s7		

		$P_{4,6}$, $P_{4,7}$, $P_{6,7}$					
[1,8]	s1,s4,s6,s7	$P_{1,2}$, $P_{1,6}$, $P_{1,7}$, $P_{2,4}$, $P_{2,6}$, $P_{2,7}$, $P_{4,6}$, $P_{4,7}$, $P_{6,7}$	$P_{2,4}$, $P_{2,6}$, $P_{4,7}$, $P_{6,7}$	[4,10]	s1,s2	$P_{1,4}$, $P_{1,6}$, $P_{1,7}$, $P_{2,4}$, $P_{2,6}$, $P_{2,7}$	$P_{1,4}$, $P_{1,6}$, $P_{1,7}$, $P_{2,4}$, $P_{2,6}$, $P_{2,7}$
[1,9]	s1,s2,s7	$P_{1,2}$, $P_{1,6}$, $P_{1,7}$, $P_{2,4}$, $P_{2,6}$, $P_{2,7}$, $P_{4,6}$, $P_{4,7}$, $P_{6,7}$		[5,6]	s1,s3,s4,s5,s6,s7		
[1,10]	s2,s4,s6,s7	$P_{1,2}$, $P_{1,4}$, $P_{1,6}$, $P_{1,7}$, $P_{4,6}$, $P_{4,7}$, $P_{6,7}$	$P_{1,4}$, $P_{1,6}$, $P_{1,7}$, $P_{2,4}$, $P_{2,6}$, $P_{2,7}$	[5,7]	s1,s3,s4,s5,s6	$P_{1,3}$, $P_{1,4}$, $P_{1,5}$, $P_{1,6}$, $P_{1,7}$	$P_{4,7}$, $P_{6,7}$
[2,3]	s1,s2,s4,s6,s7	$P_{1,2}$, $P_{1,6}$, $P_{1,7}$, $P_{2,4}$, $P_{2,6}$, $P_{2,7}$, $P_{4,6}$, $P_{4,7}$, $P_{6,7}$		[5,8]	s1,s2,s3,s5,s7	$P_{1,3}$, $P_{1,4}$, $P_{1,5}$, $P_{1,6}$, $P_{1,7}$	$P_{2,4}$, $P_{2,6}$, $P_{4,7}$, $P_{6,7}$
[2,4]	s1,s2	$P_{1,2}$, $P_{1,6}$, $P_{1,7}$, $P_{2,4}$, $P_{2,6}$, $P_{2,7}$, $P_{4,6}$, $P_{4,7}$, $P_{6,7}$		[5,9]	s1,s3,s4,s5,s6,s7	$P_{1,3}$, $P_{1,4}$, $P_{1,5}$, $P_{1,6}$, $P_{1,7}$	
[2,5]	s1,s2,s3,s5,s7	$P_{1,2}$, $P_{1,3}$, $P_{1,4}$, $P_{1,5}$, $P_{1,6}$, $P_{1,7}$, $P_{2,4}$, $P_{2,6}$, $P_{2,7}$, $P_{4,6}$, $P_{4,7}$, $P_{6,7}$		[5,10]	s2,s3,s5,s7	$P_{1,3}$, $P_{1,5}$, $P_{2,4}$, $P_{2,6}$, $P_{2,7}$	$P_{1,4}$, $P_{1,6}$, $P_{1,7}$, $P_{2,4}$, $P_{2,6}$, $P_{2,7}$
[2,6]	s2,s3,s4,s5,s6	$P_{1,2}$, $P_{1,3}$, $P_{1,4}$, $P_{1,5}$, $P_{1,6}$, $P_{1,7}$, $P_{2,4}$, $P_{2,6}$, $P_{2,7}$, $P_{4,6}$, $P_{4,7}$, $P_{6,7}$		[6,7]	s1,s3,s5,s7	$P_{1,3}$, $P_{1,4}$, $P_{1,5}$, $P_{1,6}$, $P_{1,7}$	$P_{4,7}$, $P_{6,7}$
[2,7]	s1,s2,s4,s6,s7	$P_{1,2}$, $P_{1,6}$, $P_{1,7}$, $P_{2,4}$, $P_{2,6}$, $P_{2,7}$, $P_{4,6}$, $P_{4,7}$, $P_{6,7}$	$P_{4,7}$, $P_{6,7}$	[6,8]	s1,s2,s3,s4,s5,s6	$P_{1,3}$, $P_{1,4}$, $P_{1,5}$, $P_{1,6}$, $P_{1,7}$	$P_{2,4}$, $P_{2,6}$, $P_{4,7}$, $P_{6,7}$
[2,8]	s1,s2	$P_{1,2}$, $P_{1,6}$, $P_{1,7}$, $P_{2,4}$, $P_{2,6}$, $P_{2,7}$, $P_{4,6}$, $P_{4,7}$, $P_{6,7}$	$P_{2,4}$, $P_{2,6,}$ $P_{4,7}$, $P_{6,7}$	[6,9]	s1,s3,s5,s7	$P_{1,3}$, $P_{1,4}$, $P_{1,5}$, $P_{1,6}$, $P_{1,7}$	
[2,9]	s1,s2,s4,s6,s7	$P_{1,2}$, $P_{1,6}$, $P_{1,7}$, $P_{2,4}$, $P_{2,6}$, $P_{2,7}$, $P_{4,6}$, $P_{4,7}$, $P_{6,7}$		[6,10]	s1,s2,s3,s4,s5,s6	$P_{1,3}$, $P_{1,5}$, $P_{2,4}$, $P_{2,6}$, $P_{2,7}$	$P_{1,4}$, $P_{1,6}$, $P_{1,7}$, $P_{2,4}$, $P_{2,6}$, $P_{2,7}$
[2,10]	s1	$P_{1,2}$, $P_{1,4}$, $P_{1,6}$, $P_{1,7}$, $P_{4,6}$, $P_{4,7}$, $P_{6,7}$	$P_{1,4}$, $P_{1,6}$, $P_{1,7}$, $P_{2,4}$, $P_{2,6}$, $P_{2,7}$	[7,8]	s2,s4,s6,s7		$P_{2,4}$, $P_{2,6}$, $P_{4,7}$, $P_{6,7}$
[3,4]	s4,s6,s7			[7,9]	s7		$P_{4,7}$, $P_{6,7}$
[3,5]	s1,s3,s4,s5,s6	$P_{1,3}$, $P_{1,4}$, $P_{1,5}$, $P_{1,6}$, $P_{1,7}$		[7,10]	s1,s2,s4,s6,s7	$P_{1,4}$, $P_{1,6}$, $P_{1,7}$, $P_{2,4}$, $P_{2,6}$, $P_{2,7}$	$P_{1,4}$, $P_{1,6}$, $P_{1,7}$, $P_{2,4}$, $P_{2,6}$, $P_{2,7}$, $P_{4,7}$, $P_{6,7}$
[3,6]	s1,s3,s5,s7	$P_{1,3}$, $P_{1,4}$, $P_{1,5}$, $P_{1,6}$, $P_{1,7}$		[8,9]	s2,s4,s6,s7		$P_{2,4}$, $P_{2,6}$, $P_{4,7}$, $P_{6,7}$
[3,7]			$P_{4,7}$, $P_{6,7}$	[8,10]	s1,s2	$P_{1,4}$, $P_{1,6}$, $P_{1,7}$, $P_{2,4}$, $P_{2,6}$, $P_{2,7}$	$P_{1,4}$, $P_{1,6}$, $P_{1,7}$, $P_{2,7}$, $P_{4,7}$, $P_{6,7}$
[3,8]	s2,s4,s6,s7		$P_{2,4}$, $P_{2,6}$, $P_{4,7}$, $P_{6,7}$	[9,10]	s1,s2,s4,s6,s7	$P_{1,4}$, $P_{1,6}$, $P_{1,7}$, $P_{2,4}$, $P_{2,6}$, $P_{2,7}$	$P_{1,4}$, $P_{1,6}$, $P_{1,7}$, $P_{2,4}$, $P_{2,6}$, $P_{2,7}$,

[3,9]	s7

6.1.2 Five-Tank Case Study

The five-tank system from Bhushan and Rengaswamy[181] is considered as the next case study in this work. Figure 83 shows the schematic of the process. Lists of measured variables and simulated faults are shown in Table 24 and Table 25, respectively.

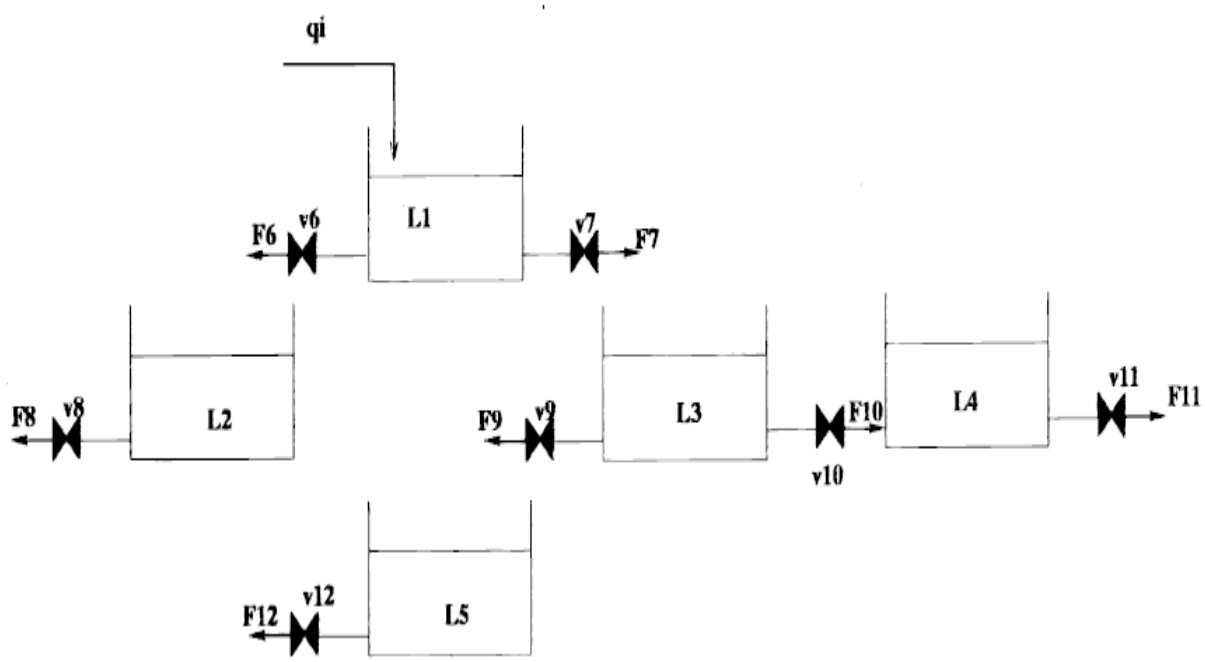

Figure 83. Schematic of the five-tank case-study[181]

Table 24. List of measured variables in five-tank case-study

Sensor no.	Measured variable	Description	Sensor no.	Measured variable	Description
s1	*L1*	Level in Tank 1	s7	*F7*	Stream 7
s2	*L2*	Level in Tank 2	s8	*F8*	Stream 8
s3	*L3*	Level in Tank 3	s9	*F9*	Stream 9
s4	*L4*	Level in Tank 4	s10	*F10*	Stream 10
s5	*L5*	Level in Tank 5	s11	*F11*	Stream 11
s6	*F6*	Stream 6	s12	*F12*	Stream 12

Table 25. List of simulated faults and the corresponding affected sensors in five-tank case-study

Fault	Description	Affected sensors

1	q_i^+	Inlet flow	s1,s2,s3,s4,s5,s6,s7,s8,s9,s10,s11,s12
2	q_i^-		s1,s2,s3,s4,s5,s6,s7,s8,s9,s10,s11,s12
3	*V6*	Valve closed	s1,s2,s3,s4,s5,s6,s7,s8,s9,s10,s11,s12
4	*V7*		s1,s2,s3,s4,s5,s6,s7,s8,s9,s10,s11,s12
5	*V8*		s2,s8
6	*V9*		s2,s3,s4,s5,s8,s9,s10,s11,s12
7	*V10*		s2,s3,s4,s5,s8,s9,s10,s11,s12
8	*V11*		s2,s3,s4,s5,s8,s9,s10,s11,s12
9	*V12*		s2,s5,s8,s12
10	*LT1*	Leakage in tank	s1,s2,s3,s4,s5,s6,s7,s8,s9,s10,s11,s12
11	*LT2*		s2,s8
12	*LT3*		s3,s4,s5,s9,s10,s11,s12
13	*LT4*		s3,s4,s5,s9,s10,s11,s12
14	*LT5*		s5,s12

The solution to the optimization problem is shown in Table 26 that compares the different algorithms. Although faults q_i^- and *LT1* are not resolvable by SDG, both FES and MR can resolve these faults. At low and medium MR threshold level, the cost of the sensor network is the same as FES as well as SDG. Interestingly, at low MR threshold level, the combination of both algorithms picks a subset of the selected sensors by both algorithms and resolves all the faults at lower sensor network cost. At medium MR threshold level, the sensor network cost is similar to the sensor network cost of the FES algorithm, thus, the combination of the algorithms will have the same result as if the algorithms are performed individually. Interestingly, the selected sensors are not a combination of sensors selected through individual algorithms since there are multiple solutions to the optimization problem when algorithms are combined. At high MR threshold value, the sensor network cost is reduced compared to other algorithms, thus, the combination of the algorithms will have the same sensor network cost as the MR algorithm. Table 25 and Table 27 show the affected variables for each fault and the fault resolution using all algorithms individually. The fault resolution of MR algorithm shown in Table 27 is shown only for low MR threshold level (value of 1.1). For compactness, only key rows of the fault resolution are shown and pairs that are combination of sensors in SDG results are not shown.

Table 26. Results of applying different algorithms to five-tank case-study

Algorithm(s)	MR threshold level	Selected sensors	Sensor network cost	Irresolvable fault sets
SDG		s2,s4,s5,s10	4	[2,10]
FES		s2,s4,s9,s12	4	[ ]
MR	Low	s2,s10,s11,s12	4	[ ]
	Medium	s2,s10,s11,s12	4	[ ]
	High	s2,s5,s10	3	[ ]

FES & MR	Low	s2,s11,s12	3	[ ]
	Medium	s2,s8,s10,s12	4	[ ]
	High	s2,s5,s10	3	[ ]

Table 27. Fault resolution by SDG, FES and MR in five-tank case-study

Fault	Resolution sensors			Fault	Resolution sensors		
	Singles	Pairs			Singles	Pairs	
		FES	MR			FES	MR
[1,4]	s2,s7,s8		$P_{5,9}$	[4,10]	s1,s3,s4,s5, s6,s9,s10,s 11,s12	$P_{2,8}$	$P_{2,7}$, $P_{2,8}$, $P_{7,8}$
[1,6]	s1,s5,s6,s7 ,s8,s9,s12		$P_{2,3}$	[4,11]	s1,s3,s4,s5, s6,s7,s9,s1 0,s11,s12		
[1,7]	s1,s4,s6,s7 ,s8,s10,s1 1	$P_{2,9}$	$P_{2,3}$,$P_{5,9}$	[6,8]	s5,s9,s10,s 11,s12	$P_{3,4}$	$P_{3,4}$
[1,8]	s1,s6,s7,s8 ,s10,s11	$P_{2,9}$,$P_{3,4}$, $P_{4,9}$	$P_{2,3}$, $P_{3,4}$	[6,9]	s3,s4,s5,s9, 10,s11	$P_{2,12}$, $P_{8,12}$	$P_{8,12}$
[2,4]	s1,s3,s4,s5 ,s6,s9,s10, s11,s12	$P_{2,8}$		[6,10]	s1,s2,s3,s4, s6,s7,s10,s 11	$P_{5,12,}$ $P_{8,9}$	$P_{5,8}$, $P_{5,9}$, $P_{5,12}$, $P_{8,9}$, $P_{8,12}$, $P_{9,12}$
[2,6]	s1,s2,s3,s4 ,s6,s7,s10, s11	$P_{5,12,}$ $P_{8,9}$	$P_{8,9}$	[6,12]	s2,s3,s4,s8, s10,s11	$P_{5,12}$	$P_{5,9}$, $P_{9,12}$
[2,7]	s1,s2,s3,s5 ,s6,s7,s9,s 12	$P_{8,10}$	$P_{4,8}$	[6,13]	s2,s3,s4,s8, s11	$P_{5,12,}$ $P_{9,10}$	$P_{5,9}$, $P_{5,12}$, $P_{9,12}$
[2,8]	s1,s2,s3,s4 ,s5,s6,s7,s 9,s12	$P_{8,10}$,$P_{8,11}$, $P_{10,11}$	$P_{8,10,}$ $P_{8,11}$, $P_{10,11}$	[6,14]	s2,s3,s4,s8, s9,s10,s11		
[2,9]	s1,s2,s3,s4 ,s5,s6,s7,s 9,s10,s11	$P_{8,12}$	$P_{8,12}$	[7,8]	s4	$P_{2,11}$, $P_{8,10}$, $P_{8,11}$, $P_{10,11}$	$P_{5,9}$, $P_{8,10}$, $P_{8,11}$, $P_{10,11}$
[2,12]	s1,s2,s6,s7 ,s8		$P_{3,4}$, $P_{3,10}$, $P_{4,10}$, $P_{5,9}$, $P_{5,11}$, $P_{9,10}$, $P_{9,12}$, $P_{11,12}$	[7,9]	s3,s4,s9,s1 0,s11,s12		$P_{2,5}$
[2,13]	s1,s2,s6,s7 ,s8,s10	$P_{3,4}$, $P_{3,11}$, $P_{4,9}$, $P_{9,11}$	$P_{3,12}$, $P_{3,5,}$ $P_{3,9,}$ $P_{3,11,}$ $P_{5,9,}$ $P_{5,11,}$ $P_{5,12,}$ $P_{9,12}$	[7,10]	s1,s2,s3,s5, s6,s7,s9,s1 2	$P_{8,10}$	$P_{4,8}$, $P_{4,10}$, $P_{4,11,}$ $P_{8,10}$, $P_{8,11}$ $P_{10,11}$
[3,6]	s1,s3,s4,s6 ,s7,s8,s10,	$P_{5,12}$		[7,12]	s2,s3,s5,s8, s9,s12		$P_{4,10}$

	s11						
[3,7]	s1,s3,s5,s6,s7,s8,s9,s12	$P_{2,4}$,$P_{2,11}$		[8,9]	s3,s4,s9,s10,s11,s12		$P_{2,5}$
[3,8]	s1,s3,s4,s5,s6,s7,s8,s9,s12	$P_{10,11}$	$P_{10,11}$	[8,10]	s1,s2,s3,s4,s5,s6,s7,s9,s12	$P_{8,10}$, $P_{8,11}$, $P_{10,11}$	$P_{8,10,}$ $P_{8,11}$, $P_{10,11}$
[3,9]	s1,s3,s4,s5,s6,s7,s8,s9,s10,s11	$P_{2,12}$		[8,12]	s2,s3,s4,s5,s8,s9,s12	$P_{10,11}$	$P_{10,11}$
[3,14]	s1,s2,s3,s4,s6,s7,s8,s9,s10,s11	$P_{5,12}$		[9,10]	s1,s2,s3,s4,s5,s6,s7,s9,s10,s11	$P_{8,12}$	$P_{8,12}$
[4,6]	s1,s2,s5,s6,s7,s9,s12			[10,12]	s1,s2,s6,s7,s8		$P_{3,5,}$ $P_{3,9,}$ $P_{3,10,}$ $P_{3,11,}$ $P_{3,12,}$ $P_{4,5,}$ $P_{4,9,}$ $P_{4,10,}$ $P_{4,11,}$ $P_{4,12,}$ $P_{5,10,}$ $P_{5,12,}$ $P_{10,11,}$ $P_{10,12}$
[4,7]	s1,s2,s4,s6,s7,s10,s11			[10,13]	s1,s2,s6,s7,s8,s10	$P_{3,4,}$ $P_{3,11,}$ $P_{4,9,}$ $P_{9,11}$	$P_{3,4,}$ $P_{3,12,}$ $P_{4,5,}$ $P_{4,9,}$ $P_{4,11,}$ $P_{4,12,}$ $P_{11,12}$
[4,8]	s1,s2,s6,s7,s10,s11	$P_{3,4}$,$P_{4,9}$	$P_{3,4,}$ $P_{5,9}$	[12,13]	s10	$P_{3,4,}$ $P_{3,11,}$ $P_{4,9,}$ $P_{9,11}$	$P_{3,4,}$ $P_{3,5,}$ $P_{3,9,}$ $P_{3,11,}$ $P_{5,12,}$ $P_{11,12}$

6.1.3 Tennessee Eastman Case Study

Tennessee Eastman (TE) process, first introduced by Downs and Vogel[194], has been widely used as a benchmark problem for process control, optimization, diagnosis and etc. Figure 84 shows the schematic of the TE process. An MPC controlled TE developed by Ricker and Lee[195] is considered in this work. A detailed description of the process with detailed qualitative SDG analysis of the process has been presented by Bhushan and Rengaswamy[196] and Maurya et al.[197] A total of 33 faults considered by Maurya et al.[197] are simulated in the process and the 40 variables are stored together for further analysis. Table 28 and Table 29 show lists of variables and faults considered in this work, respectively.

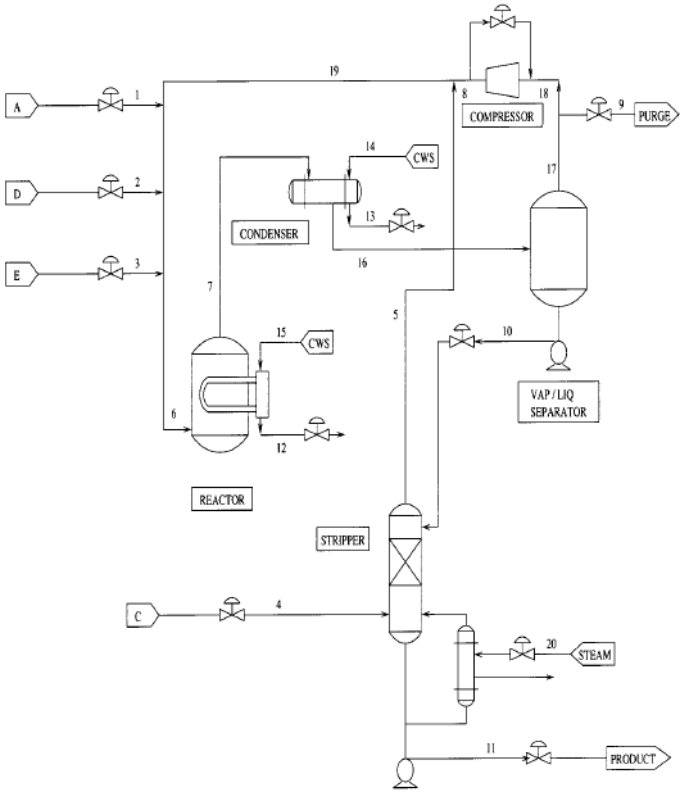

Figure 84. TE process flowsheet[196]

Table 28. List of measured variables in TE process[197]

Sensor no.	Measured variable	Description	Sensor no.	Measured variable	Description
s1	*F7*	Stream 7	s21	$y_{D,6}$	D in stream 6
s2	*F1*	Stream 1	s22	$y_{E,6}$	E in stream 6
s3	*F2*	Stream 2	s23	$y_{F,6}$	F in stream 6
s4	*F3*	Stream 3	s24	$y_{A,9}$	A in stream 9
s5	*F4*	Stream 4	s25	$y_{B,9}$	B in stream 9
s6	*F8*	Stream 8	s26	$y_{C,9}$	C in stream 9
s7	*F9*	Stream 9	s27	$y_{D,9}$	D in stream 9
s8	*F10*	Stream 10	s28	$y_{E,9}$	E in stream 9
s9	*F11*	Stream 11	s29	$y_{F,9}$	F in stream 9
s10	T_{cr}	Reactor temperature	s30	$y_{G,9}$	G in stream 9
s11	T_{cs}	Separator temperature	s31	$y_{H,9}$	H in stream 9
s12	P_r	Reactor pressure	s32	$x_{G,11}$	G in stream 11
s13	*VLr*	Reactor liquid holdup	s33	$x_{H,11}$	H in stream 11
s14	P_s	Separator pressure	s34	$P_{A,r}$	A in reactor
s15	*VLs*	Separator liquid holdup	s35	$P_{C,r}$	C in reactor

s16	VLp	Product liquid holdup	s36	$P_{D,r}$	D in reactor
s17	$F6$	Stream 6	s37	$P_{E,r}$	E in reactor
s18	$y_{A,6}$	A in stream 6	s38	VLr_e	Error signal VL_r
s19	$y_{B,6}$	B in stream 6	s39	VLs_e	Error signal VL_s
s20	$y_{C,6}$	C in stream 6	s40	VLp_e	Error signal VL_p

Table 29. List of simulated faults in TE process[197]

Fault no.	Description	Fault no.	Description
1,9	$F1^+$, $F1^-$	17,26	VLr_m^{set+}, VLr_m^{set-}
2,10	$F2^+$, $F2^-$	18,27	$VLr_{VP,bias}^{+}$, $VLr_{VP,bias}^{-}$
3,11	$F3^+$, $F3^-$	19,28	$VLs_{m,bias}^{+}$, $VLs_{m,bias}^{-}$
4,12	$F4^+$, $F4^-$	20,29	VLs_m^{set+}, VLs_m^{set-}
5,13	$F8^+$, $F8^-$	21,30	$VLs_{VP,bias}^{+}$, $VLs_{VP,bias}^{-}$
6,14	$F9^+$, $F9^-$	22,31	$VLp_{m,bias}^{+}$, $VLp_{m,bias}^{-}$
7,15	T_r^+, T_r^-	23,32	VLp_m^{set+}, VLp_m^{set-}
8	C_d^-	24,33	$VLp_{VP,bias}^{+}$, $VLp_{VP,bias}^{-}$
16,25	$VLr_{m,bias}^{+}$, $VLr_{m,bias}^{-}$		

Table 30 shows the comparison of SDG, FES and MR for TE process. FES is preferred over SDG algorithm as it has lower sensor network cost and number of irresolvable fault sets. At low MR threshold level, MR resolves same number of faults with lower sensor network cost compared to FES. As can be seen in Table 30, FES and MR have the same sensors except that "s12" -pressure sensor- is not present in the network for MR algorithm. Therefore, the combination of both algorithms takes advantage of the MR algorithm. At medium MR threshold level, MR only shows slight improvement over SDG algorithm in terms of the sensor network cost, thus, the combination of both FES and MR takes advantage of the FES. At high MR threshold level, MR shows no improvement over SDG algorithm and the combination of both FES and MR takes advantage of the FES algorithm. For compactness, presenting large matrix of affected variables and faults resolution are avoided. Table 31 only presents fault resolution for the fault sets that are resolvable by FES and MR algorithms but not SDG.

Table 30. Results of applying different algorithms to TE process

Algorithm(s)	MR value level	Selected sensors	Sensor network cost	Irresolvable fault sets
SDG		s2,s3,s7,s8,s9,s10,s11,s15,s16	7.2	[16,26],[16,27],[17,18],[17,25],[18,25],[19,29],[20,28],[22,32],[23,31],[26,27]
FES		s2,s7,s8,s9,s11,s12,s15,s16	6.6	[16,26],[17,25],[19,29],[20,28],[22,32],[23,31]

MR	Low	s2,s7,s8,s9,s11,s15,s16	6.1	Same as FES
	Medium	s2,s3,s7,s8,s9,s11,s15,s16	7.1	Same as SDG
	High	s2,s3,s7,s8,s9,s10,s11,s15,s16	7.2	Same as SDG
FES & MR	Low	s2,s7,s8,s9,s11,s15,s16	6.1	Same as FES
	Medium	s2,s7,s8,s9,s11,s12,s15,s16	6.6	Same as FES
	High	s2,s7,s8,s9,s11,s12,s15,s16	6.6	Same as FES

Table 31. Fault resolution by SDG, FES and MR in TE process

Fault	Resolution sensors			Fault	Resolution sensors		
	Singles	Pairs			Singles	Pairs	
		FES	MR			FES	MR
[16,27]		$P_{8,16}$,$P_{8,40}$	$P_{8,13}$, $P_{8,16}$, $P_{9,13}$, $P_{9,15}$, $P_{9,16}$, $P_{11,13}$, $P_{11,16}$, $P_{14,16}$, $P_{15,17}$, $P_{16,17}$	[18,25]		$P_{8,16}$,$P_{8,40}$	$P_{8,13}$, $P_{8,16}$, $P_{9,13}$, $P_{9,16}$, $P_{11,13}$,$P_{15,16}$
[17,18]		$P_{8,16}$,$P_{8,40}$	$P_{8,13}$, $P_{8,16}$, $P_{9,13}$, $P_{9,16}$, $P_{11,13}$, $P_{15,16}$	[26,27]		$P_{8,16}$,$P_{8,40}$	$P_{8,13}$, $P_{8,16}$, $P_{9,13}$, $P_{9,15}$, $P_{9,16}$, $P_{11,13}$, $P_{11,16}$, $P_{14,16}$, $P_{15,17}$, $P_{16,17}$

6.1.4 SELEXOL Process Case Study

As a unit in integrated gasification combined cycle (IGCC), the acid gas removal unit is used for removing H_2S and CO_2 contents of the syngas using SELEXOL solvent. The pressure-driven dynamic model SELEXOL process that is used in our work is developed in the work of Bhattacharyya et al.[198], where Figure 85 shows the configuration of the SELEXOL process used in their study. The entire model has 24597 variables. However, considering all the variables makes the FES and MR algorithms intractable. Therefore, only variables that respond to DG (or SDG) algorithms are taken to account since the rest of the variables will not have any effect in FES and MR. After removing such variables, 542 variables are left for performing the algorithms. In order to save space, showing the lists of all measured variables and variables that respond to each fault are avoided and only the key variables are shown in Table 32. Table 33 shows the list of faults considered in the SELEXOL process.

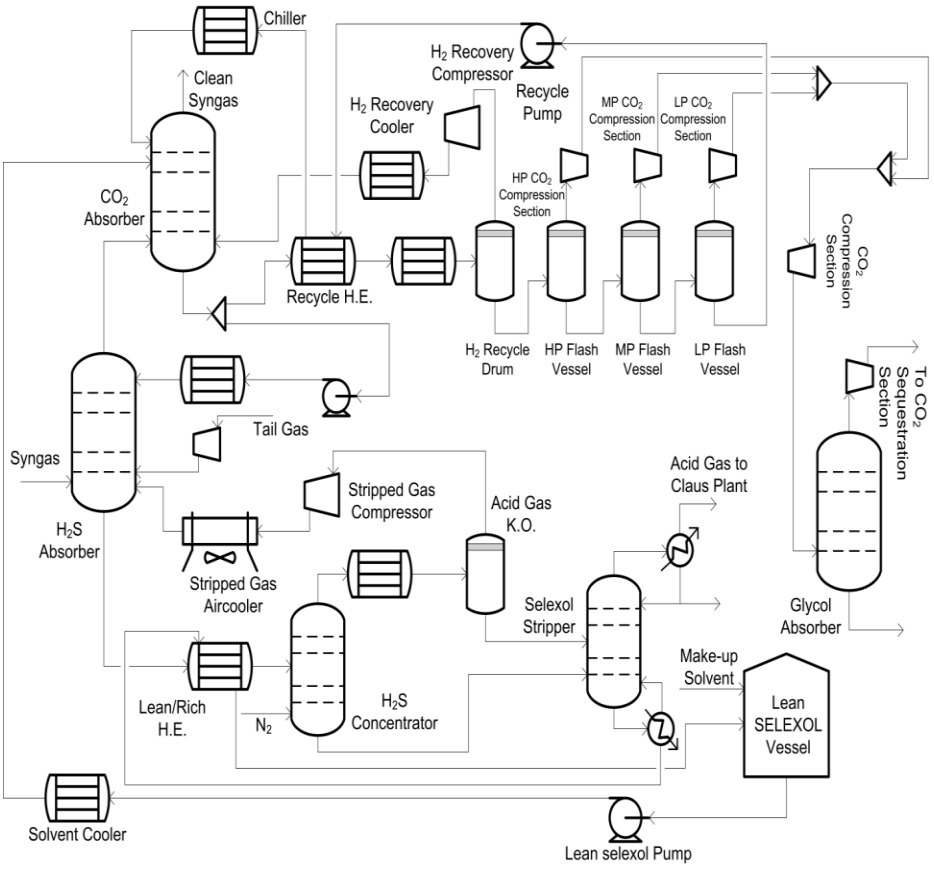

Figure 85. Schematic of the SELEXOL process[198]

Table 34 shows the comparison of different algorithms for SELEXOL process. Although all faults are resolvable by all algorithms, there is a slight improvement in sensor network cost by applying FES and MR compared to SDG. All algorithms suggest that for resolving all faults, flow and concentration sensors are mainly required. FES algorithm uses a temperature sensor less than SDG although only sensor s1 is the same in both algorithms. Therefore, the sensor network cost is reduced. At low and medium MR threshold level, less temperature sensors are selected and the sensor network cost is reduced compared to FES and the combination of FES and MR takes advantage of the results of MR. At high MR threshold level there is no improvement from SDG and the combination of FES and MR takes advantage of results of FES.

Table 32. List of measured variables in SELEXOL process

Sensor no.	Measured variable	Description
s1	*BLOCKS.("SELST").Stage(7).Mc("N2")*	N_2 composition in 7th tray of SELEXOL stripper
s2	*BLOCKS.("SELST").Stage(10).Mc("NH3")*	NH_3 composition in 10th tray of SELEXOL stripper
s3	*BLOCKS("LENPUR").T*	Pure SELEXOL from SELEXOL stripper temperature
s4	*BLOCKS("CO2ABS").Stage(10).T*	10th tray of CO_2 absorber temperature

s5	*STREAMS("LPCO2-2").T*	1st stage compression of LP CO_2 temperature
s6	*STREAMS("CO2FMMP2").F*	CO_2 stream top of flash vessel at MP flow rate
s7	*STREAMS("MKUPSEL1").F*	Make-up SELEXOL stream flow rate
s8	*BLOCKS("SELST").Stage(10).Mc("H2S")*	H_2S composition in 10th tray of SELEXOL stripper
s9	*BLOCKS("H2SCONC").Stage(6).T*	6th tray of H_2S concentrator temperature
s10	*BLOCKS("SELST").Stage(6).T*	6th tray of SELEXOL stripper temperature
s11	*STREAMS("CO2FMMP3").F*	CO_2 stream from LP flash vessel to 1st stage compressor flow rate
s12	*BLOCKS("CO2ABS").Stage(5).Mc("H2S")*	H_2S composition in 5th tray of CO_2 absorber
s13	*STREAMS("2MPHPMIX").F*	CO_2 stream from HP flash vessel to mix with MP stream flow rate
s14	*BLOCKS("H2SCONC").Stage(4).Mc("COS")*	COS composition in 4th tray of H_2S concentrator
s15	*BLOCKS("CO2ABS").Stage(7).T*	7th tray of CO_2 absorber temperature
s16	*STREAMS("2LPMPMXR").F*	CO_2 stream from MP flash vessel to mix with LP stream flow rate
s17	*BLOCKS("SELST").Stage(8).Mc("DIMET-02")*	SELEXOL composition in 8th tray of SELEXOL stripper
s18	*BLOCKS("CO2ABS").Stage(4).Mc("H2S")*	H_2S composition in 4th tray of CO_2 absorber
s19	*BLOCKS("SELST").Stage(11).Mc("NH3")*	NH_3 composition in 11th tray of SELEXOL stripper
s20	*BLOCKS("H2SSTRBT").HotOutVol(1).Mc("H2S")*	H_2S composition in bottom stream of H_2S absorber fed to concentrator
s21	*STREAMS("SEL2PMP").T*	Temperature of circulating SELEXOL stream from tank
s22	*BLOCKS("SELST").Stage(8).Mc("H2S")*	H_2S composition in 8th tray of SELEXOL stripper
s23	*BLOCKS("SELST").Stage(9).Mc("NH3")*	NH_3 composition in 9th tray of SELEXOL stripper
s24	*BLOCKS("SELMXTK").T*	SELEXOL mixing tank temperature
s25	*STREAMS("2MPHPMX1").F*	CO_2 stream from HP flash vessel to mix with MP stream flow rate

Table 33. List of simulated faults in SELEXOL process

Fault no.	Fault symbol	Description
1	*F1*	Reduction in area of 13th tray of CO_2 absorber by 15%
2	*F2*	Reduction in area of bottom (15th) tray of CO_2 absorber by 15%
3	*F3*	Reduction in area of 23rd tray of H_2S absorber by 15%
4	*F4*	Reduction in area of bottom (26th) tray of H_2S absorber by 15%
5	*F5*	Reduction in area of 4th tray of H_2S concentrator by 15%

6	*F6*	Reduction in area of bottom (6^{th}) tray of H_2S concentrator by 15%
7	*F7*	Reduction in overall heat transfer coefficient of Lean/Rich H.E. by 15%
8	*F8*	1% leakage in the H_2 recovery compressor suction line
9	*F9*	1% vapor leakage in H_2 recovery flash drum
10	*F10*	1% vapor leakage in CO_2 high pressure flash drum
11	*F11*	1% vapor leakage in CO_2 low pressure flash drum
12	*F12*	1% vapor leakage in CO_2 medium pressure flash drum
13	*F13*	Reduction in area of 8^{th} tray of SELEXOL stripper by 15%
14	*F14*	Reduction in area of bottom (11^{th}) tray of SELEXOL stripper by 15%

Table 34. Results of applying different algorithms to SELEXOL process

Algorithm(s)	MR value level	Selected sensors	Sensor network cost	Irresolvable fault sets
SDG		s1,s2,s3,s4,s5,s6,s7	22.3	[ ]
FES		s1,s7,s8,s9,10,s11	22.2	[ ]
MR	Low	s1,s7,s12,s13	22	[ ]
	Medium	s7,s8,s14,s15,s16	22.1	[ ]
	High	s1,s6,s7,s10,s15,s16,s17	22.3	[ ]
FES & MR	Low	s7,s11,s18,s19	22	[ ]
	Medium	s7,s8,s11,s20,s21	22.1	[ ]
	High	s7,s10,s22,s23,s24,s25	22.2	[ ]

6.1.5 Combined Cycle Case Study

The combined cycle island consists of a series of heat exchangers and the gas turbines (GT) and steam turbines (ST) as shown in Figure 86. Clean synthesis gas, exiting the SELEXOL unit is heated and mixed with N_2, which is used as a diluent. After going through an expander, it is sent to the combustor of the GT. Two advanced "F" class combustion turbines partially integrated with an elevated-pressure air separation unit (ASU) are modeled in Aspen Plus Dynamics. The hot flue gas exhaust from the GT is used to generate high pressure, intermediate pressure and low pressure steam in the heat recovery steam generator (HRSG). The flue gas is finally vented to the atmosphere. The steam generated using the HRSG is used to produce power in the ST.

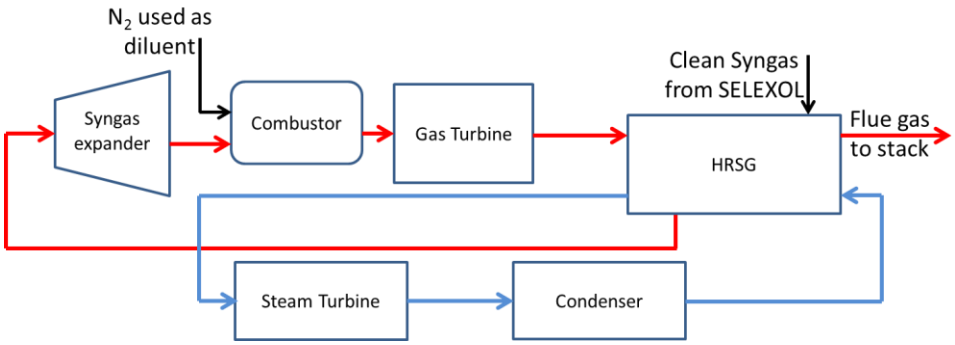

Figure 86. Schematic of the combined cycle power plant.

6.1.5.1 Model development

The combined cycle model is taken from the work of Bhattacharyya et al.[1] and has been modified to be able to incorporate faults. The gas turbine (GT) converts the chemical energy in the supplied hydrogen-rich syngas fuel into shaft work which turns a generator and produces electricity.

The GT is simulated using turbine models available in the Aspen Plus library on the basis of the specifications of a GEE 7FB turbine. N2 is used as a diluent and is manipulated by a design specification so that the lower heating value (LHV) of the syngas fuel is reduced to 4.55 MJ Nm^3 to keep the NOx concentrations in the ppmv range in the exhaust. The combustion air is compressed in an axial flow compressor which raises the ambient air to a pressure of 1.65 MPa. When the flow of combustion air is manipulated, the GT combustor temperature is maintained at 1377 °C with a specified heat loss equal to 1.5% of the lower heating value (LHV) of the syngas. The GT firing temperature is maintained at 1327 °C by a design specification which manipulates the air flow rate to the combustor outlet gas before it reaches the first expansion stage. The air flow rates to the second and third expansion stages are maintained at predetermined values. The isentropic efficiencies of the GT are manipulated such that the exhaust temperature is maintained at 566 °C. The isentropic efficiencies of all the three stages are assumed to be equal. The flue gas goes to the heat recovery steam generator (HRSG) where steam is generated at three pressure levels. The flue gas is used to superheat the HP steam generated both in the HRSG evaporator and in the radiant syngas cooler before it finally exits the system at 132 °C, well above the cold end corrosion temperature.

The steam cycle generates steam from the flue gas and other process streams at three pressure levels. The minimum temperature approach is considered to be 10 °C in this study. HP steam, generated at 12.4 MPa and 538 °C, is mainly used for generating power in the HP steam turbine (ST). IP steam is used for generating power, as well as in the reboilers. LP steam generated in the HRSG is mainly used for heating process streams and in the reboilers. Condensate at the outlet of the surface condenser and from the LP steam circuit and flash steam from the HP blow down drum are sent to the deaerator. The BFW at the outlet of the deaerator is pumped at various pressure levels for generating HP, IP, and LP steam. The HP stream is heated and sent to the RSC and HRSG. It is then superheated and sent to the HP turbine. IP BFW passes through the economizer and evaporator to generate IP steam which is sent to the IP turbine. The LP split of the BFW is used to generate LP and IP steam. The exit temperature of the flue gas above the cold end corrosion temperature is maintained by manipulating the flow of the BFW that goes to the LP steam evaporator. IP steam

The faults simulated in the combined cycle island include leakage at several locations, fouling within a few heat exchangers and an increased loss of heat through the combustor. Since the turbines itself are highly advanced and consist of several sensors that detect and report any deviation from operation immediately, faults in these units have not been simulated. The leakage faults are mainly considered for the heat exchangers where high pressure differences exist between the shell and tube sides. Fouling is a concern within the heat exchangers as well. These faults are modeled similar to the methods mentioned

earlier for the SELEXOL unit. The GT combustor has insulation to prevent heat loss to the environment. However, the insulation might get damaged in the course of operation and this can be modeled by increasing the heat loss in the GT combustor block.

6.1.5.2 Fault Simulation

The combined cycle section was segregated from the plant wide model developed in the works of Bhattacharyya et al[31]. The faults to be simulated in the combined cycle unit were identified. With the exception of Fault 5, all faults are simulated with a ramp function of 1 hour duration initiated after half an hour of simulation. The faults that were selected and implemented are as follows:

1. Leakage from the high pressure steam flash vessel

Steam at very high temperature and pressure is produced in a steam generator block using the heat from hot flue gas. The steam produced is then sent to the high pressure steam turbine. A leakage in the high pressure steam generator can cause mixing of the steam with the flue gas which could build up in the steam cycle.

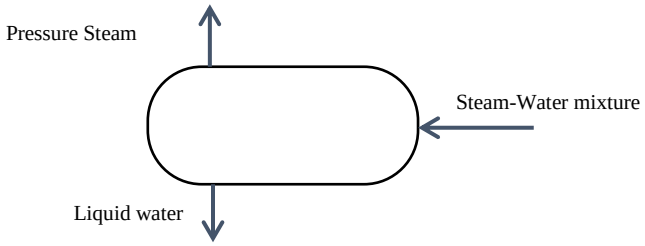

Figure 87. Schematic of the high pressure steam generation vessel.

2. Leakage within a HE between syngas and steam streams

This heat exchanger is used to heat in the hydrogen rich syngas from the Selexol plant before being sent to the combustor. The steam stream is at higher pressure and a rupture in the tube could result in steam entering the gas cycle. This could negatively impact the combustion process and the power generated in the gas turbines.

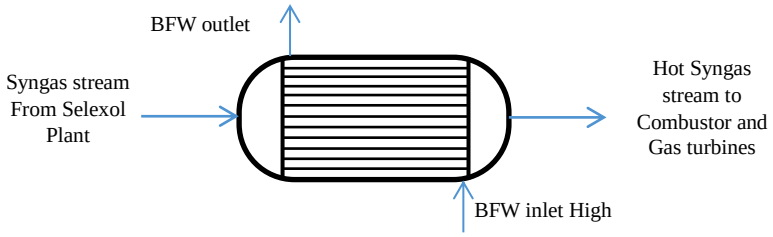

Figure 88. Schematic of the heat exchanger between the syngas stream and the high pressure steam.

3. Leakage within a Condenser between Steam and water streams

Usually a composition sensor placed at the one of the streams exiting the HE would be able to detect any leakage taking place within the HE. However, if the heat transfer involves two streams of the same material, this becomes difficult. In this unit, we have considered a leakage of cooling water into the condensing steam.

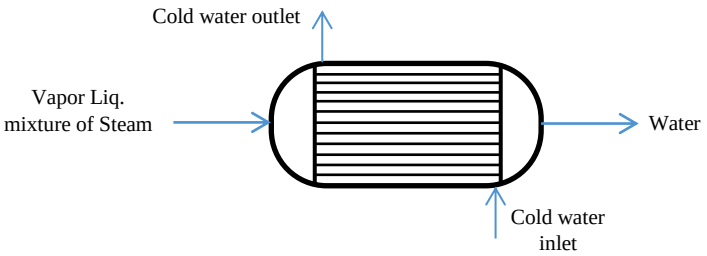

Figure 89. Schematic of the condenser where steam/condensate is cooled by cooling water.

4. Fouling simulated as loss of area within HE

A fouling fault is simulated in the heat exchanger used to cool the flue gas from the combustor using steam. The combustor flue gas could have particulate matter entrained from the N_2 stream that could deposit on the walls of the HE. This fault is simulated by decreasing the surface area of the HE.

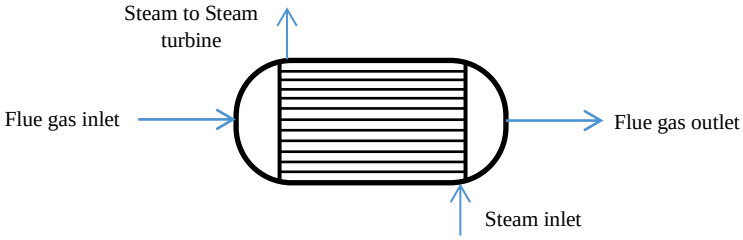

Figure 90. Schematic of the heat exchanger (part of HRSG) where the combusted syngas is used to superheat the steam.

5. Increase in heat loss from the combustor

The combustor operates at high temperatures and has insulation to limit the heat loss to the environment. However, the insulation might get damaged or may suddenly fall off in course of operation. This fault is modeled by introducing a step change in the heat loss from the GT combustor block after half an hour of simulation time.

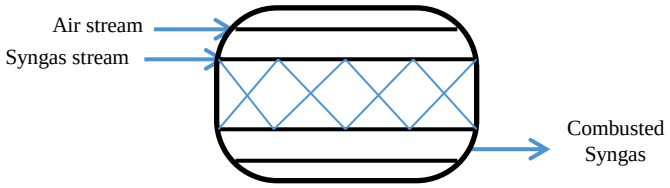

Figure 91. Schematic of the gas turbine combustor.

6. Leakage within a HE between combusted syngas and steam stream.(IPEVAP1)

A leakage in an IP steam generator HE is simulated where heat from flue gas at almost atmospheric pressure is used to generate steam. This fault is to see if a sensor can be found to differentiate faults in heat exchangers operating at different pressures.

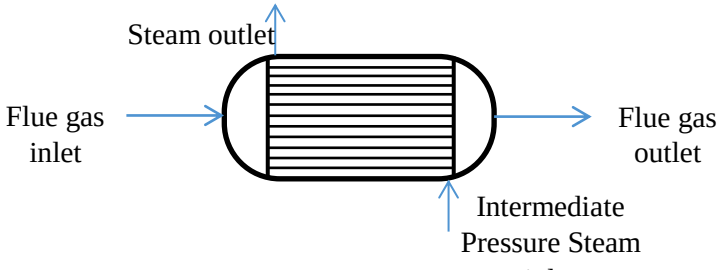

Figure 92. Heat exchanger cooling combusted syngas with intermediate pressure steam.

7. Fouling simulated as loss of area within HE

In this fault, the same HE as Fault 2 has been used to simulate a fouling fault. In the SELEXOL process, there can be some foaming or formation of undesirable chemicals on the trays of the absorbers. These materials could be carried by the syngas and could deposit on the heat exchanger surfaces thereby reducing the surface area for heat exchange.

The faults were initially simulated while recording minimum number of variables. The following guidelines were used in order to select these variables:

1. Instead of the molar flow, the volumetric flow rate is recorded. This is because, in the industry, typically the volumetric flow rates are measured.
2. Across a HE the composition is not expected to change. Therefore, only pressure, flow rate and temperature are recorded.
3. Pressure and temperatures after splitter/mixers are not recorded.
4. Only pressures after valves or other pressure-drop devices are recorded.
5. The composition of only the gas stream exiting the flash vessel is recorded. The pressure and temperature of the vessel is recorded. Note that the exiting streams will have the same pressure and temperatures as the vessel.
6. Levels in flash vessels were recorded.
7. Power outputs from turbines were recorded.

These criteria however would result in the omission of variables that could help in the detection of faults involving a leak of dissimilar materials. For example, as a result of Fault 2, the composition of the syngas stream would change. Under the previous context, these changes would go undetected as the stream does not undergo any chemical change in the section until the combustor. Each unit in the combined cycle section is checked for all possible faults that can occur, and accordingly the final set of variables to be recorded are obtained.

6.1.5.3 Study of Fault Effects

For the sake of brevity of this report, we will show the responses of only a few select variables due to a few select faults. In Fault 2, water leaks into the syngas stream. Hot water is used to heat the syngas stream from the SELEXOL unit before it is sent to the combustor of the gas turbines. Intuitively, one

might think that the temperature and flow rate of the syngas exiting the heat exchanger would increase due to the leakage. Interestingly enough, this is not the case.

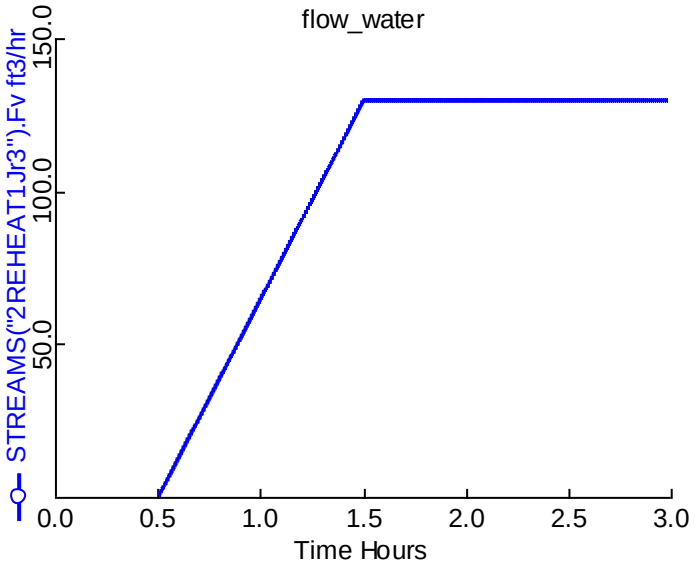

Figure 93. Volumetric flow rate of the leaking steam stream into the syngas stream due to Fault 2.

Fault 2 is initiated after half an hour simulation time. The leakage is initiated and ramped for one hour and then held steady at the final value. The mole flow rate of water is about 9% of that of the syngas stream exiting the heat exchanger. The flow of water can be seen from Figure 93 above.

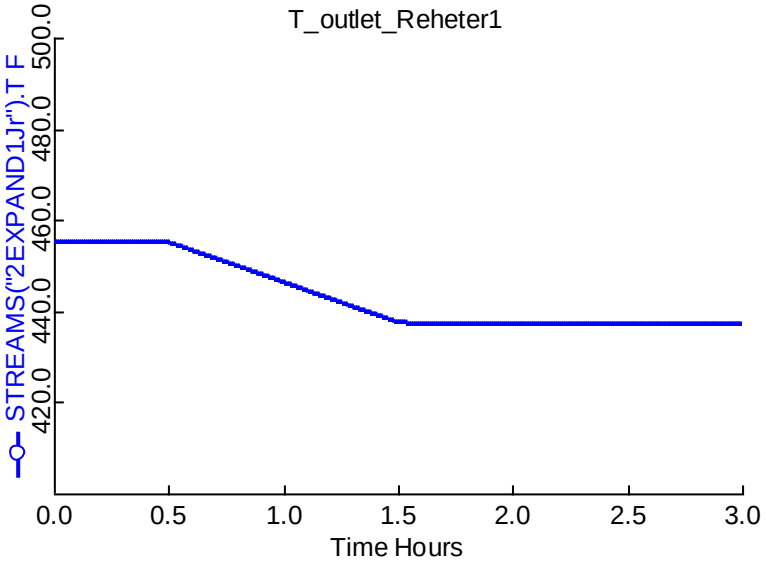

Figure 94. Temperature change of the Syngas stream at the outlet of the Heat exchanger due to Fault 2.

Due to Fault 2, the pressure of the water drops in pressure significantly leading to its evaporation. Due to the latent heat of evaporation, the syngas temperature decreases. This can be seen from Figure 94.

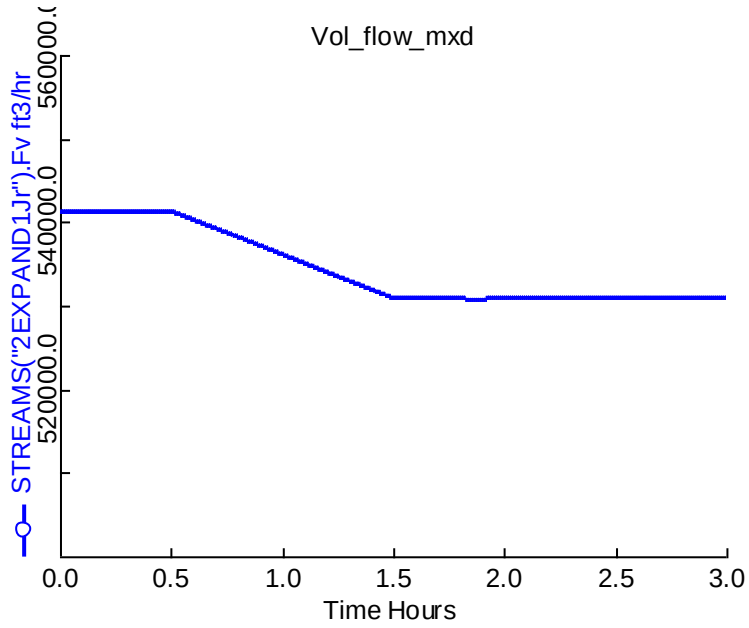

Figure 95. Flow rate change of the syngas stream exiting the heat exchanger due to Fault 2.

The effect of this is not confined to temperature itself. The volumetric flow rate is a function of temperature and the temperature of the outlet stream has decreased. In addition, vaporization of water creates backpressure decreasing the flow rate of clean syngas. Therefore, the overall volumetric flow rate of the exit syngas stream has decreased as compared to before as can be seen in Figure 95.

Furthermore, fouling faults in the heat exchangers are also simulated. This is simulated at two locations; the first one (Fault 4) was in the superheater of the HP steam, and the second one (Fault 7) was on the HE that heats the syngas before the GT combustor. Fault 4 is simulated by reducing the area of the HE by 10% over a time period of 1 hour. Figure 96 and 97 show two sample responses as a result of this fault.

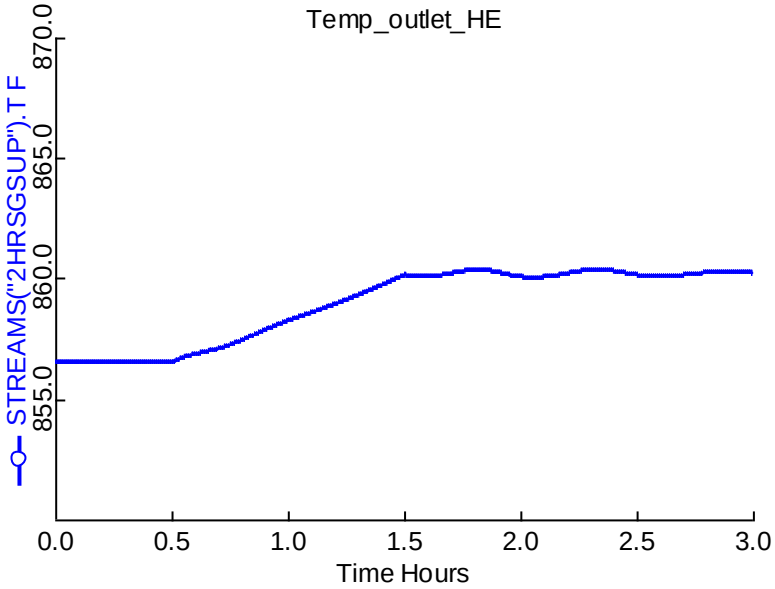

Figure 96. Temperature change of the flue gas at the outlet of the superheater due to Fault 4.

Due to the reduced area, the outlet temperature of the flue gas increases as shown in Figure 96. Due to the increase in temperature, the volumetric flow rate is also expected to increase. This can be seen in Figure 97 below.

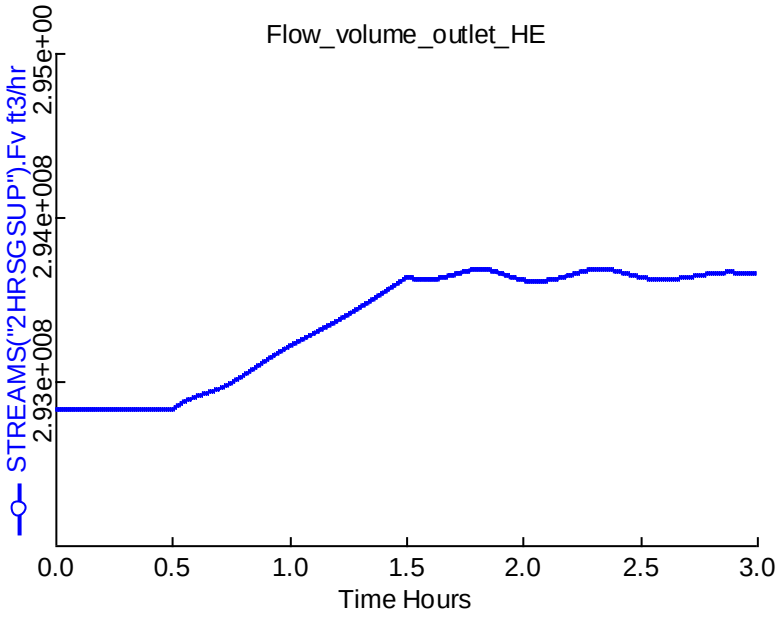

Figure 97. Change in Flow rate of Combusted Syngas stream due to Fault 4.

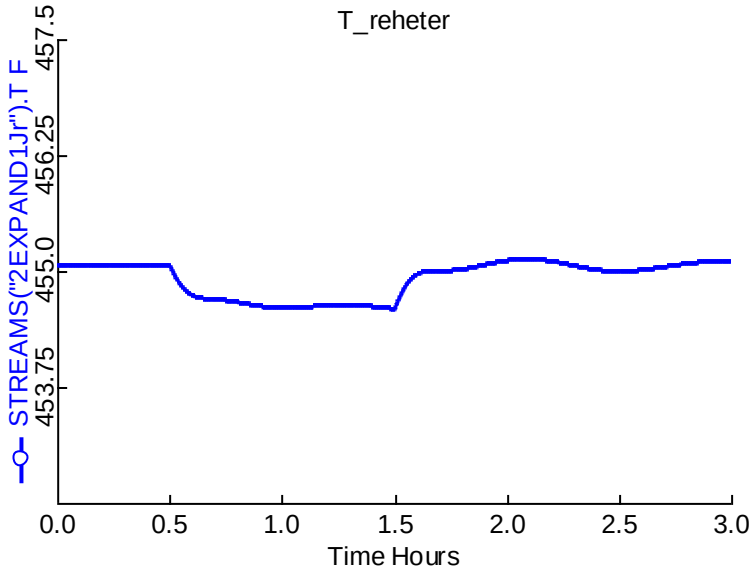

Figure 98. Change in Temperature of the outlet Syngas stream due to Fault 7.

In contrast, the temperature change due to Fault 7 as shown in Figure 98 does not respond in the same manner as it did in Fault 4 even though the reduction in the area is similar in both the cases.

Multi-severity faults

The previously shown faults in the combined cycle power plant are simulated at three severity levels. The data for the 21 faults were compiled and sent to TTU for sensor placement studies. The severity of the faults and their levels are shown in Table 35 below.

Table 35. Faults at different severity level simulated in the combined cycle model

Fault #	Fault Type	Duration	Severity
1	Ramp	1 hour	0.5%, 1%, 2% leak valve opening
2	Ramp	1 hour	0.1%, 0.2%, 0.4% leak valve opening
3	Ramp	1 hour	5%, 10%, 20% leak valve opening
4	Ramp	1 hour	80%, 90%, 95% area available
5	Step	-	90%, 95%, 98% of original heat loss
6	Ramp	1 hour	0.05%, 0.2%, 0.5% of leak valve opening
7	Step	-	85%, 90%, 95% of area available

The fault severities have been chosen such that the levels are in a high, medium and low level. The effect of the high severity level should be captured by the algorithm easily. The low level faults may not have a strong effect on the system to be resolved by the algorithm. The faults would help determine the level of severity that the sensor placement can detect and the minimum number of sensors required to detect them.

There are 736 number of variables chosen carefully for further processing. Table 36 shows the weight and threshold value for each type of variables:

Table 36. Weight and threshold of each variable in the sensor placement algorithms

Variable type	Weight	Threshold
Temperature	0.1	1 F
Level	1	1 inch
Flow	1	3%
Power	0.1	3%
Concentration(mole fraction)	10	0.01
Pressure	0.5	2 psi

Table 37 and Table 38 show the results of the different algorithm for fault resolution of combined cycle. Table 38 shows that the MR algorithm can resolve faults [8,9] in the medium ratios of range 1.3 - 1.8. However, the sensor network cost is sensitive to the MR threshold value in this range.

Table 37. SDG and FES algorithms results

Algorithm(s)	Selected sensors	Sensor network cost	Irresolvable fault sets
SDG	1,13,14,21,34,37,112,130,154,179,188,221,285	5.8	[8,9] [14,15]
FES	10,13,14,42,49,456,469,171,221,242,251,285	4.8	[8,9] [14,15]

Table 38. MR algorithm results

Algorithm	MR threshold value	Irresolvable fault sets
MR	1.1 - 1.2	[8,9] [14,15]
	1.3 - 1.8	[14,15]
	1.9 - 3	[8,9] [14,15]

Figure 99 shows the number of irresolvable faults and the corresponding sensor network cost for different MR threshold values.

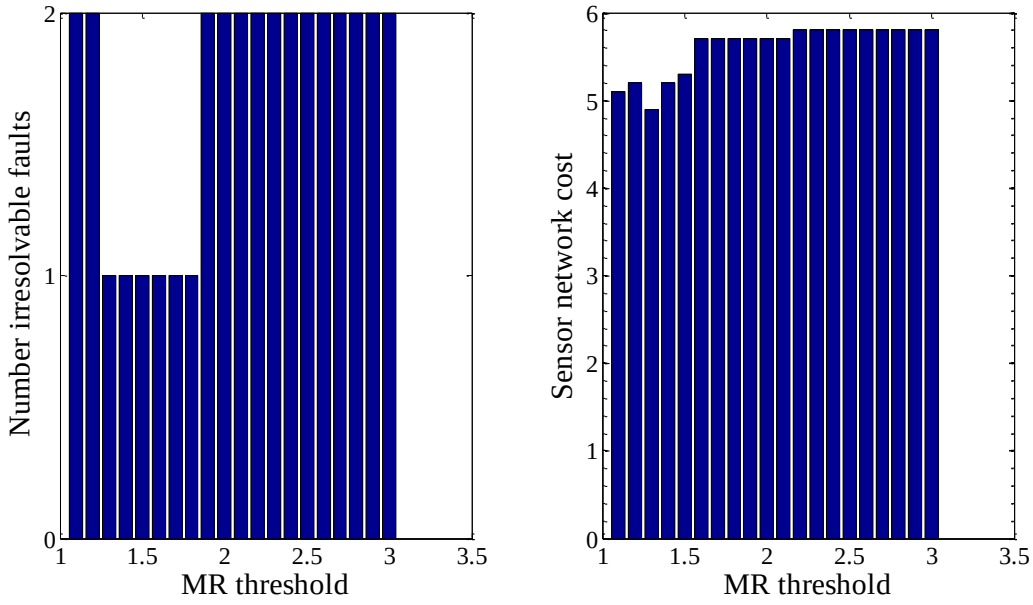

Figure 99. Number of irresolvable faults (left) and the corresponding sensor network cost (right) at different MR threshold values

6.1.6 System Decomposition

Here, we study the effect of different system and decomposition parameters on the fault detection and computation speed. The results in this section are based on a Monte Carlo simulation analysis where a pool of systems are considered and the presented results are either the probability of occurring (fault detection results) or the mean average over the pool of systems (computation speed results). The sensitivity analysis of system parameters includes the effect of number of nodes, sub-systems, and cross-connections on the computation speed, fault resolution capability and sensor network cost. For computation speed, the average computation time for fault detection of overall system (T_O) is compared with the average sum of computation times of sub-systems (T_D). For comparison, the average percent reduction in computation time by decomposition (T_R) is also presented ($T_R = (1-T_D/T_O) \times 100$). For fault resolution capability, the solutions obtained from sub-systems are augmented to form the decomposition solution. The decomposition solution is implemented in the overall system to check the resolution, which is how many of the faults cannot be resolved using the decomposition solution. The optimal resolution is always achieved by considering the overall system and counting the number of unresolvable faults. For comparison, the percentage of the systems in the pool where their decomposition have resolution greater than that of optimal resolution is presented (P_F). For sensor network cost, the cost of sensor networks for all sub-systems are summed up and compared with the sensor network cost of the overall system. For comparison, percentage of the systems in the pool that have sensor network cost different than the cost of sensor network of their overall system is presented (P_C). It should be noted that cost of placing sensor on all nodes are assumed equal with the value of 1.

Table 39 shows the sensitivity analysis of number of sub-systems. In this analysis, total number of nodes, edges, fault nodes, fault edges and cross-connections are fixed for the overall systems at 3600, 1.2 × 3600, 60, 60 and 60, respectively. In all of the subsequent studies, the number of edges is chosen to be 20% more than the number of nodes in order to have feedback/recycle edges similar to process systems; and the number of fault edges is chosen equal to the number of faults in order to ensure each fault has single outward edge. Also, the values for number of nodes, edges, fault, fault edges and cross-connections in all subsequent tables represent the parameters of each sub-system in an overall system. The random systems in each pool are generated with a specified number of sub-systems. In Table 39, for each system in each pool, number of sub-systems is fixed and the mentioned fixed parameters are divided equally among the sub-systems. For example in Table 39, pool 1 has systems where each system is consists of 2 sub-systems where each sub-system has 1800, 2160, 30, 30 and 30 number of nodes, edges, faults, fault edges and cross-connections, respectively. Only for pool 6, the number of cross-connections cannot be divided equally among the sub-systems, therefore, number of cross-connection between each sub-system is chosen randomly for each sub-system with summation equal to 60. It should be noted that it is assumed that each pair of sub-systems has at least 1 cross-connection. In order to be consistent, the maximum number of cross-connections is then 16 for pool 6.

Table 39. Sensitivity analysis of number of sub-systems

Parameters	Pool 1	Pool 2	Pool 3	Pool 4	Pool 5	Pool 6
Sub-Systems	2	3	4	5	6	10
Nodes	1800	1200	900	720	600	360
Edges	2160	1440	1080	864	720	432
Faults	30	20	15	12	10	6
Fault Edges	30	20	15	12	10	6
Cross-Connections	30	20	10	6	4	1-16
T_O (s)	1.6587	1.6587	1.6587	1.6587	1.6587	1.6587
T_D (s)	0.4372	0.2404	0.1818	0.1439	0.1186	0.0819
T_R	74%	86%	89%	91%	93%	95%
P_F	0%	0%	<1%	2%	2%	3%
P_C	44%	59%	73%	85%	90%	100%

In Table 39, the computation time of the overall system, T_O, is averaged over all 6 pools as all the overall systems have similar properties. As the number of sub-systems increase, the reduction in computation time is increasing, meaning that it takes much less time to perform fault detection for all the sub-systems than performing on the overall system. This can be seen as the average of sum of sub-systems' computation time, T_D, is reducing due to fault detection of smaller systems. One of major reasons behind the computation time reduction is the amount of time required to perform fault resolution (symmetric difference) in a system. For the overall system, the number of computations required for fault resolution is equal to the number of non-repetitive fault pairs in the overall system, which is 60×59/2 = 1770. If the system is decomposed to 10 sub-systems, the total number of computations required for fault resolution is 10×6×5/2 = 150. This means that the total number of computations, which is directly related to the computation time, has been reduced by approximately 92%. As the number of sub-systems increase, the probability of systems with more faults being unresolved is slightly increasing due to the reason that the probability of presence of nodes that can resolve those faults in the corresponding sub-system gets lower as the number of sub-systems increase. Moreover, as the number of sub-systems increase, resolving the faults in sub-systems requires more number of sensors to be placed due to the reason that sensors which could resolve multiple faults are not available for use in different sub-systems. Therefore, there is high probability that decomposition results in higher sensor network cost. In summary, choosing the appropriate number of sub-systems for decomposition is a tradeoff between computation speed, fault resolution and sensor network cost. Increasing the number of sub-systems reduces the computation time significantly while it may result in lower fault resolution and different sensor network cost.

Table 40 shows the sensitivity analysis of number of nodes and fault nodes. The number of sub-systems is fixed at 4 in this study. In pools 1-3 in Table 40, the number of nodes increases from 10 to 1000 while the number of faults are fixed at 4. Although the computation time for both overall and decomposed systems increases by increasing the number of nodes, the amount of reduction in computation time is actually

increasing, meaning that decomposition efficiently reduces the computation time as the size of the system increases. Moreover, while the number of faults is fixed, as the number of nodes increase, there are more sensors available for fault resolution; therefore, the probability of systems with more unresolved faults due to decomposition is reducing. Similarly, the probability of systems with different sensor network cost increases as the number of nodes increase due to more availability of sensors for fault resolution. However, the sensor network cost maybe greater or less than the overall system depending on the fault resolution. For example, fault resolution maybe achieved by using more sensors while if some faults cannot be resolved in the sub-systems, less number of sensors will be involved in the fault resolution, thus, resulting in less sensor network cost. In pool 4-6, the number of nodes is fixed at 1000 while the number of faults increases from 40 to 80. Pools 4 and 5 show that at higher number of faults compared to pool 3, computation time reductions are significant, however, the impact of increasing the number of fault nodes on both overall and decomposed systems' computation time is significantly larger than the effect of increasing the number of nodes. This effect can also be explained by the number of computations as in the study of number of sub-systems. The probability of systems with higher number of unresolved faults increases at higher number of faults. However, compared to pool 3, we can see that this probability has remained approximately the same for larger number of faults. An explanation is that since the number of faults is large, many faults are even unresolved in the overall system and system decomposition has little effect on fault resolution. For the same reason, the probability of systems with different sensor network cost for pools 4 and 5 is lower compared to the pool 3. For pool 6, the number of faults is too high that exceeds the computation memory of the computer, while it is still possible to perform the fault detection on the decomposed system. Therefore, no comparison can be made for pool 6. This interesting result justifies the need for system decomposition for fault detection of large systems and large number of faults.

Table 40. Sensitivity analysis of number of nodes and fault nodes

Parameters	Pool 1	Pool 2	Pool 3	Pool 4	Pool 5	Pool 6
Sub-Systems	4	4	4	4	4	4
Nodes	10	100	1000	1000	1000	1000
Edges	12	120	1200	1200	1200	1200
Faults	4	4	4	40	50	80
Fault Edges	4	4	4	40	50	80
Cross-Connections	4	4	4	4	4	4
T_O(s)	0.0257	0.0349	0.1251	14.3853	26.4105	Out of memory
T_D(s)	0.0158	0.0182	0.0288	1.3469	2.6569	4.8287
T_R	37%	48%	77%	91%	90%	
P_F	9%	3%	<1%	1%	1%	
P_C	100%	98%	97%	66%	63%	

Table 41 shows the sensitivity analysis of number of cross-connections while other parameters remain fixed. Although in a decomposed system an edge can either be inside a sub-system or between a pair of sub-systems, the following sensitivity analysis shows the effect of number of cross-connections, for example in a highly interconnected system, on computation time and fault detection when the system is decomposed. As seen in Table 41, the number of cross-connections has very little effect on the computation time reduction, although still the decomposition has resulted in significant time reduction of approximately 90%. The probability of systems with higher number of unresolved faults in the decomposed system is at a minimum when there are only one cross-connections between the sub-systems. As can be predicted, the less the interaction between the sub-systems, the more the probability of achieving optimal resolution with system decomposition. At higher number of cross-connections, although not highly probable, it is possible that the decomposition results in some faults being unresolved. Moreover, as the number of cross connections increase, the probability of system decomposition resulting in sensor network cost higher than the optimal cost gets higher. This is due to the reason that the when a system is more interconnected, it is possible that a single sensor can resolve multiple faults. Therefore, decomposing systems with more connections can result in sensor network with higher cost for achieving the optimal resolution.

Table 41. Sensitivity analysis of number of cross-connections

Parameters	Pool 1	Pool 2	Pool 3	Pool 4	Pool 5	Pool 6
Sub-Systems	4	4	4	4	4	4
Nodes	1000	1000	1000	1000	1000	1000
Edges	1200	1200	1200	1200	1200	1200
Faults	40	40	40	40	40	40
Fault Edges	40	40	40	40	40	40
Cross-Connections	1	5	10	20	40	80
T_O (s)	10.28	15.81	16.15	16.93	16.95	16.47
T_D (s)	1.26	1.44	1.50	1.55	1.3317	1.59
T_R	88%	91%	91%	91%	92%	90%
P_F	0%	2%	3%	3%	2%	2%
P_C	70%	70%	84%	93%	99%	100%

6.1.7 Conclusion

The case studies, clearly brings out the value of every piece of information that is used in sensor placement. Further, because of this, it is also easy to interpret and explain the results to the operator. If a pseudo-sensor corresponding to a MR pair helps in resolution then a corresponding explanation such as, for example, “Temp T-101 has increased by a large amount, whereas concentration C-502 shows only

moderate increase indicative of F15" fault can be provided. Further, it is possible to use these results directly in the development of a diagnostic approach for each of these case studies. Finally, the optimization algorithms are solved, even at a flow-sheet level, in a very short time. It will be extremely difficult to solve problems at this scale if one were to take recourse to a full-scale optimization problem that incorporates the nonlinear dynamic first-principles model within the optimizer. A more computationally efficient approach might be to add the detailed first principles model as the next level of information to address only the faults that are left unresolvable after MR and FES information have been used in identifying the sensor placements. Elegant computational approaches to realize this will be one avenue for future work.

The system decomposition for fault detection is promoted by a series of sensitivity analysis that promises computation time reduction while it is highly probable that the optimal resolution using the decomposed system is achieved. However, it is likely that the decomposed system will result in higher sensor network cost compared to the optimal cost. The optimal resolution and sensor network cost can be obtained by the fault detection of the original system before decomposition.

The system decomposition promises significant computation time reduction as the number of sub-systems and the system size, which includes number of nodes and fault nodes, increases. The larger the system, the more appealing the system decomposition is. It is more likely for system decomposition to achieve the optimal resolution as the size of the system increases; and when system decomposition has lower number of sub-systems and lower number of cross-connections. It is highly probable that system decomposition has higher sensor network cost while the probability is lower for larger systems, when the system is decomposed to lower number of sub-systems, and when sub-systems' interaction through cross-connections are lower.

An appropriate graph partitioning algorithm for fault detection must compromise between the computation speed for fault resolution and sensor network cost. Minimizing the number of cross-connections promises higher chance of achieving optimal resolution while the number of sub-systems is a tradeoff between computation speed, fault resolution and sensor network cost. Maximizing the number of nodes in each sub-system ensures highest computation time reduction, which can be done by equally dividing the nodes in the sub-systems as possible. Also, the less the number of fault nodes in each sub-system, the less the number of computations can be, which again means equal number of fault nodes in each sub-system can be an appropriate choice.

6.2 Distributed Sensor Placement

6.2.1 State Estimation Validation

In this section, the performance of the proposed state estimation technique is demonstrated on two examples. The first example is a nonlinear system that is akin to a batch reactor and the second example is the water gas shift reactor (WGSR), where a catalytic reaction is performed in a plug-flow reactor. The performance of the filter is demonstrated by comparison of root mean square error (RMSE) of the data and the estimated states calculated as

$$RMSE = \sqrt{\frac{\sum_{i=1}^{s}\left(x_{i,k} - \hat{x}_{i,k}^{c}\right)^{2}}{s}} \tag{219}$$

Where $x_{i,k}$ is the actual value that is specific to the simulation study and $\hat{x}_{i,k}^{c}$ is the constrained state estimates. In order to calculate the RMSE of the measurement data, $\hat{x}_{i,k}^{c}$ in Eqn. (219) is replaced by the measured value $y_{i,k}$. Another metric that is used in the following analysis is the normalized sum of squared errors (SSE) of all state estimates over the total time instance and is calculated as

$$SSE = \sum_{t=1}^{T}\sum_{i=1}^{X}\left(\frac{x_i(t) - \hat{x}_i(t)}{x_i(t)}\right)^2 \tag{220}$$

where T is the number of time instances, X is the number of variables and $x_i(t)$ and $\hat{x}_i(t)$ are i^{th} actual and estimated states at t^{th} time instance, respectively. It should be noted that in the following studies, SSE values are calculated by averaging over 100-run Monte Carlo simulations.

6.2.1.1 Example 1: Non-linear synthetic system

Our synthetic example is comprised of two differential equations and an algebraic equation. The system under study is given as

$$\begin{bmatrix}\dot{x}_1\\ \dot{x}_2\end{bmatrix} = \begin{bmatrix}8.69\times10^{-4}z(0.6 - x_1) - z\times10^{-3}\left(x_1 - \frac{x_2}{2}\right)\\ 8.69\times10^{-4}z(0.4 - x_2) + z\times10^{-3}\left(x_1 - \frac{x_2}{2}\right)\end{bmatrix} + G\begin{bmatrix}\omega_1\\ \omega_2\end{bmatrix} \tag{221}$$

$$g(x) = z^{0.3} + 0.5x_1^3 z - 10\frac{x_2}{z} = \gamma \tag{222}$$

where $G = \begin{bmatrix}0.5 & -0.5\\ -0.5 & 0.5\end{bmatrix}$ and true initial state of $x_0 = [0.431 \quad 0.569 \quad 3.546]^T$. The sampling time is chosen as Δt = 5 s and the state estimator is initialized with

$$\begin{aligned}
Q &= \begin{bmatrix}2.5\times10^{-5} & 0\\ 0 & 2.5\times10^{-5}\end{bmatrix}\\
W &= 2.5\times10^{-3}\\
R &= \begin{bmatrix}2.5\times10^{-5} & 0 & 0\\ 0 & 2.5\times10^{-5} & 0\\ 0 & 0 & 2.5\times10^{-3}\end{bmatrix}\\
P_0 &= \begin{bmatrix}10^{-4} & 0 & 0\\ 0 & 10^{-4} & 0\\ 0 & 0 & 10^{-4}\end{bmatrix}\\
x_{0|0} &= [0.555 \quad 0.456 \quad 2.822]^T
\end{aligned} \tag{223}$$

The constraint given for this system is

$$E = [1 \quad 1 \quad 0], \quad b = 1 \tag{224}$$

Note that the initial estimate does not satisfy the constraint. From the constraint, it can be seen that $E_x = [1 \quad 1]$, $E_z = 0_{1\times1}$, $E_xG = 0_{1\times2}$ and $E_xf_x = 0_{1\times1}$. The Jacobian matrix is calculated analytically as

$$\begin{bmatrix}A & B\\ C & D\end{bmatrix} = \begin{bmatrix}(-0.869z - z)\times10^{-3} & -\frac{z}{2}\times10^{-4} & \left(0.869(0.6 - x_1) - \left(x_1 - \frac{x_2}{2}\right)\right)\times10^{-3}\\ z\times10^{-3} & \left(-0.869z - \frac{z}{2}\right)\times10^{-3} & \left(0.869(0.4 - x_2) + \left(x_1 - \frac{x_2}{2}\right)\right)\times10^{-3}\\ 1.5x_1^2 z & \frac{-10}{z} & 0.3z^{-0.7} + 0.5x_1^3 + \frac{10x_2}{z^2}\end{bmatrix} \tag{225}$$

Multiplying E_x by (A-$BD^{-1}C$) yields

$$
\begin{aligned}
&E_x(A - BD^{-1}C) \\
&= [1 \quad 1]\begin{bmatrix} -8.69z\times10^{-4} - z\times10^{-3} + z\times10^{-3} & -\frac{z}{2}\times10^{-3} \\ z\times10^{-3} & -8.69z\times10^{-4} + \frac{z}{2}\times10^{-3} \end{bmatrix} \\
&= [-86.9z\times10^{-4} \quad -86.9z\times10^{-4}] \\
&= -86.9z\times10^{-4}\times[1 \quad 1]
\end{aligned}
\tag{226}
$$

From Eqn. (224), it is known that $x_1 + x_2 = 1$ after the first iteration of the filter, therefore, $E_x BD^{-1}C = 0$. From Eqn. (226), E_x is a left eigenvector of Φ. Figure 100-102 show the actual, measured and estimated values of each variables for 100 time instances. Initially, states do not satisfy the constraint, however, after the first iteration of the filter, estimated states satisfy the constraints for all time instances.

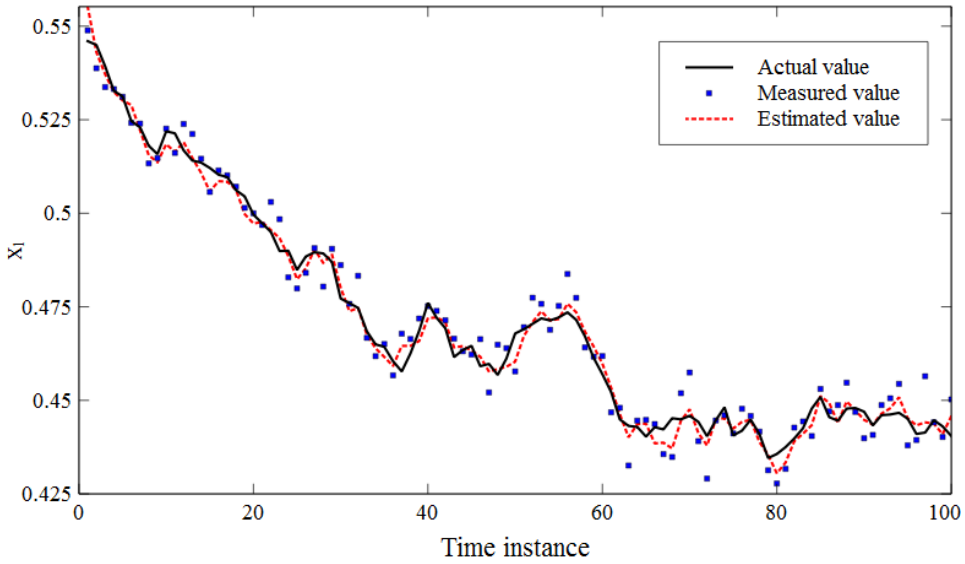

Figure 100. Actual, measured and estimated values of differential variable x_1.

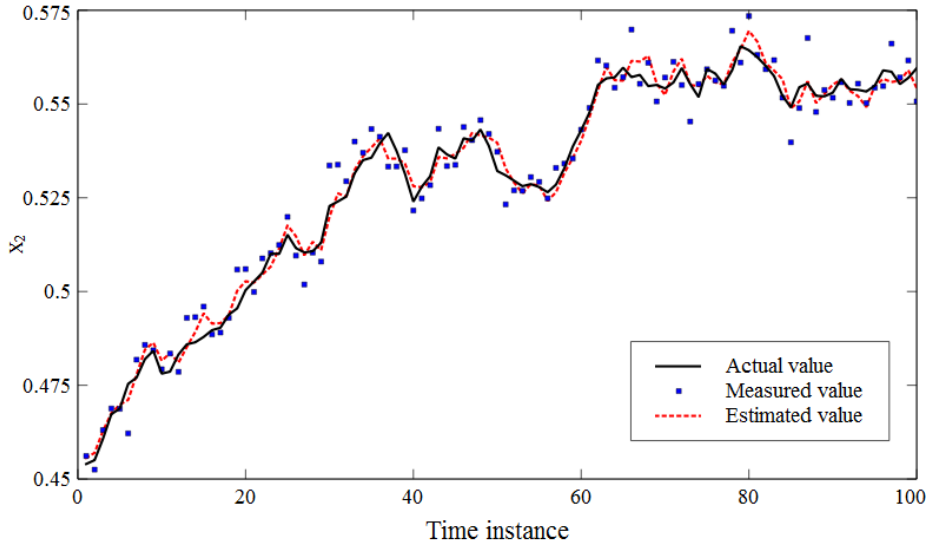

Figure 101. Actual, measured and estimated values of differential variable x_2.

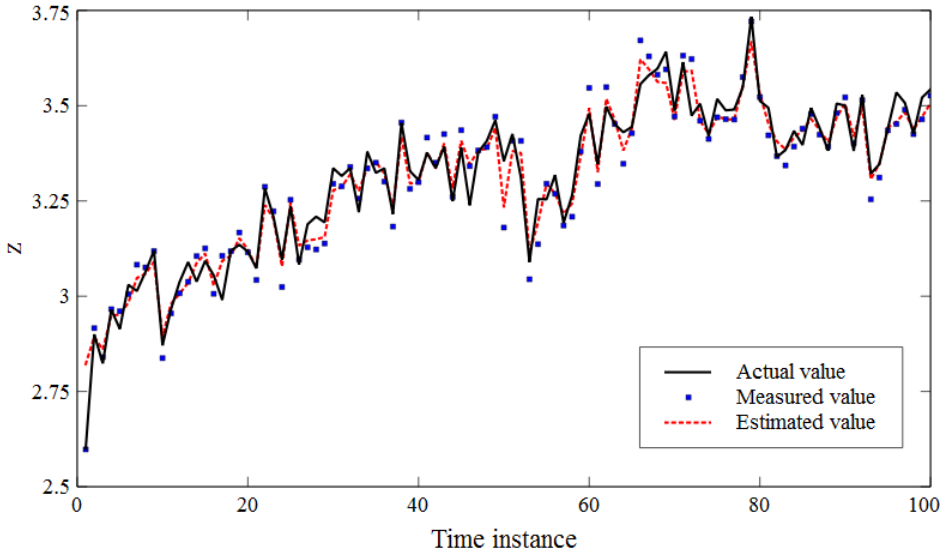

Figure 102. Actual, measured and estimated values of algebraic variable z

Table 42 shows the RMSE and SSE values of measured and estimated variables. In Table 42, RMSE and SSE are compared for filter I, with certain algebraic equation assumption as described before, and filter II, the proposed filter. It should be noted that the propagation step in filter I is modified to include the state constraints as shown in Eqn. (192). As seen in Table 42, RMSE of differential variables x_1 and x_2 using filter II are slightly reduced over using filter I although both filters result in better estimates compared to the measurements. The RMSE of the algebraic variable z for filter I is greater than that of the measurement due to underestimation of noise in its corresponding equation. This suggests that measuring the algebraic variable would result in more accurate values than using filter I. However, the reduced RMSE of the algebraic variable for filter II compared to the RMSE of the measurement justifies the correct assumption of uncertain algebraic equation. Also, the SSE value of filter II indicates significant improvement over filter I, which means the estimates are closer to the actual values. These improvements show that the proposed filter can mitigate the effect of uncertain algebraic equations and result in better estimates.

Table 42. Comparison of RMSE and SSE values for measured and estimated values

	RMSE			SSE
	x_1	x_2	z	
Measurement (data)	0.0050	0.0050	0.0501	
Filter I	0.0029	0.0029	0.0684	0.0479
Filter II	0.0027	0.0027	0.0417	0.0215

6.2.1.2 Example 2: Water gas shift reactor

State estimation of reactors has been the focus of many researchers for control and fault diagnosis. The next example is the system of interest, water gas shift reactor (WGSR), in which carbon monoxide (CO) reacts with steam (H_2O) to produce hydrogen (H_2) and carbon dioxide (CO_2), through the water gas shift reaction. A non-linear DAE model of the sour water gas shift reactor (SWGSR) has been developed in section 2.1 where in addition to the water gas shift reaction, carbonyl sulfide (COS) reacts with H_2O (i.e., COS hydrolysis), and CO_2 and hydrogen sulfide (H_2S) are produced. For simplicity, here, the sulfur content of the feed is assumed negligible and only the water gas shift reaction is considered. In addition to the reactor model, feed and product stream flowrates are controlled by valves (V1, V2 and V3) as shown in Figure 103. The corresponding equation for calculation of flows through the valves is $F_{Vi} = \left(\frac{d_{V_i} S_{V_i}}{M_{V_i}}\right)\sqrt{\rho_{V_i}\Delta P_{V_i}}$, where d_{V_i}, S_{V_i}, M_{V_i}, ρ_{V_i} and ΔP_{V_i} are flow coefficient, valve opening, average molecular weight, average density and pressure drop across the valve, respectively. Syngas and steam are passed through valves V_1 and V_2, respectively, and it is assumed that these streams are well mixed in an ideal mixer before entering the reactor. The presence of the valve adds an additional algebraic equation to the system model as described by Eqn. (227)-(231). Table 43 shows the summary of the equations used to represent the system with parameters shown in Table 44. Some of the parameters in our previous work are changed for simplicity and reduced computations. For example, the reactor size and correspondingly the number of grid points in discretization are reduced. These parameters are shown in Table 44.

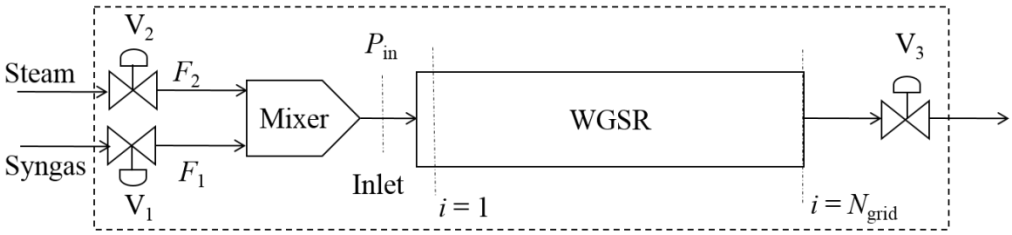

Figure 103. Schematic of the WGSR system

Table 43. Summary of equations for Water gas shift reactor

$$\frac{\partial y_i}{\partial t} = \frac{RT}{P}\left(-F_{MF}\frac{\partial y_i}{\partial z} + r_{WGS,i}\frac{1-\varepsilon}{\varepsilon}\right) + G\omega_{1,i} \quad i = \text{CO, } H_2O\text{, } CO_2 \text{ and } H_2 \tag{227}$$

$$\frac{\partial T_g}{\partial t} = \frac{1}{\rho_{gas}C_p}\left[-C_p F_{MF}\frac{\partial T_g}{\partial z} + \frac{h_f a_c}{\varepsilon}\left(T_{cat} - T_{gas}\right)\right] + \omega_2 \tag{228}$$

$$\frac{\partial T_{cat}}{\partial t} = \frac{1}{\rho_{cat}C_{p,cat}}\left[K_{cat}\frac{\partial^2 T_{cat}}{\partial z^2} - \frac{h_f a_c}{1-\varepsilon}\left(T_{cat} - T_{gas}\right) + r_{WGS}\rho_{cat}\Delta H_{R,WGS}\right] + \omega_3 \tag{229}$$

$$\frac{dP}{dz} = \frac{\rho u^2}{D_{cat}}\left(\frac{1-\varepsilon}{\varepsilon^3}\right)\left(1.75 + \frac{150}{Re}\right) + \gamma_1 \tag{230}$$

$$\Delta P_{V_3} = \frac{1}{\rho_{V_3}}\left(\frac{F_{V_3}M_{V_3}}{d_{V_3}S_{V_3}}\right)^2 + \gamma_2 \tag{231}$$

Table 44. Summary of the parameters of the WGSR model used in this work

Parameter		Value
Length		1 m
Diameter		0.5 m
Number of grids (N_{grid})		25
Valve V_1 (syngas)	Opening	50%
	Flow Coefficient	6×10^{-5}
Valve V_2 (steam)	Opening	50%
	Flow Coefficient	2×10^{-5}
Valve V_3 (products)	Opening	50%
	Flow Coefficient	10^{-4}
Inlet temperature		580 K
Feed pressure (steam and syngas)		5626121 Pa
Outlet pressure		4.5×10^6 Pa
Catalyst diameter		0.1 mm

The state vector consists of 176 states including mole fractions of CO, H_2O, CO_2, and H_2, temperature and pressure at each grid-point and pressure at the inlet of the reactor (P_{in}). The constraint for this system is imposed as the summation of mole fractions at each grid-point is equal to one. Since the actual mole fraction values must sum up to one for consistency, in simulating the actual mole fraction values, the process noise is introduced in the mole fractions in such a way that the summation of the process noises at each grid-point and time instance are equal to zero. To do this, random process noises generated for each

mole fractions at a particular grid-point are corrected by subtracting the mean average of the process noises from each. Therefore, G in system of Eqn. (181) is written such the diagonal elements are $+\frac{3}{4}$ and the elements corresponding to mole fractions of the other components at the same grid-point are $-\frac{1}{4}$. The process covariance, Q, of each equation type is assumed the same and chosen as 10^{-4} and 2.5×10^{-5} for mole fraction and temperature equations, respectively. The covariance matrix of algebraic equations (pressure) is also fixed at 4×10^{-4}. The measurement covariance, R, is also assumed in the same manner with 6.4×10^{-5}, 2.5×10^{-5} and 4×10^{-6} for mole fraction, temperature and pressure measurements, respectively. It should be mentioned that temperature and pressure variables are normalized using 580 K and 55 atm, respectively. The sampling time is chosen as Δt = 5 s and the state estimation is performed for 100 time instances. The error covariance is $P_0 = 10^{-6}\, I_{176\times176}$. The correction step for constraint is applied only once in the beginning. Note that since a large portion of the reactant is consumed in the first half of the reactor, it is more desirable to accurately estimate the states in this zone. Therefore, a random grid-point in the first half of the reactor is chosen to show the performance of the proposed filter. Figure 104 and Figure 105a show the actual, measured and estimated states at 9th grid-point using Filter II with all the states measured. The corresponding RMSE are shown in the figure captions where $RMSE_{data}$ and $RMSE_{est}$ represent RMSE in measured and estimated values, respectively. Clearly, estimated values have smaller errors compared to the measurements, thus, the proposed filter performs reasonably. It should be mentioned that for better visualization, Figure 104 and Figure 105 are shrunk for the first 30 time instances although the calculations of RMSE and SSE values are based on 100 time instances. In order to avoid comparing the RMSE of large number of variables for filter I and filter II in this example, the superiority of the proposed filter, filter II, is shown by comparing SSE values and also RMSE values at 9th grid-point for the algebraic variable P. The SSE values are 10.312 and 6.819 for filter I and filter II, respectively. Comparing the SSE values, the proposed filter results in estimated values significantly closer to the actual values as the squared error is reduced approximately by 33%. Moreover, higher $RMSE_{est}$ for filter I than $RMSE_{data}$ shows that the filter fails to outperform the measurements and produce unreliable estimates while filter II results in estimates with lower errors than of measurements. The state estimation results are presented in Figure 105a and Figure 105b for filter II and filter I, respectively. From Figure 105, it can be seen how accurately filter II tracks the changes in algebraic state compared to filter I. As mentioned before, this is due to the fact that filter II correctly accounts for the presence of noise in the algebraic state. Consequently, this is reflected in the quality of the state estimates.

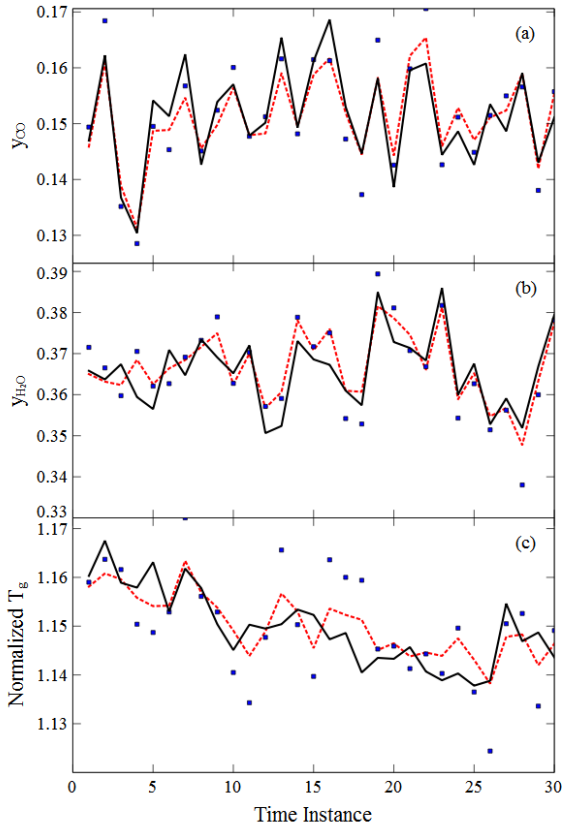

Figure 104. Actual (-), measured (*) and estimated (--) value at 9th grid-point on the reactor for (a) y_{CO} ($RMSE_{data}$ = 5.005 × 10^{-3}, $RMSE_{est}$= 3.852 × 10^{-3}) (b) y_{H_2O} ($RMSE_{data}$ = 5.003 × 10^{-3}, $RMSE_{est}$= 3.827 × 10^{-3}) (c) T_g ($RMSE_{data}$ = 7.978 × 10^{-3}, $RMSE_{est}$= 4.945 × 10^{-3})

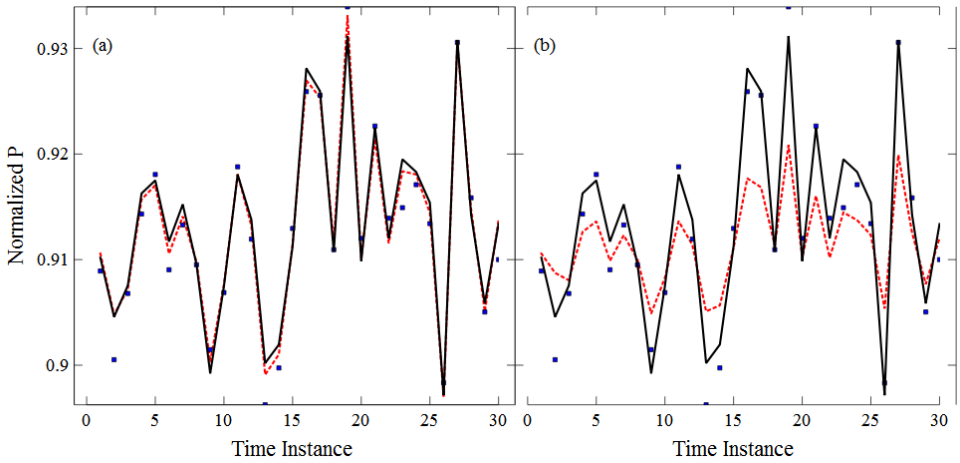

Figure 105. Actual (-), measured (*) and estimated (--) value at 9th grid-point on the reactor for (a) P ($RMSE_{data}$ = 1.998 × 10^{-3}, $RMSE_{est}$= 0.894 × 10^{-3} using Filter II) (b) P ($RMSE_{est}$= 5.312 × 10^{-3} using Filter I).

6.2.1.3 Discussion

In the previous section, our proposed filter which accurately estimates the states, especially the algebraic states, was used to estimate the states in the WGSR example. In the WGSR example, however, all the states are measured for the purpose of filtering. Practically, it is neither possible nor economical to measure all the states in the WGSR. In operating plants, as the budget and integrity of the equipment items limit the number and type of sensors that can be used for monitoring the process, state estimation becomes a challenge. Increasing the number of sensors results in more accurate estimates of the variables. On the other hand, reducing the number of sensors requires identifying the most important variables that, if measured, accurate state estimates would be obtained. However, following questions arise. What should be the type and location of the sensors? How much does each measurement type and location contribute to the accuracy of the state estimates especially when using a rigorous filter for state estimation? To answer these questions, we begin by evaluating the case where only a few measurements are available. First, it is assumed that measurements are mutually exclusive and only available at fixed locations for similar states (i.e. only mole fractions of CO, y_{CO}, or, only gas temperature, T_g, at fixed locations). The fixed grid-points are assumed to be 1st, 5th, 9th, 13th, 17th and 21st grid-points. For satisfying product specification, product concentration, temperature and pressure are usually monitored at the reactor outlet. Therefore, in subsequent studies it is assumed that all the states except the catalyst temperature, T_{cat}, are always measured at the outlet of the reactor (25th grid-point). Table 45 shows the SSE values for the corresponding available measurements with T = 100. As seen in Table 45, the lowest estimation error is achieved if the measurements of CO mole fraction (y_{CO}) are available. In contrast, if measurements of only pressure (P) are available, estimation error is comparatively higher than others in Table 45. Therefore, it can be concluded that the type of the variable that is being measured contributes to the accuracy of the estimation, and if identified, it can result in better estimation accuracy.

Table 45. Sum of squared errors value when fixed points measure the same type of states

	Measured state type					
SSE value	y_{CO}	y_{H_2O}	y_{CO_2}	y_{H_2}	T_g	P
	31.889	35.522	34.626	35.500	36.077	37.790

Next, we investigate how informative are each of the fixed measurement locations when only y_{CO} is measured. Therefore, six independent cases are considered, where in each case it is assumed that one of the measurement locations is unavailable and information from only 5 other measurement locations are used for state estimation. Table 46 shows the SSE values for each of these state estimations with T = 100. Table 46 shows that the 13th, 17th, and 21st grid-points have the highest impact on the accuracy of the estimates with approximately minimum 3% increase in the overall squared estimation error in absence of measurements from each of these grid-points individually. Moreover, even with one less measurement of y_{CO}, measurement of y_{CO} results in better estimation accuracy in comparison to the cases where temperature or pressure are measured. Next we investigate if measurements from other variables at different locations combined with measurements of y_{CO} can actually improve the accuracy of the estimates while the total number of locations are still six. For this study, y_{CO} measurements from the 13th and 17th, and 21st grid-points, which have highest impact on the accuracy, are combined with a measurements of temperature and y_{H_2O}. Table 47 shows SSE values when combinations of variables are measured at different locations. Since the number of combinations of the type and locations is large, only a few combinations are considered and shown in Table 47. Interestingly, combinations 2, 8 and 11 show improvement over when only y_{CO} is measured. Moreover, in practice, if a measurement of y_{CO} can be replaced by a temperature measurement that is significantly cheaper, a considerable reduction in cost can be achieved. This means that not only the type of the measured variable contributes to the accuracy of the

state estimates, the location where each of these variables are measured also contributes to the accuracy of the estimated values. However, if one were to consider all of the grid-points on the WGSR as candidate locations and pick the location and type of the variables with fixed total number of variables, a large number of combination need to be evaluated. This motivates further research on the development of systematic ways to answer the question: what are the best types and locations of sensors on WGSR in order to generate the most accurate estimates with limited budget?

Table 46. Sum of squared errors with one missing measurement

	Removed measurement location						
SSE value	None	1st	5th	9th	13th	17th	21st
	31.889	32.119	32.171	32.439	32.982	33.315	33.572

Table 47. SSE values with measurement combination

Iteration	Locations	SSE value
1	$T_g[21]$ $y_{CO_2}[13]$ $y_{H_2O}[5]$	32.160
2	$T_g[5]$ $y_{CO_2}[9]$ $y_{H_2O}[5]$	31.685
3	$T_g[13]$ $y_{CO_2}[5]$ $y_{H_2O}[21]$	32.087
4	$T_g[9]$ $y_{CO_2}[13]$ $y_{H_2O}[21]$	31.966
5	$T_g[5]$ $y_{CO_2}[13]$ $y_{H_2O}[17]$	31.906
6	$T_g[9]$ $y_{CO_2}[17]$ $y_{H_2O}[1]$	32.035
7	$T_g[5,13]$ $y_{CO_2}[17]$	31.964
8	$T_g[13]$ $y_{CO_2}[5,9]$	31.493
9	$T_g[21]$ $y_{CO_2}[1,17]$	32.003
10	$T_g[17]$ $y_{CO_2}[5,21]$	32.325
11	$T_g[5]$ $y_{CO_2}[1,21]$	31.432
12	$T_g[17]$ $y_{CO_2}[9,21]$	31.931

6.2.2 Optimal Distributed Sensor Placement

In this work, it is assumed that gas temperature, species mole fractions and pressure are available for measurements at each grid points and the measured values for all type of measurements are available at the same time. However, it may be difficult to make pressure and concentration measurements in practice and availability of all measured values at the same time may not be practically feasible. But, this work can be considered with the assumptions that the most easiest and rapid measurements are from temperature and perform the sensor placement for the case that only temperature measurements can be made. Also, the EKF can be tailored for the case when there are delayed measurements and so on.

6.2.2.1 Steady-state solution

Table 48 shows the parameters considered in the WGSR reactor. The system of equations are consist of 176 equations which are solved in MATLAB using 'fsolve' function; and the steady-state solution for the parameters shown in Table 48 is obtained.

Table 48. Water gas shift reactor model parameters

Parameter		Value	Parameter		Value
Inlet steam and gas pressure (Pa)		5,626,121	Inlet steam and gas temperature (K)		580
Catalyst	Diameter (mm)	0.1	Syngas Valve	Opening (%)	50
				coefficient	6×10^{-5}
	Density (g/cm^3)	0.65	Steam Valve	Opening (%)	50
				coefficient	2×10^{-5}
	Thermal conductivity (W/m-K)	35	Syngas mole fractions	CO	0.31
				H2O	0.26
				CO2	0.13
				H2	0.30
	Porosity	0.38	Reactor Length (m)		1
	tortuosity	5	Reactor diameter (m)		0.5
	Specific heat (J/Kg-K)	880	Number of grid points		25

6.2.2.2 Actual data

The actual data used in the GA's objective function is obtained by simulating the WGSR over a certain period of operation time and the actual data is stored at each sampling time. Noise simulation in the actual data is performed in two steps: (*i*) Noise with known variance in differential state are added after the states are integrated from k to k+1 using DAE solver (*ii*) after integration and obtaining noisy differential states, noise in algebraic states are introduced by solving algebraic equations with presence of algebraic noise with known variance. Random noises with known variance are added to the initial states and the initial noisy data along with the stored data at each time instant are considered as the actual data. In our work, process time is assumed as 200 seconds with a sampling time of 5 seconds. Therefore, a total of 41 set of data are obtained for use in GA. The measured values are obtained by adding the random noise with known variance to the corresponding actual values.

6.2.2.3 Sensor placement results

Based on the model descriptions explained in the previous sections, five different models are formulated and the performances of these models in the sensor placement framework are compared. The result of these comparisons will be an appropriate model that can be used for study of the effect of different parameters on the sensor placement results. The understudy models are as follows: (1) *Model I*: In this model, both state and error propagations are performed using the detailed model shown in Eqn. (181) (2) *Model II*: In this model, state propagation is performed by integrating the simplified model, but, the error propagation is performed by firstly computing the numerical Jacobian matrix around the current state estimates using the detailed model (3) *Model III*: This model has both state and error propagations performed using the simplified model. In this model, the covariance of the noise in the simplified model is assumed equal to the covariance of the noise in the detailed model (i.e. 10^{-3} for both T_g and H_2O mole fractions) and the exogenous equations are assumed to be noise free ($\Gamma_{k+1} = \mathbf{0}$), consequently, no state constraints) (4) *Model IV*: This model is similar to *Model III* except that here the error covariance matrix

is tuned to account for the lost information due to the model simplification, i.e. absence of assuming correlated noise in mole fractions. (5) *Model V*: In this model, as shown in Eqn. (213), it is assumed that the exogenous algebraic states are not noise free ($\Gamma_{k+1} \neq \mathbf{0}$) and a corresponding error covariance matrix is added in the error propagation step as in Eqn. (217) to account for the noise in CO_2, CO, H_2 mole fractions and T_{cat}. Since it is theoretically difficult to account for the correlated noise while the equations are decoupled, therefore, the error covariance matrices are tuned to account for such information loss. Table 49 shows the parameters used in each model for state estimation.

Table 49. Process noise variance values for different models

Noise Term	**Model**				
	I	II	III	IV	V
$\boldsymbol{\omega}$	$y: 10^{-3}$ $T_g: 10^{-3}$	$y: 10^{-3}$ $T_g: 10^{-3}$			
$\boldsymbol{\nu}$	$y: 10^{-3}$ $T_g: 10^{-3}$ $P: 5\times10^{-3}$	$y: 10^{-3}$ $T_g: 10^{-3}$ $P: 5\times10^{-3}$	$y: 10^{-3}$ $T_g: 10^{-3}$ $P: 5\times10^{-3}$	$y: 10^{-3}$ $T_g: 10^{-3}$ $P: 5\times10^{-3}$	$y: 10^{-3}$ $T_g: 10^{-3}$ $P: 5\times10^{-3}$
$\boldsymbol{\gamma}$	$P: 10^{-3}$	$P: 10^{-3}$	$P: 10^{-3}$	$P: 10^{-3}$	$P: 10^{-3}$
$\boldsymbol{\omega_2}$			$y_{H_2O}: 10^{-3}$ $T_g: 10^{-3}$	$y_{H_2O}: 2.5\times10^{-3}$ $T_g: 9\times10^{-4}$	$y_{H_2O}: 3.7\times10^{-4}$ $T_g: 8\times10^{-4}$
$\boldsymbol{\Gamma}$					$y_{CO}: 10^{-3}$ $y_{CO_2}: 10^{-3}$ $y_{H_2}: 10^{-3}$ $T_{cat}: 10^{-3}$

Sensor placement is studied for a fixed number of sensors (50 number of sensors) by running GA for each model separately. Figure 106 shows normalized fitness values for each model as the GA searches for the optimal sensor placement. It should be noted that the fitness values are normalized by the fitness value that is obtained if all available states are measured. In Figure 106, *Model I* has the highest fitness as the sensor placements are obtained using the detail model that has no information loss. *Model II* shows interesting results in terms of fitness value compared to *Model III* and *Model IV* as the only difference is that *Model II* uses Jacobian matrix computed from the detailed model,. This shows that more accurate Jacobian matrix for error propagation can compromise for loss of information due to use of less accurate model for state propagation. *Model V* provides highest fitness although it is fully based on the simplified model. This shows the importance of considering presence of noise in algebraic states while considering a DAE system.

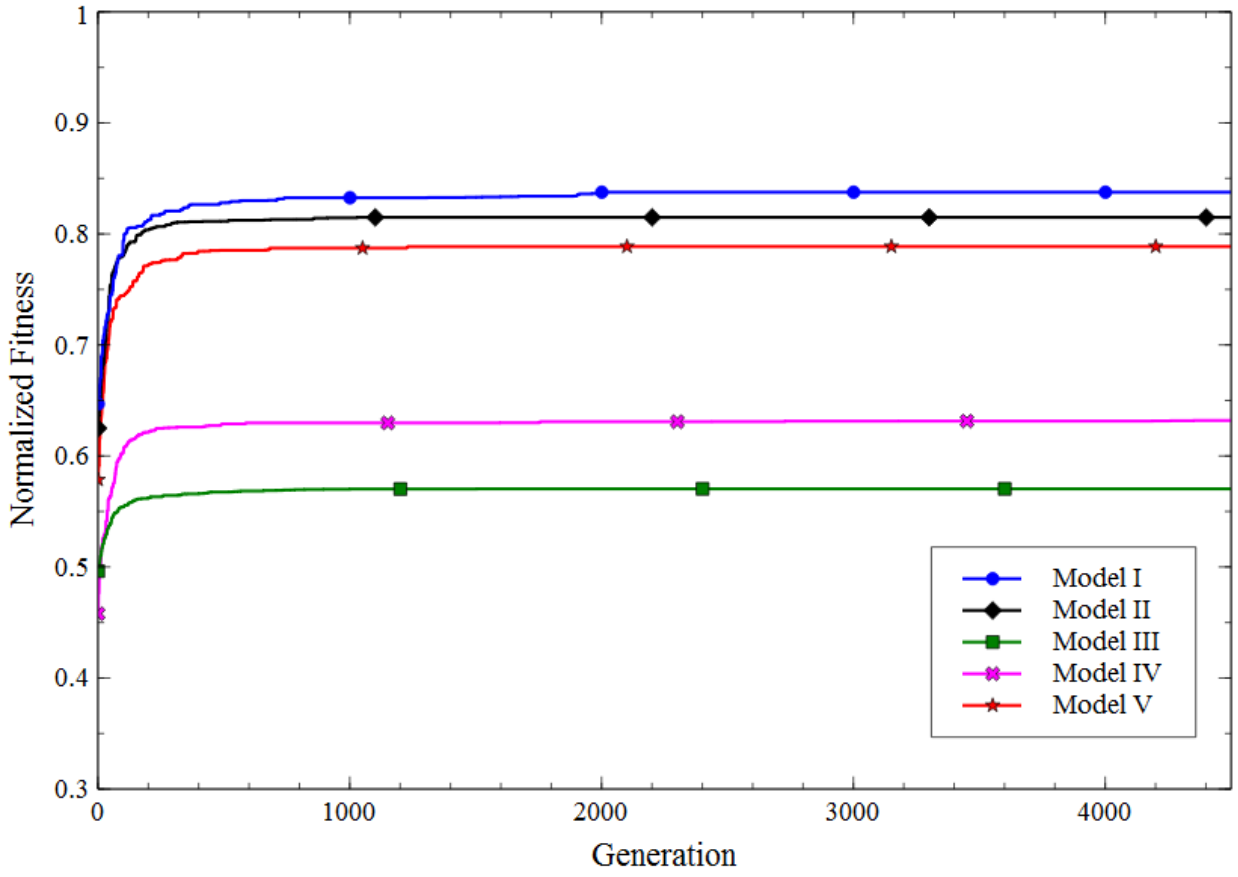

Figure 106. Normalized fitness evolution for each model

The most important factor in considering the simplified model in sensor placement is to achieve reduction in computation complexity of the model that can be studied by comparing the computation time for each model. Although the fitness values of each model in Figure 106 shows the performance of each model for state estimation, the final sensor placement results of each model must be checked against the detailed model, therefore, the reduction in computation time and sensor location of each final results will be compared. Table 50 shows the detailed analysis of the final solution of each model. In Table 50, *Model I* is the benchmark as it represent the full use of detailed model and other models are compared against *Model I* . The sensor placement from Model I is considered as the optimal solution of the SP and the SP results of other models will be compared against this solution. The first 6 columns of Table 50 show the number of sensors picked after 4500 number of generation of the GA optimization for each type of variable out of 25 available locations on the reactor, however, values in the parenthesis represent number of sensors that have similar location as the sensors picked in *Model I*. As can be seen in Table 50, none of the models pick any pressure sensors as system pressure is very high that slight variation in the system pressure due to process noise has very little effect on the accuracy of the state estimates compared with the effect of other variables. The optimal solution, *Model I*, has only a temperature sensor picked to get most accurate estimates; also, it shows that it is possible to achieve 84% of accuracy compared to the case where all states are measured. This is only achieved if the sensors are placed at optimal locations. However, the average time to achieve the optimal solution is relatively high when compared to the simplified models as the average time can be reduced up to approximately one-sixth of the original time when considering *Model V*. Number of temperature sensors picked by simplified models are relatively high compared to *Model I*, this is because that gas temperature is the only differential variable in the

simplified models and accurately estimating the only differential variable can affect the state estimates. *Model II* shows significant reduction in computation time while maintaining high fitness (0.83) when the obtained solution is evaluated in a detailed model compared to *Model I*. Although *Model III* and *IV* show significant computation time reduction, neglecting the process noise has resulted in significant information loss, therefore, lower fitness in both GA and when evaluated in detail model. Among all simplified models, *Model V* shows the lowest computation time and superiority over computation time reduction. Moreover, *Model V* results in reasonably good estimates when compared to *Model I*. This is due to fact that *Model V* accounts for process noise in algebraic variables, thus, resulting in better estimates compared to other models. Therefore, we can claim that *Model V* not only results in reasonably good estimates, it reduces the computation time significantly.

Table 50. Sensor placement results and computation time for each model

Model	**Number of sensors (Number of sensors similar to *Model I*)**						**Fitness**		**Average CPU time per generation (s)**
	CO	H_2O	CO_2	H_2	T_g	P	in GA	In detail	
I	17	6	17	9	1	0	0.84	0.84	24.33
II	16 (16)	6 (5)	17 (17)	6 (6)	5 (1)	0 (0)	0.81	0.83	8.27
III	19 (15)	2 (0)	14 (12)	6 (3)	9 (0)	0 (0)	0.57	0.77	5.14
IV	20 (15)	2 (0)	15 (12)	8 (4)	5 (0)	0 (0)	0.63	0.78	4.89
V	19 (17)	0 (0)	18 (16)	7 (7)	6 (0)	0 (0)	0.79	0.81	4.41

6.2.2.4 Study of Number of Sensors

Practically, it is more desirable to reduce the number of sensors while achieving reasonable state estimates. Therefore, sensor placements are investigated for different number of sensors and the results are tabulated. In Table 51, the sensor placement results of *Model V* is compared against the detailed model to study the effect of number of sensors on the performance of *Model V* and amount of information loss due to reducing the number of sensors. Increasing the number of sensors, the difference in normalized fitness values of *Model V* and I seem to be reducing. However, this difference in accuracy can be compensated by the computation burden reduction that is gained by simplified model. For all number of sensors, *Model V* seems to rely more on the measurements of temperature, T_g, rather than the measurements from H_2O. In contrast, as the number of sensors increases, the detailed model requires more number of H_2O sensors, whereas the numbers of temperature sensors remain fairly the same. These results are interesting in the sense that the simplified model picks more temperature sensors than the detailed model while maintaining good performance. Choosing simplified model over detailed model not only reduces the computation time for SP, in view of the sensor network cost, one would achieve less expensive sensor network by using more temperature sensors that are orders of magnitude cheaper than the concentration sensors.

Table 51. Sensor placement results comparison of Model I and Model V for different number of sensors

Number of sensors	Normalized fitness		Sensor placement {*Model I* / *Model V* (*similar to Model I*)}					
	Model I	*Model V*	CO	H_2O	CO_2	H_2	T_g	P
10	0.60	0.55	8 6 (6)	0 0 (0)	0 0 (0)	0 0 (0)	2 4 (0)	0 0 (0)
20	0.69	0.64	13 10 (10)	2 0 (0)	2 4 (1)	2 1 (1)	1 5 (0)	0 0 (0)
30	0.74	0.72	15 15 (14)	2 0 (0)	9 9 (6)	3 2 (1)	1 4 (1)	0 0 (0)
40	0.79	0.77	15 16 (14)	3 0 (0)	15 14 (12)	6 5 (5)	1 5 (1)	0 0 (0)
50	0.84	0.81	17 19 (17)	6 0 (0)	17 18 (16)	9 7 (7)	1 6 (0)	0 0 (0)

6.2.2.5 Study of Effect of Process Noise Covariance

Choosing appropriate process noise covariance matrices is important for the accuracy of the state estimates; however, it is not clear how sensor placement is affected and how much of information is lost when process noise covariance is not chosen properly. Table 52 shows the sensor placement comparison for *Model I* and *V* for different process noise covariance. In Table 52, *Model V-c* has the same parameters as *Model V* in Table 50. Underestimating and overestimating the process noise covariance, as in *Model V-a* and *V-e*, significantly reduces the performance of the obtained solution. This can be seen as the normalized fitness of the solution of these models in detail modeled have lowest normalized fitness compared to the other models. Also, SP results of these models show obvious deviation from the SP results of detailed model to such a great extent that pushes the SP algorithm to pick more of temperature sensors.

Table 52. Effect of process noise covariance on the sensor placement results

Model	Process noise covariance	Normalized fitness	Number of sensors (Number of sensors similar to Model I)					
			CO	H_2O	CO_2	H_2	T_g	P
I	$Q = 10^{-6}$	0.84	17	6	17	9	1	0
V-a	$Q_{H2O} = 10^{-8}$ $Q_{Tg} = 10^{-8}$ $Q_{alg} = 10^{-8}$	0.66	16 (10)	5 (0)	6 (5)	5 (1)	18 (1)	0 (0)

V-b	$Q_{H2O} = (3.7\times10^{-4})^2$ $Q_{Tg} = (8 \times 10^{-4})^2$ $Q_{alg} = 10^{-8}$	0.74	17 (13)	0 (0)	10 (9)	7 (3)	16 (1)	0 (0)
V-c	$Q_{H2O} = (3.7\times10^{-4})^2$ $Q_{Tg} = (8 \times 10^{-4})^2$ $Q_{alg} = 10^{-6}$	0.81	19 (17)	0 (0)	18 (16)	7 (7)	6 (0)	0 (0)
V-d	$Q_{H2O} = 10^{-6}$ $Q_{Tg} = 10^{-6}$ $Q_{alg} = 10^{-6}$	0.80	17 (16)	1 (0)	18 (16)	9 (6)	5 (0)	0 (0)
V-e	$Q_{H2O} = 10^{-4}$ $Q_{Tg} = 10^{-4}$ $Q_{alg} = 10^{-4}$	0.70	9 (9)	5 (2)	10 (9)	9 (5)	15 (0)	2 (0)

6.2.2.6 Study of Effect of initial error covariance

In this part, we examine the effect of initial error covariance of *Model V* on the SP results and compare it with the SP results of *Model I* as shown in Table 53. It should be noted that the initial error covariance is known through actual data preparation. In all models, *Model V-a* though c, no H_2O sensors are picked whereas more number of temperature (T_g) sensors are picked when comparing with the detailed model. *Model-Va* assumes higher initial error covariance. However, for other sensors except for pressure sensor, numbers of the sensors as well as the number of sensors similar to the detailed model are relatively high. In all three models, the normalized fitness of the solution remains reasonably high and confirms their reliability for not only state estimation, but also for SP. It is worth mentioning once again that in calculating the fitness of these models, the first set of state estimates are ignored and the corresponding fitness and its normalizing fitness are calculated without considering the quality of the initial estimates. It can be seen from Table 53 that the choice of initial error covariance has a slight effect on the SP results.

Table 53. Effect of initial error covariance on the sensor placement results

Model	**Initial error covariance matrix**	**Normalized fitness**	**Number of sensors (Number of sensors similar to *Model I*)**					
			CO	H_2O	CO_2	H_2	T_g	P
I	$P_0 = 10^{-6}$	0.84	17	6	17	9	1	0
V-a	$P_0 = 10^{-4}$	0.80	18 (17)	0 (0)	17 (16)	7 (6)	8 (1)	0 (0)
V-b	$P_0 = 10^{-6}$	0.81	19 (17)	0 (0)	18 (16)	7 (7)	6 (0)	0 (0)
V-c	$P_0 = 10^{-8}$	0.81	19 (17)	0 (0)	17 (16)	7 (6)	7 (1)	0 (0)

6.2.3 Conclusion

Previous EKF frameworks for DAE systems published in the literatures assume that algebraic equations are exact. However, in practice, algebraic equations could be describing a physical state and derived using modeling assumptions which introduces uncertainties in these process equations. Therefore, stochastic algebraic equations cannot be handled in the previous EKF formulations due to differentiation of white noise, which is not well-defined. Moreover, extra information about the process may be present in the

form of implicit equality constraints, such as mole balance in a reactor, which cannot be handled by previous EKF frameworks. A modification to the EKF approach that addresses these difficulties by avoiding the differentiation of the algebraic equations is proposed. The error covariance of algebraic variables are propagated as linear and non-linear combinations of error covariance of differential variables. The performance of the proposed filter is demonstrated through two examples. In the simple example, it is shown that estimates are improved over the measurements as RMSE of estimated states are considerably reduced in comparison to the RMSE of the measured data. In the WGSR example, the filter also shows considerably higher estimation accuracy of the states over the measurements when all states are measured. In both examples, the proposed filter shows superiority over the previous filtering framework by returning estimates with lower RMSE and closer to the actual values. Application of the proposed filter to the WGSR revealed that the type and location of the sensors used on the WGSR have important role in the accuracy of the state estimates.

In this section, a framework for sensor placement of water gas shift reactor is described. The proposed framework combines the state estimation technique with an evolutionary algorithm to obtain the optimal sensor locations (and types) that return most accurate estimates of the process states for a fixed number of sensors. The state estimation technique used in this work was developed for models that are described by the differential and algebraic equations (DAE). The already developed extended Kalman filter (EKF) for DAE is suitable for implementation on the reactor. A 1-D detailed model of the reactor is discretized along the reactor axis to convert partial differential equations to ordinary differential equations (ODE). This results in solving the complex mathematical equation of the reactor model at each discretization point while the discretization points are available locations for measurement for EKF. However, the number of discretization points and number of equations that must be solved at each point result in high computation time and gives rise to a need for simpler models. A common way to reduce the computational complexity of detailed models is to linearize the model around the operating point. However, since a main future application of this work is to come up with sensor placements for fault detection and identification, linearized models are ruled out due to severe drift of these model from normal operating condition as a consequence of process faults; and also linearized form of highly non-linear models carry much less information of the process and causes difficulties in tracking the crucial process variables. A simplified model through scaling analysis developed in previous sections that seem promising in effective reduction of complexity of the system while maintaining reasonable accuracy is used. The EKF for DAE is briefly re-derived for the simplified reactor model. As a result, different state estimation formulation of the system can be derived. A genetic algorithm (GA) is used to generate measurement models for use in the state estimations which represent the sensor placements. The GA searches over possible measurement models to obtain an optimal sensor placement that result in most accurate state estimates. The GA is performed for different EKF formulations and the results are compared. A significant reduction in computation time is observed by using the simplified model. However, the accuracy of each model seems not only affecting the quality of state estimates, but, different sensor placements are obtained by these model. Model V seems superior to the other model as it has lowest computation time, relatively high state estimate accuracy and closest SP results to the detailed model.

As a brief summary, the goal in this section was to develop a novel framework for sensor placement and address issues of using comprehensive models that gives rise to computational complexities. Our analysis has shown that using an appropriate simplified model can be an advantage in terms of reducing computational complexity while achieving reasonable sensor placements that can result in the performance that is comparable to the detailed model. This analysis has shown that using simplified models in both the state and error propagation can further reduce the computational load; and when appropriately tuned, it can replace the complex detailed model as the study of process noise covariance suggests. Study of the initial error covariance has shown insignificant change of the placement and performance of the solution.

However, a future application of the proposed framework is to obtain optimal sensor placements that can help in detection and identification of the faults in a system. Take catalyst deactivation in a reactor due to thermal cycling, ash decomposition and etc. as an example. One is interested in locating such abnormality in a lengthy reactor by optimally placing sensors on the reactor that not only identifies that somewhere catalyst is being/has deactivated, but, also interested in locating such abnormality and prepare for preventive/corrective action. From an economical viewpoint, since reactors' catalyst are usually removed and replaced by fresh catalyst after certain time, locating the area with deactivated catalyst reduces the catalyst replacement cost. From a process viewpoint, an optimal sensor placement can help in better monitoring of the process and assess the estimation of faults that can degrade the process or drive the system to hazardous conditions. Therefore, our future work will focus on designing a sensor network that can help in estimating possible faults that can harm the process operation and/or production.

6.3 2-tier Sensor Placement for Gasification Island

6.3.1 Fault Simulation

Faults are simulated in the combined system of the sour water gas shift reactor (SWGSR) and Selexol. These faults selected are those which occur in a short period of time. This includes the undesired accumulation of fly ash onto the catalyst of SWGSR that can reduce the porosity of the catalyst, or change its surface area (SA). Undesired materials can also poison the catalyst resulting in reduction in the catalyst activity.

6.3.1.1 Single Faults

The faults that have been simulated are as follows:

1. 10% reduction in the surface area of catalyst in the first reactor of the SGSR within 22 minutes
2. 10% reduction in the porosity of catalyst in the first reactor of the SGSR within 22 minutes
3. 5% reduction in the surface area in each of the reactors of the SGSR within 22 minutes
4. 5% reduction in the porosity of each of the reactors of the SGSR within 22 minutes
5. 10% reduction in the catalyst activity in the first reactor of the SGSR within 49 minutes.
6. 5% reduction in the catalyst activity in each of the reactors of the SGSR within 49 minutes.

Due to the size of the simulation and the number of variables being recorded, ASPEN Plus Dynamics runs out of memory if several variables are recorded. Variable selection was done such that the number of variables recorded would be reduced. Following are the responses at a particular location, viz. end of the SWGSR. The responses of the CO and COS mole fractions, and the temperature at the outlet of the SWGSR are shown below. The legends for the plots are as follows:

Representation	Fault #
	Fault 1
	Fault 2
	Fault 3
	Fault 4
	Fault 5
	Fault 6

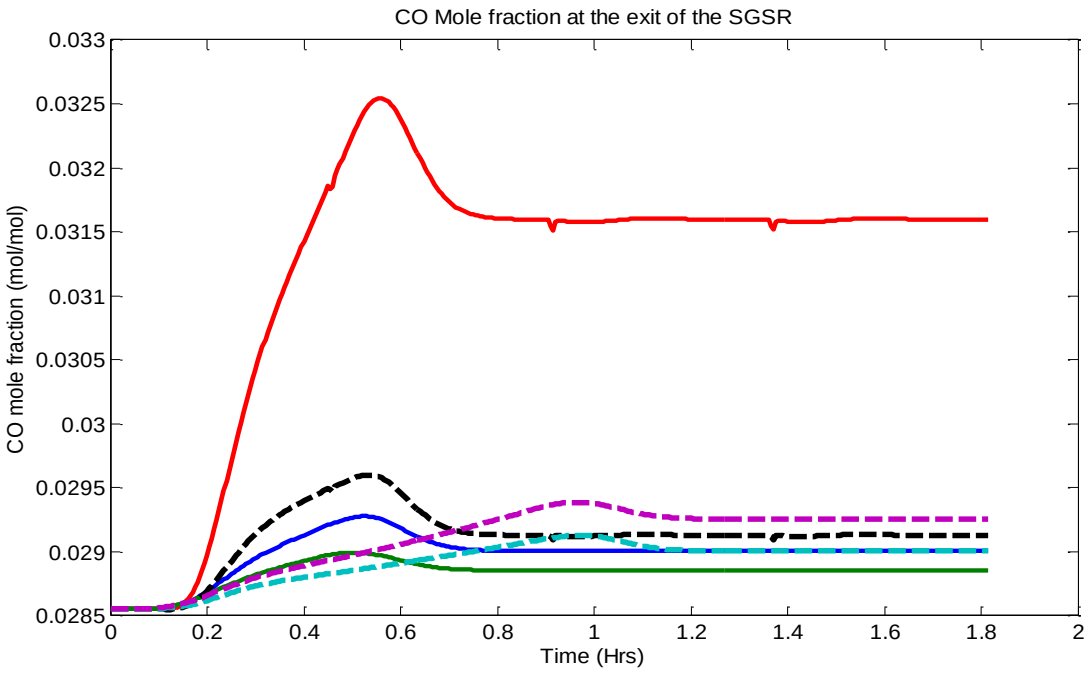

Figure 107. Change in CO mole fraction at the exit of the SWGSR due to faults.

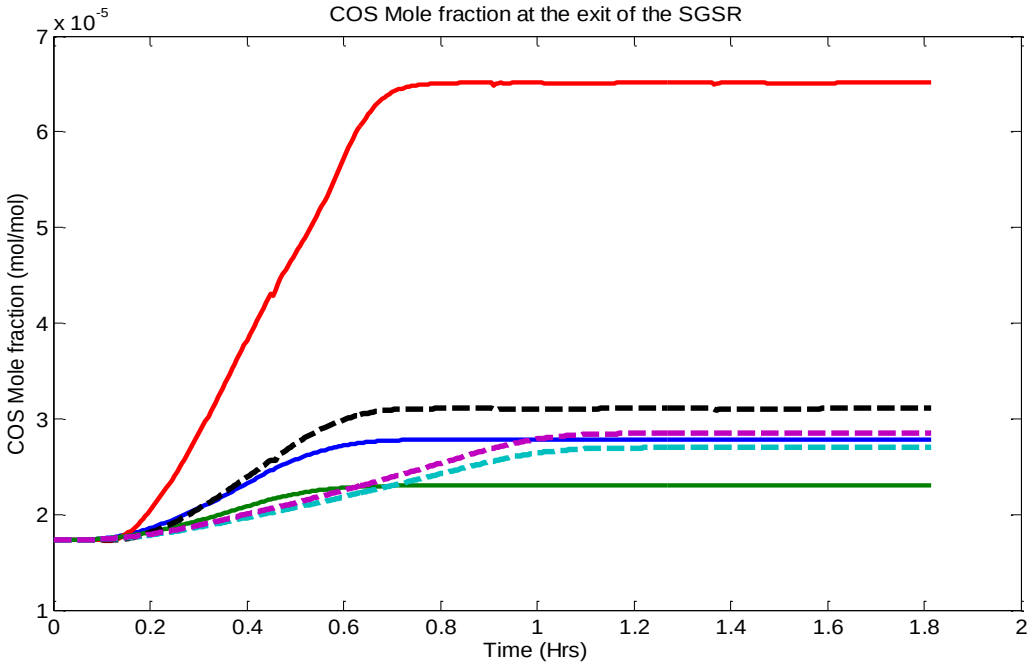

Figure 108. Change in COS mole fraction at the exit of the SWGSR due to faults.

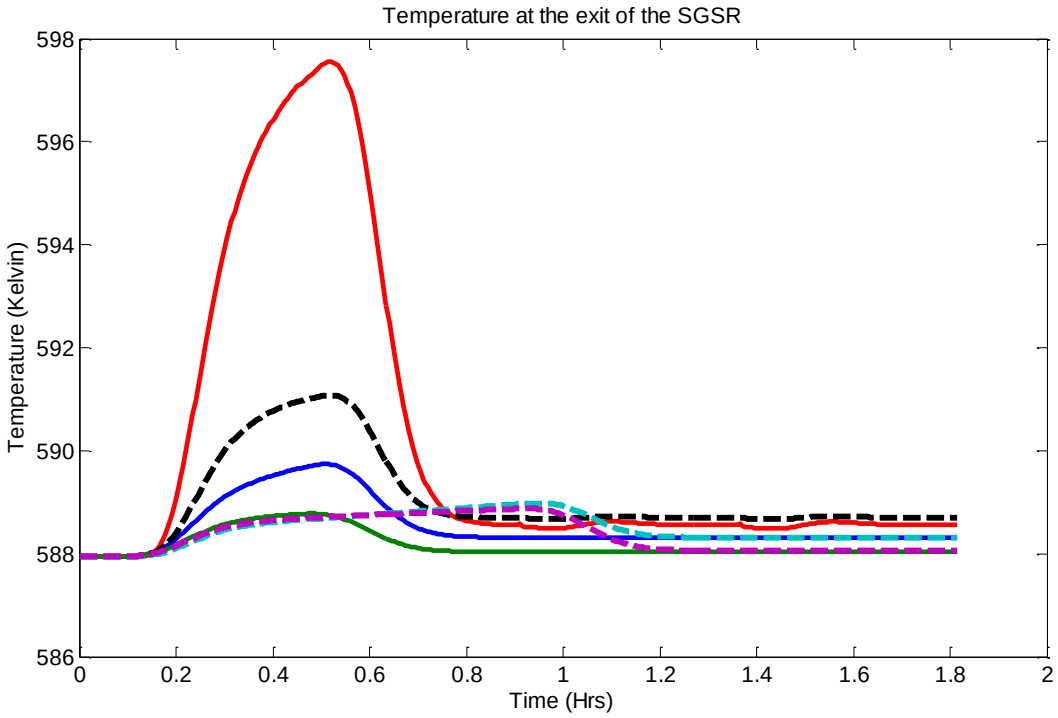

Figure 109. Change in outlet temperature of the SWGSR due to faults.

In the figures presented above, the response to Fault 2 is found to be the highest. The decrease in porosity by 10% in the first reactor results in reduced extent of reaction for the shift reaction as well as the COS hydrolysis reaction. The fault is implemented at 5 minutes and is ramped for a period of 22 minutes. When the fault stabilizes, the profile can be seen to drop and finally settle at a lower value. For Fault 2, this temperature could be a candidate variable in identifying and resolving the fault due to the amplitude of its initial response. Faults 5 and 6 are implemented for a period of 49 minutes. The CO and COS profiles for these faults differ slightly, however, the temperature profile appears to follow the similar trajectory initially.

The responses of a few variables are shown above. It should be noted that the variables that respond best will be selected by the sensor placement algorithm and the variables presented in the report are in order to show the extent and effect of the fault on a few key variables.

6.3.1.2 Multiple Severity Faults

Faults in the integrated system consisting of the sour water gas shift reactor (SWGSR) and the acid gas removal unit or SELEXOL unit were simulated. The objective of simulating multiple severities of each fault is to understand until what level of severity can the fault be observed and resolved. This would add a new dimension to the problem of sensor placement to see how the location, number and type of sensors would change given this information.

In the SELEXOL side of the integrated model, faults at 4 locations in the acid gas removal plant have been simulated. Once again, 3 fault levels were chosen at these locations. These locations and their fault severities are shown below in Table 54.

Table 54. Faults simulated on the SELEXOL side of the integrated model

Fault	Description
F_{1-3}	Reduction in the area of the bottom (15^{th})tray of the CO_2 absorber × 3
F_{4-6}	Reduction in the area of the bottom(26^{th}) tray of the H_2S absorber × 3
F_{7-9}	Reduction in the area of the bottom(5^{th}) tray of the H_2S concentrator × 3
F_{10-12}	Reduction in the area of the bottom (6^{th}) tray of the SELEXOL stripper × 3
F_{13-15}	Leakage fault at start of heat exchanger H2SSTRBT × 3
F_{16-18}	Leakage fault at end of heat exchanger H2SSTRBT × 3
F_{19-21}	Fouling fault simulated in heat exchanger H2SSTRBT × 3
F_{22-24}	Fouling fault simulated in heat exchanger PRCRE × 3

Faults were simulated previously in the SELEXOL model as part of the system level fault simulation and sensor placement studies. However, an approach was taken to improve the criteria for the selection of the location at which faults were to be simulated. The explanation for choosing this is shown below.

- CO_2 Absorber fault: simulated by reducing the 15^{th} tray area as syngas enters from bottom.
- H_2S absorber fault: simulated by reducing the 26^{th} tray area. This tray is in the vicinity of stream coning from SWGSR, stream rich with H_2S coming from SELST and gas turbine outlet containing CO_2 and H_2. Reasons could be Sulfur deposition or ash/soot carried along SWGSR.
- H_2S concentrator fault: simulated by reducing the 5^{th} tray area. N_2 stream enters at this tray. Could have particulate matter entrained in it.
- SELEXOL stripper fault: simulated by reducing the 6^{th} tray area. This is the feed tray for stream coming from H_2S concentrator. Either elemental sulfur or N_2 particulate matter entering could get deposited here.
- The heat exchanger H2SSTRBT is an important heat exchanger that heats the stream coming from the bottom of the H2S absorber and sends it to the H2S concentrator using the lean solvent stream.
- The heat exchanger PRCRE is a heat exchanger that is used to cool the solvent stream to the CO2 absorber.

A more detailed approach to simulate a fault at different locations within the same equipment is made while simulating Fault F_{13-15} and F_{16-18}. Both faults are simulated in the HE H2SSTRBT, however the configurations are different. Fault F_{13-15} is simulated in the following manners shown in Figure 110.

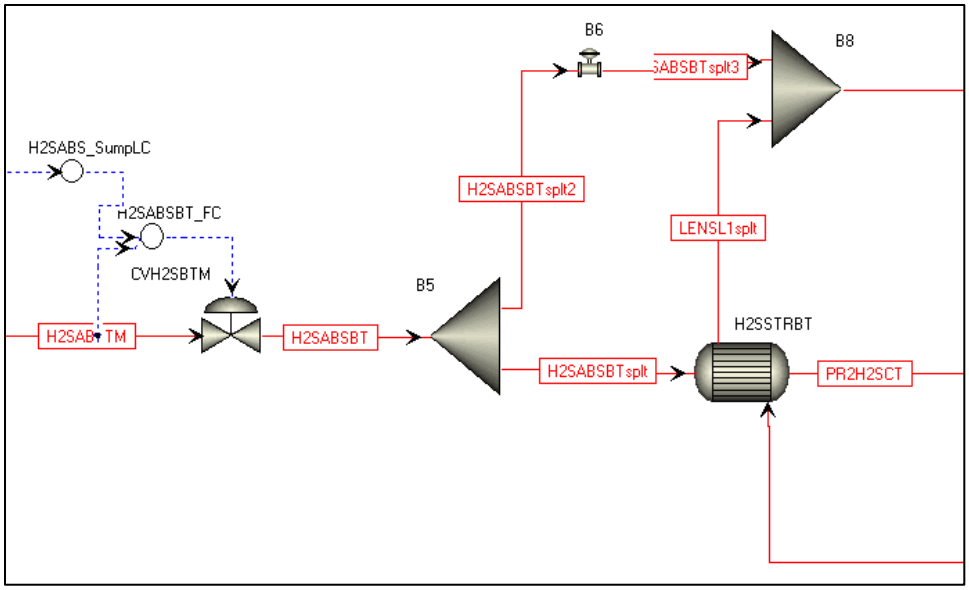

Figure 110. HE configuration 1: leak simulated as mixing of inlet high pressure stream into outlet low pressure stream.

Fault $F_{16\text{-}18}$ is simulated as shown in Figure 111.

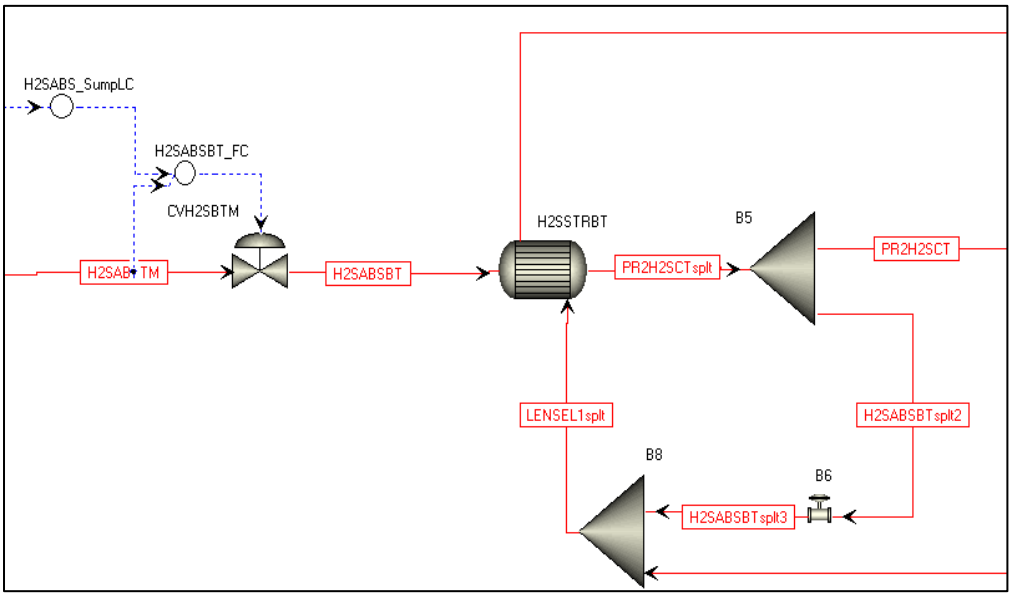

Figure 111. HE configuration 2: leak simulated as mixing of outlet high pressure stream into inlet low pressure stream.

The purpose of simulating the leak fault in two separate ways is to assess whether the sensor network could give information of the location of the leakage within the heat exchanger. In fault $F_{13\text{-}15}$, the leak has taken place closer to the entrance of the tubes while in fault $F_{16\text{-}18}$ it is simulated as if the leak has taken place towards the end of the tubes. This would bring a key information into the sensor placement study if it can detect the location within a single equipment while considering plant wide faults. Fault $F_{22\text{-}24}$ is to see whether a sensor network can be found that can distinguish between a leakage fault and a fouling fault within the same equipment.

On the SWGSR side of the integrated model a total of 17 faults were simulated i.e. 3 instances of 6 faults (except for fault F_{31-32} due to stability problems). These are shown below in Table 55.

Table 55. Faults simulated on the SWGSR side of the integrated model

Fault #	Description	Fault type	Duration	Severity
F_{25-27}	Porosity reduction (1st reactor)	Ramp	25min	2%, 5%, 10%
F_{28-30}	Porosity reduction (both reactors)	Ramp	25min	2%, 5%, 10%
F_{31-32}	Activity reduction (1st reactor)	Ramp	25min	2%, 5%
F_{33-35}	Activity reduction (both reactors)	Ramp	25min	2%, 5%, 10%
F_{36-38}	Surface area reduction (1st reactor)	Ramp	25min	2%, 5%, 10%
F_{39-41}	Surface area reduction (both reactors)	Ramp	25min	2%, 5%, 10%

6.3.2 Results

6.3.2.1 System-Level: Gasification Island

The system-level sensor placement algorithms are implemented on the gasification island and the results are presented in Table 56. From the case studies in previous sections we have learnt that the optimal results are obtained from the combination algorithm (FES & MR). Here, since the magnitude of the faults considered in the gasification island is low (maximum 10% change as a fault), therefore, we can predict that low level MR threshold should be chosen. This can be verified by the results in Table 56. The FES & MR algorithm with low MR threshold level has the lowest number of unresolvable faults and sensor network cost. The results of SDG and FES individual algorithm are shown for the sake of comparison. In order to save space, the sensors and unresolved faults of different algorithms are avoided and results are only shown for FES & MR with low MR threshold level in Table 57. Note that almost all of the sensors picked for resolution are temperature sensors except for a concentration sensor on the first stage sour WGS reactor. Since the temperature sensors are the least expensive sensors in this study, system-level fault resolution has been achieved with a significantly cost effective sensor network. Out of 703 pair of fault sets, only 25, which are shown in Table 57, cannot be resolved. This implies that more than 96% of the faults considered in the system can be resolved by a cost effective network of sensors.

Table 56. System-level sensor placement results of gasification island

Algorithm(s)	MR threshold level	Number of sensors	Sensor network cost	Number of unresolvable fault sets
SDG		112	21.8	26
FES		13	30.9	25
MR	Low	11	11.7	25
	Medium	11	21.7	26
	High	12	21.8	26

	Low	11	10.9	25
FES & MR	Medium	13	30.9	25
	High	13	30.9	25

Table 57. List of sensors and unresolved fault sets for FES & MR algorithm with low MR threshold level

Sensors	Unresolvable fault sets (where $[F_i,F_j]$ is shown as [i,j])
STREAMS("2IPSTMDR").T STREAMS("2RGCOOL5").T STREAMS("TO-AGR").T STREAMS("PR2H2SCT").T STREAMS("H2SCTBT1").T STREAMS("LENSL1").T STREAMS("PRCRPMD2").T BLOCKS("CO2ABS").Stage(9).T yco_19_R1 Tg_16_R1	[4,5] [4,6] [5,6] [7,8] [7,9] [7,21] [7,22] [7,23] [7,24] [8,9] [8,21] [8,22] [8,23] [8,24] [9,21] [9,22] [9,23] [9,24] [19,20] [21,22] [21,23] [21,24] [22,23] [22,24] [23,24]

6.3.2.2 Component-Level: First-Stage Sour Water Gas Shift Reactor

The distributed sensor placement is performed on the first stage sour WGS reactor. The actual data for the optimization problem is obtained by simulating the faults in the integrated system for each fault individually. The noise in the data is assumed as additive noise, where white Gaussian noise with known mean and variance is added to each state. The model in the state estimation is chosen as the simplified model where noise in the differential, algebraic and exogenous algebraic states are tuned due to the use of simplified model as explained in previous sections. The faults considered in the component-level are F_{25}, F_{26} and F_{27} for catalyst activity reduction; and F_{31} and F_{32} for catalyst porosity reduction. Each fault is assumed as a state and is augmented with other states in the system. Since the faults are modeled as a reduction in the catalyst activity, each fault state is assumed to be associated with a process noise, which is also tuned for in the EKF. Table 58 shows the reactor and EKF parameters. Figure 112 shows the progress of the GA for different faults. As seen in Figure 112, with only 30 sensors optimally placed on the reactor, more than 60% accuracy of measuring all the states (201 sensors on CO, H_2O, CO_2, H_2, COS and H_2S mole fractions, temperature and pressure states) has been achieved. Table 59 shows the optimal solution, sensor type and location, for each fault. The numbers in Table 59 show the grid-point number out of 25 total available grid-points of the corresponding sensor type at which measurement must be made. The grid-point numbers represent the location of the sensors on the reactor and the variable names represent the sensor type in Table 59. Using the optimal sensor placements, each corresponding fault state is estimated and plotted in Figure 113. Figure 113 shows that the fault severities are estimated with reasonable accuracy.

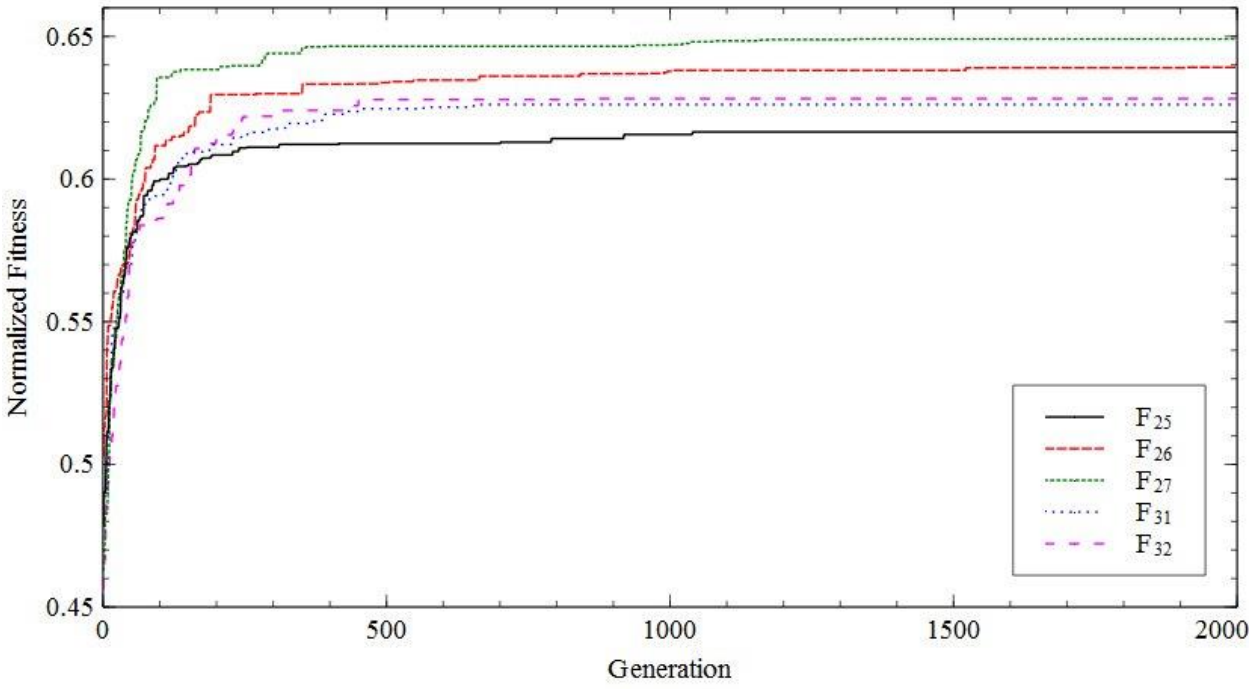

Figure 112. GA progress for different faults

Table 58. Reactor and state estimation parameters

Parameter	Value
Reactor parameters	
Length	7 m
Diameter	3 m
Inlet temperature	487.5 K
Inlet pressure	6093 kPa
Inlet Composition	
CO mole fraction	0.25711
H2O mole fraction	0.37753
CO2 mole fraction	0.11025
H2 mole fraction	0.24960
COS mole fraction	0.00014
H2S mole fraction	0.00534
EKF parameters	
Number of grids	25
Sampling time	5.4 s
Mole fraction process noise covariance	
CO, H_2O, CO_2, H_2	10^{-6}
COS, H_2S	2.5×10^{-11}
Mole fraction measurement noise covariance	
CO, H_2O, CO_2, H_2	10^{-6}
COS, H_2S	10^{-12}
Temperature process noise covariance	2.5×10^{-7}

Temperature measurement noise covariance	10^{-6}
Pressure process noise covariance	10^{-6}
Pressure measurement noise covariance	2.5×10^{-7}
Fault state process noise covariance	2.5×10^{-5}
Initial error covariance	
COS, H2S	10^{-12}
Other states	10^{-6}

Table 59. Optimal location and type of sensors for different faults

Sensor Type	Sensor Location				
	F_{25}	F_{26}	F_{27}	F_{31}	F_{32}
T_g	21,22,24	17,21	15,17	10,21	13,14,24
P					
P_{in}					
CO	13,16,21, 22,23,24,25	11,14,21, 22,23,24,25	13,20,21,22,2 3,24,25	12,13,15,19, 20,21,22,23, 24,25	19,20,21, 22,23,24,25
COS	25	23,24,25	22,23,24,25	22,24,25	19,20,21,22, 23,24,25
H_2O	13	14	13	12	
CO_2	2,7,8,9, 10,11,12,14, 15,23,24,25	4,6,8,10, 11,12,13, 15,16,22, 23,24,25	5,14,15,17, 19,20,21, 22,23,24,25	3,5,14,17, 18,22,23, 24,25	3,13,14, 16,21,23,24, 25
H_2	10,11,12, 14,15,16	12,13,15,16	14,15,17, 19,21	14,15,16, 17,18	13,14,15,16, 17
H_2S					

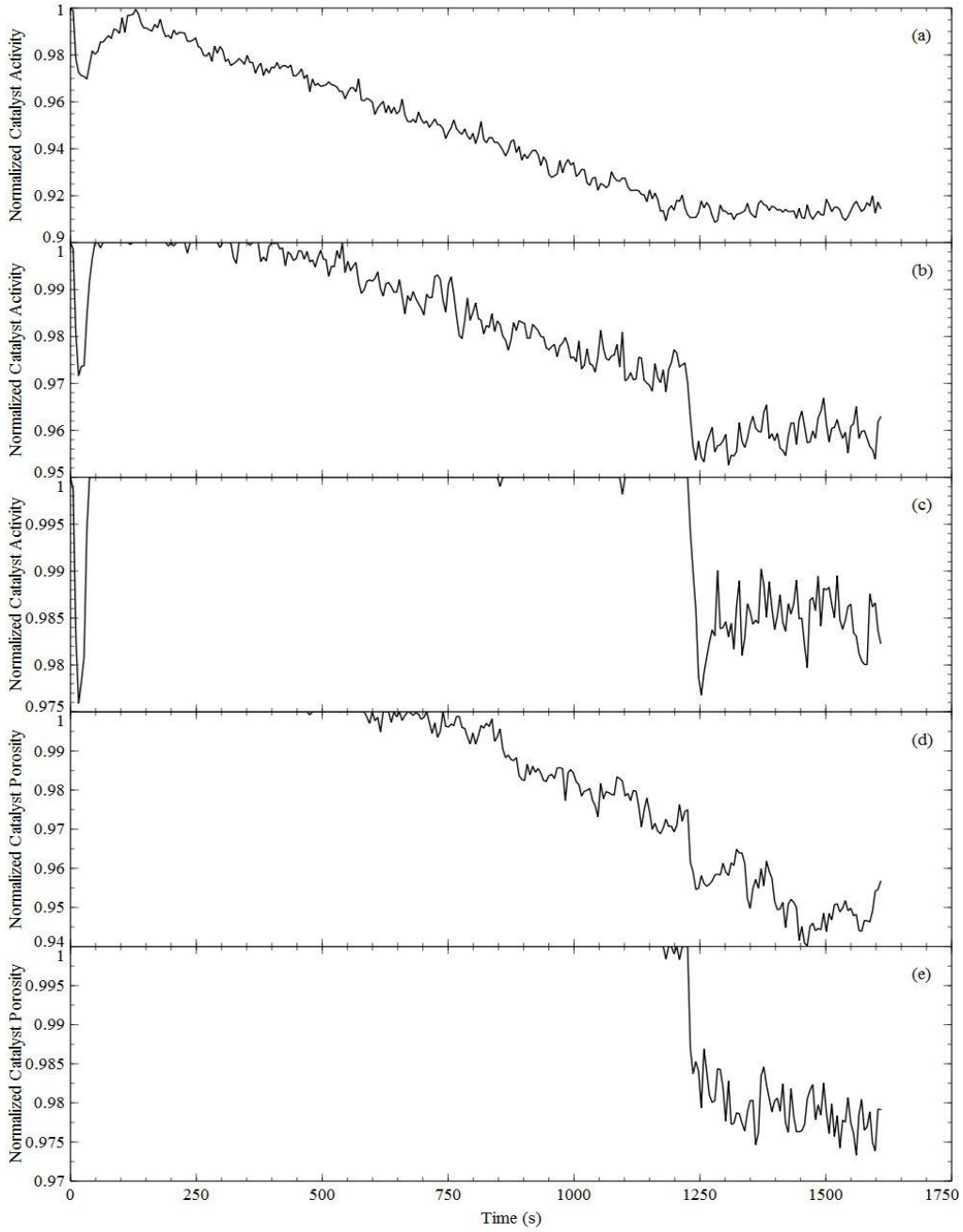

Figure 113. Fault severity estimation using optimal solution for fault (a) F_{25} (b) F_{26} (c) F_{27} (d) F_{31} (e) F_{32}

6.3.2.3 Conclusion

The system-level sensor placement resulted in a set of sensors that help in fault resolution with a great extent although some fault sets remain unresolved. For each fault in the component-level of sour WGS reactor, type and location of set of sensors with fixed quantities are obtained by solving the optimization problem where each set can be used to estimate the severity of the corresponding fault with reasonable accuracy.

A few sensors obtained by system-level sensor placement are placed on the sour WGS reactor. These sensors along with all the sensors obtained by distributed sensor placement are combined to make up the total sensors for the component monitoring and fault severity estimation. For each fault, 30 sensors are chosen to be placed on the reactor. While some sensor type and locations are similar for each fault, there are 66 unique sensors when the sensor sets are combined. These 66 sensors are combined with the two sensors placed on the reactor in system-level sensor placement. Also, since usually the states at the outlet of the reactor are measured for control and product specification purposes, 8 more sensors are placed at the reactor outlet to measure the mole fractions, temperature and pressure. This results in a set of 72 unique sensors. Therefore, in the integrated sensor placement which is the combination of the sensors obtained in the system- and component-level sensor placement, a network of 72 sensors is used for state monitoring and fault severity estimation.

Figure 114 shows the fault severity estimation for each fault using the final sensor network. Table 60 compares the normalized fitness values using the optimal sensor placements and the final integrated sensor network. Although more number of sensors can help in improved estimation of the states, the improvement in quality of the fault severity estimation is not significant. The slight improvement can hardly be seen by comparing Figure 114 with Figure 113. This is due to the reason that the improvement in the normalized fitness values represents slight improvement in the estimation quality of each state rather than significant improvement in the fault state.

Figure 115-119 shows the actual, measured and estimated states at the outlet of the reactor for mole fractions, temperature and pressure in presence of different faults using the final sensor network. Figure 115-119 shows that using the final network, the filter can estimate the states with good accuracy. States at different locations can be estimated using the final sensor network, thus, the reactor can be monitored efficiently using the sensor network.

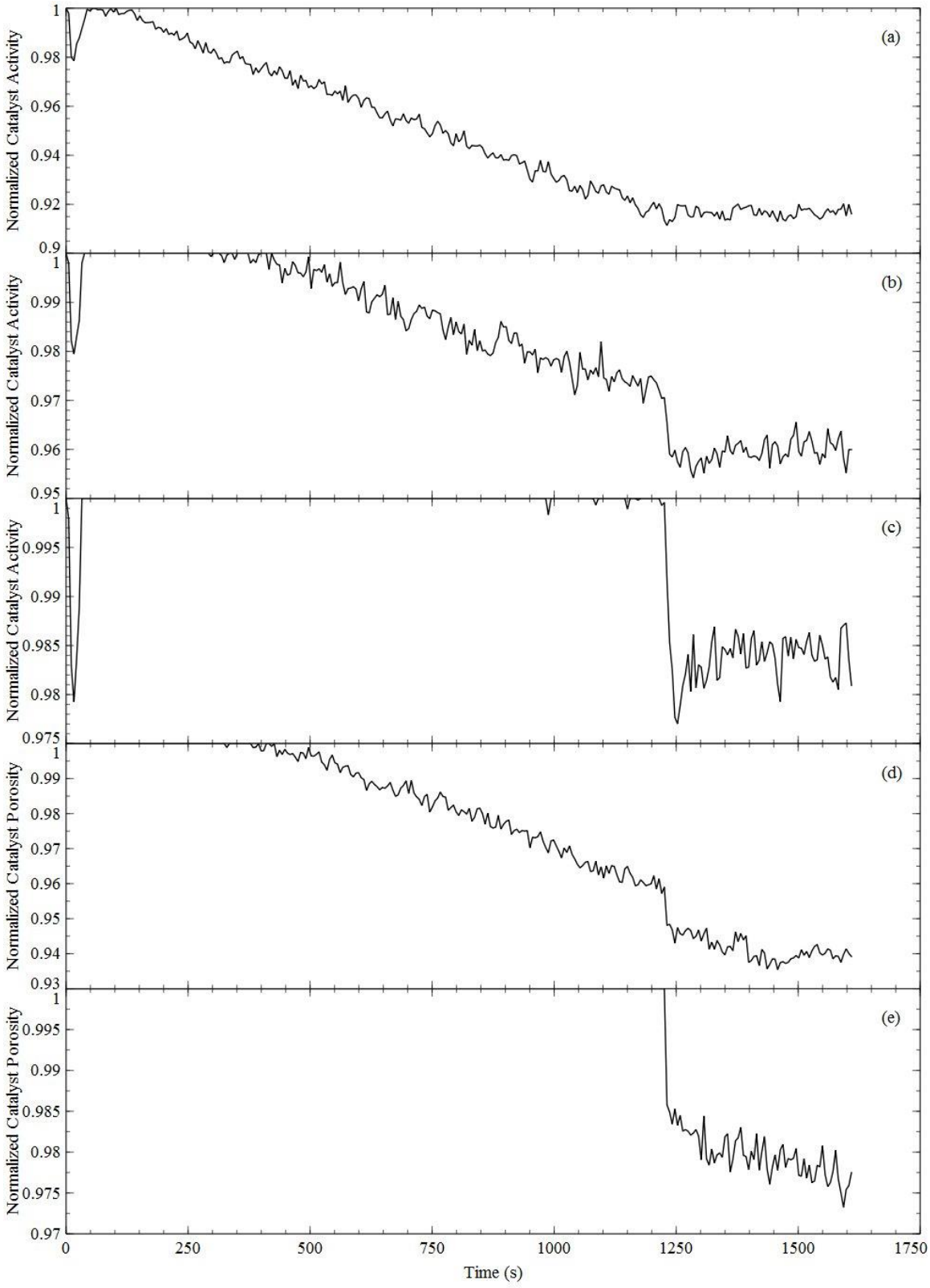

Figure 114. Fault severity estimation using final sensor network for fault (a) F_{25} (b) F_{26} (c) F_{27} (d) F_{31} (e) F_{32}

Table 60. Comparison of normalized fitness values for GA solution and final sensor network

Fault	GA solution normalized fitness	Final sensor network normalized fitness
F_{25}	0.6168	0.7561
F_{26}	0.6391	0.7716
F_{27}	0.6491	0.7751
F_{31}	0.6261	0.7800
F_{32}	0.6282	0.7749

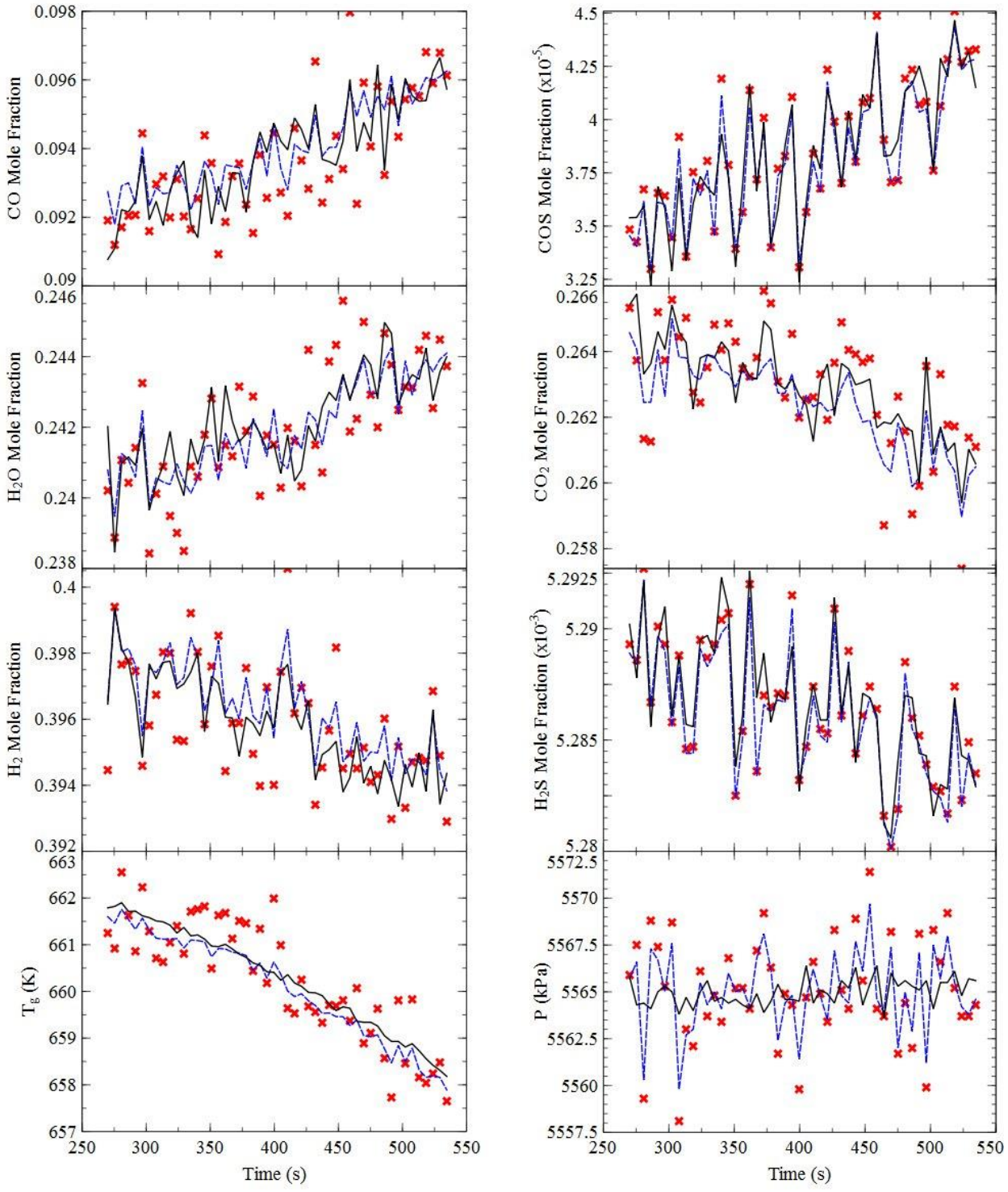

Figure 115. Actual (-), measured (*) and estimated (--) value of different states at the outlet of the reactor for fault F_{25}

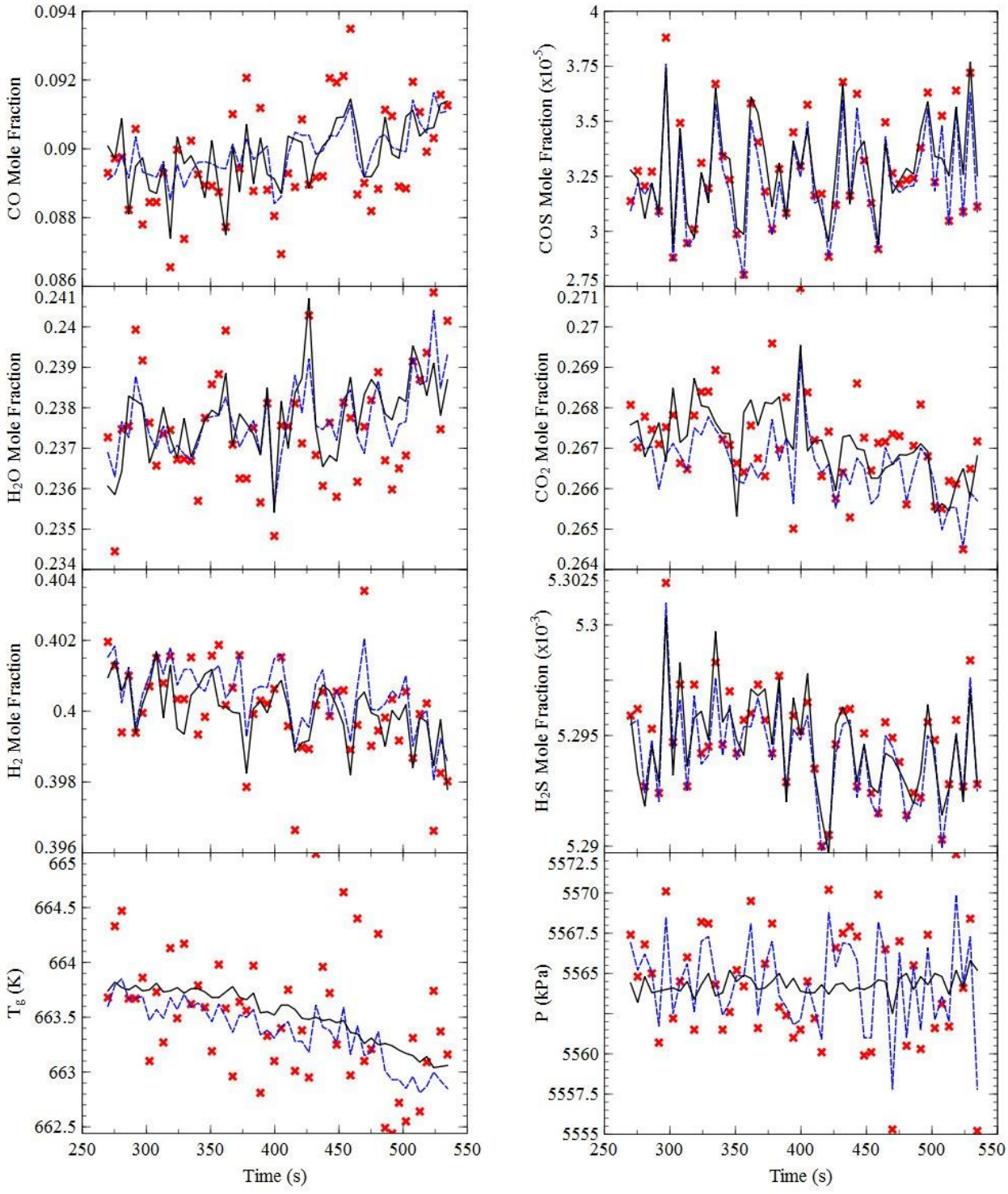

Figure 116. Actual (-), measured (*) and estimated (--) value of different states at the outlet of the reactor for fault F_{26}

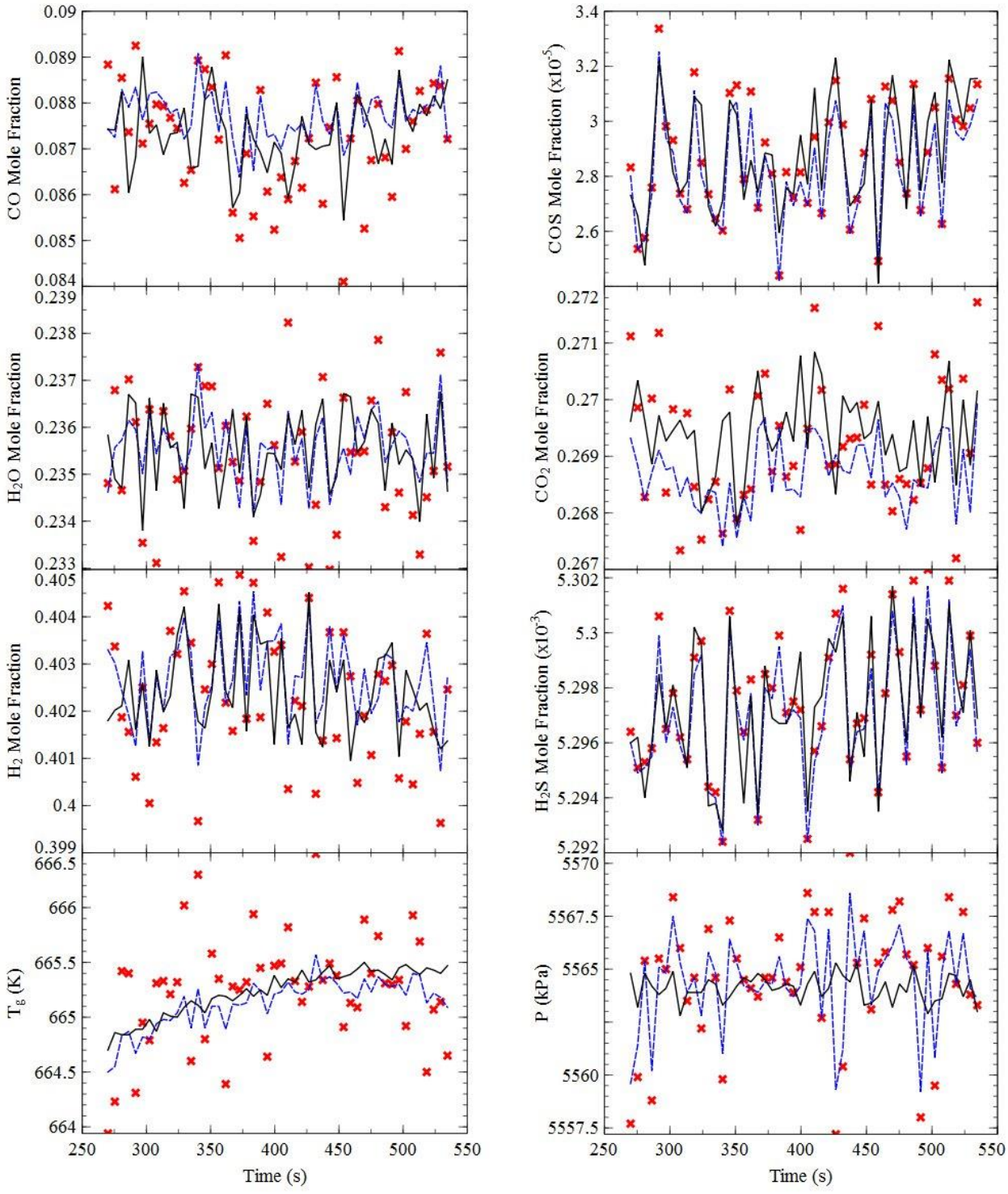

Figure 117. Actual (-), measured (*) and estimated (--) value of different states at the outlet of the reactor for fault F_{27}

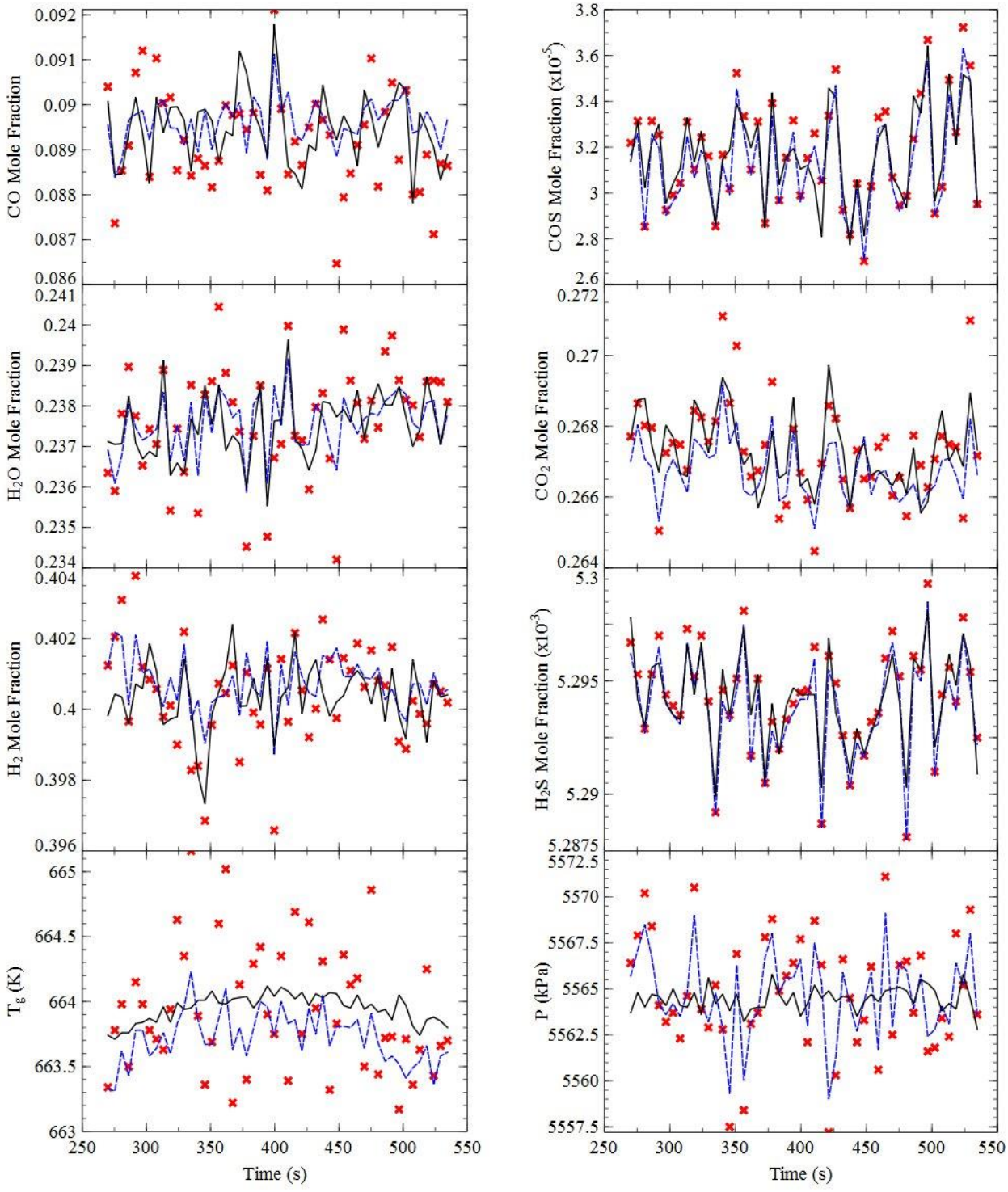

Figure 118. Actual (-), measured (*) and estimated (--) value of different states at the outlet of the reactor for fault F_{31}

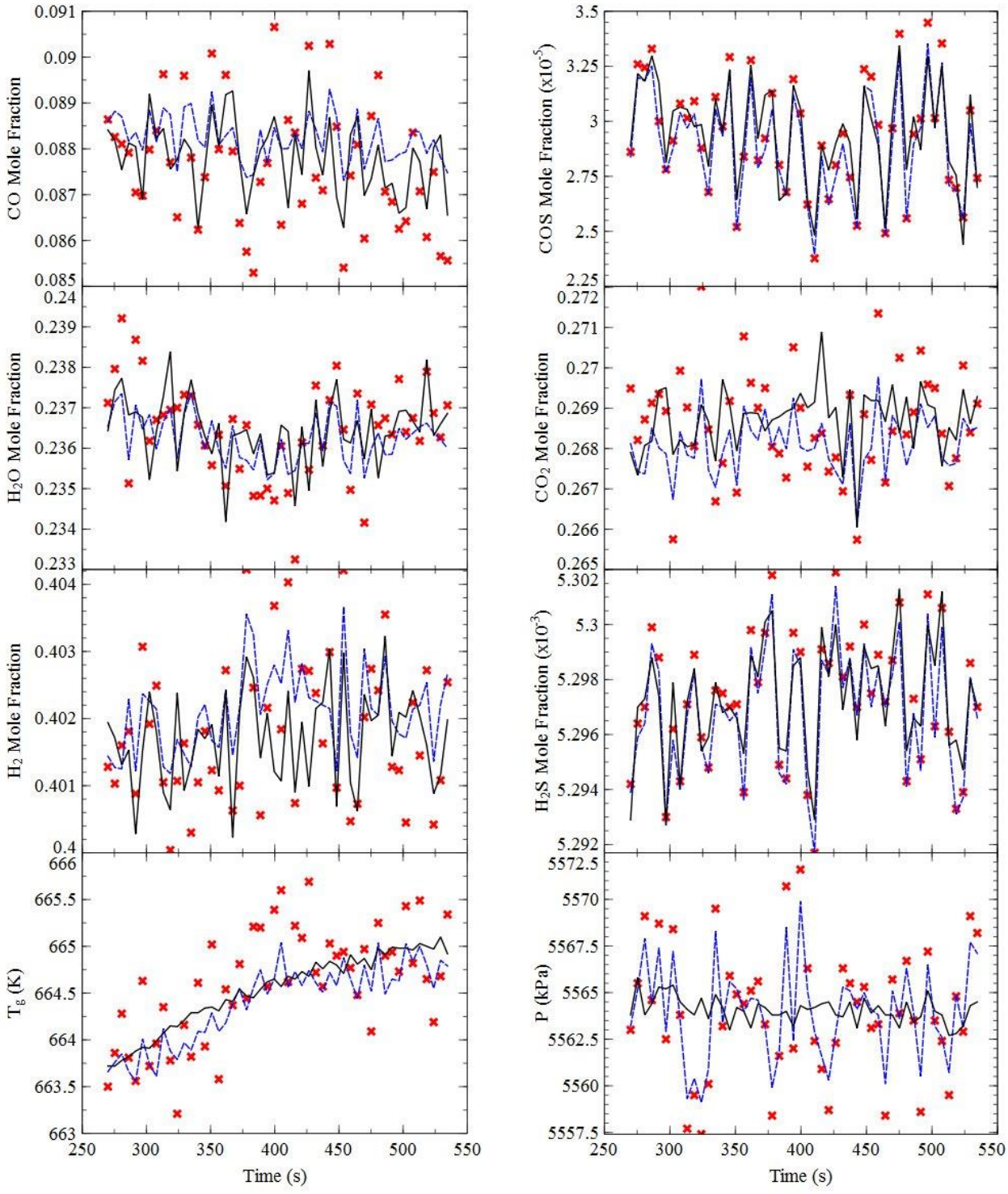

Figure 119. Actual (-), measured (*) and estimated (--) value of different states at the outlet of the reactor for fault F_{32}

7 Summary

A 2-tier sensor placement framework has been developed for condition monitoring and fault diagnosis in fossil energy systems. The framework consists of system- and component-level sensor placement approaches. The system-level sensor placement is based on a model-based qualitative analysis combined with the numerical solution. The system-level sensor placement is enhanced by introducing the magnitude ratio and fault evolution sequence algorithms. The network of the sensors obtained in the system-level help in observation and identification of the faults in the system with an optimum cost. The distributed sensor-placement is based on solving an optimization problem that minimizes the errors in estimated states of an extended Kalman filter and result in optimal location and type of the sensors. The optimization problem is solved using a genetic algorithm approach. The resulting sensors not only help in better estimation of the states, but the fault severities can also be estimated using the filter.

Each of the system- and component-level algorithms are mathematically derived and implemented on different case studies. The integrated algorithm is then implemented on the gasification island of the IGCC plant. The sensors required for fault detection and identification in gasification island are obtained by the system-level sensor placement; and the sensors required for monitoring and fault severity estimation of the gasification island are obtained by distributed sensor placement. The sensors obtained in system-level that are also present in the component level are then combined with sensors obtained in the component-level for monitoring and state estimation.

A novel dynamic model for a downward firing, slurry fed, oxygen blown, entrained flow, GEE-Texaco type gasifier has been developed in this report. Models for slag formation, detachment and deposition onto the walls of the gasifier have been developed and integrated into the gasifier model to provide a better estimate of the slag flow layer. A new hybrid shrinking core shrinking particle characterization is used, to represent the homogeneous reactions and slag detachment processes in a physically more accurate way. The dynamic simulation of the slagging gasifier model is able to capture the effect of the changing operation conditions on important variables in the gasifier including the slag layer thickness. The slag flow layer thickness is an important variable in the gasifier and a sudden increase in the layer could result in the choking of the gasifier. The slag layer is also known to interact with the refractory layer, resulting in accelerated degradation of the refractory wall. If the gasifier operating temperature is low, the slag layer could solidify and increase in thickness. Operating the gasifier at higher temperature on the other hand, could prevent slag solidification and increase the conversion of the coal, but would negatively affect the refractory by increasing the degradation rate. The current model is able to capture the effect of this trade-off quantitatively and provide a realistic picture of the gasifier operation.

Slag penetrates into the refractory and results in swelling of the refractory brick. If the slag is able to penetrate deep into the refractory brick, spalling can take place, which could accelerate the refractory degradation process and trigger a shutdown of the gasifier. A refractory model is also developed that captures the effect of refractory degradation due to compressive spalling as a result of slag penetration. The model is able to identify the location where the gasifier wall is most susceptible to slag penetration and predict the time for the first spall to take place at that location.

8 Recommendations and research output

The sensor placement developed in this report can easily be used for different processes. This requires availability of the mathematical model of the process and an appropriate state estimation algorithm. When the process model is available, fault simulations and system-level sensor placement can be performed. A major drawback would be the implementation of system-level sensor placement on very large processes. For large processes, future research on network decomposition can help in reducing the complexity of the problem and make the system-level sensor placement easier to be implemented. Through the use of process model and a state estimation technique, the component-level sensor placement

is performed. The main drawback of the component-level sensor placement is the complexity of detailed process models that increases the computations in state estimation and, thus, the optimization problem. In this work, we have shown that this issue can be tackled through the use of simplified models. Future research work in this area could be on the exploration of order reduction methods for process models. This has been initiated in this project through the method of characteristics and ISAT for implementation on the sour WGS reactor. One of the efficient uses of sensor placement framework is monitoring and fault detection of the gasification process. An important step in implementing the sensor placement algorithm on the gasification process and on the gasifier is the development of a valid mathematical model.

The slagging gasifier model and the refractory degradation model can be used to simulate changes in operating conditions of the gasifier and observe the effect of the fault severity and the condition of the refractory. The coupling between the models is one way, where certain variables of interest for a case scenario from the gasifier model are recorded and used in the refractory degradation model. The time constants in both the models are very different. While the dynamics of the gasifier manifests in seconds or minutes, the slag penetration and refractory degradation mechanisms take place over the period of months or years. Running both models together, for a simulation time of months, is impractical for the purposes of sensor placement using the approach similar to the sour water gas shift reactor. Therefore, in order to attempt sensor placement studies in the model, the gasifier model needs to be simplified and integrated with the refractory degradation model.

One method in order to reduce the simulation time for the gasifier model would be to consider a linearized model of the gasifier around the operating conditions of interest and integrate it with the refractory degradation model. The output variables in the linear model could be selected as the location at which sensors can be placed on the wall of the gasifier. Candidate locations for sensor placement will not only be limited to various locations in the axial direction, but should also include the depth into the refractory at which the sensor needs to be embedded to detect a fault. To consider the entire length of the gasifier as potential sensor location sites may result in a large number of outputs in the linear model. Therefore, it may be beneficial to identify, through other studies, locations that may respond well to change in operating conditions and narrow the range of output variables.

In the present report, the mechanism of compressive spalling due to slag penetration is selected as the only method for refractory degradation. Several other mechanisms are known to exist that may cause, or accelerate the process of degradation in the refractory. Tensile spalling is said to occur when chrome (Cr^{3+}) from the high chrome refractory migrates out of the refractory matrix. This leads to the formation of cracks in the refractory brick and a decrease in the strength of the refractory, eventually leading to spalling. Refractory degradation can take place in the absence of slag as well through mechanisms such as creep, thermal fatigue and thermal shock. These mechanisms are known to take place at high temperature and high stress conditions. Creep is the slow deformation of a material at elevated conditions which result in the loss of material strength, eventually weakening the material. Thermal fatigue is said to occur due to the cyclic variation in temperature. The properties of the material begin to deteriorate over the course of several cycles and this change is irreversible. The level of degradation due to thermal fatigue depends on the number of cycles, the temperature, its magnitude of the fluctuation of temperature and the frequency. When there is a rapid change in temperature, the sudden increase in the temperature gradient in the refractory brick could lead to a large build-up of stress. This could cause damage due to thermal shock. The formation of cracks, and in extreme cases, spalls are known to occur due to rapid changes in operational conditions. The presence of slag could accelerate these degradation mechanisms and result in faster refractory degradation.

The current refractory degradation model can be expanded to account for other degradation mechanisms. Another recommendation would be to consider the compound effect of these mechanisms so as to capture how the interdependency of these mechanisms could accelerate or control the total time to failure. This could be done, for example, by calculating effect of each of the mechanisms on the total stress, and keeping track of when the stress exceeds the maximum allowable stress. Such a model will be able to

better reflect the level of degradation in the refractory when two or more of the degradation processes occur simultaneously. Furthermore, it is likely that some degradation mechanisms may be dominant in certain sections of the gasifier, while others not. This framework for refractory degradation using stress modeling would be helpful to identify the key degradation mechanisms in various sections of the gasifier, and thus help in the selection of the appropriate type of sensors for fault detection.

Research Output

A. Conference Publications

1. Mobed, P., Maddala, J., Turton, R., Bhattacharyya, D., Rengaswamy, R. Steady-State Simulation of a Sour Water Gas Shift Reactor, *Int. Pittsburgh Coal Conf.*, Pittsburgh, PA, **2012**

B. Conference Presentations

2. Pednekar, P., Bhattacharyya, D., Turton, R., Rengaswamy, R. Condition monitoring of a gasifier in an integrated gasification combined cycle plant. *AIChE Conf.*, Atlanta, GA, **2014**.
3. Pednekar, P., Bhattacharyya, D., Turton, R., Rengaswamy, R. Modeling Slag Deposition and Refractory Degradation in an Entrained Flow Gasifier. *AIChE Conf.*, Atlanta, GA, **2014**.
4. Pednekar, P., Bhattacharyya, D., Turton, R., Rengaswamy, R. Modeling Refractory Degradation due to Slag Penetration in an Entrained-Flow Gasifier. *AIChE Conf.*, San-Francisco, CA, **2013**.
5. Pednekar, P., Bhattacharyya, D., Turton, R., Rengaswamy, R. Dynamic modeling of detachment, transport, and flow of slag in an entrained-flow gasifier. *AIChE Conf.*, Pittsburgh, **2012**.
6. Pednekar, P., Bhattacharyya, D., Turton, R., Rengaswamy, R. Development of slag sub-model for entrained flow gasifier. *Pittsburgh Coal Conference*, Pittsburgh, PA, **2012**.
7. Mobed, P., Maddala, J. Turton, R., Bhattacharyya, D., Rengaswamy, R. Dynamic modeling, data reconciliation and simulation of faults in a sour water gas shift reactor, *AIChE Conf.*, Pittsburgh, **2012**.
8. Mobed, P., Maddala, J., Turton, R., Bhattacharyya, D., Rengaswamy, R. Distributed Sensor Placement Algorithm for a Water Gas Shift Reactor in an IGCC Plant, *AIChE Conf.*, San-Francisco, CA, **2013**.
9. Mobed, P., Maddala, J., Bhattacharyya, D., Rengaswamy, R. On the Use of Magnitude Ratio in Sensor Placement Algorithms for Fault Detection and Diagnosis in Complex Energy Processes, *ISA POWID Symposium*, **2014**.
10. Mobed, P., Maddala, J., Bhattacharyya, D., Rengaswamy, R. Fault detection in an acid gas removal unit of IGCC plant using magnitude ratio algorithm, *AIChE Conf.*, Atlanta, GA, **2014**.
11. Mobed, P., Maddala, J., Bhattacharyya, D., Rengaswamy, R. A genetic algorithm-based distributed sensor placement for water gas shift reactor in IGCC plant using Kalman filter, *AIChE Conf.*, Atlanta, GA, **2014**.
12. Mobed, P., Munusamy, S., Bhattacharyya, D., Rengaswamy, R. Development of a Novel EKF-GA Approach for Distributed Sensor Placement – Application to WGSR in an IGCC plant, *AIChE Conf.*, Salt Lake City, UT, **2014**.
13. Mobed, P., Bhattacharyya, D., Rengaswamy, R. Sensor placement for fault diagnosis in large-scale networks, *AIChE Conf.*, Salt Lake City, UT, **2014**.

C. Journal Publications

1. Pednekar, P., Bhattacharyya, D., Turton, R., Rengaswamy, R. Development of a hybrid shrinking-core shrinking-particle model for entrained-flow gasifiers. *AIChE J.* **2015**, DOI: 10.1002/aic.15055.
2. Pednekar, P., Bhattacharyya, D., Turton, R., Rengaswamy, R. A dynamic model of a slagging entrained-flow gasifier including models for slag transport, deposition and slag layer. *Ind. Eng. Chem. Res.* **2015** 591(1), 279-292.
3. Mobed, P., Maddala, J., Rengaswamy, R., Bhattacharyya, D., Turton, R. Data reconciliation and Dynamic Modeling of a Sour Water Gas Shift Reactor, *Ind. Eng. Chem. Res.*, **2014**, 53(51), 19855-19869.

4. Mobed, P., Maddala, J., Pednekar, P., Bhattacharyya, D., Rengaswamy, R. Optimal Sensor Placement for Fault Diagnosis Using Magnitude Ratio, *Ind. Eng. Chem. Res.*, **2015**, 54(38), 9369-9381.
5. Pednekar, P., Bhattacharyya, D., Turton, R., Rengaswamy, R. Modeling of refractory degradation due to spalling and creep in entrained-flow gasifiers, (To be submitted).
6. Mobed, P., Munusamy, S., Bhattacharyya, D., Rengaswamy, R. Constrained Kalman Filtering of a Special Class of DAE Systems, (To be submitted)
7. Mobed, P., Munusamy, S., Bhattacharyya, D., Rengaswamy, R. Development of a Novel EKF-GA Approach for Distributed Sensor Placement of Water Gas Shift Reactor, (To be submitted)
8. Mobed, P., Bhattacharyya, D., Rengaswamy, R. Statistical Study of Sensor Placement for Fault Detection in Large-Scale Networks Using Graph Theory, (To be submitted)
9. Munusamy, Mobed, Bhattacharyya, Rengaswamy, Model Simplification Through Scaling Analysis and Method of Characteristic for Water Gas Shift Reactor, (To be submitted)
10. Munusamy, Mobed, Bhattacharyya, Rengaswamy, Efficient Sensor Network Design for Water Gas Shift Reactor Using In-Situ Adaptive Tabulation, (To be submitted)

9 References

1. Bhushan, M., Rengaswamy, R. Design of Sensor Network Based on the Signed Directed Graph of the Process for Efficient Fault Diagnosis. *Ind. Eng. Chem. Res.* **2000**, 39(4), 999-1019.
2. Bhushan, M., Rengaswamy. R. Comprehensive Design of a Sensor Network for Chemical Plants Based on Various Diagnosability and Reliability Criteria. 1. Framework. *Ind. Eng. Chem. Res.* **2002**, 41(7), 1826 – 1839.
3. Bhushan, M., Rengaswamy. R. Comprehensive Design of a Sensor Network for Chemical Plants Based on Various Diagnosability and Reliability Criteria. 1. Applications. *Ind. Eng. Chem. Res.* **2002**, 41(7) ,1840 – 1860.
4. Bhushan, M., Narasimhan, S., Rengaswamy, R. Robust Sensor Network Design for Fault Diagnosis, *Comput. Chem. Eng.* **2008**, 32, 1067-1084.
5. Han, X., Xie, K. Fault Diagnosis Based on Artificial Immune and Principal Component Analysis, *Lect. Notes ARTIF Int.* **2009**, 5589, 429.
6. Raghuraj R., M. Bhushan, R. Rengaswamy. Locating Sensors in Complex Chemical Plants based on Fault Diagnostic Observability Criteria. *AIChE J.* **1999**, 45(2), 310-322.
7. Thambirajah, J., Benabbas, L., Bauer, M., Thornhill N. Cause-and-effect analysis in chemical processes utilizing XML, plant connectivity and quantitative process history, *Comp. & Chem. Eng.* **2009**, 33, 503.
8. Allende, H., Bravo, D., Canessa, E. Robust design in multivariate systems using genetic algorithms, *Quality & Quantity* **2010**, 44, 315.
9. Duarte, E., Pozo, A., Nassu, B. Fault diagnosis of multiprocessor systems based on genetic and estimation of distribution algorithms: A performance evaluation, *Int. J. Art. Int. tools* **2010**, 19(1).
10. He, Z., Chiang, H., Li, C., Zeng, Q. Fault-Section Estimation in Power Systems Based on Improved Optimization Model and Binary Particle Swarm Optimization, *IEEE power & energy society general meeting* **2009**, 1-8, 3572.
11. Sumana, C., Venkateswarlu, C. Genetically Tuned Decentralized Proportional-Integral Controllers for Composition Control of Reactive Distillation, *Ind. Eng. Chem. Res.* **2010**, 49, 1297.
12. Upreti, S., A new robust technique for optimal control of chemical engineering processes, *Comp. & Chem. Eng.* **2004**, 28, 1325.
13. NETL_Report, Cost and Performance Baseline for Fossil Energy Plants, Volume 1:Bituminous Coal and Natural Gas to Electricity, www.netl.doe.gov, Aug, **2007**
14. McDaniel J. E., Hornick, M. POLK power station IGCC - 5th year of commercial operation, *Gasification Technologies Conference,* San Francisco, California, October 8-10, **2001**.
15. McDaniel J.E. The Tampa electric Integrated Gasification Combined Cycle Project: An update, DOE Topical Report No. 19, http://www.netl.doe.gov/technologies/coalpower/cctc/cctdp/bibliography, **2000**.
16. McDaniel J. E., Hornick, M. POLK power station IGCC - 6th year of commercial operation, Gasification Technologies Conference, San Francisco, California, October 27-30, 2002.
17. McDaniel J.E. Tampa Electric Polk Power station Integrated Gasification Combined Cycle Project, Final Technical report, http://www.netl.doe.gov/technologies/coalpower/cctc/cctdp/bibliography, **2002**.
18. Report_DOE_1996, 1996 DOE Annual Technical Report, DOE/MC/27363-29, www.netl.doe.gov, **1996**.
19. Report_DOE_2004, Tampa Electric Integrated Gasification Combined-Cycle Project, A DOE Assessment, DOE/NETL-2004/1207, **2004**.
20. Cornils B., Hibbel J. Langhoff J. and Ruprecht P. Stand der Texaco-Kohlevergasung in der Ruhrchemie/Ruhrkohle-Variante, *Chem. Ing. Tech.* **1980**, 52, 12-19.

21. Cornils B., Specks R. Experiences with the Texaco process of coal-dust Pressure Gasification using the Ruhrchemie/Ruhrkohle Technical Version, *EPRI Conference on Synthetic Fuels*, San Francisco, California, October **1980**.
22. Koog W. The Texaco Coal Gasification Process Status and Outlook, *8th Annual WATTec Energy Conference and Exhibition*, Knoxville, Tennessee, February **1981**.
23. Schlinger W. G. Coal Gasification Development and Commercialization of the Texaco Coal Gasification Process, *Energy Research* **1980**, 4, 127-136.
24. Walter F. B., Kaufman H. C., Reed T. L. The Cool Water Gasification Program – A Demonstration of Combined-Cycle Technology, EPRI Conference on Synthetic Fuels, San Francisco, California, October **1980**.
25. Cool_Water_EPRI, Cool Water Coal Gasification Program:Final Report, GS-6806, EPRI, **1990**.
26. Mills, S. J. Coal Gasification and IGCC in Europe, *IEA Clean Coal centre*, ISBN 92-9029-429-9, **2006**
27. Nagata K., Yamada T., Hiza T. Development of Load and Pressure Controller for the 200 tons per day Entrained Flow IGCC Pilot Plant in Japan, *Advances in Instrumentation and Control* **1996**, 1307-1319.
28. Notestein J. E., Commercial Gasifier for IGCC Application Study Report, DOE/METC-91/6118, www. netl.doe.gov, **1990**
29. Black, J. Cost and performance baseline for fossil energy plants Volume 1: Bituminous coal and natural gas to electricity. DOE/NETL-2010/1397: **2010**.
30. Gray, D., Plunkett, J., Salerno, S., White, C., Tomlinson, G. Current and Future IGCC Technologies—A Pathway Study Focused on Non-Carbon Capture Advanced Power Systems R&D Using Bituminous Coal, DOE/NETL-2008/1337, *National Energy Technology Laboratory (NETL)*, Pittsburgh: **2008**.
31. Bhattacharyya, D., Turton, R., Zitney, S. E. Steady-State Simulation and Optimization of an Integrated Gasification Combined Cycle Power Plant with CO2 Capture. *Ind. Eng. Chem. Res.* **2010**, 50 (3), 1674-1690.
32. Grol, E. *Assessment of Power Plants That Meet Proposed Greenhouse Gas Emission Performance Standards*. DOE/NETL-401/110509: **2009**.
33. Hou, P., Meeker, D., Wise, H. Kinetic studies with a sulfur-tolerant water gas shift catalyst. *J. Catal.* **1983**, 80 (2), 280-285.
34. Newsome, D. S. The Water-Gas Shift Reaction. *Catal. Rev.* **1980**, 21 (2), 275-318.
35. Beavis, R., Forsyth, J., Roberts, E., Song, B., Combes, G., Abbott, J., Macleod, N., Vass, E., Davies, M., Barton, P. I. A Step-Change Sour Shift Process for Improving the Efficiency of IGCC with CCS. *Energy Procedia*, **2013**, 37. 2256-2264.
36. Carbo, M. C., Jansen, D., Boon, J., Dijkstra, J. W., Van den Brink, R. W., Verkooijen, A. H. M. Staged water-gas shift configuration: Key to efficiency penalty reduction during precombustion decarbonisation in IGCC. *Energy Procedia*, **2009**, 1 (1).
37. Carbo, M. C., Boon, J., Jansen, D., Van Dijk, H. A. J., Dijkstra, J. W., Van den Brink, R.W., Verkooijen, A.H.M. Steam demand reduction of water–gas shift reaction in IGCC power plants with pre-combustion CO2 capture. *Int. J. Greenh. Gas Con.*, **2009**, 3 (6), 712-719.
38. Botha, F. J. *Simulation of a syngas from coal production plant coupled to a high temperature nuclear reactor*. Stellenbosch University, **2012**.
39. Park, J. N., Kim, J. H., Lee, H. I. A Study on the Sulfur-Resistant Catalysts for Water Gas Shift Reaction III. Modification of Mo/g-Al2O3 Catalyst with Iron Group Metals. *Bull. Korean Chem. Soc.* **2000**, 21, 1233-8.
40. Li, Y., Wang, R., Chang, L. Study of reactions over sulfide catalysts in CO–CO2–H2–H2O system. *Catal. Today* **1999**, 51 (1), 25-38.
41. Kim, J. H., Lee, H. I. A Study on the Sulfur-Resistant Catalysts for Water Gas Shift Reaction, II. Effect of Alkali Metal Salt on the Activity of CoMo Catalyst. *J. Korean Chem. Soc.* **1998**, 42, 696-702.

42. Maurstad, O. *An overview of coal based integrated gasification combined cycle (IGCC) technology*. MIT, **2005**.
43. Bell, N. H., Edgar, T. F. Modelling of a fixed-bed water-gas shift reactor: 1. Steady-state model verification. *J. Process Control* **1991**, 1 (1), 22-31.
44. Mondal, P., Dang, G. S., Garg, M. O. Syngas production through gasification and cleanup for downstream applications — Recent developments. *Fuel Process. Technol.* **2011**, 92 (8), 1395-1410.
45. Bell, N. H., Edgar, T. F. Modelling of a fixed-bed water-gas shift reactor: 2. Variable catalyst activity effects and dynamic testing. *J. Process Control* **1991**, 1 (2), 59-67.
46. Ding, O. L., Chan, S. H. Water–gas shift reaction – A 2-D modeling approach. *Int. J. Hydrogen Energy* **2008**, 33 (16), 4325-4336.
47. Adams II, T. A., Barton, P. I. A dynamic two-dimensional heterogeneous model for water gas shift reactors. *Int. J. Hydrogen Energy* **2009**, 34 (21), 8877-8891.
48. Francesconi, J. A., Mussati, M. C., Aguirre, P. A. Analysis of design variables for water-gas-shift reactors by model-based optimization. *J. Power Sources* **2007**, 173 (1), 467-477.
49. Giunta, P., Amadeo, N., Laborde, M. Simulation of a low temperature water gas shift reactor using the heterogeneous model/application to a pem fuel cell. *J. Power Sources* **2006**, 156 (2), 489-496.
50. Choi, Y., Stenger, H. G. Water gas shift reaction kinetics and reactor modeling for fuel cell grade hydrogen. *J. Power Sources* **2003**, 124 (2), 432-439.
51. Chen, W. H., Lin, M. R., Jiang, T. L., Chen, M.H. Modeling and simulation of hydrogen generation from high-temperature and low-temperature water gas shift reactions. *Int. J. Hydrogen Energy* **2008**, 33 (22), 6644-6656.
52. Gunawardana, P. V. D. S., Lee, H. C., Kim, D. H. Performance of copper–ceria catalysts for water gas shift reaction in medium temperature range. *Int. J. Hydrogen Energy* **2009**, 34 (3), 1336-1341.
53. Levent, M. Water–gas shift reaction over porous catalyst: temperature and reactant concentration distribution. *Int. J. Hydrogen Energy* **2001**, 26 (6), 551-558.
54. Lim, S., Bae, J., Kim, K. Study of activity and effectiveness factor of noble metal catalysts for water–gas shift reaction. *Int. J. Hydrogen Energy* **2009**, 34 (2), 870-876.
55. Sun, J., DesJardins, J., Buglass, J., Liu, K. Noble metal water gas shift catalysis: Kinetics study and reactor design. *Int. J. Hydrogen Energy* **2005**, 30 (11), 1259-1264.
56. Amadeo, N. E., Laborde, M. A. Hydrogen production from the low-temperature water-gas shift reaction: Kinetics and simulation of the industrial reactor. *Int. J. Hydrogen Energy* **1995**, 20 (12), 949-956.
57. Hla, S. S., Duffy, G. J., Morpeth, L. D., Cousins, A., Roberts, D. G., Edwards, J. H. Investigation into the performance of a Co–Mo based sour shift catalyst using simulated coal-derived syngases. *Int. J. Hydrogen Energy* **2011**, 36 (11), 6638-6645.
58. de la Osa, A. R., De Lucas, A., Valverde, J. L., Romero, A., Monteagudo, I., Sánchez, P. Performance of a sulfur-resistant commercial WGS catalyst employing industrial coal-derived syngas feed. *Int. J. Hydrogen Energy* **2011**, 36 (1), 44-51.
59. Andreev, A. A., Kafedjiysky, V. J., Edreva-Kardjieva, R. M. Active forms for water-gas shift reaction on NiMo-sulfide catalysts. *Appl. Catal. A Gen.* **1999**, 179 (1–2), 223-228.
60. Hakkarainen, R., Salmi, T., Keiski, R. L. Water-gas shift reaction on a cobalt-molybdenum oxide catalyst. *Appl. Catal. A Gen.* **1993**, 99 (2), 195-215.
61. Berispek, V. *Studies of an alkali impregnated cobalt-molybdate catalyst for the water-gas shift and the methanation reactions.* Virginia Polytechnic Institute and State University, **1975**.
62. Jakobsen, H. A. *Chemical reactor modeling: multiphase reactive flows*. Springer, **2008**.
63. Fiedorow, R., Léauté, R., Lana, I. G. D. A study of the kinetics and mechanism of COS hydrolysis over alumina. *J. Catal.* **1984**, 85 (2), 339-348.
64. George, Z. M. Kinetics of cobalt-molybdate-catalyzed reactions of SO2 with H2S and COS and the hydrolysis of COS. *J. Catal.* **1974**, 32 (2), 261-271.
65. Hoggan, P. E., Aboulayt, A., Pieplu, A., Nortier, P., Lavalley, J. C. Mechanism of COS Hydrolysis on Alumina. *J. Catal.* **1994**, 149 (2), 300-306.

66. Overstreet, A. D. *A screening study of a new water gas shift catalyst.* Virginia Polytechnic Institute and State University, **1974**.
67. Aspen Technology *Aspen Physical Property System*, v7.1, **2009**.
68. Aldridge, C. L. *Shift process for new catalyst.* Google Patents: **1974**.
69. Svoronos, P. D. N., Bruno, T. J. Carbonyl Sulfide: A Review of Its Chemistry and Properties. *Ind. Eng. Chem. Res.* **2002**, 41 (22), 5321-5336.
70. Fogler, H. S. *Elements of chemical reaction engineering*. Prentice-Hall, **1999**.
71. Thoenes Jr, D., Kramers, H. Mass transfer from spheres in various regular packings to a flowing fluid. *Chem. Eng. Sci.* **1958**, 8 (3–4), 271-283.
72. Ergun, S. Fluid flow through packed columns. *Chem. Eng. Prog.* **1952**, 48.
73. Satterfield, C. N. *Mass transfer in heterogeneous catalysis.* RE Krieger Publishing Company: **1981**.
74. Moe, J. Design of water-gas shift reactors. *Chem. Eng. Prog.* **1962**, 58 (3).
75. Singh, C. P. P., Saraf, D. N. Simulation of High-Temperature Water-Gas Shift Reactors. *Ind. Eng. Chem. Proc. Des. Dev.* **1977**, 16 (3), 313-319.
76. Bartholomew, C. H. Mechanisms of catalyst deactivation. *Appl. Catal. A Gen.* **2001**, 212 (1–2), 17-60.
77. Rase, H. F., Holmes, J. R. *Chemical reactor design for process plants.* Wiley New York: **1977**, Vol. 2.
78. Romagnoli, J., Sanchez, M. C. *Data Processing and Reconciliation for Chemical Process Operations.* Academic Press, **1999**.
79. Renganathan, T., Narasimhan, S. A Strategy for Detection of Gross Errors in Nonlinear Processes. *Ind. Eng. Chem. Res.* **1999**, 38 (6), 2391-2399.
80. Narasimhan, S., Jordache, C. *Data reconciliation and gross error detection: An intelligent use of process data.* Gulf Professional Publishing, **1999**.
81. Levy, A. The accuracy of the bubble meter method for gas flow measurements. *J. Sci. Instrum.* **1964**, 41 (7) 449.
82. Haggstrom, C. *Synthesis gas from black liquor - trace components and methanol synthesis.* Lulea University of Technology, Lulea, Sweden, **2011**.
83. Woods, M. C., Capicotto, P., Haslbeck, J. L., Kuehn, N. J., Matuszewski, M., Pinkerton, L. L., Rutkowski, M. D., Schoff, R. L., Vaysman, V. *Cost and performance baseline for fossil energy plants. Volume 1: Bituminous coal and natural gas to electricity final report.*NETL/DOE, **2007**.
84. Maustad O. An overview of coal based integrated gasification combined cycle (IGCC) Technology. Publication No. LFEE 2005-002 W, **2005**, *http://lfee.mit.edu/publications*
85. Bennett JP, Kwong K. Failure mechanisms in high chrome oxide gasifier refractories. *Metallurgical and Materials Transactions*. **2011**, 42A, 888-904.
86. Williford RE, Johnson KI, Sundaram SK, Pilli S. Effective diffusivity and spalling models for slagging coal gasifiers. *J Am Ceram Soc*. **2008**, 91(12), 4016-4022.
87. Clayton SJ, Siegel GJ, Wimer JG. Gasification technologies, gasification markets and technologies - present and future, an industry perspective. US Department of Energy. **2002**, DOE/FE-0447.
88. Seggiani M. Modelling and simulation of time varying slag flow in a Prenflo entrained-flow gasifier. *Fuel*. **1998**, 77(14), 1611-1621.
89. Lee HH, Lee JC, Joo YJ, Lee CH. Dynamic modeling of Shell entrained flow gasifier in an integrated gasification combined cycle process. *Applied Energy*. **2014**, 131, 421-440.
90. Pilli SP, Johnson KI, Williford RE, Sundaram SK, Korolev VN, Crum JV. Modeling slag penetration and refractory degradation using the finite element method. The Twenty-Fifth Annual International Pittsburgh Coal Conference, September 29 - October 2, Pittsburgh, PA, **2008**.
91. Bockelie MJ, Denison MK, Chen Z, Linjewile T, Senior CL, Sarofim AF. CFD modeling for entrained flow gasifiers in Vision 21 systems. Proceedings of the 19th Annual International Pittsburgh Coal Conference. September 24–26, Pittsburgh, PA, **2002**.
92. Benyon PJ. Computational modeling of entrained flow slagging gasifiers. PhD thesis, University of Sydney. **2002**. Australia.

93. Kasule JS, Turton R, Bhattacharyya D, Zitney SE. Mathematical modeling of a single-stage, downward-firing, entrained-flow gasifier. *Ind. and Eng. Chem. Research*. **2012**, 51(18), 6429-6440.
94. Shah J, Govind R. Modeling and simulation of an entrained flow coal gasifier. *AIChE J*. **1984**, 30(1), 79-92.
95. Srinivasachar S, Senior CL, Helble JJ, Moore JW. A fundamental approach to the prediction of coal ash deposit formation in combustion systems. *Symposium (International) on Combustion*. **1992**, 24(1), 1179-1187.
96. Quann RJ, Sarofim AF. A scanning electron microscopy study of the transformations of organically bound metals during lignite combustion. *Fuel*. **1986**, 65, 40-46.
97. Liang Q, Guo X, Dai Z, Liu H, Gong X. An investigation on the heat transfer behavior and slag deposition of membrane wall in pilot scale entrained flow gasifier. *Fuel*. **2012**, 102, 491-498.
98. Seames WS. An initial study of the fine fragmentation fly ash mode generated during pulverized coal combustion. *Fuel Processing Tech*. **2003**, 81, 109-125.
99. Loehden D, Walsh PM, Sayre AN, Beer JM, Sarofim AF. Generation and deposition of fly ash in the combustion of pulverized coal. *J Institute of Energy*. **1989**, 451, 119-127.
100. Yan L, Gupta RP, Wall TF. A mathematical model of ash formation during pulverized coal combustion. *Fuel*. **2002**, 81, 337-344.
101. Wang P, Massoudi M. Slag behavior in Gasifiers. Part I: Influence of coal properties and gasification conditions. *Energies*. **2013**, 6, 784-806.
102. Vaysman V, Lu Y. Quality guidelines for energy system studies. Detailed coal specifications. DOE/NETL-401/012111, **2012**.
103. Stalder AF, Melchior T, Muller M, Sage D, Blu T, Unser M. Low-Bond Axisymmetric drop shape analysis for surface tension and contact angle measurements of sessile drops. *Colloids and surfaces A: Physicochemical and Engineering Aspects*. **2010**, 364, 72-81.
104. Mehta AS, Sahajwalla, V. Influence of temperature on the wettability at the slag/carbon interface during pulverised coal injection in a blast furnace. *Scandinavian Journal of Metallurgy*. **2001**, 30, 370-378.
105. Li S, Whitty KJ. Physical phenomena of char–slag transition in pulverized coal gasification. *Fuel Processing Technology*. **2012**, 95, 127-136.
106. Li S, Wu Y, Kevil W. Ash deposition behavior during char-slag transition under simulated gasification conditions. *Energy & Fuels*. **2010**, 24(3), 1868-1876.
107. Buhre BJP, Hinkley JT, Gupta RP, Nelson PF, Wall TF. Fine ash formation during combustion of pulverised coal-coal property impacts. *Fuel*. **2006**, 18(2), 185-193.
108. Maloney D, Monazam K, Casleton KH, Shaddix CR. Evaluation of char combustion models: measurement and analysis of variability in char particle size and density. *Proceedings of the Combustion Institute*. **2005**, 30, 2197-2204.
109. Yan, L., Gupta, R., Wall, T. The implication of mineral coalescence behaviour on ash formation and ash deposition during pulverised coal combustion. *Fuel*. **2001**, 80, 1333-1340.
110. Wood, N.B. A simple method for the calculation of turbulent deposition to smooth and rough surfaces. *J. Aerosol Sci.* **1981**, 12, 275-290.
111. Ahmadi, G. Ash & pulverized coal deposition in combustors & gasifiers. Quarterly Technical Progress Report, *Pittsburgh Energy Technology Center*, USA, **1996**.
112. Guha, A. Transport and Deposition of Particles in turbulent and laminar Flow. *Annu. Rev. Fluid Mech*. **2008**, 40, 311-41.
113. Yu, D., Xu, M.H., Liu, X., Huang, J., Li, G. Mechanism of submicron and residual ash particle formation during pulverised coal combustion: a comprehensive review. *Dev. Chem. Eng. Mineral Process.* **2005**, 13(3/4), 467-482.
114. Zhang, L. Characterization of Combustion-Derived individual Fine particulates by computer controlled scanning electron microscopy. *AIChE J.* **2009**, 55(11), 3005-3016.

115. Kang, S.G. Fundamental studies of mineral matter transformation during pulverized coal combustion: residual ash formation. PhD Thesis, Department of Chemical Engineering, MIT, USA, **1991**.
116. Wang, X.H., Zhao, D.Q., He, L.B., Jiang, L.Q., He, Q., Chen, Y. Modeling of a coal-fired slagging combustor: development of a slag submodel. *Combust. Flame.* **2007**, 149, 249–60.
117. Ni, J., Zhou, Z., Yu, G., Liang, Q., Wang, F. Molten slag flow and phase transformation behaviors in a slagging entrained flow coal gasifier. *Ind. Eng. Chem. Res*. **2010**, 49, 12302-12310.
118. Yong, S.Z., Gazzino, M., Ghoniem, A. Modeling the slag layer in solid fuel gasification and combustion – formulation and sensitivity analysis. *Fuel.* **2012**, 92, 162-70.
119. Lei, C., Yong, S.Z., Ghoniem, A.F. Modeling the slag behavior in three dimensional CFD simulation of a vertically-oriented oxy-coal combustor. *Fuel Process. Technol.* **2013**, 112, 106-117.
120. Monaghan, R.F.D., Ghoniem, A.F. A dynamic reduced order model for simulating entrained flow gasifiers. Part II: Model validation and sensitivity analysis. *Fuel.* **2012**, 94, 280-297.
121. Wang, X., Zhao, D., Jiang, L., Yang, W. The deposition and burning characteristics during slagging co-firing coal and wood: modeling and numerical simulation. *Combust. Sci. Technol.* **2009**, 181, 710-728.
122. Wang, X.H., Zhao, D.Q., He, L.B., Jiang, L.Q., He, Q., Chen, Y. Modeling of coal-fired slagging combustor: Development of a slag submodel. *Combust. Flame*. **2007**, 149, 249-260.
123. Yang, Z., Wang, Z., Wu, Y., Wang, J., Lu, J., Li, Z., Ni, W. Dynamic model for an oxygen-staged slagging entrained flow gasifier. *Energy & Fuels*, **2011**, 25, 3646-3656.
124. Bo, S., Liu, Y., Chen, X., Zhou, Q., Su, M. Dynamic modeling and simulation of shell gasifier in IGCC. *Fuel Process. Technol.* **2011**, 92, 1418-1425.
125. Ye, I., Ryu, C. Numerical modeling of slag flow and heat transfer on the wall of an entrained flow gasifier. *Fuel*. **2015**, 150, 64-74.
126. Kasule JS, Turton R, Bhattacharyya D, Zitney, SE. One-dimensional dynamic modeling of a single-stage downward-firing entrained-flow coal gasifier. *Energy & Fuels*. **2014**, 28(8), 4949-4957.
127. Kumar M, Ghoniem AF. Multiphysics simulations of entrained flow gasification. Part 1: Validating nonreacting flow solver and particle turbulent dispersion model. *Energy and Fuels.* **2002b**, 46, 451-463.
128. Arastoopour H, Gidaspow D. Vertical pneumatic conveying using four hydrodynamic models. *Ind. Eng. Chem. Fund.* **1979**, 18(2), 123-130.
129. Rowe PN, Henwood GA. Drag forces in hydraulic model of fluidized bed. *Trans. Chem. Eng.* **1961**, 39, 43-54.
130. Niessen WR. Combustion and incineration processes, 3rd ed. Basel, NY: CRC Press, **2010**.
131. Fulton CH. Principles of Metallurgy. Norwood, MA: Plimption Press, **1910**.
132. Rao RM, Bhattacharyya D, Rengaswamy R. Choudhury, R. S. A two-dimensional steady state model including the effect of liquid water for a PEM fuel cell cathode. *J. Power Sources*. **2007**, 173, 375-393.
133. Syamlal M, Bissett LA. METC Gasifier Advanced Simulation (MGAS) Model, Technical Note. **1992**, NITS report No: DOE/METC-92/ 4108 (DE92001111)
134. Wen CY, Chaung TZ. Entrainment coal gasification modeling. *Ind. Eng. Chem. Process Des. Dev.* **1979**, 18(4), 684-695.
135. Haaland, S.E. Simple and Explicit Formulas for the Friction Factor in Turbulent Flow. *J. Fluids Eng. ASME*. **1983**, 105(1), 89-90.
136. Bird, R.B., Stewart, E.S., Lightfoot, E.N., Transport Phenomenon. 2nd ed., WSE Wiley, **2002**.
137. Streeter, R.C., Diehl, E.K., Schobert, H.H. Flow properties of low rank coal-ash slags Implications for slagging flow gasification. *Fuel.* **1985**, 64, 1611-1617.
138. Siegel, R., Howell, R.J. Thermal Radiation Heat Transfer, *McGraw-Hill Book Company*, New York, **1981**.
139. Aspen Custom Modeler, AspenTech, http://www.aspentech.com/.

140. McDaniel, J. Tampa Electric POLK Power Station Integrated Gasification Combined Cycle Project. Final Technical report, Tampa Electric Company, USA, **2002**.
141. Slezak, A, Kuhlman MJ, Shadle JL, Shi S. CFD simulation of entrained-flow gasification: Coal particle density/size fraction effects. *Powder Technology*. **2010**, 203, 98−108.
142. Monaghan, R.F.D., Ghoniem, A.F. Simulation of a commercial-scale Entrained flow gasifier using reduced order model. *Energy & Fuels.* **2011**, 26, 1089-1106.
143. Kazanc, F., Levendis, Y.A. Physical properties of particulate matter emitted from Combustion of Coals of various rank in O_2/N_2 and O_2/CO_2 environments. *Energy & Fuels.* **2012**, 26, 7127-7139.
144. Wu, H., Wall, T. The effect of Pressure on Ash formation during Pulverized Coal Combustion. *Energy & Fuels*. **2000**, 14, 745-750.
145. Guo, Q., Yu, G., Wang, F., Dai, Z. Influence of gasification conditions on the properties of fly ash in a bench-scale opposed multi-burner gasifier. 27th Annual International Pittsburgh Coal Conference, Pittsburgh, US, **2010**.
146. Linak, W.P., Miller, C.A. Comparison of particle size distributions and elemental partitioning from combustion of pulverized coal and residual fuel oil. *J. Air & Waste Manage. Assoc.* **2000**, 50, 1532-1544.
147. Kang, S.G., Sarofim, A.F., Beer, J.M. Effect of char structure on residual ash formation during pulverized coal combustion. *Sym. (Int.) Combust.* **1992**, 42, 1153-1159.
148. Fix, G., Seames, W., Mann, M., Benson, S., Miller, D. The effect of combustion temperature on coal ash fine fragmentation mode formation mechanism. *Fuel.* **2013**, 113, 140-147.
149. Sheng, C., Li, Y., Liu, X., Yao, H., Xu, M. Ash particle formation during O2/CO2 combustion of pulverized coals. *Fuel Process. Technol.* **2007**, 88, 1021-1028.
150. Rees, O.W. Composition of the ash of Illinois coals, Circular 365, Illinois State Geological Survey, **1964**.
151. McCollor, D.P., Zygarlicke, C.J., Allan, S.E., Benson, SA. Ash Deposit Initiation in a Simulated Fouling Regime. *Energy & Fuels*. **1993**, 7(6), 761−767.
152. Nowok, J.W. Viscosity and phase-transformation in coal ash slags near and below the temperature of critical viscosity. *Energy & Fuels.* **1994**, 8(6), 1324−1336.
153. Cho, S.H., Yoo, J.I., Turley, A.T., Miller, C.A., Linak, W.P., Wendt, J.O.L., Huggins, F.E., Gilmour, M.I. Relationships between composition and pulmonary toxicity of prototype particles from coal combustion and pyrolysis. *Proc. Combust. Inst.* **2009**, 32, 2717−2725.
154. Dahla, J.K., Weimera, A.W. and Krantz, B.W.. Sensitivity analysis of the rapid decomposition of methane in an aerosol flow reactor. *Int. J. Hydrogen Energy* **2004**, 29, 57-65.
155. Kopaygorodsky, E.M., Guliants, V.V. and Krantz, B.W. Predictive Dynamic Model of Single-Stage Ultra-Rapid Pressure Swing Adsorption. *AIChE J.* **2004**, 50, 953-962.
156. Kaisare, N.S., Lee, J.H. and Fedorov, A.G. Hydrogen Generation in a Reverse-Flow Microreactor: 1. Model Formulation and Scaling. *AIChE J.* **2005**, 51, 2254-2264.
157. Balaji, S., Lakshminarayanan, S. and Krantz, B.W. Scaling and sensitivity analysis of a reverse flow reactor. *Chem Eng. Sci.* **2008**, 63, 342-355.
158. Rao, V.R., Farooq, S. and Krantz, W. B. Design of a Two-Step Pulsed Pressure-Swing Adsorption-Based Oxygen Concentrator. *AIChE J.* **2009**, 56, 354-370.
159. Rezvanpour, A., Krantz, B.W. and Wang, C.H. Scaling analysis of the electrohydrodynamic atomization (EHDA) process or pharmaceutical particle fabrication. *Chem Eng. Sci.* **2012**, 80, 81-90.
160. Baldea, M., Daoutidis, P. Dynamics and control of autothermal reactors for the production of hydrogen. *Chem Eng. Sci.* **2007**, 62, 3218-3230.
161. Krantz, W.B. Scaling analysis in modeling transport and reaction processes.. Willey, New York, **2007**.
162. Krantz, B.W., Lee, H., Chaudhuri, R.S. and Hwang, S. Nonbuoyancy Density-Driven Convective Mass and Heat Transfer: Scaling Analysis and Solution Methodology. *AIChE J.* **2011**, 58, 678-689.
163. Munusamy, S., Narasimhan, S. and Kaisare, N.S. Approximate dynamic programming based control of hyperbolic PDE systems using reduced-order models from method of characteristics. *Comput.*

Chem. Eng. **2013**, 57, 122-132.
164. Munusamy, S., Narasimhan, S. and Kaisare, N.S. Order reduction and control of hyperbolic, countercurrent distributed parameter systems using method of characteristics. *Chem. Eng. Sci.* **2014**, 110, 153-163.
165. Pope, S.B. Computationally efficient implementation of combustion chemistry using *in situ* adaptive tabulation. *Combustion Theory Modeling* **1997**, 1, 41-63.
166. Mazumder, S. Adaptation of the in situ adaptive tabulation (ISAT) procedure for efficient computation of surface reactions. *Comput. Chem. Eng.* **2005**, 30, 115-124.
167. Kumar, A and Mazumder, S. Adaptation and application of the *in situ* Adaptive Tabulation (ISAT) procedure to reacting flow calculations with complex surface chemistry. *Comput. Chem. Eng.* **2011**, 35, 1317-1327.
168. Hedengren, J.D. and Edgar, T.F. Approximate nonlinear model predictive control with in situ adaptive tabulation. *Comput. Chem. Eng* **2008**, 32, 706-714.
169. Abrol, S., Lu., M., Hill, D., Herrick, A., and Edgar and T.F. Faster Dynamic Simulation using In Situ Adaptive Tabulation. *Ind. Eng. Chem.* **2010**, 49, 7814-7823.
170. Kramer, M., Mah, R. Model-based monitoring, *Proc. Int. Conf. On Foundations of Computer Aided Process Operations* (FOCAPO) **1993,** 45-68.
171. Bagajewicz, M. A review of techniques for instrumentation design and upgrade in process plants. *Can. J. Chem. Eng.* **2002**, 80 (1), 3-16.
172. Frank, P., Ding, S., Marcu, T. Model-based fault diagnosis in technical processes. T. I. Meas. *Control* **2000**, 22 (1), 57-101.
173. Venkatasubramanian, V., Rengaswamy, R., Yin, K., Kavuri, S. A review of process fault detection and diagnosis: Part I: Quantitative model-based methods. *Comput. Chem. Eng.* **2003**, 27 (3), 293-311.
174. Iri, M., Aoki, K., O'Shima, E., Matsuyama, H. An algorithm for diagnosis of system failures in the chemical process. *Comp. Chem. Eng.* **1979**, 3 (1–4), 489-493.
175. Tsuge, Y., Shiozaki, J., Matsuyama, H., O'Shima, E. Fault diagnosis algorithms based on signed directed graph and its modifications. *Ind. Chem. Eng. Symp. Ser.* **1985,** 92 133-144.
176. Kramer, M., Palowitch, B. A rule-based approach to fault diagnosis using the signed directed graph. *AIChE J.* **1987**, 33 (7), 1067-1078.
177. Raghuraj, R., Bhushan, M., Rengaswamy, R. Locating sensors in complex chemical plants based on fault diagnostic observability criteria. *AIChE J.* **1999**, 45 (2), 310-322.
178. Lambert, H. Fault trees for locating sensors in process systems. *Chem. Eng. Prog*. **1977**, 81.
179. Madron, F., Veverka, V. Optimal selection of measuring points in complex plants by linear models. *AIChE J*. **1992**, 38 (2), 227-236.
180. Chang, C., Mah, K., Tsai, C. A simple design strategy for fault monitoring systems. *AIChE J*. **1993**, 39 (7), 1146-1163.
181. Bhushan, M., Rengaswamy, R. Design of Sensor Network Based on the Signed Directed Graph of the Process for Efficient Fault Diagnosis. *Ind. Eng. Chem. Res*. **2000**, 39 (4), 999-1019.
182. Bhushan, M., Rengaswamy, R. Design of sensor location based on various fault diagnostic observability and reliability criteria. *Comput. Chem. Eng*. **2000**, 24 (2–7), 735-741.
183. Bhushan, M., Rengaswamy, R. Comprehensive Design of a Sensor Network for Chemical Plants Based on Various Diagnosability and Reliability Criteria. 1. Framework. *Ind. Eng. Chem. Res*. **2002**, 41 (7), 1826-1839.
184. Bagajewicz, M. Design and retrofit of sensor networks in process plants. *AIChE J*. **1997**, 43 (9), 2300-2306.
185. Bhushan, M., Narasimhan, S., Rengaswamy, R. Robust sensor network design for fault diagnosis. *Comput. Chem. Eng*. **2008**, 32 (4–5), 1067-1084.

186. Yang, F., Xiao, D., Shah, S. optimal sensor location design for reliable fault detection in presence of false alarms. *Sensors* **2009**, 9 (11), 8579-8592.
187. Chen, J., Chang, C. Development of an Optimal Sensor Placement Procedure Based on Fault Evolution Sequences. *Ind. Eng. Chem. Res*. **2008**, 47 (19), 7335-7346.
188. Liptak, B. Process measurement and analysis. CRC Press: **1995**, Vol. I.
189. Maurya, M. R., Rengaswamy, R., Venkatasubramanian, V. A Systematic Framework for the Development and Analysis of Signed Digraphs for Chemical Processes. 1. Algorithms and Analysis. *Ind. Eng. Chem. Res*. **2003**, 42 (20), 4789-4810.
190. Mavrovouniotis, M., Stephanopoulos, G. Formal order-of-magnitude reasoning in process engineering. *Comput. Chem. Eng*. **1988**, 12 (9–10), 867-880.
191. Raiman, O. Order of magnitude reasoning. Artif. Intell. **1991**, 51 (1–3), 11-38.
192. Downs, J., Vogel, E. A plant-wide industrial process control problem. *Comput. Chem. Eng.* **1993**, 17 (3), 245-255.
193. Ricker, N., Lee, J. Nonlinear model predictive control of the Tennessee Eastman challenge process. *Comput. Chem. Eng.* **1995**, 19 (9), 961-981.
194. Bhushan, M., Rengaswamy, R. Comprehensive Design of a Sensor Network for Chemical Plants Based on Various Diagnosability and Reliability Criteria. 2. Applications. *Ind. Eng. Chem. Res*. **2002**, 41 (7), 1840-1860.
195. Maurya, M., Rengaswamy, R., Venkatasubramanian, V. Application of signed digraphs-based analysis for fault diagnosis of chemical process flowsheets. *Eng. Appl. Artif. Intell.* **2004**, 17 (5), 501-518.
196. Bhattacharyya, D., Turton, R., Zitney, S. Steady-state simulation and optimization of an integrated gasification combined cycle power plant with CO_2 capture. *Ind. Eng. Chem. Res.* **2011**, 50 (3), 1674-1690.
197. Kumar Mandela, R., Rengaswamy, R., Narasimhan, S., Sridhar, L. N. Recursive state estimation techniques for nonlinear differential algebraic systems, *Chem. Eng. Sci.* **2010**, 65(16), 4548–4556.
198. Simon D. Kalman Filtering With State Constraints a Survey of Linear and Nonlinear Algorithms, *IET Control Theory Appl.* **2010**, 4(8), 1303–1318.
199. Petzold', L. Differential/Algebraic Equations Are Not ODE's, *SIAM J. ScI. STAT. Comput.* **1982**, 3(3), 367–384.
200. Takamatsu, M., Iwata, S. Index reduction for differential-algebraic equations by substitution method, *Linear Algebra Appl.* **2008**, 429, 2268–2277,.
201. Chisci, L., Zappa, G. Square-root Kalman filtering of descriptor systems, *Syst. Control Lett.* **1992**, 19, 325–334,.
202. Darouach, M., Boutayeb, M., Zasadzinski, M. Kalman filtering for continuous descriptor systems, *Proc. 1997 Am. Control Conf. (Cat. No.97CH36041)* **1997**, 3, 0–4.
203. Darouach, M., Bassong Onana, A., Zasadzinski, M. State estimation of stochastic singular linear systems: convergence and stability, *Int. J. Syst. Sci.* **1993**, 24, 1001–1008.
204. Dai, L. State estimation schemes for singular systems, *Preprints of the 10th IFAC World Congress*, **1987**.
205. Deng Z. L., Liu, Y. M. Descriptor Kalman estimators, *Int. J. Syst. Sci.* **1999**,30, 1205–1212.
206. Nikoukhah, R. Willsky, A. S., Levy, B. C., Member, S. Kalman Filtering and Riccati Equations for Descriptor Systems, *IEEE Trans. Automat. Contr*. **1992**, 37(9), 1325–1342.
207. Becerra, V. M., Roberts, P. D., Gri, G. W., Park, C., Oax, C. C. B. Applying the extended Kalman filter to systems described by nonlinear differential-algebraic equations, *Control Eng. Pract.* **2001**, 9, 267–281.
208. Åström, K. J. *Introduction to stochastic control theory*. Courier Corporation, **2012**.
209. Campbell, S. L. WP-3-1 2 : OO DESCRIPTOR SYSTEMS I N THE 90's, **1990**.

210. Schon, T., Gerdin, M., Glad, T., Gustafsson, F. A modeling and filtering framework for linear differential-algebraic equations, *42nd IEEE Int. Conf. Decis. Control (IEEE Cat. No.03CH37475)* **2003**, vol. 1, 3.
211. Vachhani, P., Rengaswamy, R., Gangwal, V., Narasimhan, S. Recursive estimation in constrained nonlinear dynamical systems, *AIChE J.* **2005**, 51(3), 946–959.
212. Bernstein, D. S. *Matrix mathematics: theory, facts, and formulas*. Princeton University Press, **2009**.
213. Teixeira, B. O. S., Chandrasekar, J., Tôrres, L. A. B., Aguirre, L. A., Bernstein, D. S. State estimation for linear and non-linear equality-constrained systems, *Int. J. Control* **2009**, 82, 918–936.
214. Korbicz, J. Discrete-scanning observation problem for stochastic non-linear discrete-time distributed parameter systems, *Int. J. Syst. Sci.* **1991**, 22, 9, 1647–1662.
215. Alaña, J. E., Theodoropoulos, C. Optimal location of measurements for parameter estimation of distributed parameter systems, *Comput. Chem. Eng.* **2011**, 35, 1, 106–120.
216. Alaña, J. E., Theodoropoulos, C. Optimal spatial sampling scheme for parameter estimation of nonlinear distributed parameter systems, *Comput. Chem. Eng.* **2012**, 45,38–49.
217. Mehra, R. Optimal inputs for linear system identification, *IEEE Trans. Automat. Contr.* **1974**, 19(3).
218. Walter, E., Pronzato, L. Qualitative and quantitative experiment design for phenomenological models—A survey, *Automatica* **1990**, 26(2) 195–213.
219. Nahor, H. B., Scheerlinck, N., Van Impe, J. F., Nicolaï, B. M. Optimization of the temperature sensor position in a hot wire probe set up for estimation of the thermal properties of foods using optimal experimental design, *J. Food Eng.* **2003**, 57(1), 103–110.
220. Papadimitriou, C. Optimal sensor placement methodology for parametric identification of structural systems, *J. Sound Vib.* **2004**, 278(4–5), 923–947.
221. Joshi, S., Boyd, S. Sensor Selection via Convex Optimization, *IEEE Trans. Signal Process.* **2009**, 57(2).
222. Waldraff, W., Dochain, D., Bourrel, S., Magnus, A. On the use of observability measures for sensor location in tubular reactor, *Journal of Process Control* **1998**, 8(5–6), 497–505.
223. López, T., Alvarez, J. On the effect of the estimation structure in the functioning of a nonlinear copolymer reactor estimator, *J. Process Control* **2004**, 14(1), 99–109.
224. Vande Wouwer, A., Point, N., Porteman, S., Remy, M. An approach to the selection of optimal sensor locations in distributed parameter systems, *J. of Process Control* **2000**, 10(4),291–300.
225. El Jai, A. Distributed systems analysis via sensors and actuators, *Sensors Actuators A Phys.* **1991**, 29(1), 1–11.
226. Kubrusly, C. S., Malebranche, H. Sensors and controllers location in distributed systems—A survey, *Automatica* **1985**, 21(2), 117–128.
227. Omatu, S., Koide, S. Soeda, T. Optimal sensor location problem for a linear distributed parameter system, *IEEE Trans. Automat. Contr.* **1978**, 23(4).
228. Olanrewaju, M. J., Al-Arfaj, M. A. Estimator-based control of reactive distillation system: Application of an extended Kalman filtering, *Chem. Eng. Sci.* **2006**, 61(10), 3386–3399.
229. Harris, T. J., Macgregor, J. F., Wright, J. D. Optimal sensor location with an application to a packed bed tubular reactor, *AIChE J.* **1980**, 26(6), 910–916.
230. Colantuoni, G., Padmanabhant, L. Optimal sensor locations for tubular-flow reactor systems, *Chem. Eng. Sci.* **1977**, 32(9), 1035–1049.
231. Kumar, S., Seinfeld, J. H. Optimal location of measurements in tubular reactors, *Chem. Eng. Sci.* **1978**, 33(11), 1507–1516.
232. Musulin, E., Benqlilou, C., Bagajewicz, M. J., Puigjaner, L. Instrumentation design based on optimal Kalman filtering, *J. Process Control* **2005**, 15, 6, 629–638.
233. Sumana, C., Venkateswarlu, C. Optimal selection of sensors for state estimation in a reactive distillation process, *J. Process Control* **2009**, 19(6), 1024–1035.
234. Watanabe, K., Sasaki, M., Himmelblau, D. M. Determination of optimal measuring sites for fault detection of non-linear systems, *Int. J. Syst. Sci.* **1985**, 16(11), 1345–1363.
235. Madron, F., Veverka, V. Optimal selection of measuring points in complex plants by linear models,

AIChE J. **1992**, 38(2), 227–236.
236. Ali, Y., Narasimhan, S. Sensor network design for maximizing reliability of linear processes, *AIChE J.* **1993**, 39(5), 820–828.
237. Bagajewicz, M. J. Design and retrofit of sensor networks in process plants, *AIChE J.* **1997**, 43(9), 2300–2306.
238. Raghuraj, R., Bhushan, M., Rengaswamy, R. Locating sensors in complex chemical plants based on fault diagnostic observability criteria, *AIChE J.* **1999**, 45, 2, 310–322.
239. Müller, P. C., Weber, H. I. Analysis and Optimization of Certain Qualities of Controllability and Observability for Linear Dynamical Systems, *Automatica* **1972**, 8(3), 237–246.
240. Singh, A. K., Hahn, J. Sensor location for stable nonlinear dynamic systems: Multiple sensor case, *Ind. Eng. Chem. Res.* **2006**, 45(10), 3615–3623.
241. Brewer, J., Huang, Z., Singh, A. K., Misra, M., Hahn, J. Sensor Network Design via Observability Analysis and Principal Component Analysis, *Ind. Eng. Chem. Res.* **2007**, 46, 8026–8032.
242. Dochain, D., Tali-Maamar, N., Babary, J. P. On modelling, monitoring and control of fixed bed bioreactors, *Comput. Chem. Eng.* **1997**, 21(11), 1255–1266.
243. Van Den Berg, F. W. J., Hoefsloot, H. C. J, Boelens, H. F. M., Smilde, A. K. Selection of optimal sensor position in a tubular reactor using robust degree of observability criteria, *Chem. Eng. Sci.* **2000**, 55(4), 827–837.
244. Alvarez, J., Romagnolit, J. A., Stephanopoulos, G. Variable measurement structures for the control of a tubular reactor, *Chem. Eng. Sci.* **1981**, 36(10), 1695–1712.
245. Romagnoli, J., Alvarez, J., Stephanopoulos, G. Variable measurement structures for process control, *Int. J. Control* **1981**, 33(2), 269–289.
246. Hermann, R., Krener, A. Nonlinear controllability and observability, *IEEE Trans. Automat. Contr.* **1977**, 22(5).
247. Athans, M. On the determination of optimal costly measurement strategies for linear stochastic systems, *Automatica* **1972**, 8(4), 397–412.
248. Fahroo, F., Demetriou, M. A. Optimal actuator/sensor location for active noise regulator and tracking control problems, *J. Comput. Appl. Math.* **2000**, 114(1), 137–158.
249. Punithakumar, K., Kinrubarajan, T., Hernandez, M. Multisensor deployment using PCRLBS, incorporating sensor deployment and motion uncertainties, *IEEE Trans. Aerosp. Electron. Syst.* **2006**, 42(4), 1474–1485.
250. Alonso, A. A., Kevrekidis, I. G., Banga, J. R., Frouzakis, C. E. Optimal sensor location and reduced order observer design for distributed process systems, *Comput. Chem. Eng.* **2004**, 28(1–2), 27–35.
251. Jørgensen, S. B., Goldschmidt, L., Clement, K. A sensorlocation procedure for chemical processes, *Comput. Chem. Eng.* **1984**, 8(3–4), 195–204.
252. Morari, M., O'Dowd, M. J. Optimal sensor location in the presence of nonstationary noise, *Automatica* **1980**, 16(5), 463–480.
253. Morari, M., Stephanopoulos, G. Studies in the synthesis of control structures for chemical processes: Part III: Optimal selection of secondary measurements within the framework of state estimation in the presence of persistent unknown disturbances, *AIChE J.* **1980**, 26(2), 247–260.